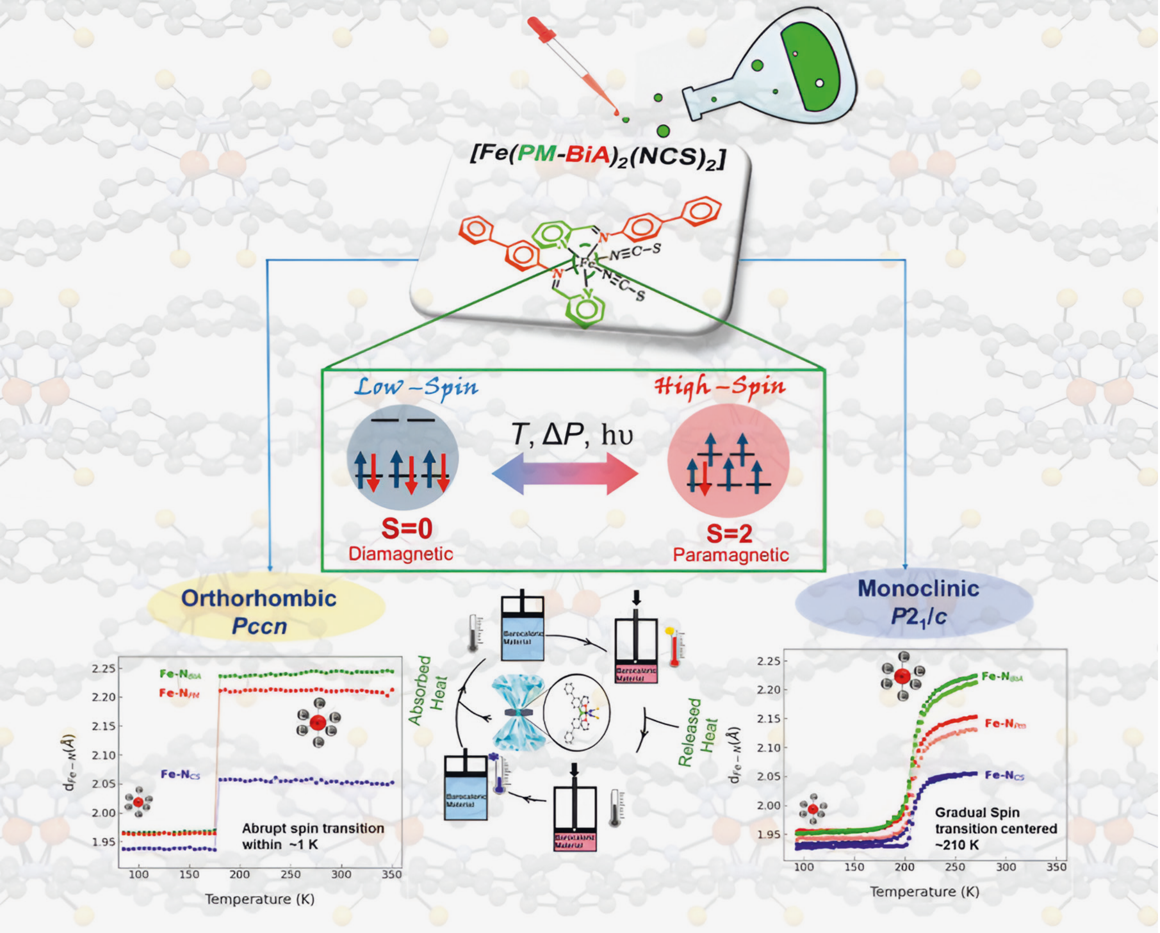

Elucidation of Barocaloric Effect in Spin Crossover Compounds

Hend Salim Abdel Raof Shahed

Energie & Umwelt / Energy & Environment
Band / Volume 630
ISBN 978-3-95806-758-5

Mitglied der Helmholtz-Gemeinschaft

JÜLICH
Forschungszentrum

Schriften des Forschungszentrums Jülich
Reihe Energie & Umwelt / Energy & Environment Band / Volume 630

Forschungszentrum Jülich GmbH
Jülich Centre for Neutron Science (JCNS)
Quantenmaterialien und kollektive Phänomene (JCNS-2/PGI-4)

Elucidation of Barocaloric Effect in Spin Crossover Compounds

Hend Salim Abdel Raof Shahed

Schriften des Forschungszentrums Jülich
Reihe Energie & Umwelt / Energy & Environment Band / Volume 630

ISSN 1866-1793 ISBN 978-3-95806-758-5

Bibliografische Information der Deutschen Nationalbibliothek.
Die Deutsche Nationalbibliothek verzeichnet diese Publikation in der
Deutschen Nationalbibliografie; detaillierte Bibliografische Daten
sind im Internet über http://dnb.d-nb.de abrufbar.

Herausgeber und Vertrieb: Forschungszentrum Jülich GmbH
Zentralbibliothek, Verlag
52425 Jülich
Tel.: +49 2461 61-5368
Fax: +49 2461 61-6103
zb-publikation@fz-juelich.de
www.fz-juelich.de/zb

Umschlaggestaltung: Grafische Medien, Forschungszentrum Jülich GmbH

Druck: Grafische Medien, Forschungszentrum Jülich GmbH

Schriften des Forschungszentrums Jülich
Reihe Energie & Umwelt / Energy & Environment, Band / Volume 630

D 82 (Diss. RWTH Aachen University, 2024)

ISSN 1866-1793
ISBN 978-3-95806-758-5

Abstract

The search for new materials for energy-efficient and environmentally friendly refrigerant technologies is a key challenge to replace conventional vapor compression technology. An attractive alternative approach uses the barocaloric refrigeration cycle, which is based on the adiabatic temperature and isothermal entropy change of a material upon tuning an external hydrostatic pressure.

Recently, spin crossover (SCO) compounds have been pointed out as promising candidates, which exhibit large barocaloric effects: large isothermal entropy changes have been reported for some of these SCO compounds at fairly low hydrostatic pressures (< 1.2 GPa).

In SCO complexes, the central metal ion switches between a low spin (LS) state at low temperature / high pressure and a high spin (HS) state at high temperature/low pressure. The LS to HS transition involves an increase of the spin entropy, but the larger part of the entropy change originates from changes in the intramolecular vibrations. The fundamental understanding of the nature of HS-LS transition and its effect on the physical properties is still being explored fervently, and in particular, the microscopic knowledge of the transition mechanism is essential to tailor new materials.

Although the spin crossover is by essence a molecular scale phenomenon, the large diversity in the spin transition characteristics makes it challenging to predict. The spin transition is controlled by cooperativity, which is a parameter that describes to what extent the spin transition occurs collectively across the material rather than in isolated molecules. The exploration of the intricate interplay between cooperativity and structural changes in the SCO material is in the focus of this thesis. The compound $\mathrm{Fe(Pm\text{-}Bia)_2(NCS)_2}$, where Pm-Bia = ($N$-(2′-pyridylmethylene)-4-amino-bi-phenyl), is an ideal candidate for these studies, as it exists in two different polymorphs which exhibit SCO transitions with significantly different characteristics.

In our work, we attempt to correlate the changes in the macroscopic physical behavior with the microscopic structural changes in the orthorhombic and monoclinic polymorphs of $[\mathrm{Fe(PM\text{-}Bia)_2(NCS)_2}]$; by utilizing single crystal and powder X-ray diffraction, magnetization, and DSC measurements as a function of temperature/ pressure, and scan rate dependence. The detailed structural study based on a considerable quantity of data allows to visualize the structural changes induced by the spin transition in both polymorphs with excellent resolution.

Our results demonstrate that the two polymorphs exhibit markedly different transition behaviors. The orthorhombic polymorph undergoes a swift HS-LS transition within a narrow temperature range, while applying pressure at room temperature fails to induce a spin transition, leading instead to the formation of a superstructure at 2.02 GPa. On the other hand, the monoclinic polymorph ex-

hibits a gradual HS-LS transition across a broad temperature range and exhibits an incomplete HS-LS transition at pressure below 1.36 GPa.

Through a meticulous examination of microscopic features, our investigation delves into the intricate dependencies of the macro- and micro- properties of cooperativity. A principal point of our discussion is the pivotal role played by hydrogen bonding and $\pi - \pi$ interactions in influencing the observed behaviors. We explore how the alteration of these interactions occurs with variations in crystal packing and spin state, providing insights into the underlying mechanisms by applying pressure, temperature, and several scan rates.

The packing in the monoclinic polymorph is governed by $\pi - \pi$ interactions, leading to a temperature-induced spin transition observed over a large temperature range and the formation of random HS and LS entities during the transition. With applying pressure, the HS-LS transition is also induced. During the pressure-induced transition, additional H-bonding is formed, which we assume to be responsible for inhibiting the completion of the HS-LS transition due to space limitations. On the other hand, the orthorhombic polymorph undergoes a swift temperature-induced spin transitions facilitated by H-bonding, with the formation of larger HS and LS domains. Under pressure, H-bonding sterically hinders the spin transitions, and at 2 GPa, a new superstructure is formed.

We observe a scan rate-dependent intermediate state in magnetization measurements for the orthorhombic polymorph for a polycrystalline sample, which is absent in the monoclinic polymorph. Strikingly, this intermediate state, also seen in diffraction experiments, exhibits a doubled c-lattice parameter, similar to the superstructure observed under pressure.

To quantify the cooperativity, we employ the Slichter-Drickamer model to numerically extract entropy, enthalpy, and cooperativity. This quantitative analysis enhances our understanding of the thermodynamic aspects associated with the two polymorphs. Additionally, our study extends to the kinetics of these polymorphs, examining the dependence of magnetization on temperature scan rate. In this context, scan rate studies and isothermal kinetics studies provide valuable insight into the hysteretic behaviour of the spin crossover.

Based on our findings and their interpretation, we propose seeking out potential candidates for barocaloric applications that exhibit robust intermolecular interactions, resulting in enhanced cooperativity and sharp transitions. Such candidates should also possess large room to accommodate volume changes induced by pressure and facilitate pressure-induced transitions without being impeded by space limitations.

Kurzzusammenfassung

Die Suche nach neuen Materialien für energieeffiziente und umweltfreundliche Technologien zur Kühlung ist eine zentrale Herausforderung, um die herkömmlichen Kompressionstechnologien zu ersetzen. Ein attraktiver alternativer Ansatz ist der barokalorische Kältekreislauf, der auf der adiabatischen Temperatur- und isothermen Entropieänderung eines Materials beim Einstellen eines externen hydrostatischen Drucks beruht.

Kürzlich wurden Spin-Crossover-Verbindungen (SCO) als vielversprechende Kandidaten identifiziert, die große barokalorische Effekte aufweisen. So wurden für einige dieser SCO Verbindungen große isotherme Entropieänderungen bei relativ niedrigem hydrostatischen Druck ($<$ 1.2 GPa) berichtet.

In SCO-Komplexen wechselt das zentrale Metallion zwischen einem Niedrigspin (LS) Zustand bei niedriger Temperatur/hohem Druck und einem Hochspinzustand (HS) bei hoher Temperatur/niedrigem Druck. Der Übergang von LS zu HS ist mit einem Anstieg der Spin-Entropie verbunden, jedoch resultiert der größte Teil der Entropieänderung aus Änderungen in den intramolekularen Schwingungen. Das grundlegende Verständnis der Natur des HS-LS-Übergangs und seiner Auswirkungen auf die physikalischen Eigenschaften, und insbesondere die mikroskopische Kenntnis des Übergangsmechanismus ist für die Entwicklung neuer Materialien unerlässlich.

Obwohl der Spinübergang im Wesentlichen ein Phänomen auf molekularer Ebene ist, macht die große Vielfalt der Eigenschaften der Spinübergänge es schwierig, sie vorherzusagen. Der Spinübergang wird von der Kooperativität gesteuert, einem Parameter, der beschreibt, inwieweit der Spinübergang kollektiv im gesamten Material und nicht nur in isolierten Molekülen stattfindet. Die Erforschung des komplizierten Wechselspiels zwischen Kooperativität und strukturellen Veränderungen im SCO-Material steht im Mittelpunkt der vorliegenden Arbeit. Die Verbindung $\mathrm{Fe(Pm\text{-}Bia)_2(NCS)_2}$, mit Pm-Bia = (N -(2′-Pyridylmethylen)-4-amino-bi-phenyl), ist ein idealer Kandidat für diese Studien, da es in zwei verschiedenen Polymorphen vorliegt, die SCO-Übergänge mit deutlich unterschiedlichen Charakteristika aufweisen.

In meiner Arbeit versuche ich, die Veränderungen im makroskopischen physikalischen Verhalten mit den mikroskopischen strukturellen Veränderungen in den orthorhombischen und monoklinen Polymorphen von $\mathrm{[Fe(PM\text{-}Bia)_2(NCS)_2]}$ zu korrelieren; dazu verwende ich Einkristall- und Pulver-Röntgenbeugung, Magnetisierung und DSC-Messungen als Funktion der Temperatur/Druck- und Scanraten-Abhängigkeit. Die detaillierte Strukturstudie, die auf einer beträchtlichen Datenmenge basiert, ermöglicht es, die durch den Spinübergang induzierten strukturellen Veränderungen in beiden Polymorphen mit hervorragender Auflösung zu visualisieren.

Die Ergebnisse zeigen, dass die beiden Polymorphe ein deutlich unterschiedliches

Übergangsverhalten aufweisen. Das orthorhombische Polymorph durchläuft einen schnellen HS-LS Übergang innerhalb eines engen Temperaturbereichs, während die Anwendung von Druck bei Raumtemperatur keinen Spin-Übergang auslöst, sondern zur Bildung einer Überstruktur bei 2.02 GPa führt. Auf der anderen Seite zeigt das monokline Polymorph einen graduellen HS-LS-Übergang über einen breiten Temperaturbereich und zeigt zudem einen unvollständigen HS-LS-Übergang bei einem Druck unterhalb von 1.36 GPa.

Durch eine sorgfältige Untersuchung der mikroskopischen Merkmale werden die komplizierten Abhängigkeiten zwischen den makroskopischen und mikroskopischen Eigenschaften und der Kooperativität verdeutlicht. Eine zentrale Rolle für die beobachteten Phänomene und Vorgänge spielen dabei die Wasserstoffbrücken und $\pi - \pi$- Wechselwirkungen. Die Ergebnisse zeigen, wie sich diese Wechselwirkungen bei Variationen der Kristallpackung und des Spinzustands ändern. Zusätzliche Einblicke in die zugrunde liegenden Mechanismen werden gewonnen, indem Druck, Temperatur und unterschiedliche Scanraten als variable Parameter miteinbezogen werden.

Die Packung der Moleküle im monoklinen Polymorph wird durch $\pi - \pi$- Wechselwirkungen bestimmt, Dies führt zu einem temperaturbedingten Spin-Übergang, der über einen großen Temperaturbereich beobachtet wird, und zur Bildung von kleinen, isoliert vorliegenden HS- und LS-Einheiten während des Übergangs führt. Bei Anwendung von Druck wird der HS-LS-Übergang ebenfalls induziert. Während des druckinduzierten Übergangs werden zusätzliche H-Brücken gebildet. Vermutlich verhindern diese einen vollständig abgeschlossenen Übergang vom HS zum LS Zustand, da innerhalb der Struktur die zusätzliche Volumenverringerung nicht mit dem Platzbedarf der H-Brücken kompatibel ist. Andererseits durchläuft das orthorhombische Polymorph einen raschen temperaturinduzierten Spinübergang, der durch H-Bindungen erleichtert wird, mit der Bildung von größeren HS- und LS-Domänen. Unter Druck behindert die H-Bindung wiederum sterisch die Spinübergänge, und bei 2 GPa bildet sich eine neue Überstruktur.

Bei Magnetisierungsmessungen beobachtet man für das orthorhombische Polymorph einer polykristallinen Probe einen von der Scanrate abhängigen Zwischenzustand, der im monoklinen Polymorph nicht vorhanden ist. Auffallend ist, dass dieser Zwischenzustand, der auch in Beugungsexperimenten beobachtet wird, einen verdoppelten c-Gitterparameter aufweist, ähnlich der unter Druck beobachteten Überstruktur.

Um die Kooperativität zu quantifizieren, verwenden wir das Slichter-Drickamer-Modell, um Entropie, Enthalpie und Kooperativität numerisch zu extrahieren. Diese quantitative Analyse verbessert unser Verständnis der thermodynamischen Aspekte, die mit Phasenübergängen in beiden Polymorphen einhergehen. Darüber hinaus erstreckt sich unsere Studie auf die Kinetik der Übergänge und untersucht die Abhängigkeit der Magnetisierung von der Scanrate. Die Experimente zur Scanrate und zur isothermen Kinetik liefern einen wertvollen Einblick in das hysteretische Verhalten des Spin-Crossovers.

Auf der Grundlage unserer Ergebnisse und ihrer Interpretation wären potenzielle Kandidaten für barokalorische Anwendungen solche, die robuste intermolekulare Wechselwirkungen aufweisen, die zu erhöhter Kooperativität und scharfen Übergängen führen. Zusätzlich sollten diese Materialien auch über einen großen Raum für Volumenänderungen verfügen, so dass die Übergänge nicht durch Platzmangel behindert werden.

Contents

Chapter 1

Introduction

1.1 Motivation

The modern world would not be possible without cooling. Production, supply, and food storage wholly depend on consistently accessible cooling. Even more, health care and the entire medical industry would collapse if refrigeration were unavailable. The technological world surrounding us requires cooling on all scales, from computer chips requiring temperature control to large nuclear power facilities.

The cooling capacity required for each of these distinct uses consumes enormous energy. According to a survey [1], electric fans and air conditioners contribute more than 20% of the world's total electricity demand for buildings. It is expected that by 2050, the energy required to cool residential structures will increase by up to 750% compared to 2010 [2].

A particularly innovative approach to achieving efficient and environmentally friendly cooling is through caloric cooling [3–5]. In caloric materials, applying and removing a particular driving field induces a reversible change in entropy, which gives rise to the associated caloric effect [6]. Applying or withdrawing a field can be carried out adiabatically or isothermally. While the former process causes an adiabatic temperature change, ΔT_{ad}, resulting from an exchange of entropy between the intrinsic degrees of freedom of the material, the latter process causes an isothermal entropy change, ΔS_{iso}. The external driving fields give a name to the caloric effects.

External fields in the magnetocaloric (MCE) and electrocaloric (ECE) effects are magnetic and electric fields [7, 8]. There are two types of mechanical-driven fields: uniaxial stress fields with associated elastocaloric effects and hydrostatic pressure corresponding to barocaloric effects [9, 10], both are summarized under the name of mechanocaloric effect [11]. Depending on how the field is applied, a change in the material's entropy will either result in a temperature change or be related directly to an isothermal release or absorption of heat [5].

A typical caloric cooling cycle is depicted schematically in Figure 1.1. At the initial state of the caloric cooling cycle (step 0), the material is at ambient temperature, and there is no external field. As an external field is applied adiabatically in step (0–1), the caloric material temperature rises and achieves its maximum temperature as a result of the caloric effect. In the subsequent steps (1-2), the material releases heat to a heat sink while maintaining a constant field. The temperature of the caloric element then decreases as the field is removed adiabatically (steps 2-3). In the following step (3), the caloric material can absorb heat from a heat source under constant field conditions. The material returns to its initial state 0, and the cycle begins again. By splitting the two heat flows appropriately, the released and absorbed heat in stages 2 and 3 can be used for cooling and heat pumping.

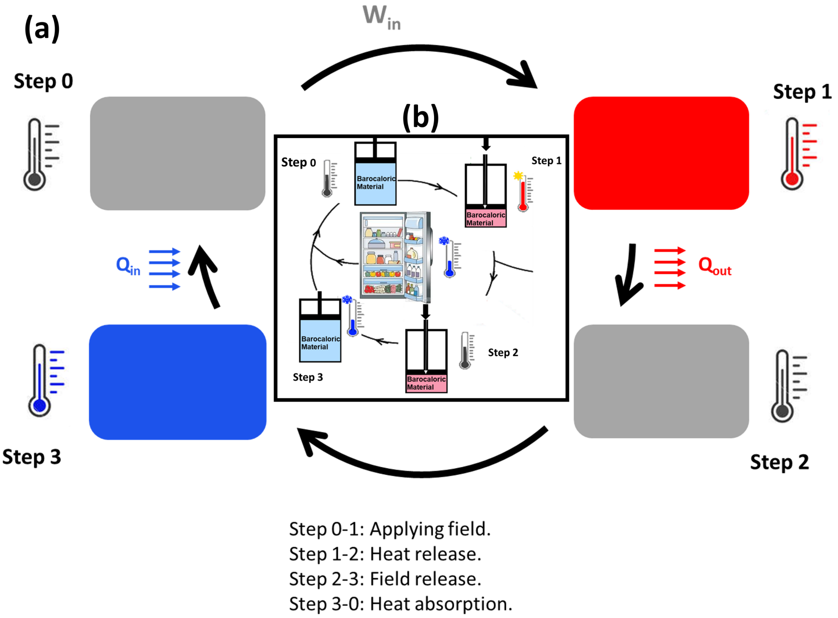

Figure 1.1: **(a)** A generalized caloric cooling cycle. The four processes that make up a caloric cooling cycle start with applying field and heating up the material (step **0-1**), then heat releases to a heat sink (step **1-2**), after that the field releases and the material cools down (steps **2-3**), and finally, the material absorbs heat from a source and the cycle restarts (step **3-0**). **(b)** Shows a schematic diagram of the barocaloric cooling cycle.

While caloric materials respond dynamically to external fields, the exploration of barocaloric materials leads us into a new arena where external hydrostatic pressure becomes a key player. When external hydrostatic pressure is introduced or removed, it induces a change in the volume of the barocaloric material, which is related to a change in the isothermal entropy and/or adiabatic temperature. This is known as the barocaloric effect (BCE) (Figure 1.1**(b)**). In general, the barocaloric effect occurs in all material systems because a system's free energy correlates directly to pressure [12].

Research on barocaloric effects in solid-state materials has received little attention due to the expectation of negligible thermal effects, and it was initially not recognized as a potentially potent independent phenomenon with potential for mainly use in refrigeration systems [13]. In the past, hydrostatic pressure was mainly used as an external stress field to boost the MCE in magnetic materials, with the expectation that doing so would reinforce the first-order character of the magnetic phase transition [14–16]. However, the discovery of enormous BCE in popular magnetocaloric materials like $Ni_{49.26}Mn_{36.08}In_{14.66}$ [17], $Gd_5Si_2Ge_2$[18], and $LaFe_{11.33}Co_{0.47}Si_{1.2}$ [19], suggested that significant caloric effects can be achieved by applying hydrostatic pressure as an independent tuning parameter.

Organic compounds such as neopentylglycol [20], tris(hydroxymethyl)aminomethane [20], and fullerene C_{60} [21], as well as inorganic compounds such as AgI [22], $(NH_4)_2SO_4$ [23], and $(Pr_4N)[Mn(dca)_3]$ (Pr = propyl, dca = dicyanamide) [24] provide a rich playground for the discovery of novel giant-BCE materials. In addition, barocaloric effects are observed in various material systems, such as rubbers [25, 26], and plastic crystals [20, 27]. In 2016, Karl Sandeman [28] recommended investigating the spin crossover class of materials for barocaloric application, as a substantial change in their volume is observed at the transition temperature, $T_{1/2}$. In 2019, a giant barocaloric effect was observed in a spin crossover compound for the first time [29].

The concept of investigating the caloric effect across the SCO transition gained prominence only recently, following Sandeman's observation [28] of the enormous caloric effect for various SCO complexes. He observed, adiabatic temperature shifts close to 8 K and of entropy changes in the range of $80\,\mathrm{J\,kg^{-1}\,K^{-1}}$ at spin transition temperatures $T_{1/2} = 170\,\mathrm{K}$. This effect was obtained by applying a comparatively small pressure of less than 0.1 GPa. By constructing a microscopic model of the spin transition between the LS and HS states, von Ranke [30] explained the barocaloric effect and demonstrated that the caloric contribution is mostly due to phonons. He was able to fit data from the literature for various values of applied pressure using a proposed microscopic (Ising-like) model to characterize the LS/HS fractions, in which the compressibility and intermolecular elastic interaction served as the fitting parameters. Using the mean-field approach, the total entropy of the system was determined, and consequently, the entropy changes at low pressures were deduced. The earlier microscopic model was improved by von Ranke and co-authors [31] by considering electronic, configurational, and lattice contributions. Further experiments were published along with these theoretical achievements [32].

It is worth noting that the large barocaloric effect that results from the significant local volume changes across the SCO transition gives these materials a wide range of potential applications. To achieve a large BCE, it is necessary to have a material that exhibits (i) a substantial volume change near the SCO transition, (ii) a large temperature derivative of the HS molar fraction near the SCO transition, and (iii) negligible thermal hysteresis near the SCO transition. Nevertheless, it is a challenge to meet all of these three requirements simultaneously.

Sandman [28] reported several examples of pressure-induced spin crossover compounds. Among them is the $Fe(Pm\text{-}Bia)_2(NCS)_2$ compound, where PM-Bia = N-(2'-pyridylmethylene)-4-(aminobiphenyl), NCS^- = thiocyanate, which shows a substantial entropy change across the spin transition $\Delta S = 59\,\mathrm{J\,mol^{-1}\,K^{-1}}$ ($84\,\mathrm{J\,kg^{-1}\,K^{-1}}$) [33], which as from differential scanning calorimetry (DSC) measurement. Based on magnetic susceptibility measurements, under applied pressure, the shift in the transition temperature is estimated to be $\partial T_{1/2}/\partial p$ = 66 K/GPa [34]. The maximum possible ΔT_{ad} can be estimated through ΔT_{ad} = - $T\Delta S/C_p$ [5], where c_p is the specific heat capacity $c_p = 2000\,\mathrm{J\,kg^{-1}\,K^{-1}}$ [35, 36]. Thus, the value ΔT_{ad} is 8.4 K due to the high heat capacity, per kg, of these materials. Therefore, the pressure induced the spin transition and required to generate this maximum ΔT_{ad} is equal to 0.12 GPa [28]. It is evident that the pressure required to induce the spin transition is relatively fairly low. This observation, coupled with the substantial entropy change and adiabatic temperature change (ΔT_{ad}) provides the motivation for this in-depth investigation by making this compound a highly promising candidate as a barocaloric material.

The complex Fe(Pm-Bia)$_2$(NCS)$_2$, is among the most extensively studied spin-crossover (SCO) compounds. It crystallizes in two polymorphs (orthorhombic and monoclinic polymorphs), providing a nice example of how small and seemingly important structural changes can lead to significantly different magnetic behavior. The orthorhombic polymorph undergoes an abrupt transition at $T_{1/2\downarrow}$ =175 K and $T_{1/2\uparrow}$ =180 K with a thermal hysteresis of 5 K, while the monoclinic polymorph undergoes a gradual transition centered about 210 K (see Section 7.1, Figure 7.1). It is worth noting that for both polymorphs, the HS and LS crystal structures are well-known under ambient temperature and ambient pressure [33, 37, 38]. However, the crystal structures of the two polymorphs under pressure have not been reported previously.

The objectives of this study are to further investigate and explore the unique SCO behavior of the two polymorphs of the Fe(Pm-Bia)$_2$(NCS)$_2$ complex and intensively map the structural changes throughout the spin transition to provide valuable insights into the temperature-induced structural-property evolution of the two polymorphs. This research aims to deepen our understanding of the nature of the spin-crossover properties exhibited by these two polymorphs and focus on the effects of cooling/heating rates on the spin transition feature. At the macroscopic scale, the transmission efficiency of the spin-state change within the material is determined by its cooperativity. Hence, materials with low cooperativity (weak coupling between SCO centers) will display smooth SCO curves, whereas those with high cooperativity (strong coupling between SCO centers) will exhibit abrupt spin transitions. The transition temperature ($T_{1/2}$) together with the cooperativity defines the SCO behavior. Indeed, weak ligand fields are known to stabilize the HS configuration and consequently, lead to low transition temperatures. Conversely, strong ligand fields stabilize the LS configuration and drive to higher $T_{1/2}$. Nevertheless, both parameters, cooperativity and $T_{1/2}$, have a certain degree of interdependence, since the crystal packing may induce subtle electronic (electron-donating or electron-withdrawing) and/or steric (molecular distortion, internal pressure) effects transmitted through the intermolecular contacts. Thus, the control and understanding of both parameters are of utmost importance in the SCO research area. It should be noted that the presence of polymorphism in this complex offers the possibility of evaluating how the intermolecular interactions influence both key parameters and constitute a singular platform to shed light on the microscopic mechanisms that control the SCO phenomenon in the solid state. Understanding the driving mechanism(s) of the system is not only important for fundamental reasons but also provides scope for the development of multifunctional materials.

1.2 Introduction to spin crossover

The spin crossover (SCO) phenomena were first discovered by Cambi and Szego in the 1930s [39–41]. During their studies on the anomalous magnetism in iron (III) dithiocarbamates complexes, they observed electronic states which were temperature-dependent. Three decades later, White et al. [42] proposed the first interpretations based on the ligand field theory; this theory made it possible to describe these observations as a temperature-dependent thermal equilibrium between two possible ground states predicted for an octahedral coordinated metal ion with a d^5 configuration. The first synthetic iron (II) SCO system is $[Fe(phen)_2(NCS)_2]$ [43], in which Mössbauer spectroscopy showed that a spin transition occurs around a temperature region where the magnetic properties of these compounds show a sudden change [44]. Major milestones in the understanding of the SCO phenomenon were achieved by König [45–47], Gütlich [48, 49], and Kahn [50].

The spin crossover phenomenon describes the change of the spin state from the low-spin (LS) to the high-spin (HS) state of a transition metal ion ($3d^4$-$3d^7$) and vice versa as a result of external stimuli such as temperature [51, 52], pressure [53, 54], or light irradiation [55]. Nevertheless, other stimuli, such as magnetic [48] or electric [56] fields, can also be used. The switching between the two spin states is accompanied by significant changes in molecular shapes and unit cell volumes, driven by changes in metal-ligand distances (see Section 4.1 for more details). The transition is accompanied by magnetic, optical, electronic, and structural changes, thus making SCO compounds favorable for potential applications in, e.g., information storage, optical devices, and displays [57–60]. Due to an increase in magnetic and vibrational entropy, the LS state undergoes a transition to the HS state as the temperature increases. The HS state has a larger spin multiplicity (2S + 1) and broader potential energy well [61], inducing pronounced weakening and lengthening of metal-ligand bonds (see Section 4.1 for more details).

The most studied SCO materials are iron (II) systems, particularly those containing six nitrogen donor ligands $[Fe-N_6]$, but SCO has also been reported for Fe(III) [54] Co(II) [51, 62], Co(III) [63, 64], Cr(II) [65, 66] Mn(II) [67], Mn(III) [52, 68], Ni [69] and Mo(II) [70] complexes. Examples of dinuclear [71, 72], trinuclear [73], tetranuclear [74], or polymer [75] SCO systems have also been studied.

1.3 Polymorphism in spin crossover system

Polymorphism occurs when more than one crystal forms with different arrangements of atoms within the unit cell exists [76, 77]. Even though polymorphs of the same substance share the same chemical composition, they might have different physical and chemical characteristics. Many physical qualities can differ across polymorphic forms due to differences in intermolecular interactions as well as modifications in molecule organization. Polymorphs of a compound may vary from one another in a variety of physical parameters, including melting or sublimation temperature, heat capacity, solubility, density, and refractive index.

Polymorphism can be caused due to a variety of crystallization processes [78–82], and can be divided into several categories; including packing, conformational, synthon, tautomeric, and concomitant. It is worth noting that polymorphs frequently could fall into multiple polymorphism categories. Packing polymorphism happens when molecules in a crystal structure are arranged differently, resulting in different symmetries. Conformational polymorphism is more common in larger, more flexible molecules,[1] since larger and more flexible molecules can rotate around covalent bonds. Therefore, they can take on different forms within a small energy window [83]. Synthon polymorphs exhibit distinct intermolecular interactions, and molecules with multiple hydrogen bonding capabilities seem more likely to form synthon polymorphs [84, 85]. Synthon polymorphism is the least common type of polymorphism [78]. Tautomeric polymorphism happens when an acidic proton is able to move to different locations on the molecule. Concomitant refers to polymorphs that crystallize under identical experimental conditions [86].

Polymorphism effects in SCO have been known since the first study on $[Fe(L_2)(NCX)_2]$ where $L = phen$, $(X = S, Se)$. It was reported by König and his co-workers [87, 88], where differences in the abruptness of a complete and incomplete transition, and the transition temperatures were detected between polymorphs resulting from different synthesis procedures. Since then, polymorphism has received increasing interest in the SCO community in recent years, because polymorphs exhibit different crystal packing, which, in turn, affects the transition behavior of SCO complexes. In light of this, a number of such SCO complexes exhibiting polymorphism were explored, and the relationship between the polymorphs and the nature of the spin transition was thoroughly investigated [89–92]. Additionally, the polymorphism phenomena in SCO compounds provides convincing evidence of the significance of the crystal packing for spin-crossover in the solid state.

1.4 Cooperativity

The different types of spin transitions (see Section 2.1) depend on the degree of cooperativity (see Section 4.5 for more details). Cooperativity explains the interactions between metal sites in which a change in environment at one metal site propagates throughout the material in the solid state via elastic and intermolecular interactions in the lattice [36]. Different intermolecular interactions such as van der Waals [93], π- π stacking [94, 95], and hydrogen bonds [96, 97] are suitable as information transmitters. Each form of contact existing in the solid will influence the strength of intra- and intermolecular interactions in its own way, ultimately influencing the spin transition behavior. Control and comprehension of these variables is still an outstanding question [50].

---

[1] A conformer is an isomer of a molecule that differs from another isomer by rotation of one of the molecule bonds.

It has been reported that the change in bond lengths between the HS and LS states creates "internal pressure" that causes SCO to spread throughout a material [98, 99]. According to these elastic interaction studies, the differences in bond lengths induce the formation of a point defect in the lattice, which can propagate the transition throughout the entire lattice [100, 101]. As a consequence, the transition takes place through the formation of domains of molecules with identical spin state and spreads throughout the lattice. The stronger the metal-lattice coupling, the faster the domains spread and the more abrupt the transition.

According to the literature, there are three different kinds of spin transition mechanisms (Figure 1.2):

- A random mechanism corresponds to the homogeneous distribution of HS and LS entities in the lattice [102, 103].
- A domain mechanism in which the spin state of each entity within a domain is the same [103–107].
- A mechanism characterized by the appearance of an intermediate phase in which HS and LS entities are structurally ordered [108, 109].

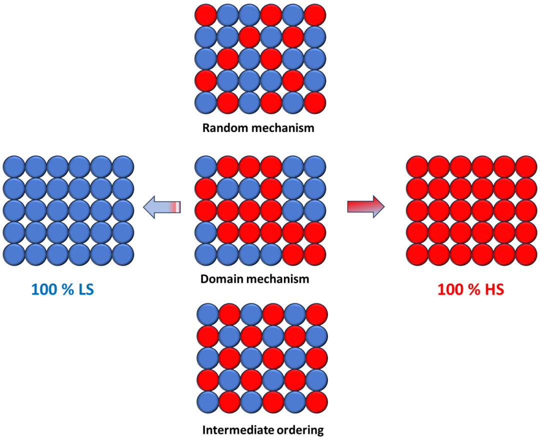

Figure 1.2: The three possible spin transfer mechanisms, with HS entities in red and LS entities in blue.

It is worth noting that pressure-induced structural changes in the material alter the cooperativity of the spin transition and change the stability of the spin state, sometimes leading to changes in the hysteresis breadth or the development of a mixed spin state that can result in steps in the spin transition profile (see Section 2.1 for various forms of spin transition) [53, 110].

1.5 Intermolecular interactions

The formation and structure of molecular crystals—also known as crystal packing are governed by the interactions between molecules [111]. In light of this, one of the most crucial tasks in elucidating the cooperativity of the spin transition is to get a thorough understanding of the intermolecular interactions that are inherent in the solid state, which is essential for manipulating the strength of these interactions. This is especially important in molecular crystals that can pack in many different ways forming polymorphs (see Section 1.3 for more details), because different polymorphs can have different macroscopic properties (magnetism, conductivity, etc.), and many of these macroscopic properties are governed by the relative packing and interactions of the molecules within the crystal [112]. Each polymorph is a local minimum in the free energy of the crystal structures. It is the result of a balance between all the possible intermolecular interactions among the molecules that make up the crystal.

In general, molecular forces can be divided into two categories:

- Short-range interactions: These are primarily of the coulombic and electronic exchange type, which comprise ionic or/and covalent bonds and are the result of orbital overlap. They can be attractive or repulsive and represent the strongest forces in a molecular system.
- long-range interactions: These interactions can be generically characterized as being proportional to r^{-m} (where r is the intranuclear distance and m is a positive integer; the smaller m the stronger the interaction). These interactions include hydrogen bonding, van der Waals, and π - π interactions. These forces are primarily responsible for the formation of supramolecular complexes.

Intermolecular forces are significantly weaker than intramolecular forces of attraction, but they are crucial because they determine the physical properties of compounds, such as their boiling point, melting point, density, and enthalpies of fusion and vaporization. It is worth noting that the hydrogen bond ($25\,\mathrm{k\,cal\,mol^{-1}}$ - $48\,\mathrm{k\,cal\,mol^{-1}}$) is significantly weaker than an ionic bond ($> 700\,\mathrm{k\,cal\,mol^{-1}}$) or covalent bond ($> 200\,\mathrm{k\,cal\,mol^{-1}}$), but stronger than van der Waals ($10\,\mathrm{k\,cal\,mol^{-1}}$-$30\,\mathrm{k\,cal\,mol^{-1}}$) and π-π interactions ($< 10\,\mathrm{k\,cal\,mol^{-1}}$) [113].

Therefore, intermolecular interactions tend to be dominated by hydrogen bonding (see Section 1.5.1 for more details), followed by van der Waals (Section 1.5.2 for details), and π-π interactions (if aromatic components are present, see Section 1.5.3). It is important to understand the intermolecular interactions involved in the formation of SCO systems, as these dictate the spin transition behavior in the solid state.

1.5.1 Hydrogen bond

The hydrogen bond[1] or the hydrogen bridging[2] concept was first used to describe the internal structure of water in 1920. Among all intermolecular interactions,

---

[1] In 1939, Pauling [114] used the term "bond" in a precise and unambiguous manner when he stated: *"Under certain conditions, an atom of hydrogen is attracted by rather strong forces to two atoms, instead of just one, so that it may be considered to be acting as a bond between them."*

[2] Since hydrogen bonds are so distinct from covalent bonds, referring to them as hydrogen bridges would be preferable for some scientists. The term "hydrogen bridge" is sometimes used when referring to weak hydrogen bonding [115, 116].

hydrogen bonds are one of the strongest and, in addition, they are directional interactions. Hydrogen bonding is defined simply as *"a weak electrostatic chemical bond that forms between covalently bonded hydrogen atoms and a strongly electronegative atom with unpaired electrons"* [117]. In other words, this interaction involves a hydrogen atom located between a pair of atoms having a high electronegativity.

There have been various books on hydrogen bonding [118–120] and numerous studies conducted in the literature focus on, e.g., the question of the fundamental nature of a hydrogen bond [121–123].

A hydrogen bond, which is commonly represented as X-$H\cdots Y$, occurs between a functional group $X-H$ in one molecule and an atom Y in a different molecule. Both the proton donor atom X and the proton acceptor atom Y possess electronegative characteristics (Figure 1.3). The donor atom X generally is a carbon, chlorine, fluorine, phosphorus, bromine, sulfur, iodine, nitrogen, or oxygen atom, which is covalently bonded to a hydrogen atom ($-CH$, $-ClH$, $-FH$, $-PH$, $-BrH$, $-SH$, $-IH$, $-NH$, or $-OH$); their high electron attraction causes the hydrogen to take on a slight positive charge. The acceptor atom, typically F, N, P, S, Br, I, or O, often has an unshared electron pair, or "lone pair", which gives it a slightly negative charge. This helps to create the negative electrostatic charge that attracts the slightly positive hydrogen atom bonded to the donor atom. Therefore, due to electrostatic attraction, the donor atom effectively shares its hydrogen with the acceptor atom, forming a bond.

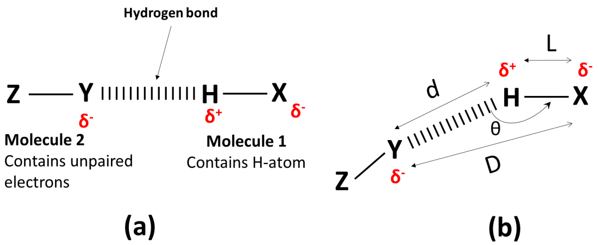

Figure 1.3: **(a)** Description of a hydrogen bond; X is the donor atom, partially negative charged, H is partially positive charged, and Y is the acceptor atom which has lone electrons negatively charged. **(b)** illustrates the definitions of the parameters d, D, L, and θ used in the text to describe simple hydrogen bonds: d represents the distance between H and the acceptor atom Y, D represents the distance between the donor atom X and acceptor atom Y, L is the distance between H atom and the donor atom X, and θ is the angle between the donor atom X, the hydrogen H, and the acceptor atom Y in a hydrogen bond.

Hydrogen bonding has been widely investigated using both spectroscopic and structural tools, including IR and NMR spectroscopy, and neutron/X-ray diffraction. The H-bonding interactions lead to a shortening of the $X\cdots Y$ distance, in which the distance becomes less than the sum of the van der Waals radii of the two atoms X and Y, and is followed by a lengthening of the covalent

$X - H$ distance as if the proton would be almost splitted equally between the two electronegative atoms. As a consequence, a substantial red shift (of the order of $100\,\mathrm{cm}^{-1}$ is observed in the $X - H$ stretching vibrational frequencies [124].

The H-bond distance is critical, as it has been demonstrated that the strength of the bond decays exponentially with distance [124]. Slight deviations from linearity in the bond angle (up to 30°) have only a slight effect on H-bond strength.

The three different forms of H-bonding interactions that are most frequently discussed in the literature are weak,[1] moderate and strong. Table 1.1 gives an overview for determining the strength of the hydrogen bonds. It must be emphasized, though, that the strength of interactions greatly depends on the type of material being considered [124]. Hydrogen bonds are stronger when hydrogen can be withdrawn from atom X as H^+ [125].

Table 1.1: General properties of the three basic forms of H-bonds. Comparisons are shown on the basis of numerical data [126, 127].

H-bonding parameter	**Strong**	**Moderate**	**Weak**
Bond energy ($\mathrm{k\,J\,mol^{-1}}$)	60-120	16-60	< 12
d (Å)	1.2-1.5	1.5-2.2	$>$ 2.2-3.2
L (Å)	0.08-0.25	0.02-0.08	< 0.02
L Vs. d	$\mathrm{L} \approx \mathrm{d}$	$\mathrm{L} < \mathrm{d}$	$\mathrm{L} \ll \mathrm{d}$
D (Å)	2.2-2.5	2.5-3.2	$>$ 3.2-4
θ (°)	170-180	130-180	90-150
Examples	Strong acids	Acids, Alcohols	C- H H-bonds

In the world of molecular compounds, the presence of an acid and its conjugate base is expected to be strong hydrogen bonds of several tens of $\mathrm{k\,J\,mol^{-1}}$ [127]. This strong H-bond is marked by an X—H$\cdot\cdot\cdot\cdot Y$ ($X = F$, O, N) angle of almost 180°, a short $X \cdot\cdot\cdot\cdot Y$ distance, and a long $X - H$ bond distance.

Medium-strength hydrogen bonds are the most common when hydrogen is coupled to electronegative elements (especially oxygen). The range of the θ angle is between 178° and 130°, with a typical θ angle of about 155°-160° [126]. The hydrogen bonding distance can vary by more than 0.5 Å [126].

When hydrogen bonds with a neutral atom like carbon, the resulting hydrogen bond is weak in strength when compared to a bond with oxygen or nitrogen, which results in moderate strength. Weak hydrogen bonds frequently appear when the acceptor group, Y, has π-electrons instead of, e.g., lone pair electrons [128]. The hydrogen bond is also weak when it includes both weak acceptors, such as heavy

---

[1] Some of them exhibit the characteristics of a hydrogen bond, whereas others do not (for example, not all interactions are attractive, and an interaction must be energetically favorable to be a bond).

atoms (Br, S, Se), and weak donors, such as C—H bonds.[1] Distances and angles can cover a wide range, and the low drop-off of electrostatic interactions with distance (1/r dependence) means that even very long separations in the region of 4 Å cannot be ruled out. Weak hydrogen bonds can completely dominate a structure in the absence of strong interactions.

The family of hydrogen bonds known as C-$H\cdots\cdot Y$ ($Y = F$, O, N, S, Cl, Br, I) are recognized for their relatively weak nature. These intermolecular interactions are commonly observed in molecular crystals, particularly in organic molecular crystals or those involving organic ligands [117, 129]. For instance, the Cambridge Structural Database lists a significant number (thousands) of the crystal structure shows connections for the pair C-$H\cdots S$ that are considerably shorter than the total of their respective van der Waals radii (1.8 Å + 1.7 Å = 3.5 Å) [130]. The θ angle (Figure 1.3), which is close to 180° for high directionality can be bent to as low a value as 120° [128]. Figure 1.4 illustrates histograms obtained from the Cambridge Structural Database, depicting $C-H\cdots\cdot S$ distances (Figure 1.4(**a**)) which reveal that the distance shows maxima centered at 3.8 Å, and $C-H\cdots\cdot S$ angles (Figure 1.4(**b**)). Interestingly, only very few crystal structures show a $C\cdots\cdot S$ distance shorter than 3.5 Å along with an angle less than 120°, which could be indicative of the presence of H-bonding.

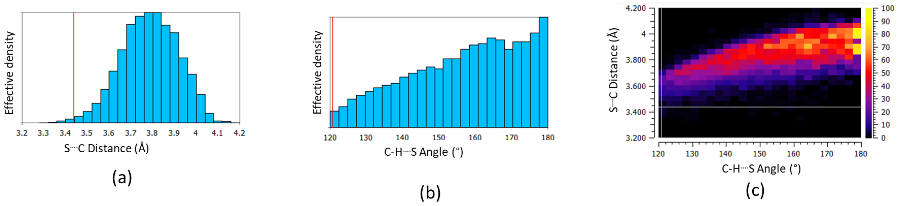

(a)

(b)

(c)

Figure 1.4: Histograms obtained from the CSD for **(a)** the $C\cdots\cdot S$ distances, and **(b)** C - $H\cdots\cdot S$ angles. **(c)** A 3D histogram of the CSD entries contributing to the $C\cdots\cdot S$ distances and $C-H\cdots\ S$ angles.

Although highly precise structural information is now available, the location and refinement of H atom positions still remain limited [131, 132]. In X-ray structure determinations, the distances between the H atoms and the bonded heavier atoms ($C-H$, $N-H$, and $O-H$) are, on average, 0.1 Å - 0.2 Å shorter than the internuclear distances. This occurs as a result of the fact that electrons scatter X-rays and the atomic position determined for a H atom is close to the centroid of the electron density. The latter is moved in the direction of atom X rather than being centered on the H nucleus [123]. The use of neutron diffraction analysis solves this problem because the scattering centers are the atomic nuclei themselves. As a result, the distances acquired by neutron analysis are basically identical to the interatomic distances, making neutron diffraction a crucial approach for determining precise hydrogen bond constants.

---

[1] The $C-H$ bond can act as a hydrogen bond acid in cases where the carbon is attached to an electronegative group or is otherwise acidic, such as in arenes, acetylenes, ethers, chloroalkanes, etc [126].

1.5.2 Van der Waals interactions

Van der Waals forces [133–135] are caused by changes in the charge density of particles. As a consequence, an atom or molecule becomes polarized, having positive charges on one end and negative charges on the other. Electrostatic forces develop between two atoms or molecules as a result of polarization (Figure 1.5), and the atoms or molecules are held together by these weak forces. The radius of van der Waals is equal to half the spacing between the centers of the two approaching nuclei [130] (Figure 1.6).

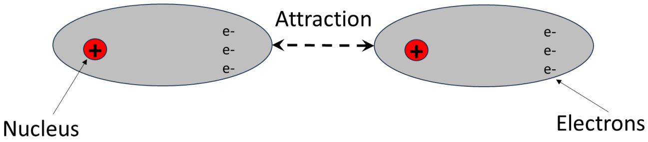

Figure 1.5: Schematic representation of van der Waals interaction.

As the distances between the atoms or molecules grow, van der Waals forces start to vanish due to the reduced interaction between the electron clouds (the force is proportional to the inverse power of the distance between the interacting atoms [136]). Van der Waals forces can either be repulsive forces, which prevent the collapse of all molecules, or attractive forces, which result from interactions between the partial electric charges of polar molecules.

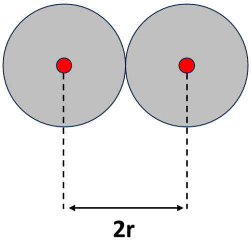

Figure 1.6: Van der Waals radius (denoted by r) equals half the distance between two nuclei of two neighboring molecules in a solid state.

Van der Waals interactions are divided into three categories; Firstly, if molecules have a dipole moment, they can interact with each other in a head-to-tail arrangement (a dipole-dipole interaction). It is worth noting that hydrogen bonds can be considered as dipole-dipole interactions that involve at least one hydrogen atom [116]. Secondly, if one molecule has a dipole moment and the other is nonpolar but polarizable, the polar molecule may produce a dipole in the nonpolar molecule (a dipole-induced dipole interaction). These two dipoles, one of which is permanent and the other of which is induced, will interact the same way as two dipoles. The strength of this interaction is determined by the magnitude of the polar molecule's permanent dipole moment as well as the polarizability of the second molecule [137].

Finally, it is also possible for two nonpolar molecules to interact in attractive, low-energy interactions. These interactions, also known as London dispersion forces, involve a nonpolar molecule inducing a modest instantaneous dipole formed by temporary electron density fluctuations in a surrounding polar molecule [138]. Each interaction type has unique molecular characteristics which are the result of different mechanisms [128].

1.5.3 π - π interactions

Aromatic π-π interactions are non-covalent interactions, also known as π-π stacking interactions. In aromatic compounds,[1] the lowest-energy molecular orbital is filled with 2 electrons (spin up and spin down), and each subsequent energy level is filled with 4 electrons. As a consequence, aromatic compounds are electron-rich as they occupy every bonding orbital without filling any antibonding orbitals, resulting in electron-poor aromatic compounds [139]. π-π interactions play a significant role in the crystal packing of aromatic compounds [126, 139] and determine the properties of functional aromatic materials [140].

There are three fundamental types of π -π interactions as illustrated in Figure 1.7:

- Face-to-Face "Sandwich": In this configuration (Figure 1.7 **(a)**), the two aromatic rings are aligned parallel along the same axis. The angle between the ring planes is almost zero, and the distance between the centroids, should be less than the sum of van der Waal radii ($< 3.4\,\text{Å}$ [130]).
- Displaced Stacking "Parallel displaced": In the stacked configuration (Figure 1.7 **(b)**), the centroids of the aromatic ring do not coincide, but the rings are still next to parallel. Compared to a face-to-face configuration, the distance between the centroids is smaller. Usually, there is an offset angle between the rings of about 20° (Figure 1.8) [141]. Nevertheless, it has been reported that this displaced stacked structure has a contribution from π- σ attractive interactions that increase with increasing the offset angle [142].
- Edge-to-Face "T-shape": In the configuration (Figure 1.7 **(c)**), one aromatic ring is perpendicular to the other, forming a T-like arrangement. The angle between the ring planes and the centroids is about 90°. It is worth noting that edge-to-face interaction due to a slightly electron deficient hydrogen atoms of one aromatic ring and the electron-rich π-cloud of another ring can be considered as weak hydrogen bonds [126]. Edge-to-face π-interactions are common in compounds with three or more aromatic rings [126].

In order to quantitatively anticipate the interaction energies and to explain the variety of geometries observed for π-π stacking interactions, Sanders and Hunter have suggested a model [143], which effectively explains observed experimental data. They consider the π system as a sandwich of two negatively charged π-electron clouds and a relatively positively charged framework (Figure 1.7). They reported that favorable interactions require quadrupolar electrostatic repulsion to be compensated

---

[1] It is worth noting that in molecular orbitals, those lower in energy than an isolated p orbital are classified as bonding, while orbitals higher in energy are antibonding. Orbitals at the same level as an isolated p orbital are called non-bonding orbitals.

by attractive dispersion, with electrostatic effects determining the geometry of the interaction and van der Waals interactions contributing significantly to the magnitude of the observed interaction. However, the van der Waals interaction between aromatic rings is proportional to the area of π overlap, but this cannot explain the actual geometries as this would imply that a stacked geometry is favored as it maximizes π overlap. The observed geometries of π-π interactions must therefore be the result of additional forces acting on the two molecules.

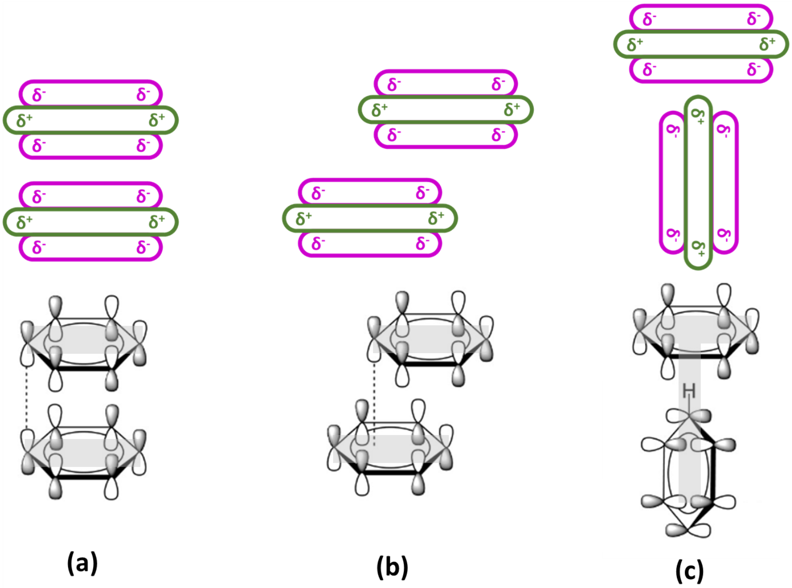

Figure 1.7: Diagram illustrating the three π- π interactions: **(a)** face-to-face "sandwich" , **(b)** displaced stacked "parallel displaced", and **(c)** edge-to-face "T-shape" (*adapted from* [144]). A schematic representation of the charge distribution for each structure is shown.

It is crucial to note that while these classifications provide a conceptual framework, the exact geometry of π-π interactions can vary depending on the molecules involved and their surroundings. For instance, the strength of the interaction can be influenced by other factors, such as substitutes on aromatic rings and the presence of other functional groups. Based on both the centroid-centroid distances and the offset angle created between the ring planes, the strength of π-π interactions is classified into three categories; strong, moderate, and weak.

With the help of theoretical methods, a number of studies have been conducted to obtain an in-depth understanding of the origins, strength, and orientation dependence of π- π interaction [145, 146]. Interestingly, the results from these investigations indicate two particularly preferred configurations: parallel displaced and T-shaped geometries as are very similar in energy, while the sandwich configuration is higher in energy (less stable) [147].

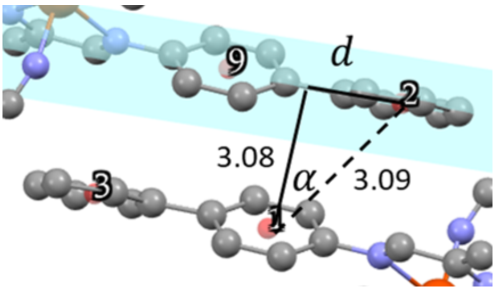

Figure 1.8: The π-π stacking in crystal structure. The distance between two centroids is represented by d, while the offset angle (α) is the angle between the ring normal and centroid-centroid vector. (*Obtained from this study*).

1.5.4 Intermolecular interactions in SCO compounds

Intermolecular contacts serve to modify the electronic structure of a ligand and to transmit information about the spin state along the lattice. Any change in these connections, such as e.g. solvent loss results in a change in the structure-dependent properties.

A denser crystal has a more confined environment around each molecule, which cannot easily tolerate the structural rearrangement associated with a thermal spin transition. This can explain why high spin polymorphs with a high density do not undergo a spin transition, while polymorphs with a lower density do show SCO behavior. It is worth noting that, typically, the density of the high-spin polymorph which does not undergo spin transition is larger than that of the spin-crossover polymorph. Table 1.2 contains examples of compounds where the denser high-spin polymorph is associated with more intermolecular $\pi - \pi$ stacking compared to the lower density SCO polymorph [91, 92, 148, 149].

Table 1.2: Densities of polymorphs exhibiting spin transition or not. Values refer to the room temperature. "ST" stands for spin transition.

Compounds	**Density (ST)** ($\mathrm{g\,cm^{-1}}$)	**Density (No ST)** ($\mathrm{g\,cm^{-1}}$)
$[Fe(btz)_2(NCS)_2]$ [150, 151]	1.525	1.646
$[Fe(abpt)_2(NCS)_2]$ [92, 148]	1.496, 1.498, 1.499	1.519
$[Fe(abpt)_2(NCSe)_2]$ [90]	1.686	1.698
$[Fe(abpt)_2(NCNCN)_2]$ [149]	1.48	1.533

Weber et al. linked the spin-crossover hysteresis in Fe(II) Jager Schiff base complexes and other literature compounds to the number of short intermolecular interactions in the crystal [152]. The higher the number of interatomic contacts[1] between molecules in the lattice, the higher the cooperative spin-crossover in these compounds (see Section 4.5 for more details on cooperativity).

It is challenging to generalize how hydrogen bonding affects spin-crossover. Hydrogen bonding between spin-crossover centers in a crystal is predicted to transmit cooperativity effectively. Compounds such as $[Fe(Im)_2(L^1)]$, [Fe(5,5′-di{nitro}saltrien)] [153, 154], and its derivative $[Fe(mph)_2]ClO_4$ (Hmph = 2-methoxy-6-{pyridine- 2-ylhydrazonomethyl}phenol) [155–157] and $[Fe(tpa)_2(m\text{-}C_6\ OH_2\ O_4)]$- $[BF_4]_2$ (tpa = *tris*-pyrid-2-yl{methyl}amine) [158] are examples of SCO compounds in which the formation of such hydrogen bonds has the potential to play a role in the generation of highly cooperative spin transitions. However, there are many examples of SCO compounds that exhibit weaker cooperativity, despite having intermolecular hydrogen bonding [92, 148, 149]. While hydrogen bonding is commonly observed between a complex and solvent, its impact on the interaction between molecules is generally unpredictable. For instance, compounds containing a solvent exhibit different spin-crossover behaviors, including abrupt transitions [108, 159–161] and gradual transitions [150, 159, 162–165].

Besides hydrogen bonds, π-π stacking are also important intermolecular interactions in SCO despite the fact that they are often ignored, as they are relatively weak. Due to the fact that the majority of spin-crossover complexes contain phenyl rings as ligand donors, π - π interactions are frequently utilized for connecting them together in the crystal. The investigation of complexes in the series $[Fe(abpt)_2(A)_2]$, with A = tcm, tcnome, or tcnoet, has clearly demonstrated that the geometry of these types of interactions directly determines the presence of SCO. π - π interactions have also been used to explain the behavior of the materials $[Fe(pap)_2]X$ ($X^- = BF_4^-$ and ClO_4^-) and $[Fe(qsal)_2]NCX$ (X = S or Se; see Chapter 3), which exhibit strongly cooperative spin transitions with hysteresis widths of 15 −70 K [166].

In conclusion, understanding the spin transition behavior and features depends critically on the arrangement of molecules within the crystal lattice, influenced by intermolecular interactions. It is still difficult to predict exactly how the crystalline structure would change during SCO as it depends critically on the particular molecule and its environment.

---

[1] "Contacts" refer to the close approach between two or more molecular entities. These entities could be atoms or molecules. If the short contacts (< sum of vdW radii) are present, the intermolecular interaction is strengthened.

1.6 Outline

This dissertation is organized as follows: The motivation is followed by an introduction to spin crossover compounds, polymorphism, cooperativity phenomenon, and molecular interactions, with a specific focus on the $Fe(Pm\text{-}Bia)_2(NCS)_2$ compound in **Chapter 1**. We continue with an overview on spin crossover transition in **Chapter 2**. In **Chapter 3** we explore the previously published work on the family of Fe $(Pm\text{-}L)_2(NCS)_2$ compounds, emphasizing the current state of research with regard to the crystal structure and the electronic properties.

The theory of crystal field, phase transitions, and thermodynamic models are introduced in **Chapter 4**. An overview of the experimental techniques used in this study is provided in **Chapter 5**. Moving forward, in **Chapter 6**, the processing procedures for the data treatment that is obtained from DSC, magnetization, low temperature, and high pressure X-ray diffraction are discussed.

Chapter 7 then presents and discuss the results based on the measured data. This chapter is divided into three sections: the determination of thermal properties, the electronic properties of magnetization as functions of temperature, and the crystal structure as a function of temperature and pressure, as well as the cyclic measurements. Finally, future research directions are highlighted in **Chapter 8**.

Chapter 2

Overview on Spin Transition

2.1 Spin transition nature

A convenient way to describe the spin transition behavior in a SCO system is to represent it with a spin transition curve, by plotting the high spin fraction (γ_{HS}) versus temperature or pressure. γ_{HS} represents the relative concentrations or fractions of HS and LS state molecules. γ_{HS} can be derived from measurements of physical properties such as magnetic susceptibility measurements, nuclear environment (Mössbauer spectroscopy), color (UV-vis spectroscopy), vibrational motion (IR & Raman spectroscopy), and bond lengths along with other structural features (diffraction techniques). When γ_{HS}=γ_{LS}= 0.5, the corresponding transition temperature or pressure is donated as $T_{1/2}$, $P_{1/2}$, respectively. Spin transition curves show different forms; the most common types are illustrated in Figure 2.1.

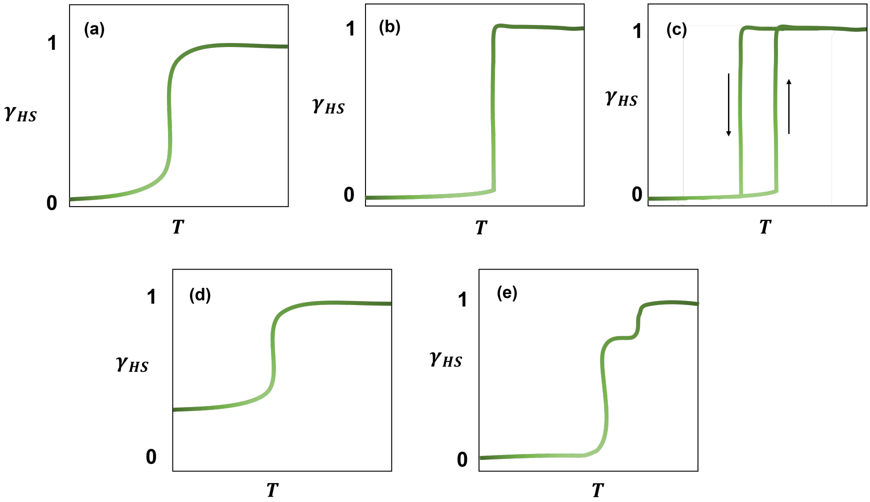

Figure 2.1: High spin fraction as a function of temperature illustrating different types of spin transition curves: **(a)** gradual, **(b)** abrupt, **(c)** with hysteresis, **(d)** incomplete, and **(e)** step-like transition.

- Gradual transition (Figure 2.1**(a)**):
  When the SCO transition takes place over a wide temperature range up to several hundred Kelvin, it is called a gradual transition. Such a transition simply follows Boltzmann's law [167]. This behavior is observed when compounds are in solution or solid state, in systems where the metal centers undergo the transition relatively independently of each other without being influenced by their neighbors. In other words, cooperative interactions are weak for such systems.

- Abrupt transition (Figure2.1**(b)**):
  When the spin transition occurs in a temperature range of less than 10 K, it is called an abrupt transition [167]. The sharp transition is an indication of the presence of (strong) cooperativity in the crystal structure [96].

- Abrupt with hysteresis transitions (Figure 2.1**(c)**):
  The hysteresis is a sign of bistability. It occurs when the system response during warming does not follow the same way as during cooling (see Section 4.3.2 for more details). Such systems exhibit different $T_{1/2}$ during cooling and warming cycles. The presence/absence of hysteresis is crucial for possible applications such as memory devices or molecular switches.

- An incomplete transition (Figure 2.1**(d)**):
  It occurs when a complex is unable to reach either a fully HS or fully LS state during SCO. It can have various origins such as defects and some particular ligand fields being too strong or weak to induce a full spin transition. In addition, it can occur through thermal spin state trapping, where the cooling rate kinetically traps the relaxation of the metal center from a HS to LS state [168], or through structural packing, where the transition to the LS state of certain metal sites prevents the transition of other sites due to the introduction of structural stress [169].

- Step-like transition (Figure 2.1**(e)**):
  It shows a stepwise spin crossover, which occurs usually in dinuclear complexes. Also, it can occur in mononuclear and polynuclear materials as a result of the specific interactions between the metal centers.

These different types of transitions depend on the degree of cooperativity (see Section 4.5). The abruptness of the transition and the hysteresis width are characteristics that are highly dependent on material cooperativity [37, 95, 170, 171].

2.2 Factors influencing spin transition

Numerous factors influence the spin transition, some of which are related to the sample itself (grinding, compression, handling, and preparation), while others are related to physical influences [167] (pressure [60, 172], light irradiation [55, 173], hard X-rays [174], and external magnetic field [175]).

2.2.1 Thermal cycling and scan-rate dependence

If the material's response remains constant over repeated thermal cycles of cooling and heating, it is reproducible. It is important to scan the cooling and heating cycles more than once for samples that undergo SCO with thermal hysteresis because it is common that in the first cycle, an irreversible change is produced (for instance, the loss of solvent molecules at the high temperature, as in the case reported in [176]). Although typically, the subsequent scans overlap after the initial cycle, this is not always the case; therefore, reproducibility should be checked rather than be assumed a priori.

The investigation of spin transition under various scan rates focused mainly on powder samples [177, 178]. However, there are some experimental scan rate studies on single crystals, which were carried out by Hauser et al. [179, 180] on the series of crystals $Zn_{1-x}Fe_x(bbtr)_3(ClO_4)_2$. These studies used dynamical mean-field theory and elastic models for simulation. In addition, investigation by Morgan et al., [181] on an SCO system, which undergoes an abrupt transition, has revealed remarkable unexpected effects on the dependence of the thermal hysteresis width with respect to the temperature scan rate; the spin transition on warming is unaffected by the scan rate while the spin transition on cooling varies with different scan rate. This behavior was attributed to the asymmetric nature of the spin transition in terms of the change in the thermal expansion coefficient of the material during heating and cooling [182]. The hysteresis can be scan rate dependant in a symmetric way, with faster scan rates typically resulting in a larger thermal hysteresis [177, 183]. Real et al. [184] showed that the opposite is also possible by observing a larger hysteresis width when the scan rate is slowed down.

2.2.2 Pressure and magnetic field

The spin crossover transition is known for inducing a significant change in the volume of the metal coordination sphere and, consequently, a change in the volume of the unit cell (see Section 4.4.3 for more details). S. Usha et al.,[185] studied the temperature-dependence of the magnetization of the systems $[Fe(phen)_2(NCS)_2]$ and $[Fe(dipy)_2(NCS)_2]$ at varying pressures. It was found that both compounds exhibit an increase in the spin-crossover temperature as a function of the applied pressure [34, 185]. Interestingly, the compound $[Fe(py)_4(NCS)_2]$ does not undergo a thermal spin crossover but instead, it undergoes a spin transition under high pressure at room temperature [186]. The complexes $[Fe(phen)_2(NCS)_2]$, $[Fe(btz)_2(NCS)_2]$, and $[Fe(py)_2bpym(NCS)_2]$ [186] exhibit a spin crossover at high pressure between 5 kbar - 7 kbar and room temperature.

Literature regarding the determination of the crystal structures of spin crossover systems under high pressure is extremely scarce. Only a few of them have been examined using single-crystal X-ray diffraction at room temperature under pressure. Most of them relate to iron complexes of the $[Fe(Pm\text{-}L)_2(NCS)_2]$ family [38, 187]. Furthermore, no structural investigation of a spin-crossover complex under high pressure at low temperatures has been published so far.

In certain cases, Raman spectroscopy under pressure was efficiently employed to probe the spin state in order to define the pressure domain to be examined in the X-ray examination [109, 188]. These studies have improved understanding of how pressure affects SCO [51, 53, 189, 190] and prompted the development of several theoretical models [99, 191–195] to explain the pressure-driven mechanism.

Static (DC) or pulsed (AC) magnetic fields can also trigger the spin transition process [175]. The first studies carried out with a static field by Gutlich et al. showed that by applying a field of 5.5T, the transition of the compound [Fe(phen)$_2$(NCS)$_2$] was shifted by 0.12 K [196]. To obtain more significant effects, measurements were carried out with a pulsed magnetic field, this technique making it possible to reach up to 60T [48] leading to an irreversible change in the spin state of the complex. However, the observed effects remain weak and require the application of very high fields.

2.2.3 Radiation of light

It has been observed that when a LS compound is irradiated with light of sufficient energy, it can cause a population of the high spin state $^1T_1$ energy level via a spin-allowed transition (satisfying the spin selection rules) from the LS ground state $^1A_{1g}$ at low temperatures (Figure 2.2). This excitation is followed by rapid radiationless decay in the intersystem crossing, from the $^1T_1$ to the $^3T_2$ level and subsequently to the HS $^5T_2$ state. However, since radiative relaxation from the $^5T_{2g}$ to the $^1A_{2g}$ state is forbidden (by the spin selection rules), and decay via thermal tunneling is slow at low temperatures, this results in significant lifetimes for the HS state. This process is known as light-induced excited spin state trapping, or the LIESST effect [197] (Figure 2.2**(a)**). For many Fe(II) compounds, the lifetime of the meta-stable high spin state at temperatures below 50 K ranges from hours to days [173, 198]. It has been demonstrated that the LIESST effect occurs in many systems undergoing thermal transition [61, 173].

It is also possible that at low temperatures, the HS state may return to the LS state using a longer wavelength than that initially used to induce a meta-stable state. In this case, an excitation occurs from the $^5T_2$ to the ^5E_g state, with intersystem crossing to the $^3T_2$ state, again followed by the subsequent relaxation to the $^1A_{1g}$ states. This process is known as reverse LIESST. A schematic illustration of reverse LIESST is shown in Figure 2.2**(b)**.

2.3 Detecting spin crossover behaviour

A remarkable range of experimental techniques has been employed to study and investigate the SCO phenomenon. However, none give a complete picture of the process, and in order to fully characterize the transitions, a combination of techniques is required. The principal techniques employed in this thesis for detecting a spin transition are herein briefly described. Further details of the operation of these and other conventional methods are given in Chapter 5.

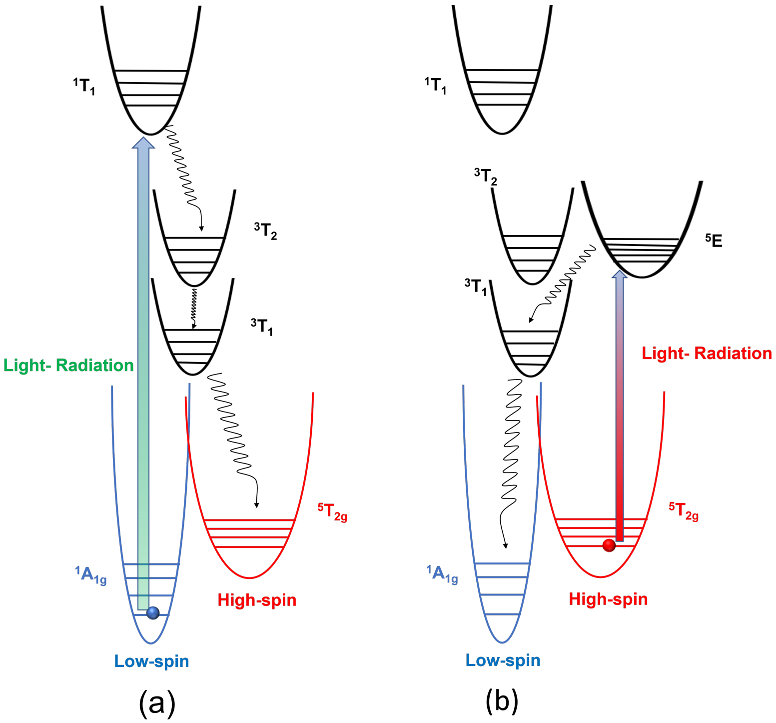

Figure 2.2: The mechanism of the LIESST and reverse-LIESST effect in Fe(II) compounds.

2.3.1 Magnetic measurements

Measurement of the macroscopic magnetic properties is a convenient technique to follow a SCO transition. The magnetic susceptibility χ can be traced as a function of temperature using traditional magnetometers such as SQUID (Superconducting Quantum Interference Device), and χ is sensitive to a change of the spin state (HS: paramagnetic, LS: diamagnetic) for iron(II) complexes and the spin transition profile; this data is used to deduce the spin transition curve (see Sections 4.2 and 2.1). According to Curie's law, χT is constant at all temperatures in a paramagnetic material; therefore, any change in a χT vs. T plot will be uniquely related to SCO in the system and is readily identified.

2.3.2 X-ray diffraction

Both single crystal and powder X-ray diffraction techniques can yield detailed structural insights into the SCO phenomenon, i.e., metal-ligand distances and the deformations of the angles between bonds. By determining the crystal structure of a given SCO sample above and below the transition temperature, the structures can be compared directly, and a potential change of the crystallographic phase can be illustrated. Furthermore, possible intra- and intermolecular interactions such as hydrogen bonding or $\pi - \pi$-stacking can be identified.

Several parameters have been defined which help to quantitatively define the structure of the metal center and relate these characteristics to features of the spin crossover properties. Besides the dramatic changes in the bond lengths and volume of the coordination octahedron, new parameters Σ and ζ have been identified as means of quantifying the distortion of the metal coordination sphere:

- The angle distortion (Σ): which is defined as the summation of the deviations from 90° of the 12 $N - Fe - N$ angles in the coordination sphere of Fe(II) (Figure 2.3). For a perfect octahedron, where all the $L - Fe - L$ angles are 90°, Σ is equal to zero.

$$\Sigma = \sum_{i=1}^{12} |90^\circ - \phi_i| \tag{2.1}$$

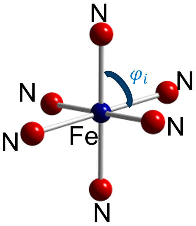

Figure 2.3: Definition of the angle distortion Σ, calculated from the 12 cis angles (ϕ_i), which are 90° in a perfect octahedron.

- The length distortion (ζ): which is defined as the summation of the deviations from the mean of the Fe–L distance (<Fe–L>). For a perfect octahedron, where all the $Fe - L$ distances are equal, ζ is also equal to zero.

$$\zeta = \sum_{i=1}^{6} | < Fe - L > -(Fe - L)| \tag{2.2}$$

- The trigonal distortion (Θ): which is defined as deviation (twist) from the ideal octahedral towards a trigonal prismatic coordination (Figure 2.4). For a perfect trigonal prism, the twist angle is 0°, whereas angles of 60°, are for perfect octahedra. Θ is obtained by the sum of the differences of the absolute value of all 24 unique angles θ (Equation 2.3). In the low spin state, the geometry is close to the perfect octahedron (O_h) while in the high spin state, the geometry of the complex deviates from perfect octahedral (O_h) towards trigonal prismatic geometry (D_{3h}). The spin crossover from LS to HS is typically accompanied by structures with intermediate twist angles [199]. The twist angle Θ is defined as:

$$\Theta = \sum_{i=1}^{24} |60^\circ - \theta_i| \tag{2.3}$$

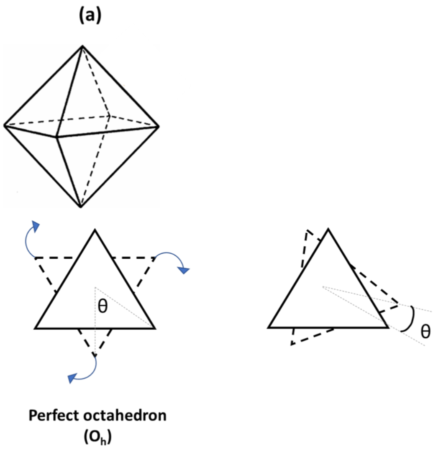

Figure 2.4: Trigonal twist angle (θ) from a perfect octaherdon to a perfect prismatic geometry, passing through intermediate geometry. θ is used to calculate the twist distortion Θ. *Adapted from reference* [199].

2.3.3 Differential scanning calorimetry and other techniques

Changes in thermodynamic properties, for example, enthalpy and entropy, can be examined using calorimetry. A large jump in heat capacity (C_p) occurs at the spin transition temperature, and this has led to understanding and defining the SCO phenomena as an entropy-driven process in the solid state.

The relatively large change in the metal-ligand bond lengths on going through the transition makes vibrational spectroscopies such as Raman and infrared very valuable sources of information on both the structure and nature of the spin transition. The Fe(II)- ligand bands in the region of 250 cm^{-1} for the high spin state move to around 400 cm^{-1} for the low spin state [200]. The change in bond lengths often extends into the ligand system rather than just being confined to the metal-ligand bonds, which provides a sensitive probe for Fe(II) systems containing NCS^- or $NCSe^-$ ligands in which the $N = C$ modes (marker bands) in the region of 2000 cm^{-1} are shifted by about 40 cm^{-1} towards higher frequencies for high to low spin state transition [201]. These methods are also useful for the determination of the spin transition under pressure and/or with varying temperatures.

Chapter 3

Family of [Fe(PM-L)$_2$(NCS)$_2$] Compound

The [Fe(PM-Bia)$_2$(NCX)$_2$] compounds which are studied in this work belong to the [Fe(PM-L)$_2$(NCX)$_2$ family. Therefore, it is worthwhile to have a general overview of this family. Since the late 1990s, the mononuclear iron (II) complexes of the [Fe(PM-L)$_2$(NCX)$_2$] family have been under investigation (Figure 3.1), where PM = N-(2′-pyridylmethylene) and L represents an aromatic sub-unit, forming the base ligand. A neutral complex is obtained by using an NCX$^-$ anion, where X = S or Se. Various aromatic ligands, L, have been selected to investigate the role of intermolecular interactions to propagate and transfer the spin transition of the metal centers throughout the lattice. This family exhibits extremely diverse properties of spin transition, showing differences in their cooperativity ranging from gradual, abrupt to abrupt with hysteresis transition. Also, a large range of transition temperatures ($T_{1/2}$ = 95 K - 243 K) is observed among distinct complexes. Therefore, the compounds of this family offer a unique opportunity to examine the critical coupling between the structure and magnetic properties of spin transition complexes. Between 1997 and 1998, single crystals of four complexes (shown in Figure 3.1) were successfully synthesized and the crystal structures were investigated using X-ray diffraction [34, 37, 59, 102, 202, 203]. The schematic diagram of the four complexes is shown in Figure 3.1 and their nature of transition is summarized in Table 3.1.

The schematic representation of some of this family members is shown in Figure 3.1. Six nitrogen atoms are coordinated to an ion (II) as follows:

- Two thiocyanate (NCS$^-$) arms are coordinated to the iron atom by their nitrogen atom.
- Two N-2′-pyridylmethylene groups are linked to the iron atom via two nitrogen atoms.
- Each of these two groups is connected to an aromatic ligand L.

Table 3.1: Spin transition behavior of the reported SCO compounds in the family of [Fe(PM-L)$_2$(NCX)$_2$] with two NCX branches (X = S, Se).

Compound	**ST behaviour**	**$T_{1/2}$ (K)**	**Ref.**
[Fe(PM-A)$_2$(NCS)$_2$]	Incomplete		[34]
[Fe(PM-Aza)$_2$(NCS)$_2$]	Gradual	189	[102]
[Fe(PM-Bia)$_2$(NCS)$_2$]-Orthorhombic	Abrupt with small hysteresis	$T_{1/2\uparrow}$=173, $T_{1/2\downarrow}$=168	[59]
[Fe(PM-Bia)$_2$(NCS)$_2$]-Monoclinic	Gradual	$T_{1/2\uparrow}$=173, $T_{1/2\downarrow}$=198	[59]
[Fe(PM-PeA)$_2$(NCS)$_2$]	Abrupt with large hysteresis	$T_{1/2\uparrow}$=255, $T_{1/2\downarrow}$=188	[203]
[Fe(PM-PeA)$_2$(NCSe)$_2$]	Abrupt with large hysteresis	$T_{1/2\uparrow}$=305, $T_{1/2\downarrow}$=267	[202]
[Fe(PM-FIA)$_2$(NCS)$_2$]	Abrupt	165	[203]
[Fe(PM-FIA)$_2$(NCSe)$_2$]	Gradual	236	[203]
[Fe(PM-abpt)$_2$(NCS)$_2$]	Gradual	180	[148]

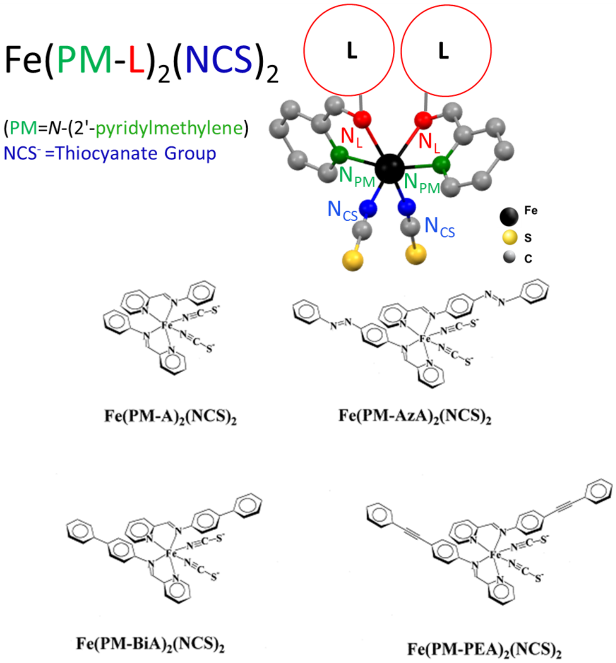

Fe(PM-A)$_2$(NCS)$_2$ Fe(PM-AzA)$_2$(NCS)$_2$

Fe(PM-BiA)$_2$(NCS)$_2$ Fe(PM-PEA)$_2$(NCS)$_2$

Figure 3.1: The [Fe(PM-L)$_2$(NCS)$_2$] family includes, for example, PM = N-(2' - Pyridylmethylene), A= aniline, AzA =4-(Azophenyl) aniline, Bia = 4-(Aminobiphenyl) aniline, , PEA = 4-(phenylethylnyl) aniline, respectively. *Adapted from* [34].

As shown in Figure 3.2, every complex demonstrates different spin transition characteristics. For instance, [Fe(PM-A)$_2$(NCS)$_2$] undergoes an incomplete spin change (60% conversion) [34, 204]. [Fe(PM-PEA)$_2$(NCS)$_2$] exhibits an abrupt spin transition with a 37 K hysteresis, centered at 212 K, with T$_{1/2}$ = 194 K on cooling and T$_{1/2}$ = 231 K on warming [205]. This hysteresis is accompanied by a structural transition upon cooling from a monoclinic, $P2_1/c$, HS phase to an orthorhombic, $Pccn$, LS phase. The orthorhombic polymorph of [Fe(PM-Bia)$_2$(NCS)$_2$] exhibits a sharp spin transition with a modest hysteresis of 5 K, with $T_{1/2}\downarrow = 168$ K and $T_{1/2}\uparrow = 173$ K. On the other hand, the monoclinic polymorph of the [Fe(PM-Bia)$_2$(NCS)$_2$] shows a gradual transition with T$_{1/2}$ at 198 K [33, 37, 59, 95, 206]. [Fe(PM-Aza)$_2$(NCS)$_2$] exhibits a gradual spin conversion without hysteresis at T$_{1/2}$ = 189 K [102]. All these four compounds undergo isostructural spin transitions except for the [Fe(PM-PEA)$_2$(NCS)$_2$] compound.

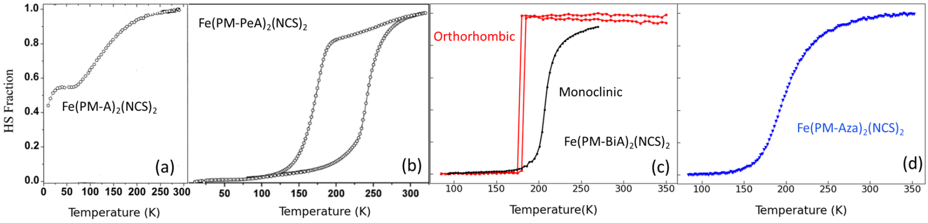

Figure 3.2: HS fraction vs. temperature of the chosen compounds from the [Fe(PM-L)$_2$(NCS)$_2$] family. **(a)** and **(b)** are *adapted from* [34] and [207], respectively. **(c)** and **(d)** are from this study.

The idea behind studying the compounds of this family was that raising the length of the L part of the ligand with aromatic cycles would make the $\pi - \pi$ interactions between molecules stronger, leading to stronger cooperativity. By extending the length of the aromatic ligand, the [Fe(PM-PEA)$_2$(NCS)$_2$] complex revealed a 37 K hysteresis [205]. Since then, the [Fe(PM-L)$_2$(NCS)$_2$] family has continued to grow, although it was soon realized that increasing the size of the aromatic ligands was not suitable for enhancing cooperativity further [95]. In reality, ligand elongation significantly reduced cooperativity and, in some circumstances, eliminated it (for instance, in the case of Fe(PM-TeA)$_2$ (NCS)$_2$). TeA = 4-(aminoterphenyl) displays an exceptionally smooth and imperfect transition [95].

The thermodynamical data presented in Table 3.2, enables us to assess the role of the S/Se substitution which seems to have no major effect on the enthalpy change for the compounds. However, it has a substantial impact on entropy and transition temperature by shifting it to higher temperatures. It has been pointed out that, a much heavier selenium atom replaced at the edge of the molecule will certainly affect the ΔS_{vib} [203]. It has been reported that for the intermolecular interactions where the sulfur is involved for the H-bonding $C-(H)\cdots S$, cooperativity is either maintained or even enhanced by substituting sulfur with selenium. However, the substitution of sulfur with selenium results in a loss of cooperativity if sulfur is not involved in the intermolecular interaction [208].

Table 3.2: Transition temperature $T_{1/2}$ (K), change in enthalpy ΔH ($\mathrm{k\,J\,mol^{-1}}$) and entropy ΔS ($\mathrm{J\,mol^{-1}\,K^{-1}}$) change of the [Fe(L)$_2(NCX)_2$](X = S, Se) family.

Compounds	**T$_{1/2}$**	ΔH	ΔS
[Fe(phen)$_2$(NCS)$_2$] [209]	176.29	8.60	48.78
[Fe(phen)$_2$(NCSe)$_2$] [209]	231.26	11.60	51.22
[Fe(PM-PeA)$_2$(NCS)$_2$]	$T_{1/2\uparrow} = 188$, $T_{1/2\downarrow} = 255$	8.86	59.65
[Fe(PM-PeA)$_2$(NCSe)$_2$]	$\mathrm{T}_{1/2\uparrow} = 305$, $\mathrm{T}_{1/2\downarrow} = 267$	12.8	45.02
[Fe(PM-FIA)$_2$(NCS)$_2$]	165	5.19	31.45
[Fe(PM-FIA)$_2$(NCSe)$_2$]	236	6.68	28.31
[Fe(PM-abpt)$_2$(NCS)$_2$] [148]	180	5.80	33
[Fe(PM-abpt)$_2$(NCSe)$_2$] [148]	224	8.60	38

Variable temperature studies monitoring the unit cell evolution and characterizing only the HS and LS structures were carried out [188]. The various transition profiles observed within this family illustrate the complex relationship between structural parameters and magnetic properties. It is important to understand what causes these differences in order to be able to control the magnetic behavior of spin-transition materials and to make them suitable for different applications. Therefore, it is crucial to investigate chemically similar compounds in order to reduce the parameters that could affect the spin transition features of these material. Several structural studies have made it evident how factors like polymorphism, presence of counteranions, solvent molecules, or host molecules can alter the crystal stacking via hydrogen bonds, $\pi - \pi$, or van der Waals interactions, and hence change the spin transition properties.

3.1 [Fe(PM-Bia)$_2$(NCS)$_2$]

Interestingly one of the most studied spin-crossover materials, Fe(PM-Bia)$_2$(NCS)$_2$ compound, is intriguing in many ways. Firstly, the presence of polymorphs in this compound makes it possible to study the structural properties of SCO and provide more precise insights into the relationship between the polymorphs' crystal structure and the nature of the spin transition. Secondly, Fe(PM-Bia)$_2$(NCS)$_2$ shows modest hysteresis and pressure-induced transitions making it of great interest for potential caloric applications. Therefore, the Fe(PM-Bia)$_2$(NCS)$_2$ compound's ability to undergo reversible transitions under pressure, coupled with its polymorphism nature, opens avenues for exploring its suitability and performance in various applications.

The complex [Fe(PM-Bia)$_2$(NCS)$_2$], where PM-Bia = N-(2'-pyridylmethylene)-4-(aminobiphenyl), NCS$^-$ = thiocyanate (Figure 3.3), was first reported about twenty five years ago by Létard et al., [206]. This complex has two distinct crystallographic forms depending on the synthesis route. The method of precipitation (slow or rapid precipitation in combination with varying concentrations of reagents) determines the structure of the synthesized complex. The first polymorph, obtained by slow precipitation, crystallizes in the orthorhombic, space group *Pccn*, and the second polymorph, obtained by fast precipitation, crystallizes in the monoclinic, space group $P2_1/c$ [59]. The spin transition behavior of the two polymorphs is different, while the orthorhombic polymorph shows a very abrupt SCO transition in a narrow temperature range of about 1 K at $T_{1/2\uparrow} = 181$ K, $T_{1/2\downarrow} = 177$ K and with a thermal hysteresis of 4 K (Figure 3.4**(a)**), the monolinic polymorph shows a gradual spin transition at $T_{1/2} = 210$ K, which, however, stretches over a large temperature range from 150 K to 250 K (Figure 3.4**(b)**). The crystal structures of the orthorhombic and monoclinic polymorphs have been reported only at two temperature points in the HS and LS states in the literature [37, 38, 95]. Table 3.3 lists the lattice parameters of the two spin states of the two polymorphs.

Table 3.3: Lattice parameter and unit cell volume for both polymorphs of $Fe(PM\text{-}Bia)_2(NCS)_2$ in the HS and LS spin states as obtained from this study and from references [33, 37].

	Monoclinic ($P2_1/c$)			
	This study		Reference [37]	
Temperature	93 K	270 K	94 K	293 K
Spin state	**Low-spin**	**High-spin**	**Low-spin**	**High-spin**
a (Å)	17.1496(2)	17.3421(2)	17.28(1))	17.570(5)
b (Å)	12.26250(10)	12.48360(10)	12.37(1)	12.602(5)
c (Å)	16.9243(2)	17.2399(2)	17.080(1)	17.358(5)
β (°)	115.8137(16)	115.7397(15)	115.83(1)	115.68(1)
V ($Å^3$)	3203.98(7)	3361.96(7)	3291(1)	3464(2)

	Orthorhombic (*Pccn*)			
	This study		Reference [33]	
Temperature	85 K	350 K	140 K	293 K
Spin state	**Low-spin**	**High-spin**	**Low-spin**	**High-spin**
a (Å)	12.3332(2)	12.9662(8)	12.370(3)	12.949(7)
b (Å)	14.6757(2)	15.3404(2)	14.764(3)	15.183(2)
c (Å)	18.2772(2)	17.2399(2)	18.281(4)	17.609(5)
V ($Å^3$)	3308.14(8)	3498.2(3)	3339(2)	3462(2)

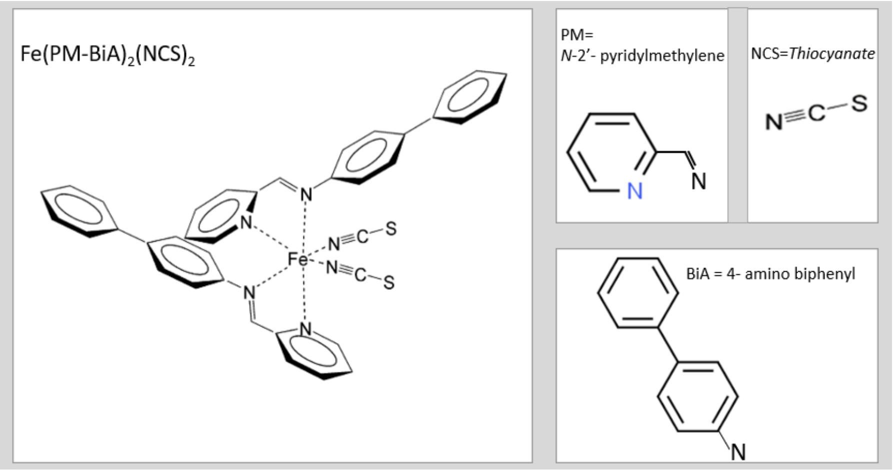

Figure 3.3: Schematic diagram of the ligands making up the Fe(PM-Bia)$_2$(NCS)$_2$ compound.

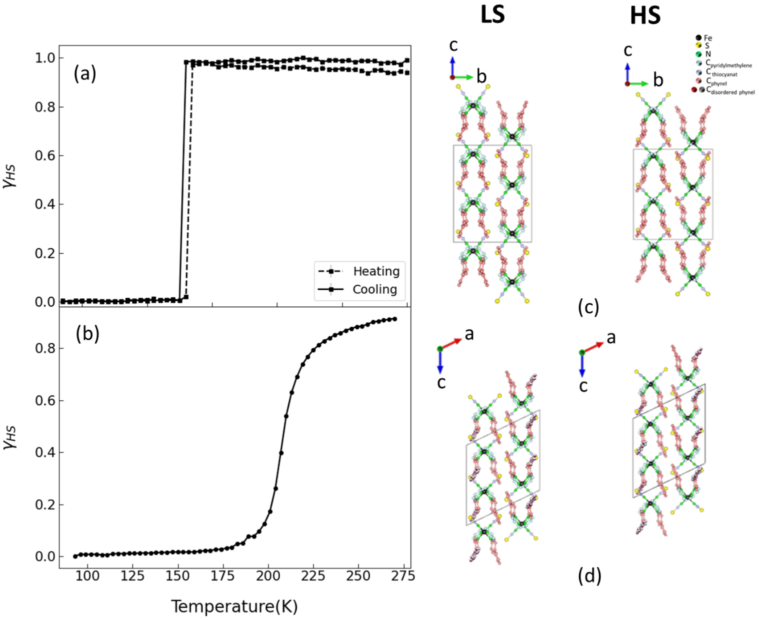

Figure 3.4: Spin transition nature (γ_{HS} vs. T) of the orthorhombic **(a)** and monoclinic **(b)** polymorphs obtained from this study (see Section 7.4). Crystal structure arrangements of the high spin (right) and low spin (left) states of the orthorhombic **(c)** and monoclinic **(d)** polymorphs obtained from this study.

3.2 Effect of pressure on [Fe(PM-Bia)$_2$(NCS)$_2$]

Pressure favors the lower-volume LS state by increasing the energy gap by ($P\Delta V_{HL}$) with respect to the low spin state (see Section 4.4.3). With a substantial entropy change $\Delta S = 59\,\mathrm{J\,mol^{-1}\,K^{-1}}$ ($84\,\mathrm{J\,kg^{-1}\,K^{-1}}$) across the spin transition [33], an ideal condition for harnessing a remarkable caloric effect is provided, which led Sandman [28] to recognize Fe(PM-Bia)$_2$(NCS)$_2$ as a potential candidate for caloric applications.

The effect of pressure on Fe(PM-Bia)$_2$(NCS)$_2$ has been examined using magnetic susceptibility [34], optical reflectivity [210], and neutron diffraction investigations [211, 212].

Ksenofontov [34] has shown that high-pressure magnetic susceptibility measurements of the orthorhombic polymorph, can be divided into two regions of pressure, as illustrated in Figure 3.5. In region I from 0.1 GPa to 0.6 GPa, the spin transition temperature increases, and the hysteresis width becomes narrower, but in region II from 0.73 GPa to 0.8 GPa, the width of the hysteresis loop increases to up to 25 K and the transition becomes monotonically more gradual. A further increase in pressure to about 1.3 GPa has no additional impact. The formation of this large hysteresis for P > 0.7 GPa is fully reversible.

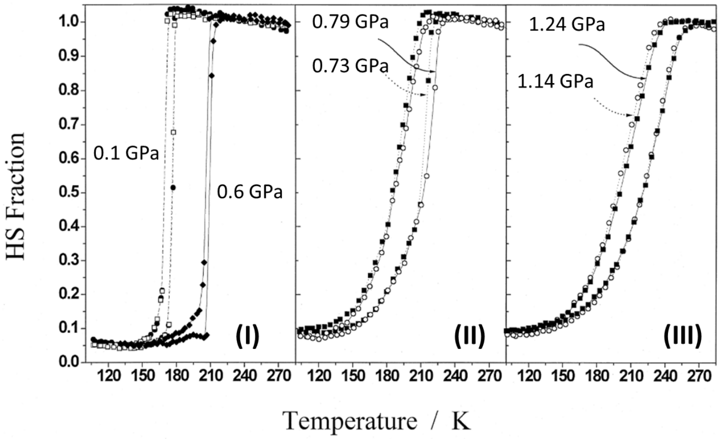

Figure 3.5: Magnetic susceptibility at hydrostatic pressures for the orthorhombic polymorph of the Fe(PM-Bia)$_2$(NCS)$_2$ determined in the heating and cooling modes while compression (filled squares) and decompression (open circles) [60].

Based on neutron powder diffraction under high pressure, it has been suggested that a pressure-induced structural phase transition from the orthorhombic to the monoclinic polymorph takes place at a pressure of ≈ 0.8 GPa [212]. This study suggests that such a structural transition from one polymorph to another could serve as a plausible explanation for the previously observed unusual increase in hysteresis width [211–213].

Research conducted by Rotaru et al. [210] investigated the effect of hydrostatic pressure up to 0.18 GPa on the thermal spin transition of the orthorhombic polymorph of [Fe(PM-Bia)$_2$(NCS)$_2$], using diffuse reflectivity. They concluded that in this pressure range, a progressive transition towards a new cooperative phase takes place. As the diffuse reflectance signature of this latter phase differs from that of both polymorphs, the monoclinic and the orthorhombic one, the novel structural phase was labeled as PIII.

A theoretical study based on DFT and molecular dynamic simulations was recently applied to predict (P, T, hν) phase diagram of [Fe-(PM-Bia)$_2$(NCS)$_2$]. Utilizing the experimental isobaric and isothermal structural parameter dependency, theoretical calculations utilizing DFT and molecular dynamics techniques allowed to characterize the complete (P, T) zones that the experiment barely reaches [188, 213, 214]. At low temperatures and mild pressure, the complete phase diagram shows that the spin state could change along with a change from one polymorph to another, from a LS state orthorhombic polymorph to a HS state monoclinic polymorph. Neutron diffraction experiments combining low temperature and high pressure have verified some aspects of this calculated phase-diagram [211].

Chapter 4

Theoretical Background

4.1 Ligand field theory

An ideal starting point for explaining spin transitions is by utilizing crystal field theory (CFT) [215]. The CFT electrostatic model [216] assumes that the ligands are negatively charged, whereas the metal is positively charged. An electron distribution described by CFT is used to explain the interaction between ligands in coordination complexes with transition metals under various symmetries. For the purpose of this thesis, the crystal field considerations will be focused on the octahedral transition metal complex.

In an ideal isolated metal ion, all five *d* orbitals of the transition metal $\mathrm{d}_{x^2-y^2}$, d_{z^2}, d_{xy}, d_{yz} and d_{xz} are energetically degenerate (Figure 4.1). If the metal is surrounded by a sphere of negative charge, the *d* orbitals would remain degenerate, but their energies will increase due to the repulsion between the electrons of the metal and the ligand, i.e., the *d* orbital will be destabilized relative to the free metal. When the metal ion is surrounded by six ligands in an octahedral geometry, the degeneracy will break, resulting in different sets of orbitals of different energies (Figure 4.1).

Ligand Field Theory (LFT) is an extension of Molecular Orbital (MO) theory to transition metals that rationalizes the interaction of ligands with metal ions [217]. In contrast to CFT, this theory takes a covalent approach by considering the overlap of symmetrical ligand and metal orbitals to generate bonding and anti-bonding molecular orbitals. The analysis of the molecular orbitals (MOs) can help to understand the interaction and establish a connection between the electronic configuration of the metal and the binding energy. Molecular orbitals are usually expressed as linear combinations of atomic orbitals of the different atoms or molecules that constitute the studied system. The bonding MO has a lower-energy orbital and thus is more stable, whereas the antibonding has a higher-energy orbital and is less stable, which is considered a driving force for this interaction [216].

Ligands can, therefore, be classified as σ-donors, π-donors, and π-acceptors (Figure 4.2). σ-interactions occur with an axial orbital overlap and π interactions with lateral overlap. The axial is more efficient than the lateral overlap; thus, σ bonds are generally stronger than π bonds. Ligands with available p-orbitals have the proper orbital symmetry to interact with the d_{xy}, d_{xz}, and d_{yz} orbitals, allowing

M-L π-interactions to occur. There are two types of ligands: those that acting as "π-donors," where electrons are transferred from a full p-orbital in the ligand to an unoccupied one in the metal, and the others that acting as "π-acceptors," where electrons are transferred from full t_{2g} orbitals in the metal to a full p-orbital in the ligand. The latter occurs, especially when the ligand is strongly π-accepting, and is referred to as π-backbonding.

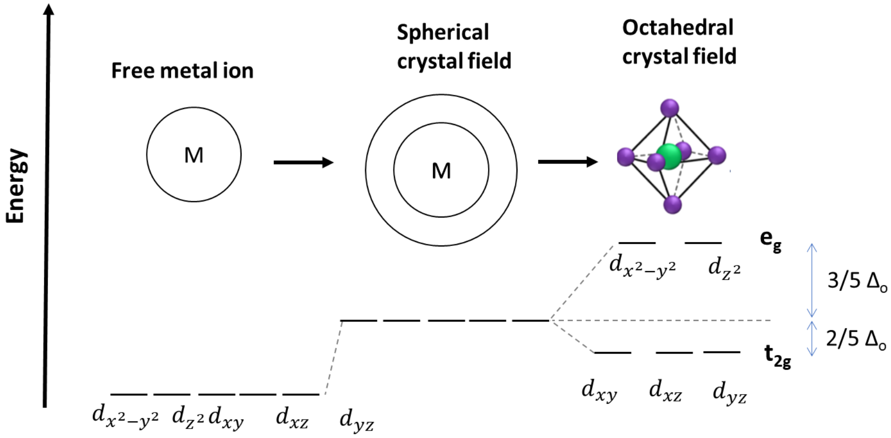

Figure 4.1: Energy Levels of the 5d orbitals: Due to the crystal field splitting, the free metal ion original degenerate 5d orbitals are split into two distinct groups that have different energy levels, denoted as e_g and t_{2g}. *Adapted from* [218].

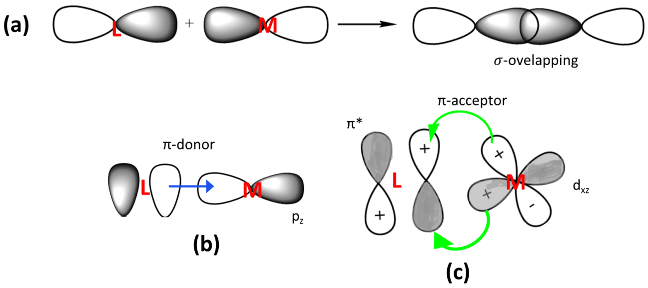

Figure 4.2: **(a)** σ donation. π-interactions between ligand and metal orbitals; **(b)** π-donor and **(c)** π-accpetor. *Taken from* [219].

The molecular orbital distribution will depend on the symmetry of the ligand arrangement. Ligands approach the metal ion along the x-, y-, and z-axes as illustrated in Figure 4.3**(a)**. For octahedral coordination, the d orbitals which are lying along the axes pointing toward the ligands ($d_{x^2-y^2}$ and d_{z^2} orbitals, Figure 4.3**(b)**) will suffer destabilization and experience strong repulsion, which leads to raising energy to a greater extent forming anti-bonding combinations (e_g). On the other hand, the orbitals directed between the axes (d_{xy}, d_{yz} and d_{xz}) are stabilized and exhibit lower energy to form non-bonding orbitals (t_{2g}). Thus, the degenerate *d* orbitals are now split into two sets; 2-fold degenerated (e_g) and 3-fold degenerated (t_{2g}), separated by $\Delta_O = 10$ Dq[1] and the process is called crystal field splitting. This moderates the metal complex to a more stabilized energy by an amount known as the Crystal Field Stabilization Energy (CFSE) (Figure 4.1) [221]. The degree of stabilization and destabilization is inversely related to the degeneracies, $2/5\Delta_O$, and $3/5\Delta_O$, respectively (Figure 4.1). The anti-bonding orbitals e_g ($d_{x^2-y^2}$ and d_{z^2}) have a higher energy than the non-bonding orbitals t_{2g} (d_{xy}, d_{yz} and d_{xz}) (Figures 4.1 and 4.3).

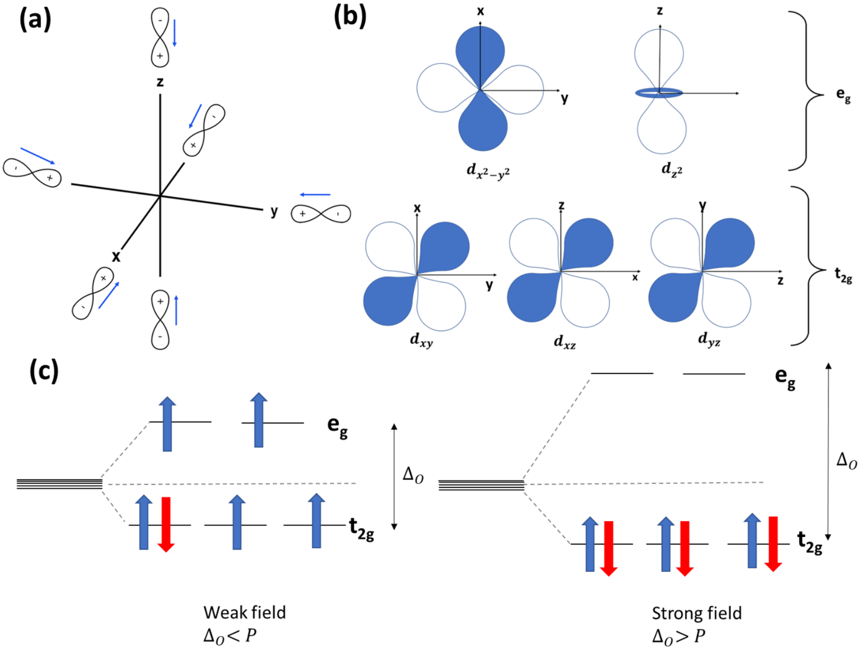

Figure 4.3: **(a)** Octahedral field, in which the central metal ion is located at the origin, and the six ligands are approaching from the +x, -x, +y, -y, +z, and -z directions. **(b)** Spatial orientation of the five *d* orbitals depicting their orientation in space along different crystallographic axes. **(c)** Effect of ligand field strength on the magnitude of Δ_O and the occupation of the d-orbitals for the case of a d^6 metal ion in a weak (left) and a strong ligand field (right).

This thesis primarily investigates a compound consisting of the Fe (II) ion. Consequently, we will focus on the case study of Fe(II), which has 6d-electrons and is in octahedral coordination. The distribution of the 6d-electrons along the two sets of orbitals depends on whether Δ_O is greater or less than the electron pairing energy

---

[1] Dq corresponds to a semi-empirical parameter related to crystal field force [220].

P.[1] When the spin pairing energy (P) is greater than ligand field strength (Δ_O), t_{2g} and e_g orbitals are occupied by obeying Hund's rule (filling the orbitals with a maximum number of unpaired electrons) in such a way that the spins of all electrons are parallel, and according to the Pauli principle, the remaining electrons will align anti-parallel in the lowest energy level and occupy t_{2g} orbitals. This leads to the paramagnetic HS state with configuration $t_{2g}^4e_g^2$ providing the net spin multiplicity S = 2. When the ligands exert a stronger influence, the energy difference Δ_O increases. Above a certain level of ligand field strength, the difference in energy between the low-energy and high-energy orbitals gets too large and results in breaking Hund's rules; all six d-electrons are then in the t_{2g} lower-energy orbitals. Therefore, this spin state has no unpaired electrons, leading to the electronic configuration of $t_{2g}^6e_g^0$ with a net multiplicity of S = 0, resulting in the so-called diamagnetic LS state.

If the energy difference between the LS and HS states is small enough, an external stimulus such as temperature, pressure, light irradiation, or magnetic field can induce a so-called reversible spin transition. Thus, it is possible to explain the SCO phenomena as an intra-ionic electron transfer, in which the electrons switch between the e_g and the t_{2g} orbitals [197].

The magnitude of P is constant for a specific metal ion in a given coordination geometry, as being a function of its electron configuration and effective nuclear charge. Almost all cases of thermal spin transition happen in coordination complexes of 3d metal ions. On the basis of ligand field theory, this is not expected for 4d and 5d transition element compounds, because the strength of the ligand field increases significantly (by approximately 50% from 3d to 4d and also from 4d to 5d) relative to analogous 3d compounds and is generally much greater than the spin pairing energy; thus, virtually all 4d and 5d transition metal complexes exhibit LS behavior. Spin transitions appear to occur most frequently in six-coordinate iron (II) complexes with the subsequent change in electron configurations.

The magnitude of Δ_O depends on several factors, including the metal and its oxidation state, as well as the type, geometry, and number of ligands. The ability of a ligand to split the ligand field depends on its position in the spectrochemical series:

$$\begin{aligned}\textbf{Low } \Delta_O : I^- < Br^- < S^{-2} < NCS^- < Cl^- < N_3^- < F^- < HO^- \\ < O^{-2} < H_2O < SCN^- < Pyd, NH_3 < Bpyd, Phen \\ < ON^{-2} < CN^- < CO^- \quad : \textbf{High } \Delta_O\end{aligned} \tag{4.1}$$

Nevertheless, the ligand field strength Δ_O also depends on the metal-ligand distance $Fe - L$ by:

$$\Delta_O \propto \frac{1}{(Fe-L)^m} \tag{4.2}$$

---

[1] The pairing energy P is the energy cost of placing two electrons in the same orbital, which results from the electrostatic repulsion of adjacent electrons, P typically has a value of around 15 000 cm^{-1} (1.86 eV) for 3d elements [61].

With $m = 5-6$. The $Fe-L$ bond lengths in a HS complex are much larger than those in the corresponding LS complex due to the population of the anti-bonding e_g orbitals (in the low spin state, all the electrons are restricted to the non-bonding orbitals t_{2g}, which affects the electron back-donation between the metal ion and the unoccupied π^* orbitals of the ligands). The lengthening or shortening of the metal-ligand bond length is influenced by both σ and π bonding [197]. For anti-bonding orbitals, the density of electrons in the orbital is concentrated outside the bonding region and acts in such a way that it pulls one nucleus away from the other, causing repulsion between the metal-ligand, resulting in a weakening and lengthening of the chemical bond. Typical values for Fe(II) SCO complexes with N_6 donor sets are 1.95 – 2.00 Å for the LS and 2.1 - 2.2 Å for the HS state, hence the difference $\Delta(Fe-L)$ is about 0.2 Å [61, 222]. Consequently, during the spin conversion, a dramatic change in molecular size and structure occurs, which will be discussed and explored further in this thesis.

The effect of the ligand field strength is further visualized in the corresponding Tanabe-Sugano diagram [223], where the energy of the ground and excited state terms are plotted against the ligand field strength in the units of the so-called Racah parameter B. The Racah Parameter B is a measure of the electrostatic repulsion between individual d electrons [224]. A simplified Tanabe-Sugano diagram for Fe(II) ($3d^6$ configuration) along with the typical octahedral configuration and LS/HS electron arrangements is illustrated in Figure 4.4.

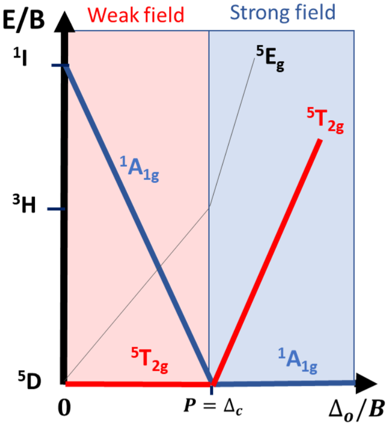

Figure 4.4: Tanabe-Sugano diagram (*adapted from* [197]) for a $3d^6$ ion in an ideal octahedral ligand field. The energy of the ligand field states is plotted against the ligand field strength Δ_0, given in the units of the Racah parameter B of the electron-electron repulsion. For clarity, only the relevant states are emphasized.

If the metal is a free ion then $\Delta_O = 0$ (y-axis). When the ligand field is applied, the free state of the ^5D ion splits into two states: the $^5T_{2g}$ HS ground state and the ^5E_g excited state. $^5T_{2g}$ retains the ground state until the critical value Δ_c of the ligand field strength ($\Delta_O = P$) is reached. When $\Delta_O > \Delta_c$, the $^1A_{1g}$

state is energetically stabilized and becomes the ground state with no unpaired electrons (S=0). SCO compounds are found close to the crossing point Δ_c, where the difference between Δ_O and P is of the same order of magnitude as the thermal energy (k$_B$T). Therefore, a possible transition between $^5T_{2g}$ and $^1A_{1g}$ can occur, leading to SCO behaviour. Thus, in this region, any external perturbation capable of stabilizing one of the two states may result in a spin-state transition. The Tanabe-Sugano diagram is insufficient to understand the phenomenon of spin crossover and the full significance of the Δ_c point because it only depicts the energies of excited states with respect to the stable ground state.

In the harmonic approximation, the potential energy of the high spin ($^5T_{2g}$) and low spin ($^1A_{1g}$) states can be condensed as two parabolic potential wells, displaced vertically and horizontally relative to each other. Due to the higher energy of the e$_g$ orbitals, the adiabatic potential of the HS state $^5T_{2g}$ is shifted towards higher energy and a larger r_{Fe-L} in comparison to the LS state $^1A_{1g}$, in which the vertical displacement depends on the ligand properties.

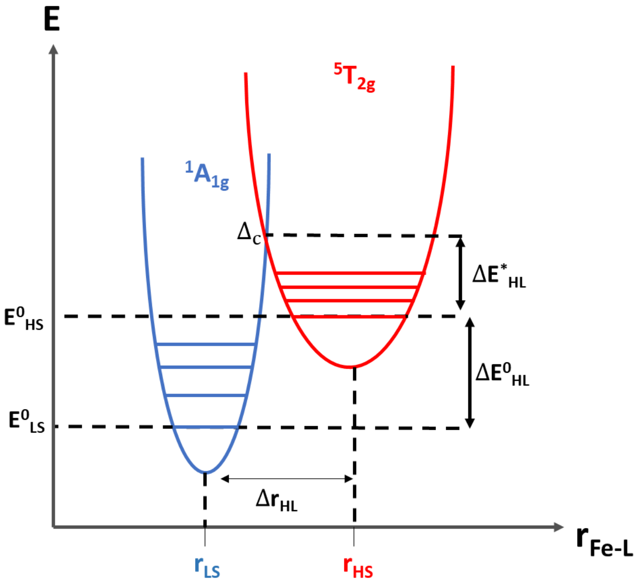

Figure 4.5: A schematic illustration of the metal-ligand distance r_{Fe-L} and the adiabatic potential well for the HS and LS states of a Fe(II) complex. The horizontal lines represent the vibrational energy levels; ΔE^0_{HL} is the zero-point energy difference and ΔE^*_{HL} is the activation energy. The condition for the spin transition is $\Delta E^0_{HL} \approx$ k$_B$T. *Adapted from* [61, 197].

The difference between E^0_{HS} and E^0_{LS} determines the zero-point energy difference (ΔE^0_{HL}) between the two states, while the energy difference between the crossover point (Δ_c) and E^0_{HS} determines the activation energy (ΔE^*_{HL}). When the difference between the zero point energies of the LS and HS states ΔE^0_{HL} falls within the range of available energy $\approx$ k$_B$T, the thermal population of the HS states may occur at high temperatures. The transition happens because the entropy of the HS state is greater (see Sections 4.3 and 4.4, for more details) due to its higher density of vibrational states. The increase in the vibrational density of state is a consequence of the relationship between angular frequency (ω) and momentum (k), as described by the density of state expressions (DOS) $D^{(1D)}(\omega) = \frac{1}{\omega}\frac{1}{d\omega/dk}$ and $D^{(3D)}(\omega) = \frac{k^2}{2\pi^2}\frac{1}{d\omega/dk}$ [225].[1] The potential energy (V) of the molecule, when the distance between the two atoms r is not equal to the bond length ($r - r_0$), is given by:

$$V = \frac{1}{2}k(r - r_0)^2 \tag{4.3}$$

where k stands for bond stiffness parameters (which is the force constant of a spring), and r_0 corresponds to the spring elongation between neighboring molecules. According to Hook's law, the force is proportional to $(r - r_0)$ by:

$$F = -k(r - r_0) \tag{4.4}$$

Thus, the solution of this differential equation is given by:

$$r(t) \propto \sin(\sqrt{\frac{k}{m}}t) \tag{4.5}$$

As ω is the angular frequency of the harmonic motion $\sin(\omega t)$, thus, ω is proportional to the force constant k and the reduced mass of the atom m:

$$\omega = \sqrt{\frac{k}{m}} \tag{4.6}$$

The vibrational energy for the various levels E$_i^{vib}$ (i = HS or LS) is determined by:

$$E_i^{vib} = \hbar\omega_{vib}(n + \frac{1}{2}) \tag{4.7}$$

However, k can be obtained directly from the second derivative of the energy:

$$k = \frac{\partial^2 E}{\partial r^2} \tag{4.8}$$

The metal-ligand bond length in the LS state is shorter (stronger) than the HS state [226]; therefore, resulting in a stiffer LS lattice as compared to the HS lattice (k$_{LS}$ > k$_{HS}$) [227]. The larger k means that the curvature of the potential energy parabola is larger (Equation 4.8), resulting in a narrower, deeper potential energy well around the equilibrium bond length. According to Equation 4.6, the larger force constant results in higher vibrational energy for the LS state ($\omega_{LS} > \omega_{HS}$), which leads to a greater spacing between vibrational energy levels as the number of vibrational levels per unit of energy is larger for the HS state than for the LS state (Equation 4.7). In other words, a stronger bond results in more spaced energy levels and lower vibrational entropy.

---

[1] In more detail, the HS state is characterized by weaker bonds, resulting in smaller bond stiffness k (Equation 4.4) and, consequently, lower angular frequencies ω_{vib} (Equation 4.6). This small angular frequency leads to an increased density of vibrational states, contributing to the higher entropy observed in the high spin state.

4.2 Magnetization

Studying spin crossover phenomena requires an understanding of magnetism, as it is intimately related to the behavior of magnetic moments (spins) in materials and thus provides a direct connection between the electronic configuration of metal ions and their magnetic properties. Thus, the main characterization method of spin crossover compounds is the measurement of the magnetic susceptibility (χ) as a function of temperature (T). Where χ indicates the ability of magnetization in response to an applied magnetic field H (Equation 4.9). This is because the magnetic properties of the HS state are fundamentally different from those of the LS state. In the HS state, there are more unpaired electrons than in the LS state (see Section 4.1), so the paramagnetic contribution to the complex magnetic moment is bigger. According to Curies' law (introduced later), the χ·T product is constant at all temperature values in a paramagnetic material; therefore, any change in a $\chi.T$ vs. T plot may be related to SCO in the system.

$$M = \chi H \tag{4.9}$$

Equation 4.9 is given in the SI system, in which M and H are measured in the same unit *Amperes/m* (A/m), χ is dimensionless. The susceptibility can also be defined as molar magnetic susceptibility χ_M (referring to the number of moles in the material) with the units of $cm^3\ mol^{-1}$, in the cgs system. In this thesis, molar susceptibility is used as the fundamental unit of measurement for magnetic susceptibility.

The response of an ion to a magnetic field is given by two contributions. The first is always present and induces a small magnetic moment opposite to the applied magnetic field. This so-called diamagnetic contribution is proportional to the applied field and is temperature-independent. The plot of the magnetization (M) for a diamagnetic material versus an external magnetic field (H) shows a linear relationship with a negative slope, as illustrated in Figure 4.6.

$$\chi_M^D = \chi_M^D < 0 \tag{4.10}$$

The second, so-called paramagnetic contribution is present only if the ion has a permanent magnetic moment, in our case, originating from the partially filled 3d electrons of Fe^{2+}. The spin is the principal source of magnetic moment $m_s = g\mu_o S$, with g is the Landé g-factor for an electron (g = 2.0023), and S, the net sum of the $3d$ electron spins, $\frac{1}{2}$ for the spin up and $-\frac{1}{2}$ for the spin down. According to Figure 4.3**(c)** for Fe^{2+} in the low-spin state, the spin up and spin down cancel out, leading to no permanent magnetic moment, whereas for the high-spin state, there is a spin moment of $4\mu_B/Fe$.[1] If the permanent moment is present, the paramagnetic contribution is typically much larger than the diamagnetic one. The molecular susceptibility is the algebraic sum of the diamagnetic contribution (χ_M^D) and positive paramagnetic contribution (χ_M^P):

---

[1] μ_B is the Bohr magneton $\mu_B = e\hbar/2m_e$, where e is the elementary charge, $\hbar$ is the reduced Planck constant, and m_e is the electron mass. Its approximate value equals 9.27×10^{-24}J/T ($= 0.927 \times 10^{-20}$ emu, in the cgs unit).

$$\chi_M = \chi_M^D + \chi_M^P \tag{4.11}$$

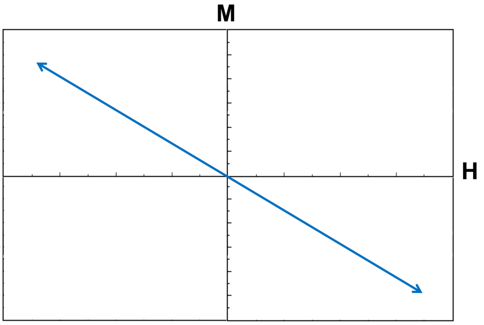

Figure 4.6: Plot of M vs. H for diamagnetism, where $\chi_M = \frac{M}{H} < 0$.

For an ideal octahedral coordination, the orbital magnetic moment contribution is up to $1\mu_B/Fe$ in the high spin state. However, in our case, due to the significant distortion (see Sections 2.3.2 and 7.4.2), this is likely quenched. The applied field tends to orient the permanent moment into its direction, which is counteracted by the disordering effects of the temperature. As a result, the (positive) magnetization, which represents how strongly the material responds to an applied magnetic field, is given by the so-called Brillouin function (see Appendix Section A for more details) of the $\chi = H/T$ going from 0 at x=0 to saturation ($4\mu_B$) as $x \to \infty$. For very small x (which is the case for the range of fields and temperatures covered within this work)[1], the Brillouin function (plotted in Figure 4.7) translates into Curie's law. The magnetization (M) can be described using the Brillouin function ($B_J(x)$) as follows:

$$M = M_s \; B_J(x) \tag{4.12}$$

The magnetization is said to be saturated in M_s given by:

$$M_s = n g_J \mu_B J \tag{4.13}$$

where J is the total angular momentum quantum number, n represents the number of atomic moments of the atomic system, g is Landé g-factor, μ_B is the Bohr magneton. The value of M_s corresponds to the horizontal part of the magnetization curve as shown in Figure 4.7.

---

[1] In sufficiently low magnetic fields and at not too low temperatures $\mu_B \mu_0 H / K_B T \ll 1$. The magnetization of a paramagnetic varies linearly with the applied magnetic field yielding a field-independent susceptibility. However, in higher fields and at lower temperatures the magnetization is no longer a linear function of the magnetic field (and consequently Curie's law is no longer valid).

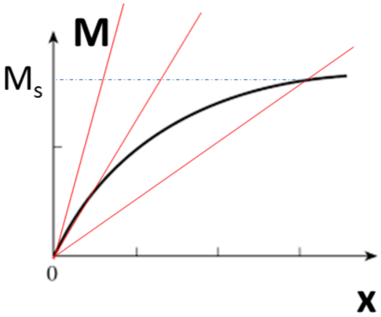

Figure 4.7: The black solid line represents the Brillouin function $B_J(x)$ and red straight lines with a temperature-dependent slope can be used to graphically determine the mean-field magnetization (B_{mf}).

The unit for the magnetic moment is the Bohr magneton (μ_B). For paramagnetic materials, the effective magnetic moment (μ_{eff}) is often considered to be temperature independent.

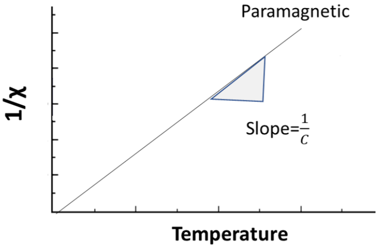

Figure 4.8: The inverse susceptibility of a paramagnetic material that follows Curie's law exhibits a linear relationship with temperature and passes through the origin.

It should be noted that magnetic ordering arises from magnetic interactions between magnetic ions, either dipolar (usually negligible) [228] or exchange (usually super-exchange) [229]. Spin-carrier molecules are usually almost isolated in the crystal, resulting in a very weak magnetic coupling between the spin-crossover sites, which makes it difficult to observe bulk magnetization in the spin-crossover complexes reported up to date. In a spin-crossover system, the spin sites have to be directly connected by a tiny coordinating ligand to form a three-dimensional network in order to establish magnetic ordering. In our case study, there is only one magnetic ion per molecule and only weak intermolecular interaction (e.g., van der Waals); thus, there is no significant magnetic interaction between magnetic ions. As a consequence, our compounds indeed exhibit spin crossover behavior, but no magnetic ordering is observed since the paramagnetic centers are isolated from one another.

4.3 Phase transition

"Phase" refers to a distinct, homogeneous region of a material with certain physical features, separated by a well-defined border. Structural transformations occur as a consequence of a change between two phases. Many materials exhibit phase transitions between two phases with entirely distinct characteristics, such as para- to ferromagnetic or metal-insulator transitions. Nevertheless, the system's physical features can be controlled by triggering the system transition with an external parameter.

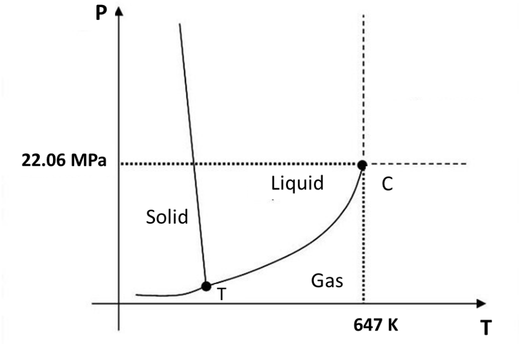

Figure 4.9: P–T diagram for water (solid-liquid-gas phase diagram). The coexistence lines are signified in bold. That solid-liquid-gas coexistence at a triple point "T", and the critical point "C" corresponding critical temperature. *Taken from* [230].

A schematic phase diagram, as illustrated in Figure 4.9, has regions that show the different states or phases of a substance, such as solid, liquid, and vapor. The lines shown in bold are known as phase boundaries or coexistence lines. A point on this line indicates a substance that is occupying two different phases at the same time, whereas crossing the phase boundaries signifies changing from one phase to another, the so-called "phase transition", such as boiling, freezing, or melting. All three coexistence curves can meet at the triple point T, at which all three phases coexist. The region of critical phenomena is represented by point C, the "critical point" corresponding to the "critical temperature". When two distinct phases are present, there is no entropy of mixing. Surface tension causes solids and liquids to cluster; as a result, even when there are many phases, they always remain separated, and the mixing entropy is minimal, if not completely nonexistent [231].

The behavior of thermodynamic parameters when the material is changing from one phase to another can be used to classify transitions. At constant temperature and pressure, equilibrium is determined by minimizing the Gibbs free energy G (Figure 4.10).

$$G = min\{G_A(T,p), G_B(T,p)\} \tag{4.14}$$

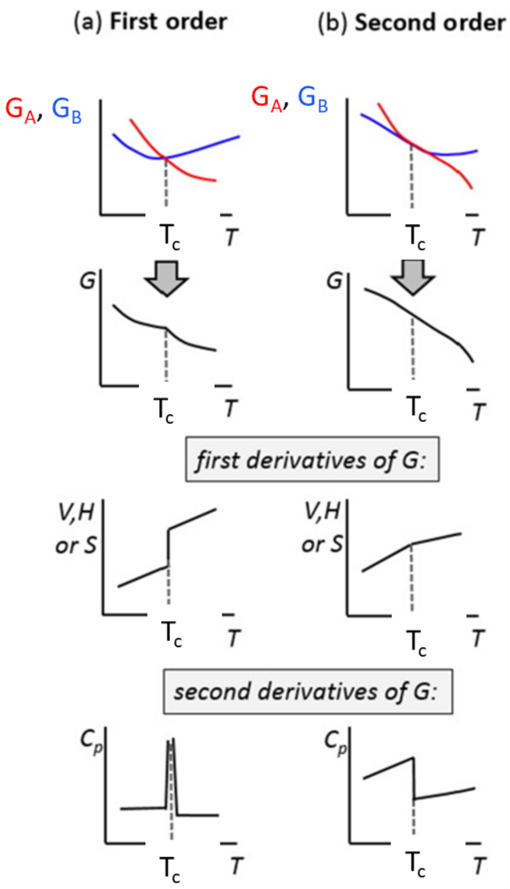

Figure 4.10: **(a)** and **(b)** illustrate the behavior of the Gibbs potential G and its derivatives with respect to temperature for the first and second-order phase transitions at the transition temperature T_c, respectively. First-order phase transitions depicted by the Gibbs free energy correspond to a discontinuity in the entropy S, while second-order (continuous) phase transitions have a corresponding non-discontinuous entropy S whereas the discontinuity is instead seen in the heat capacity C_p. The red and blue curves represent the Gibbs free energy of A and B phases, respectively. *Taken from* [232].

As shown in Figure 4.10, the Gibbs free energy G changes slope at T_c for a first-order transition. A first-order phase transition takes place when a coexistence line exhibits a "kink", when a critical temperature is crossed. Thus, the first derivative of Gibbs free energy shows a discontinuity or singularity (Figure 4.10, Equations 4.15 and 4.16). Since, in this case, the entropy of mixing is absent, one phase completely annihilates the other.

$$(\frac{\partial G}{\partial P})_T = V \tag{4.15}$$

as the slope is negative $(\frac{\partial G}{\partial T})_P$;

$$(\frac{\partial G}{\partial T})_P = -S \tag{4.16}$$

The change in Gibbs free energy G(T, P), which is an essential thermodynamic quantity to account for the effect of temperature and pressure on the system, is described as the difference between the change in enthalpy (ΔH), the product of temperature (T), and the change in entropy (ΔS) of the system (Equation 4.17).

$$\Delta G(T,P) = \Delta H - T\Delta S \tag{4.17}$$

To evaluate the stability of a given phase from a thermodynamic perspective, we consider the Gibbs energy, which is composed of both the enthalpy H and entropy S terms. At equilibrium temperature or pressure, the Gibbs free energies of the two phases are equivalent, so ΔG = 0 (therefore, from Equation 4.18, ΔH = T ΔS).

$$\Delta G = G_A - G_B = \Delta H - T\Delta S = 0 \tag{4.18}$$

The second law of thermodynamics states that the system will tend to minimize its Helmholtz free energy, $F = U - TS$, where U is the system's internal energy and T is the temperature. It is obvious that a system at constant temperature can reduce its free energy in one of two ways: either by increasing entropy S or by decreasing internal energy U. Examining the statistical mechanical expressions for entropy is necessary for gaining a better understanding of the factors that influence phase transitions. The most basic starting point is to utilize Boltzmann's expression for the entropy of an isolated system of N particles in volume V with an energy U.

$$S = k_B \ln(\Omega) \tag{4.19}$$

where the proportionality constant k_B is known as the Boltzmann constant, and Ω represents the total number of (quantum) states available to the system. The most common interpretation of Equation 4.19 is that the number of accessible states of a system is a measure of the "disorder" in that system. The larger the disorder, the greater the entropy (Section 4.1). In general, the entropy of mixing two phases A and B can be approximated by the entropy of mixing an ideal mixture.

$$S_{id}(X) = -Nk_B[X\ln X + (1-X)\ln(1-X)] \tag{4.20}$$

X represents one component's molar fraction: $X_A = \frac{N_A}{N_A+N_B}$. Therefore, if phase separation occurs, $S_{id}(X)$ will always decrease. This suggests that phase separation can only occur if the resulting decrease in energy U is greater than the increase in -TS_{id}.

If, on the other hand, phases A and B are mixed together without interacting with each other, the Gibbs free energy changes smoothly as a function of temperature or pressure, as shown in Figure 4.10. In this circumstance, the role that the mixing entropy plays is particularly significant. The mixing entropy has a significant impact on the smoothness of the Gibbs free energy. Therefore, the first derivative of Gibbs free energy is continuous (as the entropy and volume of the system remain constant[1]);

---

[1] Due to the absence of entropy S in the transition, there is also no enthalpy H in the transition.

on the other hand, the second derivative is discontinuous. This is what is called the second-order transition. As illustrated in Figure 4.10 the second-order phase transition shows a discontinuity in the second derivatives of free energy, i.e., heat capacity C_p (Equation 4.21), thermal expansion (Equation 4.22), and compressibility (Equation 4.23).

$$\frac{\partial^2 G}{\partial T_P^2} = -(\frac{\partial S}{\partial T_p}) = -\frac{C_p}{T} \tag{4.21}$$

$$\frac{\partial^2 G}{\partial P \partial T} = (\frac{\partial V}{\partial T_P}) = V\alpha \tag{4.22}$$

$$\frac{\partial^2 G}{\partial P_T^2} = (\frac{\partial V}{\partial P_T}) = -V\beta \tag{4.23}$$

Ehrenfest defined the order of phase transition as *The order of the lowest derivative of the Gibbs enthalpy G showing a discontinuity at the transition.* Thus, a transition showing a discontinuity in the first derivative of Gibbs free energy with respect to pressure and volume is called a first-order phase transition (Equations 4.15 and 4.16), whereas a transition showing a discontinuity in the second derivative of G(T, P) is called a second-order phase transition (Equations 4.21, 4.22, 4.23).

The first-order transition is frequently associated with drastic changes in structure, e.g., in bond lengths and angles. These changes are dramatic near the transition point (discontinuity accompanied with $\Delta S \neq 0$), and associated with significant latent heat. On the other hand, the absence of latent heat[1] identifies the continuous "second-order". As heat is added during a first-order phase transition with a critical temperature of $T_{1/2}$, the temperature remains constant at T = T$_{1/2}$ until all of the matter has transformed into the new phase. The latent heat L is given by $L = \frac{Q}{M} = \frac{T\Delta S}{M}$.

According to Equations 4.15 and 4.16, volume (V) and entropy (S) are the first derivatives of the free energy with respect to pressure (P) and temperature (T), respectively. They can be quantified, for example, using X-ray diffraction and differential scanning calorimetry (DSC), as detailed in Sections 5.4.2, 5.4.3 and 5.3. While DSC is likely the simplest method for testing for phase transitions, not all transitions are effectively detectable using DSC. The technique is particularly effective for first-order transitions, where the heat capacity exhibits a sharp peak, which provides a clear indication of the transition point. Nevertheless, in some cases, the DSC peak may appear broadened, potentially due to specific disruptions caused by disorder within the system undergoing a first-order transition. This disorder can lead to a broader DSC peak, making it more challenging to precisely identify and characterize the transition. Second-order transitions are more challenging to measure because the changes are typically considerably smaller (there is no latent heat).

---

[1] To understand latent heat, consider adding heat to a block of ice at a constant rate. Its temperature gradually rises until we reach 0°C. With the constant addition of heat, it remains constant until all the ice has melted. All the heat input at 0°C is utilized to dissolve the ice without increasing its temperature; this heat is the latent heat of transformation.

Second-order phase transitions are usually reversible. In the case of a first-order phase transition, the internal state of a material may lag behind the change in the external field acting upon it. This is referred to as hysteresis, and it will be discussed further in Section 4.3.2. During the first-order transition, a system absorbs or emits a fixed (and typically substantial) amount of energy.

In the hysteresis zone, an SCO system can be observed in either of two different macroscopic states, depending on its recent history. Thermal hysteresis develops as a result of a change in the transition temperatures depending on whether the transition is approached from low or high temperatures (Figure 4.11). Hysteresis has its origin in a material's local ordering and, in a way, derives from the overall response being slower than the field causing the transition (see Section 4.3.2 for further details).

It is worth noting that the presence of symmetry-breaking is critical for phase transition behavior. A process that breaks symmetry occurs whenever there is a transition from a more symmetrical phase to a less symmetrical phase. For instance, during the fluid-to-solid phase transition (a first-order transition), continuous translation symmetry is broken. Symmetry-breaking transitions can be first- or second-order.

4.3.1 Phase transition in spin crossover

In the early 1960s, Baker and Bobonich [43] reported the first experimental evidence for discontinuous (first-order) spin transitions in the SCO compound [Fe(phen)$_2$(NCS)$_2$] (which König and Madeja [233] later confirmed); however, the presence of a thermal hysteresis loop (see section 4.3.2 for more details) was not yet explicitly reported from the temperature-dependent magnetic susceptibility measurements. Sorai and Seki [209, 234] confirmed the first-order nature of the spin transition in this compound by reporting a sharp anomaly in the heat capacity at the transition temperature from precise differential scanning calorimetry (DSC) measurements.

In a spin crossover transition, the process of the transition can be substantially shifted across the two polymorphs, going from a crossover (gradual spin-state conversion) to a first-order transition (discontinuous change in the HS fraction) [235]. In the case of an abrupt spin transition exhibiting hysteresis, the transition is considered as a first-order phase transition. On the other hand, the gradual spin crossover is a feature of a crossover transition [236]. Nevertheless, a discontinuity in a first-order phase transition causes a significant entropy change compared to a continuous transition. This is a key issue in determining a material's suitability for caloric applications, as discussed in Section 1.1. It is worth noting that some spin crossover compounds undergo a symmetry-breaking structural change accompanied by a spin transition. Several literature reported structural phase transitions and discuss the structure-property relationships in the corresponding compounds [95, 105, 237–239].

4.3.2 Hysteresis

The temperature width of the transitional hysteresis is the key factor influencing the reversibility of (baro)caloric materials. As a consequence of thermal hysteresis, the phase transition on heating does not occur at the same temperature as on cooling, which in turn reduces the range of temperature at which caloric materials can operate, as well as limiting the ΔS available and consequently reducing the thermal efficiency. Thus, one of the main goals of this thesis is to understand how factors such as different scan rates might affect the thermal hysteresis width by elucidating and understanding the mechanisms creating hysteresis.

The origin of hysteresis can be related to extrinsic effects (associated with microstructure) or intrinsic contributions (associated with atomic-scale electrical features).

In the context of the spin crossover, the so-called cooperativity (explained in detail in Section 4.5) causes the formation of macroscopic free energy coupled to the phase transition in the solid, which gives its bistability. Bistability, which refers to the ability of a compound to exist in two different electronic states under similar external conditions, combined with distinct physical properties associated with each spin state, provides these materials with a memory effect for potential applications.

Depending on whether the transition is approached from low or high temperatures, as illustrated in Figure 4.11, thermal hysteresis results in a difference in the transition temperatures. The transition does not take place at the actual equilibrium temperature T_{eq} (when the free energy of the two phases are exactly equal) but rather at higher and lower temperatures that are typically indicated by the letters $T_{1/2\uparrow}$ and $T_{1/2\downarrow}$, respectively, delimiting the metastable (hysteresis) zone.

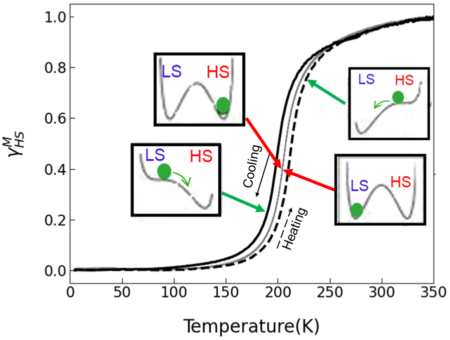

Figure 4.11: A schematic diagram illustrating a thermal spin transition, featuring a hysteresis loop. The transition temperatures when coming from high or low temperatures are denoted as $T_{1/2\downarrow}$ and $T_{1/2\uparrow}$, respectively. T_{eq} is the equilibrium temperature at which the free enthalpies of the LS and HS phases are exactly equal. It is worth noting that in general, $T_{eq} \neq (T_{1/2\downarrow} + T_{1/2\uparrow})/2$. Small boxes show the usual evolution of the free enthalpy at various locations of the thermal hysteresis loop. *Adapted from* [240].

The principle of bistability is as follows: within the temperature range [$T_{1/2\uparrow}$, $T_{1/2\downarrow}$], the material can exist in either the HS or LS states depending on its history. This history refers to the cycles of heating and cooling it has undergone. Therefore, regardless of its initial state, if the compound has experienced cooling to a temperature below $T_{1/2\downarrow}$ and then heating to the domain $T_{1/2\uparrow}$ it will be in the LS state within the temperature region defined by thermal hysteresis. Similarly, if it has undergone heating to a temperature higher than $T_{1/2\uparrow}$ and then cooling to the domain $T_{1/2\downarrow}$, it will be in the HS state within the thermal hysteresis.

4.3.3 Volume compression and bulk modulus

When applying pressure (P) to a volume (V), the work done (W) is given by $W = -P\Delta V$, resulting in negative ΔV in compressed materials. The compressibility of a solid is a measure of how much its relative volume changes in response to a change in pressure. The inverse value of the compressibility is referred to as the solid's bulk modulus (hard materials always have high bulk moduli). Bulk modulus is defined as how easily the material is deformable (the smaller the value the more deformable the material). The volume change is linked to changes in both intermolecular and intramolecular distances within the material. As the amount of these changes is directly proportional to inter- and intramolecular distances, a deep investigation of structural changes with pressure can reveal key information about the different responses to compression of e.g., two polymorphs [241]. Further investigation enables the characterization of individual bond compressibilities, which can provide a hint as to the true nature of the material's resistance to pressure.

The third-order Birch–Murnaghan equation of state [242, 243] given by:

$$P(V) = \frac{3B_0}{2} \cdot \left[\left(\frac{V_0}{V}\right)^{\frac{7}{3}} - \left(\frac{V_0}{V}\right)^{\frac{5}{3}} \right] \cdot \left\{ 1 + \frac{3}{4}\left(B_0' - 4\right) \left[\left(\frac{V_0}{V}\right)^{\frac{2}{3}} - 1 \right] \right\} \tag{4.24}$$

can be used to describe how a material's volume changes with pressure when the temperature remains constant. Here, V_0 the unit cell volume at ambient conditions, the bulk modulus (at ambient conditions) B_0, and the first derivative of the bulk modulus with respect to pressure B_0', are commonly used to parameterize and measure the equations of state [244].

4.4 Thermodynamic aspects

According to the First Law of Thermodynamics, a system's heat, Q, is correlated with its internal energy, U, and the work, W, the system performs on its surroundings. Clausius proposed in 1850 [245] the now-famous form of a differential equation of internal energy U;

$$dU = \delta Q - \delta W \tag{4.25}$$

If the system is in adiabatic isolation, dQ = 0 and dU = -dW. The differentials of the heat and work variables indicate their path dependence, unlike the internal energy U, which is path-independent. Clausius also related the entropy "S" to the transfer of heat Q to a closed system in the Second Law of Thermodynamics [245].

$$\delta Q = TdS \tag{4.26}$$

When Equations 4.25 and 4.26 are combined, the result is:

$$dU = TdS - \delta W \tag{4.27}$$

Depending on experimental conditions, the system can perform work in various ways for the δW term. When the pressure in the system is different from atmospheric pressure, the variation in internal energy (U) can be represented in terms of the work done by the pressure (pV) and the variation in enthalpy (H) as follows:

$$\Delta H = \Delta U + p\Delta V \tag{4.28}$$

Work in thermodynamics is characterized by changes in the properties of the system, denoted as x_i. The system properties, which can include volume (V), magnetization (M), polarization (p), and stress (σ), are considered variables that respond to the application of generalized force, often referred to as X_i. These generalized forces correspond to their conjugate properties of the system, such as pressure (P), magnetic (B), electric field (E), or strain (ϵ). The relationship between these properties (x_i) and their conjugate generalized forces (X_i) is fundamental in thermodynamics, dictating how the system evolves and adapts to external stimuli.

$$X_i = (\frac{\partial W}{\partial x_i})_T \tag{4.29}$$

Therefore, the first law of thermodynamics can be expressed as:

$$dU = TdS - PdV - BdM - Edp + \epsilon d\sigma \tag{4.30}$$

The differential form of the Gibbs free energy $G(x_i)$ is:

$$dG = -SdT + VdP - MdB + pdE + \epsilon d\sigma \tag{4.31}$$

In the following parts, we focus our discussion on changes in temperature and pressure. By comparing the second derivatives of the thermodynamic potential $((\frac{\partial^2 G}{\partial P \partial T})_T = (\frac{\partial^2 G}{\partial T \partial P})_P)$, and by taking the derivative of both sides of 4.31, the Maxwell relation is obtained:

$$(\frac{\partial S}{\partial P})_T = -(\frac{\partial V}{\partial T})_P \tag{4.32}$$

The heat capacity C_i is a measure of the change in heat caused by a change in temperature, i.e., $\delta Q = C_i\ dT$ (see Section 6.2). The heat capacity of a substance is defined in general, with respect to a constant parameter, i as follows:

$$C_i = \frac{dQ}{dT}|_i \tag{4.33}$$

Entropy can be related to heat capacity by combining Equation 4.33 with the Second Law of Thermodynamics:

$$S(T,V) = \int_0^T \frac{C(T',P)}{T'}\, dT' \tag{4.34}$$

Integrating the Maxwell relation, Equation 4.32, with regard to an applied pressure yields the following expression for the change in the entropy from initial to final values:

$$\Delta S = -\int_{P_i}^{P_f} (\frac{V}{T})_P\, dP' \tag{4.35}$$

For adiabatic conditions, where $dS_{system} = 0$, the adiabatic temperature change (Equation 4.36) is obtained by combining the Maxwell relation 4.32 with Equation 4.34.

$$\Delta T_{ad} = -\int_{P_i}^{P_f} \frac{T}{C(T,V)} (\frac{\partial V}{\partial T})_P\, dP' \tag{4.36}$$

4.4.1 Thermodynamics of spin-crossover

Studying thermodynamic parameters (entropy and enthalpy) allows for the characterization of spin transition behavior and provides insights into the driving forces behind the switching process.

Gibbs's free energy provides insight into the feasibility of a spin transition. Thus, it is possible to describe the SCO phenomenon as the equilibrium between two phases of HS and LS states in a system constituted by no interaction between the assemblies of the isolated molecules. At equilibrium, G is constant; therefore, $\Delta G = 0$ (Equation 4.17). The critical temperature for the spin transition (where $\Delta G(T_{1/2})$ vanishes) is defined as the temperature at which half of the molecules are in the high spin state (as illustrated in Figure 4.12).

$$T_{1/2} = \frac{\Delta H}{\Delta S} \tag{4.37}$$

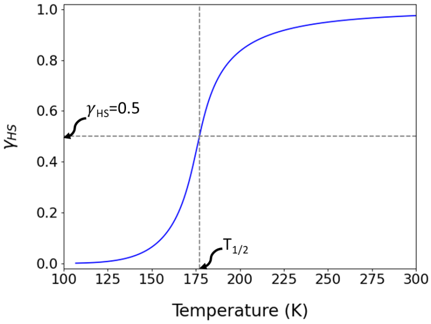

Figure 4.12: Thermal evolution of the High spin fraction γ_{HS} (blue line). The equilibrium temperature $T_{1/2}$, where γ_{HS}=0.5 is illustrated by a gray dotted line

4.4.2 Entropy driven spin crossover

The spin transition is driven by entropy and is nearly a quantitative process, as the HS state has a greater density of vibrational states and a greater spin multiplicity. In other words, the gain in entropy compensates for the enthalpy difference between the two states, promoting a HS arrangement. In quantum physics, the LS state is always the ground state, but once the temperature is high enough, the HS state becomes the thermodynamically preferred configuration. The entropy change (ΔS_{LH})[1] is expressed through the thermodynamic probability [246]:

$$\Delta S_{LH} = k\ ln(g_{HS}) - k\ ln(g_{LS}) = k\ ln\left(\frac{g_{HS}}{g_{LS}}\right) > 0 \tag{4.38}$$

where g_{LS} and g_{HS} are the degeneracy of the HS and LS states, respectively; thus, ΔS_{LH} is always positive. This is illustrated in equation 4.17 by showing that Gibbs energy change is positive below a certain temperature $T_{1/2}$ in which the enthalpy dominates, and it is negative above $T_{1/2}$ where entropy becomes the dominant factor.

The entropy variation has four main contributions, namely electronic, vibrational, rotational, and configurational [197, 201, 247], and can be expressed as:

$$\Delta S_{tot} = \Delta S_{ele} + \Delta S_{vib} + \Delta S_{rot} + \Delta S_{conf} \tag{4.39}$$

ΔS_{el} is attributed to the change of the total spin momentum S_{tot}:

$$\Delta S_{ele} = R\ ln\left(\frac{2S_{HS}+1}{2S_{LS}+1}\right) \tag{4.40}$$

where R is the universal gas constant. For Fe(II), $\Delta S_{el} = 13.38\,\mathrm{J\,K^{-1}\,mol^{-1}}$ (S_{HS}=2, S_{HS}=0) [63], which represents approximately 25% of the total entropy gain.

Heat capacity measurements in Fe(II)-based SCO complexes have demonstrated that the ΔS_{tot} during the spin crossover has typical values between $50 - 80\,\mathrm{J\,K^{-1}\,mol^{-1}}$ [248]. Since these values are considerably higher than those of a simple change in spin multiplicity, an additional contribution having a vibrational origin, ΔS_{vib} has to be considered. Equation 4.41, which describes the vibrational limit at high temperatures, provides a convenient expression for the entropy change between the HS and LS forms. The adiabatic potential for the HS state is more flat, the force constant is smaller, and the vibrational energy (wavenumber) is lower (see Section 4.1), which results in a higher vibration partition function Z for the HS state. Therefore, the entropy increases as vibrational frequencies decrease in the HS state [249] (a more detailed analysis is described in Ref [250]).

$$\Delta S_{\mathrm{vib}} = R\sum_{\lambda} ln\left[\frac{\nu_{\lambda}^{LS}}{\nu_{\lambda}^{HS}}\right] \tag{4.41}$$

Then, the variation in vibrational entropy can be deduced as follows:

$$\Delta S_{\mathrm{vib}} = S_{\mathrm{vib}}^{HS} - S_{\mathrm{vib}}^{LS} = R\sum_{\lambda}^{15} \ln\left[\frac{\nu_{\lambda}^{LS}}{\nu_{\lambda}^{HS}}\right] = 15R\left[\frac{\nu^{LS}}{\nu^{HS}}\right] \tag{4.42}$$

---

[1] $\Delta S_{LH} = S_{HS} - S_{LS}$ with S_{HS} and S_{LS} correspond to the system entropy in the HS and LS states, respectively.

The vibrational contribution comes mainly from the stretching and distortional modes of the FeN$_6$ octahedron, ($\lambda = 15$ vibrational modes for octahedron [250]). The energy of the stretching vibrational modes ν_{FeN} are greater in the LS state than in the HS state with typical ratio $\left[\frac{\nu_{FeN}^{LS}}{\nu_{FeN}^{HS}}\right]$ ranging from 1.1 to 1.9 [251]. It is worth noting that the total entropy ΔS_{tot} can be calculated from calorimetric data [209, 252, 253]. Raman and infrared spectroscopies, neutron and nuclear inelastic scattering can be used to evaluate vibrational characteristics [251, 254, 255].

In most cases, the configurational (S_{con}) and rotational entropy (S_{rot}) contributions can be neglected. Nevertheless, care must be taken because SCO can occur in some compounds along with changes in static and dynamic orientational disorder or changes in rotational motions of ligands, counterions, and guest molecules. According to crystallographic studies of the SCO compound [Fe(DAPP)(abpt)](ClO$_4$)$_2$, the disordering of the DAPP ligand and one of the ClO$_4$ ions contributed 11.5 J K^{-1} mol^{-1} to the total entropy change of 84 J K^{-1} mol^{-1} [256].

4.4.3 Pressure driven spin crossover

The spin crossover transition is known for its significant change in the volume of the metal coordination sphere (see Section 4.1) and, consequently, a change in the volume of the unit cell. Therefore, it is no surprise that materials of this sort are susceptible to applying pressure. By applying pressure, the decrease in volume is associated with a more closely packed ligand around the metal ion, the entropy is minimized corresponding to an increase in ΔH, ultimately favoring the formation and stabilization of the low spin state (refer to Section 4.1, Equation 4.28). It is noteworthy, that it is also possible to induce a transition from the low spin state to the high spin state at ambient temperature by exposing the sample to pressure less than atmospheric pressure [257].

Applying pressure strongly influences the energy of the vibrational states and alters the LS ↔ HS equilibrium in SCO systems. As increasing pressure is applied, the LS state is stabilized, leading to shifting the transition temperature to a higher temperature. Referring to the energy diagram of Fe(II) systems (Figure 4.13) the applied pressure ($P2 > P1$) raises the energy of the high-spin state potential well (vertical shift) [53, 197]. As a result, the zero-point energy difference (ΔE^0_{HL}), between the two spin states increases by $p\Delta V^0_{HL}$, which results in a decrease in the activation energy (ΔE^*_{HL}).

As pressure application favors a volume reduction, a pressure-induced HS → LS transition can take place in systems at temperatures where a thermally-driven one would not occur. Transition temperature variations by more than 100 K can be obtained by increasing pressure from the ambient pressure to values of a few of GPa. Most SCO systems have a linear relationship of $T_{1/2}(P)$ vs. P [53], and the mean-field theory of phase transitions in SCO complexes predicts a decrease in hysteresis width with increasing pressure [185, 193, 258]. Also, a smoother transition is predicted with applying pressure [247]; however, some experimental studies contradict these expectations [154].

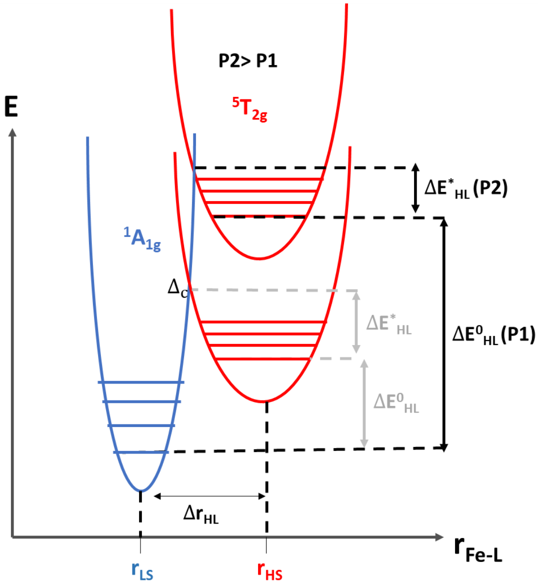

Figure 4.13: The effect of pressure on the adiabatic potential wells of the HS and LS state. The HS potential well is shifted vertically towards higher energy. The zero-point energy ΔE^0_{HL}(P) is increased, whereas the activation energy ΔE^*_{HL}(P) is decreased.

The influence of pressure on $T_{1/2}$ can be modeled using the Clausius-Clapeyron relation (Equation 4.32) [247].

$$\frac{\delta T_{1/2}}{\delta P} = \frac{\Delta V_{HL}}{\Delta S_{HL}} \tag{4.43}$$

ΔV_{HL}, ΔS_{HL} are the changes in volume and entropy, respectively, occurring in a HS → LS transition [54, 247].

4.5 Spin transition cooperativity

Cooperativity is one of the most difficult-to-track concepts in spin crossover phenomena. The nature of the interactions has been a source of controversy for physicists and theorists for more than 30 years and continues to be a source of interest [259, 260].

The Slichter and Drickamer model from 1972 [191] for a solution approach and the Sorai and Seki approach for a domain model from 1972 [234], are the two main models that have been proposed to explain and predict the cooperative feature of the spin transition. A number of theories, such as the electron-phonon coupling [261], MaGarvey et al. [262], Zimmermann and Köning [263], Spiering et al. [193], and Ising-like models [250] have been proposed to explain the spin transition, but the cooperativity mechanism is still unknown [264]. Aside from theoretical research, a number of empirical evaluations of these phenomena have also been conducted. Very dilute metal systems exhibit slow spin changes, which can be explained by a Boltzmann distribution, which clearly highlights the importance of intermolecular interactions in controlling the nature of the spin transition, but it also demonstrates that spin crossover is a feature of individual molecules rather than of the bulk material.

The cooperativity nature of the spin transition is directly linked to the efficiency of communication between SCO centers to transfer spin transitions throughout the material; the faster the transfer of the spin transitions, the higher the cooperativity (see Section 1.4).

4.5.1 Non-interacting molecules

In the absence of intermolecular interactions, it is possible to introduce the Gibbs free energy expression (G) and mixing entropy term (S_{mix}) corresponding to the loss of statistical information for a system. S_{mix} has been introduced due to the fact that there are numerous ways to distribute the HS entities among all of the molecules present. This term is expressed as:

$$S_{mix} = -R[\gamma_{HS} ln(\gamma_{HS}) + (1-\gamma_{HS}) ln(1-\gamma_{HS})] \tag{4.44}$$

S_{mix} has a maximum value when $\gamma_{HS} = 0.5$ and vanishes when all the molecules are purely in the HS state or in the LS spin state. By taking into account the S_{mix} term, the Gibbs free energy becomes:

$$G = \gamma_{HS}\, G_{HS} + (1-\gamma_{HS})\, G_{LS} - TS_{mix} + I \tag{4.45}$$

with G_{HS} and G_{LS} corresponding to the Gibbs free energies for the electronic states HS and LS, respectively. Where the intermolecular interaction term I in this approximation is neglected [246]. At the thermodynamic equilibrium in the SCO at constant temperature and pressure, the partial derivative of G as a function of γ_{HS} equals zero ($\frac{\partial G}{\partial \gamma_{HS}} = 0$).

$$\frac{\partial G}{\partial \gamma_{HS}}|_T = G_{HS} - G_{LS} + RT\ ln\left(\frac{\gamma_{HS}}{1-\gamma_{HS}}\right) = 0 \tag{4.46}$$

so that the HS fraction can be expressed as:

$$\gamma_{HS} = \frac{1}{1 + \exp\left[(\frac{\Delta H}{R})(\frac{1}{T} - \frac{1}{T_{1/2}})\right]} \tag{4.47}$$

According to this model, at $T = 0$, all molecules are in the LS state. However, an incomplete SCO transition with $\gamma_{HS} < 1$ is predicted at the high-temperature limit (Figure 4.14). The SCO transition curve is fairly gradual across a wide temperature range. As a consequence, no phase transition actually takes place. Such a condition can be observed in solutions where the mechanism of spin crossover is almost molecular in nature, with a loss of cooperativity, as observed in diluted materials, e.g., $[Fe_{1-x}Zn_x(\text{2-picolylamine})_3]Cl_2 \ldots EtOH$ [265].

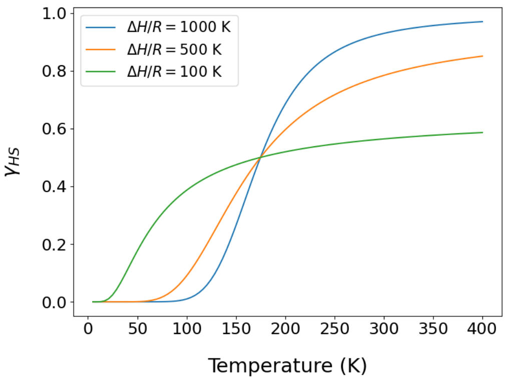

Figure 4.14: High spin fraction γ_{HS} evolution as a function of temperature for a non-interacting model by illustrating Equation 4.47 ($T_{1/2} = 175\,\mathrm{K}$).

4.5.2 Domain model (Sorai and Seki model)

In the Early 1970s, Sorai and Seki proposed that molecules with the same spin state form domains and interact in the crystal lattice based on experimental investigations using heat capacity measurements of cooperative compounds Fe(II)(phen)$_2$(X)$_2$ (with phen = 1,10-phenanthroline, X = NCS$^-$ and NCSe$^-$) [209]. Regardless of the temperature, the size of these domains remains constant. There is no interaction between domains. The authors have proposed two related factors, "N" and "n," where "N" is the number of domains per mole of a substance and "n" is the number of molecules per domain ($nN = 1$). The larger the n value (the larger the domain size), the smaller the number of domains (smaller N value), and the more abrupt the transition. These domains are randomly located in the crystal lattice (Figure 4.15), and the value, which is often referred to as $T_{1/2}$ is the temperature at which the number of domains in the LS and HS state is equivalent. Equation 4.48 can be used to determine the value of n by fitting the thermal dependence of high spin fraction γ_{HS}.

$$\gamma_{HS} = \frac{1}{1 + \exp\left[\frac{n\Delta H}{R}\left(\frac{1}{T} - \frac{1}{T_{1/2}}\right)\right]} \tag{4.48}$$

This model emphasizes the fact that the evolution of γ_{HS} as a function of temperature shows increasing transition abruptness with increasing numbers of particles per domain (Figure 4.16). However, this method is used only to analyze abrupt transitions in the absence of thermal hysteresis. Contrary to the non-interacting model, a model with a large value of n, predicts a complete SCO transition at high temperatures (Figure 4.16).

The domain model is partially successful in interpreting calorimetric measurements, like the C_p vs T curve, which is λ-shaped around $T_{1/2}$. It cannot account for the hysteresis effect when domains remain clustered uniformly. Nevertheless, hysteresis might manifest if the size of the domains during the heating and cooling are different.

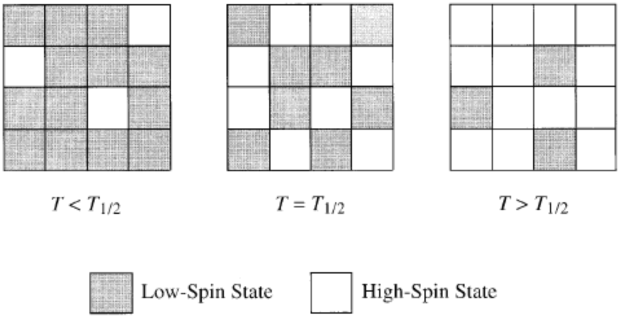

Figure 4.15: Schematic diagram of the domain model [266]. The crystal lattice is thought to be made up of domains that are all the same size and have the same amount of spin-crossover complexes in each one. $T_{1/2}$ is the temperature where the number of LS domains equals the number of HS domains.

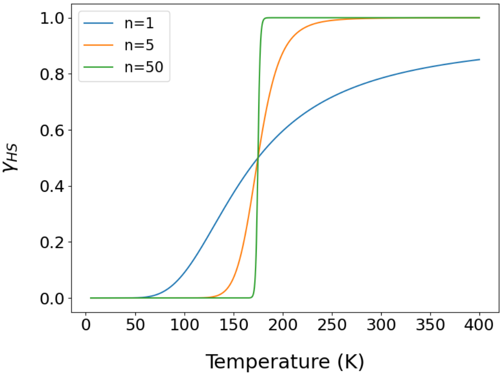

Figure 4.16: The spin transition becomes more abrupt as the number of particles per domain n increases (Equation 4.48, $\Delta H/R = 500$ K, $T_{1/2} = 175\,\mathrm{K}$).

4.5.3 Solution model (Slitcher and Drickramer model)

The previously described model of the isolated molecules with no interactions system corresponds to the so-called Gibbs-Boltzmann thermodynamics approach, which accounts for the SCO phenomenon through intramolecular modifications but completely ignores the fact that in a real system, the molecules interact with each other. Slitcher and Drickramer model [191] introduces a new factor, Γ, where the cooperativity is taken into account. It is worth noting that cooperativity in SCO compounds is predominantly positive, meaning that when one SCO center undergoes a spin transition, it often enhances or encourages nearby molecules to follow; thus, for "isolated molecules", where there is minimal interaction between SCO centers, it is expected that $\Gamma = 0$ [267]. The cooperativity is related to the intermolecular interaction I via:

$$I = \Gamma \gamma_{HS}(1 - \gamma_{HS}) \tag{4.49}$$

and the free energy can be expressed in the following way [249]:

$$G = \gamma_{HS} G_{HS} + (1 - \gamma_{HS}) \times G_{LS} + \Gamma \gamma_{HS}(1 - \gamma_{HS}) - T S_{mix} \tag{4.50}$$

where Γ describes the effective cooperativity parameter strength, and S_{mix} is the mixing entropy. By taking the derivative of Equation 4.50, and considering the equilibrium condition of temperature and pressure ($\frac{\partial G}{\partial \gamma_{HS}}|_T = 0$), the following expression is obtained [249]:[1]

$$T = \frac{\Delta H + \Gamma(1 - 2\gamma_{HS})}{R\ ln(\frac{1-\gamma_{HS}}{\gamma_{HS}}) + \Delta S} \tag{4.51}$$

where R (J mol^{-1}) is the universal gas constant. There are three distinct scenarios that can be identified using Equation 4.51, depending on the magnitude of the interaction coefficient (Γ). Figure 4.17 illustrates the evolution of γ_{HS} as a function of temperature.

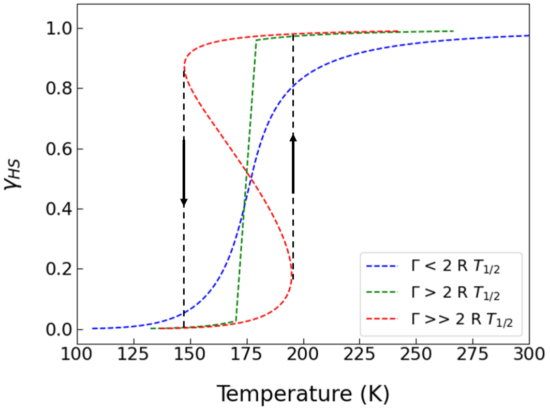

Figure 4.17: Simulation of thermally-induced spin transition with the Slichter and Drickamer model for different interaction strengths. Variations in enthalpy and entropy are $10.5\,\mathrm{k\,J\,mol^{-1}}$ and $59\,\mathrm{k\,J\,mol^{-1}\,K^{-1}}$, respectively. Three different values of Γ have been chosen to illustrate three different situations: the spin conversion (gradual, blue dashed line) Γ $2000\,\mathrm{k\,J\,mol^{-1}\,K^{-1}}$ < 2 R $T_{1/2}$, the abrupt transition (green dashed line) $\Gamma = 5000\,\mathrm{k\,J\,mol^{-1}\,K^{-1}}$ > 2 R $T_{1/2}$, and the first-order transition with hysteresis phenomenon (red full line) $\Gamma = 6000\,\mathrm{k\,J\,mol^{-1}\,K^{-1}} > > 2$ R $T_{1/2}$.

---

[1] This is not a mathematical function since one γ_{HS} corresponds to a multi-value of temperature.

- If $\Gamma < 2$ R $T_{1/2}$, the cooperativity is small and the transition is a gradual curve (blue curve in Figure 4.17).
- If $\Gamma \geqslant 2$ R $T_{1/2}$, the transition is abrupt (green curve in Figure 4.17).
- If $\Gamma \gg 2$ R $T_{1/2}$, the curve shows hysteresis and represents a strong molecular interaction (red curve in Figure 4.17).

The cooperativity coefficient C, defined as $C = \frac{\Gamma}{2RT_{1/2}}$, has also been employed [203, 267]. The three cases of weak, strong, and very strong contacts are represented by C $<$ 1, C $=$ 1, and C $>$ 1, respectively. In the case of weak contacts, C $<$ 1, the system experiences a spin transition, and the evolution of HS fraction with respect to temperature is relatively gradual, as seen in diluted systems. When C $>$ 1, the transition becomes steeper for stronger interactions as the interaction between molecules dominates the spin phenomenon. It is worth noting that the solution model is capable of describing the hysteresis effect.

Chapter 5

Experimental Methods

5.1 Sample preparation

According to the methods described in the previous study [59], the monoclinic polymorph of compound Fe(PM-Bia)$_2$(NCS)$_2$ was produced. In an inert N$_2$ atmosphere, single crystals of the monoclinic polymorph were made by a layered solution of [Fe(NCS)$_2$(py)$_4$] (12.2 mg, 0.025 mmol) in methanol (1 mL) with a solution of the ligand Bia-PM (12.9 mg, 0.05 mmol) in diethyl ether (1 mL). A layer of the 1:1 mixed solvents (1 mL) was inserted between the two layers to delay the reaction in order to control the reaction kinetics. Single crystals formed after a week.

Single crystals of the orthorhombic polymorph were obtained by inserting [Fe(NCS)$_2$(py)$_4$] powder (48.8 mg, 0.1 mmol) and Bia-PM powder (51.6 mg, 0.2 mmol) on opposite sides of an H-shaped tube. Methanol was gently added until the solvent linked the two solids, and the process was repeated until single crystals formed. After two weeks, single crystals were obtained.

Elemental analysis and powder X-ray diffraction verified the purity of the samples. The synchrotron PXRD results show that the orthorhombic polymorph is pure, while the monoclinic polymorph has approximately 5% impurities of the orthorhombic phase (Figure 5.1).

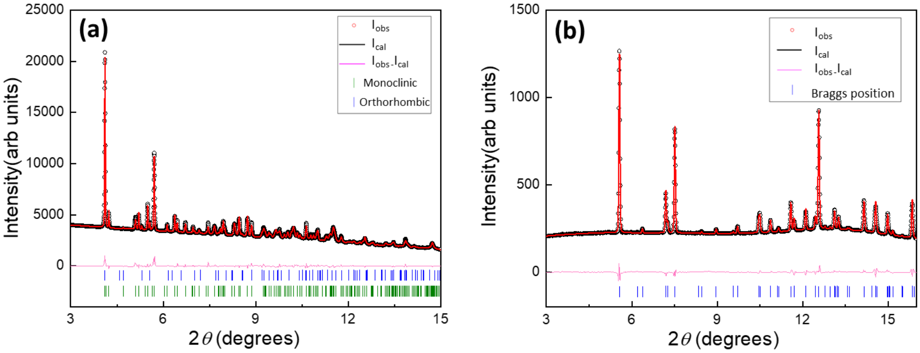

Figure 5.1: Refinement of the powder diffraction pattern using the Rietveld method for: **(a)** monoclinic polymorph; data measured at PSI at 270 K and **(b)** orthorhombic polymorph; data measured at ESRF at 250 K. The blue and green ticks represent the Bragg reflections from the orthorhombic and monoclinic polymorphs, respectively. Small impurity peaks can be seen in **(a)**. These peaks correspond to the orthorhombic polymorph that has a phase fraction of about 5%. The solid black line corresponds to the Rietveld fit, whereas the open red circles are observed data points. The difference between observed and calculated patterns is shown by the pink solid line.

5.2 Magnetization

The effects of the spin transition on the magnetic susceptibility of SCO materials were investigated by a Magnetic Property Measurement System *MPMS XL* [268] and a Physical Property Measurement System *Quantum Design PPMS DynaCool* [269]. Both magnetometers are based on the principle that a moving or changing magnetic moment induces a current in a detection coil.

5.2.1 Methods and instruments

5.2.1.1 SQUID

The Magnetic Property Measurement System *MPMS XL* is a Superconducting Quantum Interference Device (SQUID) magnetometer, which is very sensitive and used to measure extremely small magnetic fields and magnetic moments and detect subtle changes within the material. The SQUID does not measure the magnetization directly from the sample, but it is a flux-to-voltage transducer which converts a slight change in magnetic flux (which is hard to measure) into voltage (which is easy to measure).

Through the superconducting pick-up coil, the sample is moved up and down (known as flux transformers). The change in magnetic flux generated by the sample motion, by crossing the magnetic field line, induces a current, which flows within the pick-up coils. The current is then carried along superconducting wires to the SQUID input coil. As the pick-up coils, superconducting wires, and SQUID input coil are all part of a closed system, the current recorded at the SQUID is directly proportional to the change in magnetic flux generated by the moving sample. The SQUID sensor itself is located in a protected environment, immersed in liquid helium, away from the sample chamber.

The basic SQUID consists of a small loop of superconducting material with one (AC-SQUID) or two Josephson junctions (DC-SQUID). A schematic diagram of a SQUID is shown in Figure 5.2. Josephson junctions consist of two superconductors separated by thin insulating layers. Two parallel Josephson junctions are connected on a closed superconducting loop. If the SQUID is symmetrical and the junctions are identical, a DC current I that enters the device through A, will be divided into two parts, I_1 and I_2. The currents I_1 and I_2 undergo a phase shift while crossing the Josephson junctions P and Q and become I_1' and I_2' respectively. The currents I_1' and I_2' interact at B.

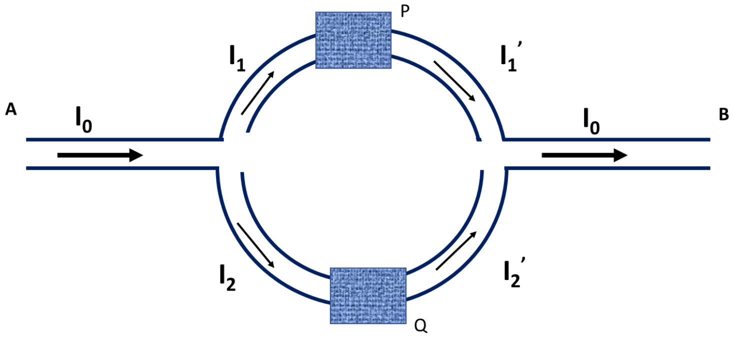

Figure 5.2: A schematic diagram of a dc SQUID loop consisting of two Josephson junctions (Q and P) arranged to a ring structure. A Josephson junction is an insulating layer between two superconductors.

The SQUID magnetometer can be operated in two modes; the RSO (Reciprocating Sample Option) and the DC mode. The RSO allows to average over a number of repeated movements of the sample through the pick-up gradiometer within a reasonable time frame. In the DC mode, the sample moves linearly (a DC motion) along the symmetry axis.

The most crucial factors to avoid measurement errors in SQUID magnetometry are sample size and location. The $2 \times 2\,\mathrm{mm}^2$ bunch of crystals used in this work for magnetometry measurements allowed for the best magnetic resolution to be obtained by using the RSO method (Figure 5.3). Once the sample was placed on the sample holder and inserted into the device, a centering scan was carried out in order to locate the sample at the optimum measurement position inside the gradiometer. A small magnetic field was applied to the sample inside the chamber in order to cause a magnetic response. A stepper motor was then used to raise and lower the sample inside the chamber. The response is displayed as a "Voltage vs. Position" graph by the MPMS program (Figure 5.3). A sample is perfectly centered when the raw magnetic response from the sample aligns with the fit to the dipole model generated by the instrument (Figure 5.3). The MPMS computer software interface allows for simple programming of a measurement sequence, that includes control over the applied field, temperature, field sweep rate, temperature sweep rate, AC frequency, etc.

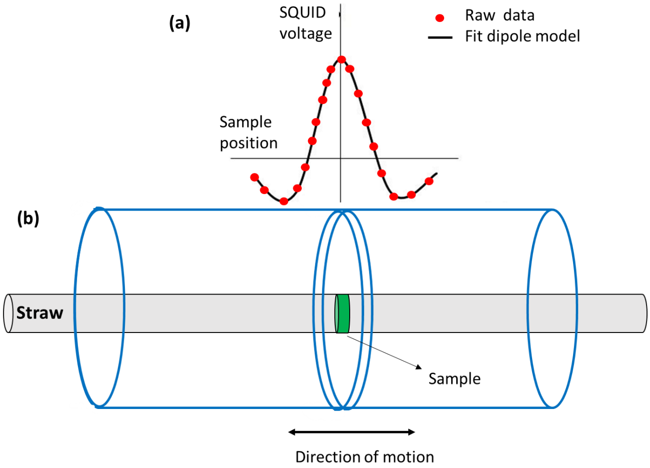

Figure 5.3: Representation of a low-amplitude RSO measurement. **(a)** displays the optimal SQUID response for a dipole, and **(b)** illustrates the movement of the sample inside the pickup coils of the SQUID.

5.2.1.2 PPMS Dynacool

The Quantum Design Physical Property Measurement System *PPMS DynaCool* is very sensitive and reported to be less than 10^{-6} emu by the manufacturer and measurements can be performed in a temperature range between 1.4 K and 400 K [269]. The investigation of the magnetic susceptibility was performed with a Vibrating Sample Magnetometer (VSM) option.

The principle at the basis of a Vibrating Sample Magnetometer (VSM) is the detection of magnetic flux changes when a vibrating sample is inserted in a uniform magnetic field. According to Faraday's law, the magnetization variation due to the sample's motion induces an AC voltage between pickup coils, which is then amplified, and finally converted to magnetic moment [270]. The mathematical relationship between magnetic flux, time, and voltage induced can be expressed by Equation 5.1.

$$V_{coil} = \frac{d\phi}{dt} \tag{5.1}$$

For a sinusoidal motion, their relation is given by:

$$V_{coil} = 2\pi f C m A \sin(2\pi f t) \qquad (5.2)$$

where f is the frequency of the oscillation, C is coupling constant, A is the amplitude of the sinusoidal oscillation, and m is the magnetic moment of the sample.

5.2.2 Measurements

5.2.2.1 SQUID measurements

The magnetic properties of single crystal samples presented in this thesis were studied using SQUID, RSO option of a Quantum Design magnetic property measurements system *MPMS XL* with applying a constant field of $\mu_0 H=$ 2T and 500Oe for the orthorhombic and monoclinic polymorphs, respectively,[1] with a temperature range between 5 K - 300 K at different scan rate of 0.2 , 0.5 , 1 , 2 , 5 , 8 , 10 K/min were carried out. In addition, several measurements were carried out using magnetic fields of varying strengths ($\mu_0 H=$ 0.8T, 2T, 3T) in order to investigate the effect of the magnetic field on the spin transition.

The magnetic susceptibility measurements for both polymorphs were performed on bunches of single crystals tapped with scotch on drinking straws used as sample holders. The straw was fastened to the end of the sample rod and inserted into the MPMS.

Two types of magnetization measurements were carried out in the measurements for this thesis (see section 7.1): zero-field cooled (ZFC), and field-cooled (FCC: Field Cooled Cooling and FCW: Field Cooled Warming). These protocols allowed for a comprehensive examination of the magnetization characteristics of the sample while varying the temperature under the influence of a constant magnetic field. In the case of the ZFC protocol, the sample was cooled down in the absence of a magnetic field, once the sample reached the desired temperature, a magnetic field was applied and the magnetization of the sample was measured on warming. For the FCC protocol, the magnetic moment of the sample was measured while cooling in a magnetic field and for obtaining FCW the moment was measured by applying the field upon warming.

For the field-dependent magnetization measurements, the magnetic moment was measured in RSO mode by applying a field of -2T to 2T at different temperatures 350 , 220 , 170 K. The temperature-dependent measurements were corrected for the diamagnetic and paramagnetic contribution of the sample and the sample holder (see Section 6.1 for more details).

---

[1] In order to keep the diamagnetic contribution to magnetization to a minimum, the measurement for the monoclinic polymorph was carried out with a low value of the external field (50 mT). For the orthorhombic polymorph, measurements under an applied field of 50 mT resulted in very noisy data. Thus, in order to improve the statistics, the magnetic field was raised to a value (2 T) at which the magnetization could be measured more reliably.

[1] It should be noted that even when the applied field is zero, a residual magnetic field may still exist. This remnant field can be corrected by applying a field of 1 or 2 *Oe* while performing the ZFC measurement.

5.2.2.2 Dynacool measurements

The investigation of the magnetic susceptibility of the polycrystalline sample in this thesis was performed using PPMS Dynacool, VSM option [269]. The polycrystalline samples were weighed, then filled into a plastic sample holder, coated with Teflon, and tightly placed inside a brass tube (Figure 5.4). The brass tube was attached at the end of the sample rod. Before each experiment, a centering process was carried out to make sure that the sample oscillations were centered in the pickup coils. The amplitude of the sample oscillations were typically between $2-3\,\text{mm}$ depending on the amount of material (usually a few mg).

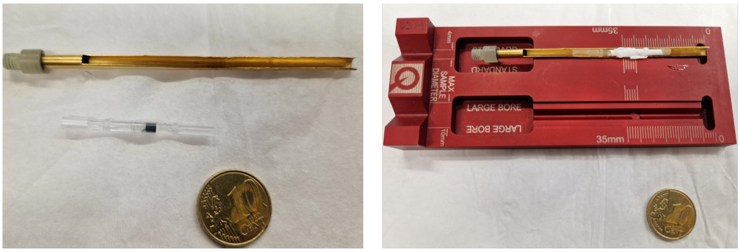

Figure 5.4: (Left) Sample filled into a VSM plastic capsule. (Right) The plastic capsule covered with Teflon is loaded into the brass sample holder in preparation for the VSM measurement.

DC-magnetization measurements were performed as a function of temperature with an applied magnetic field (H) of 500Oe at a slow rate of 0.2 K/min. In addition, several measurements were performed at different scan rates of 0.2 , 0.5 , 1 , 2 , 5 , 8 , 10 K/min. To check the effect of the magnetic field on the spin transition, several measurements with different magnetic field $\mu_0 H=$ 0.8T, 2T and 3T were carried out. Raw data were corrected for diamagnetism and paramagnetic contributions of the sample holder and the sample itself. The extraction of the magnetic susceptibility χ via the relation $M = \chi H$ is then straightforward from the ratio M/H (see Equation 5.3) and knowing the sample weight as well as the molar mass of the compounds.

$$\chi_M.T = \frac{M \times Molecular\ mass}{H \times sample\ mass} T \tag{5.3}$$

5.3 Differential scanning calorimetry (DSC)

5.3.1 Methods and instruments

Differential scanning calorimetry (DSC) is a technique used to investigate the presence and the nature of thermal phase transitions in a solid material. A DSC experiment monitors the change in heat capacity of a sample as the temperature is varied by comparing the heat flow, i.e., the amount of heat required to raise its temperature at a constant rate, with respect to a reference. The sample is placed in a pan and heated/cooled in a predetermined temperature range. The heat flow, usually taken as the difference in heat flow between the sample and the reference (empty pan), can be either positive for exothermic transitions, or negative for endothermic ones. A typical DSC thermogram for an SCO material displays a peak in correspondence of the LS to HS transition on heating (endothermic) and an inverse peak on cooling when the HS to LS conversion occurs (exothermic), as illustrated in Figure 5.5.

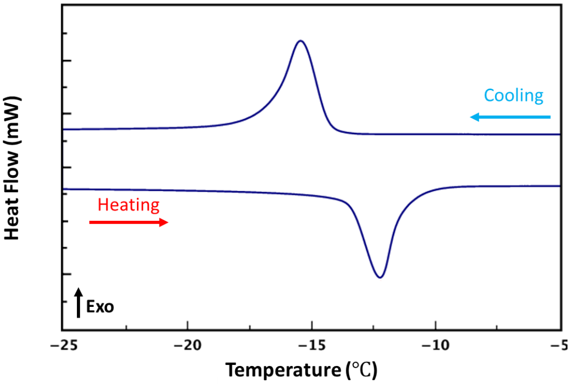

Figure 5.5: Thermogram of a SCO material featuring SCO with hysteresis. The spin transition is endothermic on heating (LS → HS) and exothermic on cooling (HS → LS).

5.3.2 Measurements

The DSC measurements were performed using a Perkin Elmer Pyris Diamond DSC-2000 calorimeter (Figure 5.6: **4**). A few mg of material[1] (polycrystalline sample) were placed in the aluminum pan (Figure 5.7 **(a)** & **(b)**) and sealed with the capsule press (Figure 5.7**(c)**). The DSC instrument is made up of an insulated chamber with two platforms in the shape of discs, as illustrated in Figure 5.7**d**. One platform houses the sample, while the other houses the reference. The experiments were running under constant nitrogen flow (50 mL/min).

All the measurements were carried out while cooling and heating in the temperature range of 300 K and 140 K with a scan rate of typically 10 K/min with an equilibration time of 1 minute at 300 K and at 140 K. Several thermal cycles (up to 6 cycles) were carried out for each measurement. The final temperature was gradually increased from 300 K to 310 K, 320 K, 330 K, 340 K, and up to 350 K to investigate the response of the sample to higher temperatures.

The DSC measurements for the orthorhombic polymorph involved a special protocol to map and obtain detailed information on the intermediate transition:

1. Initial cooling without any measurement :

---

[1] Since the sample's mass is exactly related to the C_p of the substance, hence its exact mass value should be recorded.

   - The sample was initially cooled from 350 K to 210 K at a rate of 10 K/min.
   - Once the temperature reaches 210 K, the sample was held at this temperature for 15 min.
   - The sample was then slowly cooled from 210 K to 140 K at a rate of 0.2 K/min. This slow cooling rate allowed for detailed observations of any transitions occurring in this temperature range.
   - After reaching 140 K, the same rate of 0.2 K/min was used to slowly heat the sample to 179 K.

2. Start of measurement:
   - The DSC measurement was started while heating the sample from 179 K to 350 K at a rate of 10 K/min.

3. Measurements on cooling:
   - After reaching 350 K, the same cooling process was repeated to measure the behavior of the sample.
   - The measurement was taken from 180 K to 350 K and subsequently from 181 K to 350 K.

4. Investigation on the influence of the cooling rates:
   - Finally, several cooling rates were used.
   - The cooling rates applied were: 20 K/min, 7 K/min, 4 K/min, 2 K/min, 1 K/min, and 0.5 K/min.
   - The heating scan rate was maintained constant at 10 K/min during these experiments.

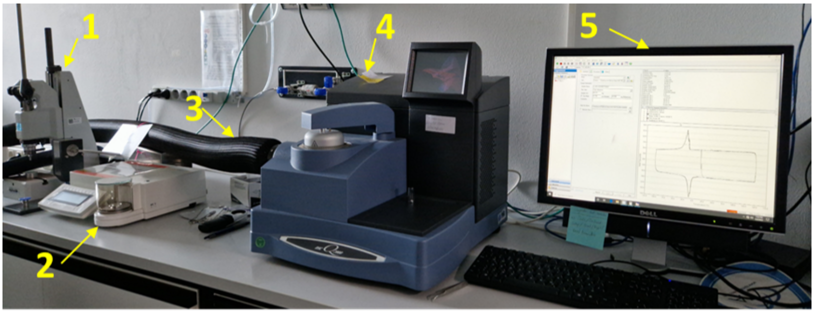

Figure 5.6: The differential scanning calorimeter (DSC) used in this study, includes the following components: **1:** Sample encapsulating press, **2:** Microbalance to weigh the samples. **3:** Nitrogen hose, **4:** Perkin Elmer Pyris Diamond DSC-2000, **5:** Desktop computer.

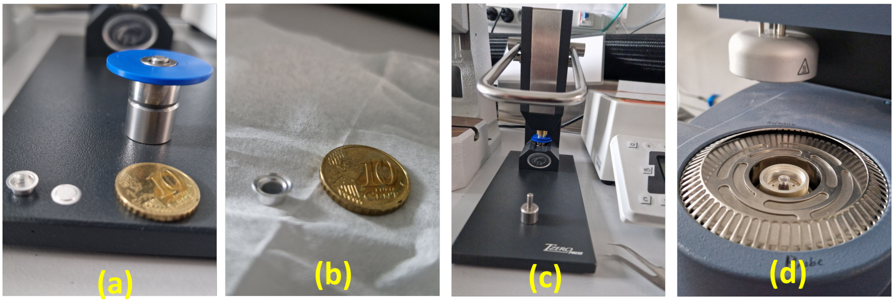

Figure 5.7: **(a)** Aluminium containers with lids utilized to securely encapsulate the samples ($-140°C < T < 600°C$). **(b)** Capsule press to seal a sample inside pan and lid. **(c)** Sample inside Aluminum pan and lid sealed with capsule press. **(d)** The sample pan and empty reference pan on the two platforms.

5.4 Powder diffraction

Powder diffraction is fundamentally different from single-crystal diffraction (discussed later in Section 5.4.3) due to the random orientation of the numerous crystallites present in the sample. This gives rise to a series of diffraction rings rather than the discrete spots seen from the diffraction of a single crystal.

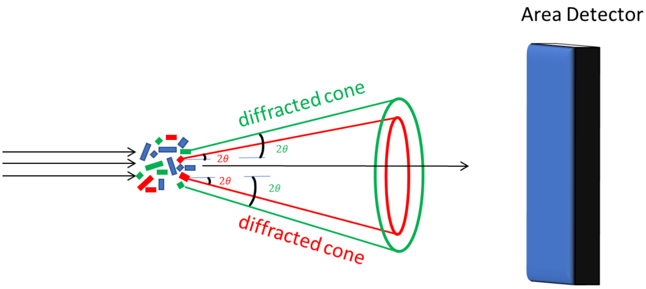

Figure 5.8: Schematic of a powder diffraction experiment. A diffracted cone of neutrons/X-rays is recorded as a ring on the detector.

5.4.1 Neutron powder diffraction

Due to the high sensitivity of neutrons to hydrogen, neutron diffraction is a valuable tool for investigating hydrogen-bonding interactions in spin crossover compounds.

The High-Resolution Powder Diffractometer for Thermal Neutrons (HRPT) [271, 272] situated at the SINQ neutron spallation source within the Paul Scherrer Institute (PSI) in Villigen, Switzerland was used in this thesis. This instrument is specifically designed for the study of structural and magnetic order in materials using neutron diffraction techniques. The HRPT neutron powder diffractometer operates at wavelengths ranging from 0.84 Å and 2.96 Å, allowing two different modes for data acquisition - high intensity and high resolution.

The collimated neutron beam is monochromatized and directed to the sample position by a focusing Ge($h\ k\ k$) monochromator [271]. Incoming neutrons are counted using a neutron beam monitor. A position-sensitive ^{3}He detector is used to detect the scattered neutrons.

The measurement at HRPT was performed on the monoclinic polymorph at different temperature points at ambient pressure between 1.5 K, 100 K and 300 K. Temperature control was achieved using a standard Orange He cryostat. For the measurement, about 3g of the monoclinic polycrystalline sample was filled into a vanadium can (10 mm diameter, and 55 mm height). The sample container was continually rotated to minimize the effect of inhomogeneity and preferred orientation. At room temperature, the incoherent scattering from hydrogen dominated the scattering at large Q, so a wavelength of 2.45 Å was used to optimize the measurement towards Q-resolution with exposure time $\approx$ 16h. At 100 K, a shorter wavelength ($\lambda = 1.8857$ Å) was used to increase the Q-range with exposure times $\approx$ 7h, as peaks at large Q could be clearly distinguished from the background at this temperature. At 1.5 K two different wavelength were used 2.45 Å with exposure times $\approx$ 10h and 1.8857 Å with exposure time $\approx$ 7h.

5.4.2 X-ray powder diffraction

5.4.2.1 In-house PXRD instrument

Powder X-ray diffraction experiments were performed on a *HUBER Imaging Plate Guinier Camera G670* (HUBER Diffraktionstechnik GmbH & Co. KG, Rimsting, Germany, [273]) using monochromatized Cu K_α radiation with $\lambda = 1.54$ Å. The imaging plate detector has a curved shape and covers an angular range of up to 100° in 2θ.

A schematic drawing of the diffractometer (Figure 5.9) illustrates the transmission geometry. The diffractometer comprises an X-ray tube, a monochromator, a divergence slit, located between the X-ray source and the sample, and a detector. A closed-cycle cryostat is integrated with the powder diffractometer and employed to achieve the desired temperatures. The closed-cycle Helium cooling System is supplied by an air-cooled compressor. The in-house powder diffractometer was used to determine the evolution of lattice parameters and unit cell volume as a function of temperature and to verify the phase purity of the synthesized polycrystalline samples.

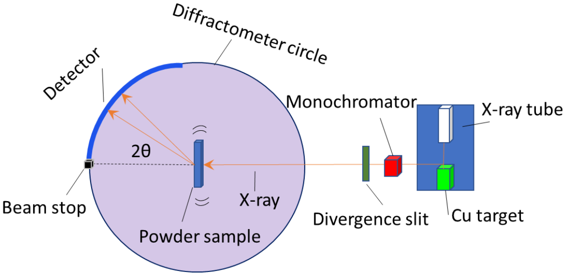

Figure 5.9: Schematic drawing of the setup of the *HUBER G670* powder diffractometer.

5.4.2.2 In-house measurement

For the measurements, a few milligrams of powder were distributed on a thin foil on top of the sample holder. To improve the homogeneity of the sample dispersion, a drop of solvent (isopropanol) was added. A second foil was placed on top of the powder and secured by a metal ring pressed onto the sample holder. To reduce the effect of sample inhomogeneities and increase the statistics, the sample holder oscillated horizontally at a frequency of about 1 Hz.

The same protocol was followed for all temperature-dependent powder diffraction measurements. The sample was initially cooled to 25 K. The measurements were carried out on heating from 25 K to 300 K with a step size of 5 K at a rate of 6 K/min. Each temperature point had 15 min waiting time. 8 scans were preformed with a measurement time of 360 min at each measurement point.

5.4.2.3 Synchrotron measurement

Data were collected at the material science beamline X04SA-MS at the Swiss Light Source (SLS), PSI, Switzerland [274]. A MYTHEN II (microstrip system for time-resolved experiments) detector by DECTRIS (covering 120° with over 60,000 channels) was used. The high-resolution data were collected at a resolution of 3.7 mdeg in 2θ.

A sample capillary of 0.01 mm-thick borosilicate glass with an outer diameter of 0.3 mm and a length of 80 mm was utilized. The capillary was mounted in the sample holder and rotated at a certain speed during data collection to reduce inhomogeneity and preferred orientation. An OXFORD cryojet was used to cool the sample.

The high-resolution powder diffraction data on the monoclinic polymorph was collected using the wavelength of λ =0.708 Å following the protocol (Figure 5.10):

1. First run:
    - One measurement was carried out at room temperature.
    - The sample was cooled down from room temperature to 100 K with a cooling rate of 6 K/min without any measurement.

   - Another measurement was carried out at 100 K.
   - The sample was heated up to 150 K with a rate of 6 K/min.
   - The data collection started while warming up with a rate of 6 K/min from 150 K to 250 K, with 5 K temperature steps.
   - The sample was heated up to 300 K with a rate of 6 K/min and a measurement at room temperature was carried out.

2. Second run:
   - The data were collected while cooling down at a rate of 2.5 K/min from 300 K to 120 K, with 5 K temperature steps.

3. Third run:
   - The data were remeasured while warming up from 120 K to 250 K at a rate of 2.5 K/min, with 5 K temperature steps.

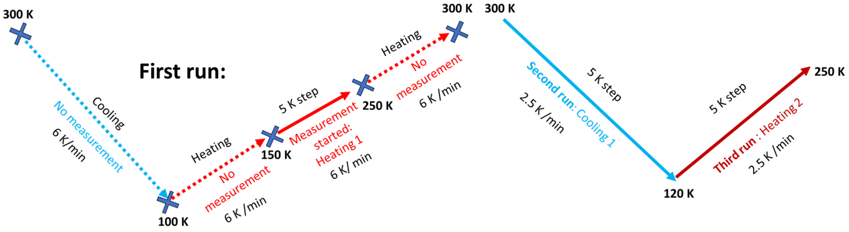

Figure 5.10: Data acquisition procedure for the monoclinic polymorph, including cooling and warming steps, temperature ranges, and rates. Dashed lines signify temperature ranges where no measurements were conducted, while straight lines indicate the execution of sequential measurements.

5.4.3 Single crystal X-ray diffraction

5.4.3.1 In-house instrument

The main instrument used for laboratory single crystal diffraction experiments was the 4-circle diffractometer Rigaku SuperNova equipped with a Si monochromator and a dual source with molybdenum K_α ($\lambda = 0.709$ Å), and copper K_α ($\lambda = 1.54$ Å) microfocus tubes (Figure 5.11) [275]. The detector is a charge-coupled device area detector (CCD).

The 4-circle κappa geometry diffractometer incorporates four rotation axes: ϕ, ω, κ, and 2θ-axes (Figure 5.11). Figure 5.12 shows the outline of the 4-circle diffractometer axes. Three of them are orthogonal axes: omega (ω), chi (χ), and phi (ϕ) in which the ω-axis coincides with the 2θ-axis. 2θ represents the rotation of the detector around the sample. The ϕ-axis is responsible for rotating the sample by rotating the goniometer head. By changing the value of ϕ, the sample can be rotated around the vertical axis of the goniometer head. The κ-axis is positioned on the κ-block, which can rotate independently. When κ is 0°, the ϕ angle coincides with ω-and θ-axes and can rotate on the same axes and when κ is 90° its axis is perpendicular to that of ω and 2θ.

5.4.3.2 In-house measurement

The in-house single-crystal diffractometry was used to assess the quality of single crystals for later synchrotron X-ray investigations. In addition, complete measurements at 90 K and at 300 K were carried out to verify the HS and LS crystal structure of the two polymorphs.

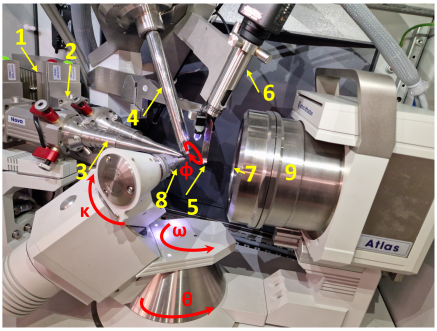

Figure 5.11: Experimental set-up of SuperNova: **1**- X-ray tube, **2**- X-ray shutter, **3**- Collimator,**4**- Cryojet, **5**- Beamstop, **6**- Video microscope, **7**- Beryllium window, **8**- Sample holder and goniometer head, **9**- Detector.

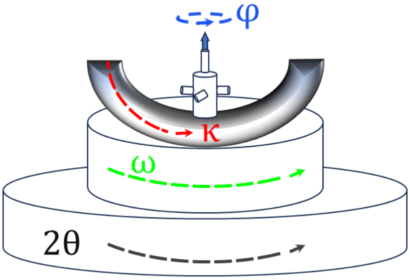

Figure 5.12: Schematic Kappa 4-circle diffractometer geometry showing the relation between the angles with the κappa-geometry.

Single crystals of dimension $50-100\,\mu\text{m}$ were chosen under polarized light. Once a suitable single crystal was selected, it was mounted on the diffractometer and centered. Nevertheless, before performing a complete measurement of a single crystal X-ray diffraction experiment, a pre-experiment (a set of $\approx$ 100 XRD-frames which can be collected for a relatively short time $\approx$ 30 min) was carried out to test the crystal quality and to optimize the experimental parameters.

The measurements were recorded using ω scans at different ϕ settings. Parameters defining the individual data collection for the experiment on both polymorphs at low temperature in the LS state and at room temperature at the high spin state.

5.4.3.3 Synchrotron single crystal diffraction

The single crystal X-ray diffraction experiments as a function of temperature were performed at the Swiss Norwegian Beamline, BM01 at the ESRF (the European Synchrotron Radiation Source) in Grenoble, France.

The general layout of the optics enclosure of BM01 is shown in Figure 5.13. The beam is vertically collimated using a Rh-coated X-ray mirror with a reflection angle of 3×10^{-3} rad (approximately 0.17°). A pair of two parallel Si monochromator crystals produces a monochromatic beam.

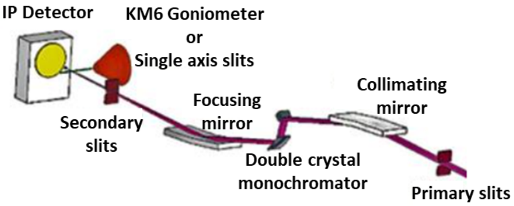

Figure 5.13: Schematic layout of BM01 at SNBL, ESRF [276].

5.4.3.4 Synchrotron measurement

Single crystal samples were measured using an ω-scan, which rotates the crystal 360° about the vertical axis. A Pilatus 2M detector [277] was set up to record frames during the rotation with a step size of typically 0.1° (Figure 5.14). During the measurements, the beam size at the sample was about 300 µm × 270 µm. An Oxford Cryostream 700+ was used for cooling. The in-house software program *Pylatus* controls the measurements [277]. The SNBL ToolBox, a Swiss army knife for Pilatus data, was used to process the data [277] (see Section 6.4.5).

LaB_6 (NIST standard 660, $a \approx 4.156\,46$ Å) powder and a single crystal of *Alaun* ($KAl(SO_4)_2$) was used as a standard to calibrate detector parameters prior to the measurements.

For the monoclinic polymorph, the measurements were performed using a wavelength of 0.630(5) Å, and data were collected while cooling from 270 K to 93 K with a 3 K temperature step. The temperature was changed at a rate of 6 K/min with a 1.5 min waiting time at each step (Appendix Table B.1).

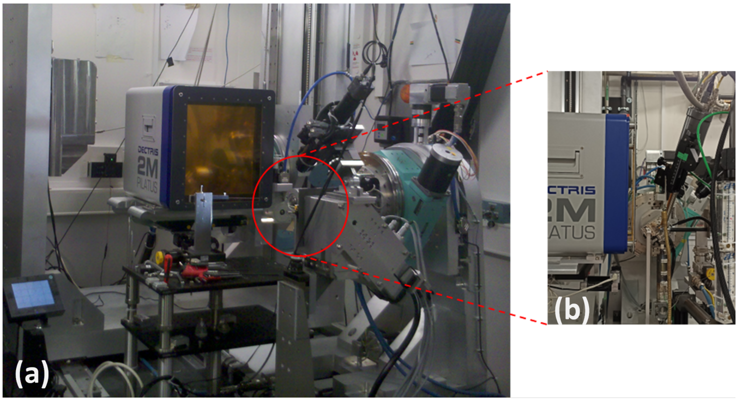

Figure 5.14: **(a)** Experimental setup at BM01 beamline at the ESRF demonstrating the principle components showing the multipurpose diffractometer PILATUS2M. **(b)** Close-up of the sample environment showing the primary beam, the camera, the beam stop, and the motorized stages.

Cyclic measurements were carried out for the orthorhombic polymorph using a wavelength of 0.650(5) Å with an exposure time of 0.5 s and a waiting time of 2 min at each temperature (Appendix Table B.1). The following steps were followed (Figure 5.15):

1. First run:
   - The sample was heated up to 350 K at a rate of 6 K/min without measuring and kept at this temperature for 2 min.
   - Data were collected on cooling from 350 K to 85 K with 5 K temperature steps at a rate of 6 K/min with a waiting time of 3 min per step.
2. Second run:
   - Data were collected on warming in temperature steps of 5 K from 85 K to 350 K at a rate of 6 K/min.
3. Third run:
   - Data were remeasured on cooling from 300 K to 200 K in 50 K increments at a rate of 6 K/min.
   - To map the transition region in more detail, finer temperature steps of 1 K were chosen.
   - Data collection was carried out during this step from 190 K to 165 K with 1 K step with no waiting time.
4. Final run:

---

[1] After the second cycle, the crystal was removed from at 330 K and kept for the next 48 h at room temperature.

- Data were re-measured during warming from 165 K to 190 K with a scan rate of 6 K/min.
- The temperature steps were 1 K during this stage with no waiting time.

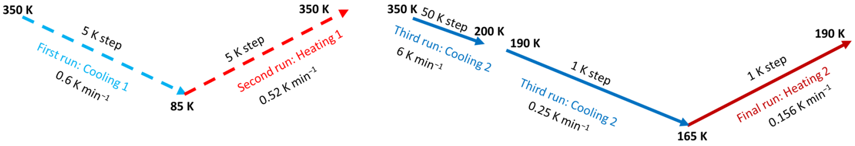

Figure 5.15: Data acquisition procedure for the orthorhombic polymorph, including cooling and warming steps, temperature ranges, measurement rates, and waiting times.

5.4.4 High pressure diffraction

A diamond anvil cell (DAC) is an apparatus that can generate exceptionally high pressures by compressing samples between two diamonds. Diamonds are extraordinarily resilient and transparent to a broad spectrum of electromagnetic radiation, including X-rays, gamma rays, and visible light. Figure 5.16 illustrates a diamond anvil cell in schematic form.

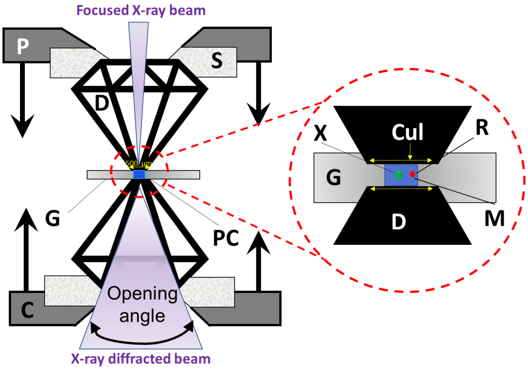

Figure 5.16: A schematic of a DAC. The direction of compression is shown by arrows. P, C = steel body, S = seats, D = diamond anvils, G = gasket, and PC = pressure chamber. For details of the pressure chamber: Cul = Culet, X = crystal, D = diamond-anvils, M = pressure-transmitting medium, G = gasket, and R = ruby.

The most crucial component of a DAC are the two diamond anvils, which are separated by a gasket, a thin metal disk. In the center of the gasket, a hole is drilled; its diameter corresponds to about half the diameter of the culet (front smallest facet) of the diamond (Figure 5.16). This gasket hole holds the sample, a ruby for pressure measurement, and the pressure-transmitting medium. The latter serves the purpose of translating the uniaxial pressure to hydrostatic pressure conditions. Various fluids have been reported to be good hydrostatic pressure-transmitting media, yet all pressure mediums only ensure hydrostatic conditions up to a limiting value. Diamonds with culet sizes of $500 - 600\,\mu\text{m}$ are utilized for experiments up to 20 GPa, whereas diamonds with smaller culets are utilized for higher pressure generation up to 150 GPa. The diamond backing plates have apertures which allow X-ray radiation to enter the sample chamber. The opening angle of the DAC determines the accessibility to reciprocal space in a diffraction experiment.

For the high-pressure investigations in this study (see Section 7.6), the Boehler-Almax DAC [278] has been utilized. The Boehler-Almax type DAC generates pressure by bending the backing plates, which have a conical aperture angle of 90° [278]. As a pressure mechanism, a "screw-drive" is used, which applies pressure to the culets of the diamond by tightening three screws in the steel body (Figure 5.17).

Some challenges arise during high-pressure experiments:

a) The coverage of reciprocal space is limited because of the restricted angular access to the sample.

b) The diffraction signal from the sample is contaminated by contributions from parts of the DAC such as the two single-crystal diamond anvils, backing plates, pressure transmitting medium, gasket, etc. Hence, careful consideration of experimental conditions and careful interpretation of diffraction data are essential for obtaining reliable results (see Section 6.5).

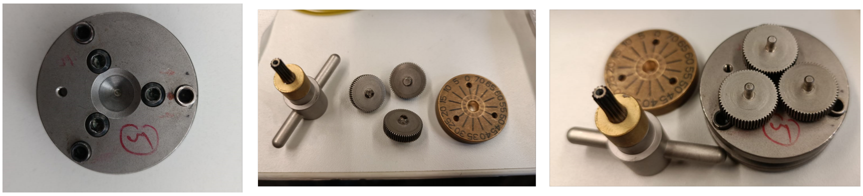

Figure 5.17: Boehler-Almax Diamond Anvil Cell is made from stainless steel with a screw drive to apply pressures.

For single-crystal XRD measurements in the diamond anvil cell, the sample must be the right size to fit in the sample chamber. To prevent the crystal from damage between diamonds, the thickness of the crystal should be less than the thickness of the pressure chamber at the maximum anticipated pressure.

5.4.4.1 Pressure determination

The ruby luminescence method is a standard technique for determining the pressure within a diamond anvil cell (Figure 5.18).

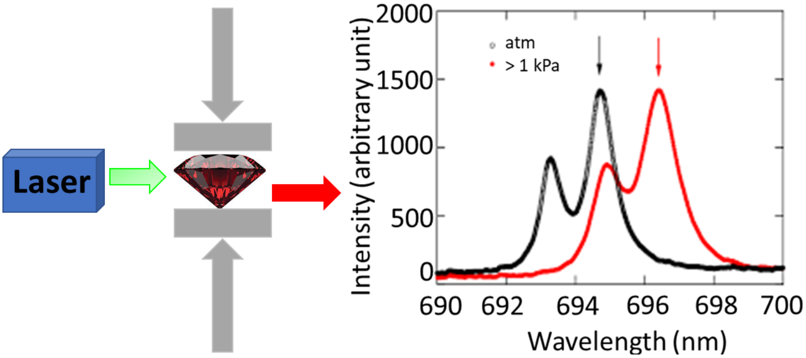

Figure 5.18: A ruby sphere is loaded in the cell and the laser-induced fluorescence is measured. The wavelength shift of the ruby fluorescence is used to measure the pressure in the DAC.

Ruby is a doped aluminum oxide (Al_2O_3) with Cr^{3+} ions. The ruby crystal has three distinct energy states that are used: the ground state (E_1), the metastable state (E_2), and an excited state (E_3), with $E_3 > E_2 > E_1$. When a photon with a suitable energy hits an electron in the ground state, the electron absorbs the energy and jumps into an excited state, which has a lifetime in nanoseconds (E_3 in Figure 5.19). It is followed by a rapid non-radiative transition of the electron to the metastable state (E_2 in Figure 5.19), which is split into two energy levels. Electrons will eventually fall from the split E_2 levels to the ground state, by emitting a photon. The R_1 and R_2 ruby spectrum lines are represented by the photons produced as a result of the higher and lower of the two split E_2 states, respectively. The R_1 and R_2 fluorescence lines of ruby are located at 6942.4 Å and 6929 Å, respectively, under ambient pressure and temperature.

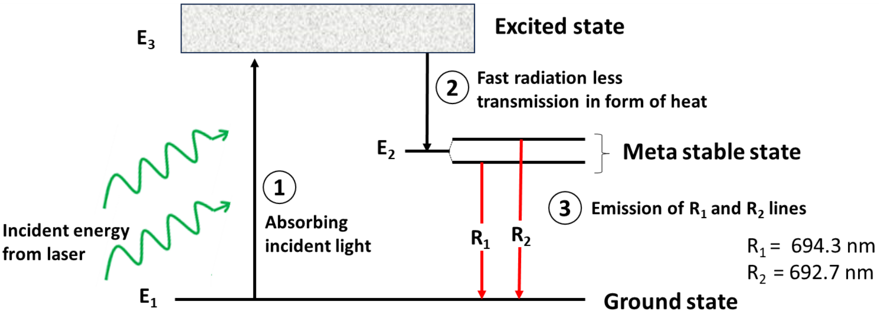

Figure 5.19: Energy level diagram for fluorescence of ruby.

Two characteristics of the energy levels from which these lines are emitted are crucial for the use of ruby luminescence for pressure estimation. First, they are very narrow, resulting in significantly sharp emission lines. This allows for accurate wavelength determination of these lines. Second, the applied pressure affects the energy level because the neighboring ions within the crystal structure are pushed closer together, leading to shifting the energy level to higher energy [279]. Under pressure, both R$_1$ and R$_2$ lines initially shift to longer wavelengths at a rate of $+3.646$ Å GPa^{-1} [280]. The R$_1$ line can be shifted in response to changes in pressure, as shown in Equation 5.4:

$$P(GPa) = \frac{A}{B}[(\frac{\lambda}{\lambda_0})^B - 1] \tag{5.4}$$

where λ is the measured wavelength of the ruby R_1 line, $\lambda_0 = 694.24$ nm at ambient pressure value at 298 K, and $A = 1904$ and $B = 5$ are the least-squares-fit parameters. The ruby luminescence pressure scale [281] can then be used to figure out the pressure by measuring the change in the R_1 wavelength in a given experiment.

5.4.4.2 Synchrotron high pressure diffraction

5.4.4.2.1 P24 PETRA III

The high-pressure X-ray diffraction experiments were carried out using synchrotron X-ray radiation at beamline P24 at the synchrotron X-ray source PETRA III at DESY in Hamburg, Germany [282]. The X-ray radiation is generated in an undulator, which produces a narrow radiation cone of high brilliance (see Reference [283] for details). After being narrowed by a slit system, at least one attenuator and two mirrors in the beam path act as band-pass filters to reduce the thermal load on the subsequent components. To define the energy (wavelength) of the radiation, a monochromator is employed. At P24, it consists of a pair of either Si(111) or Si(311) crystals, which allow energies between 2.4 keV ($\lambda = 5.17$ Å) and 44 keV ($\lambda = 0.28$ Å). To focus the beam after monochromatization, a series of beryllium compound refractive lenses (Be CRL) is inserted. Afterwards, a collimator is placed to limit the beam divergence.

5.4.4.2.2 Measurement

Our experiment was conducted at EH1 on the four-circle κappa diffractometer, with a Pilatus CdTe 1M area detector and a beam energy of 30 keV ($\lambda = 0.413$ Å). The Boehler-Almax type of diamond anvil cells with culet size of 500 µm, pre-loaded with a single crystal of roughly 50 µm × 50 µm× 50 µm, a ruby chip, and isopropanol as pressure-transmitting medium (remain hydrostatic up to 4 GPa at room temperature), were used to perform the high-pressure experiments for both polymorphs. Utilizing a ruby luminescence system, the pressure was determined for all high-pressure measurements. At each pressure point, two ϕ-scan and two ω-scans were measured. Each polymorph has been measured at four different pressure points. The precise run parameters, which can be found in Appendix Table B.2 for the orthorhombic and the monoclinic polymorph, were selected in accordance with the diamond anvil cells (opening angle) and the exposure time needed. After each pressure measurement, the cells were given approximately one day for pressure equilibration, then the pressure was increased and the newly set pressures were measured again.

Chapter 6

Data Processing

6.1 Magnetization data

High-spin SCO materials do have unpaired electrons which contribute to the paramagnetic behavior above the spin transition temperature (see Figure 6.1). The paramagnetic susceptibility decreases with an increase of temperature and follows Curie's law. The paramagnetic susceptibility is in general independent of field strength but markedly dependent on the temperature.

The total measured magnetic susceptibility, denoted as χ_{meas}, can be expressed as the sum of the paramagnetic (χ_{para}) and diamagnetic (χ_{Dia}) contributions:

$$\chi_{meas} = \chi_{para} + \chi_{Dia} \tag{6.1}$$

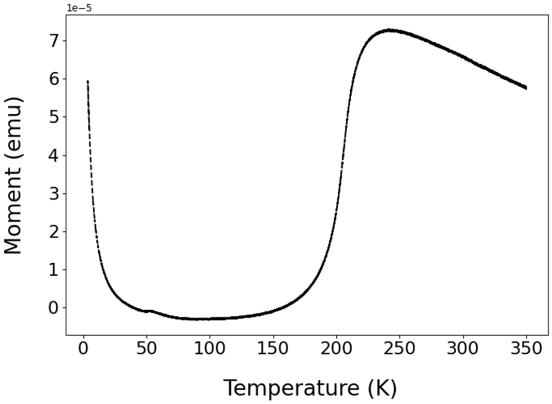

Figure 6.1: Raw data of the magnetic moment (emu) versus temperature (K).

An example of raw magnetization data is illustrated in Figure 6.1, in which three distinct regions can be observed: one above the spin transition (230 K - 350 K), one around the transition region (100 K - 230 K), and one below the spin transition (5 K - 100 K). While the high-temperature susceptibility obeys Curie's law, the low-temperature susceptibility indicates the existence of some paramagnetic impurities (possibly high spin $^{+2}$Fe residuals), which are not expected in a complete spin transition.

It is common to use Pascal's constants to estimate the diamagnetic correction for organic compounds [284]. Yet, either field-dependent or temperature-dependent magnetization experiments can yield a more accurate estimation. In this work, a correction using variable temperature plots at a constant field is employed to adjust the susceptibility data.

The measured susceptibility must be corrected for the underlying diamagnetic effects, because most of the materials do contain paired electrons in valance or deeper shells. The diamagnetic correction could be applied to provide a more precise depiction of the magnetic unique behavior of the spin crossover transition, enabling a better understanding of the real magnetic properties of the SCO material in connection to its spin transition. Diamagnetic susceptibility is generally temperature-independent. It should be noted that the diamagnetic corrections were applied not only for the contribution of the sample itself but also for the sample holder.

The diamagnetic and the paramagnetic components in the two spin states can be estimated by performing a least square fit to the data using the following expression:

$$Moment = \frac{\alpha}{T} + \beta \tag{6.2}$$

where α and β are the free parameters, representing the paramagnetic (temperature-dependent) and diamagnetic (temperature-independent) contributions, respectively. Both temperature regions are utilized for the fitting in a largely independent way; however, using the constraint the diamagnetic contribution (β) is set to be the same in the high-spin and low-spin states.

Due to the unpaired electrons, the high spin state exhibits a significantly large value of the paramagnetic parameter (α_2) as compared to the value (α_1) obtained at low temperatures, which originates only from impurities (Figure 6.2). The diamagnetic parameter (β) is obtained from fitting the two regions simultaneously. Subsequently, the corrected magnetic moment, denoted as $Moment_{\text{corr}}$, can be calculated using the following equation:

$$Moment_{\text{corr}} = Moment_{\text{raw}} - \left[\frac{\alpha_1}{T} + \beta\right] \tag{6.3}$$

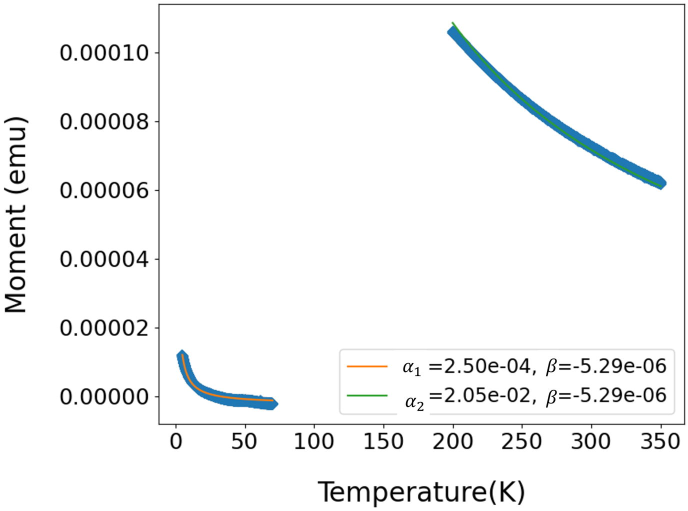

Figure 6.2: The two temperature regions, where the solid line represents the best fitting of the data using Curie's law. The diamagnetic parameter is set to be equal in both regions.

6.2 Differential scanning calorimetry

The excess heat capacity ΔC_p, measured by varying the temperature of a sample, is related to phase transitions of a compound when it undergoes SCO transition. The change in enthalpy can be computed by integrating the change in the specific heat $\Delta C_p (= dQ/dT)$ over the desired temperature range.

$$\Delta H = \int_{T_1}^{T_2} \frac{dQ}{dT} \, dT \tag{6.4}$$

The data obtained from the calorimetric measurements include the temperature (T), the heat flow (dQ/dt), and time (t). The analysis of these data is carried out using the Universal Analysis 2000 acquisition system (version 4.5A, Build 4.5.05), which is preinstalled in the DSC instrument. The following sequence of steps describes in detail the method followed for obtaining the values of entropy and enthalpy.

- Calculation of Heat Capacity (C_P): To calculate the heat capacity C_P, the heat flow is divided by the corresponding rate of change of temperature (dT/dt), and the entire quantity is then normalized with respect to mass. The mathematical expression used for this calculation is given below;

  $$C_p = \frac{1}{m} \frac{\delta Q}{\delta T} = \frac{1}{m} \frac{\frac{\delta Q}{dt}}{\frac{\delta T}{dt}} \tag{6.5}$$

  where m represents the sample weight, $\delta Q/dt$ is the heat flow, and $\delta T/dt$ is the rate of temperature change.[1]

---

[1] Note that $1\text{W} = 1\,\text{J}\,\text{s}^{-1}$, so that $C_p(J/g^{\circ}C) = \frac{(Heat\ Flow,\ mJ)\times(60,\ min)}{(Weight\ of\ Sample,\ mg)(Scan\ Rate,\ ^{\circ}C/min)}$.

- Calculation of enthalpy (ΔH): To calculate the enthalpy change (ΔH), a relevant peak associated to a transition is identified. Then a baseline correction is applied to this peak using spline functions to remove the background contribution (Figure 6.3) [285, 286]. Following this, in accordance with Equation 6.4, this peak is integrated within appropriate temperature limits to obtain the area under the curve. For our calculations, a temperature range was chosen which covers 80% of the spin transition, starting from the temperature point where 90% of the molecules are in the high-spin (HS) state at high temperature (T_{90}) to the temperature point where 10% are in the HS state at low temperature (T_{10}). The corresponding temperature ranges are defined from magnetization measurements. The final expression is then given as follows;
$$\Delta H = \int_{T_{10}}^{T_{90}} \frac{dQ}{dT}\, dT \tag{6.6}$$
- Calculation of entropy (ΔS): The change in entropy can be calculated using the value of enthalpy ΔH and $T_{1/2}$. $T_{1/2}$ corresponds to the transition temperature and can be defined as the temperature which divides the area being integrated in half. The expression governing the relationship between these variables is given as:
$$T_{1/2} = \frac{\Delta H}{\Delta S} \tag{6.7}$$

The analysis of cyclic measurements followed the same protocol as explained above.

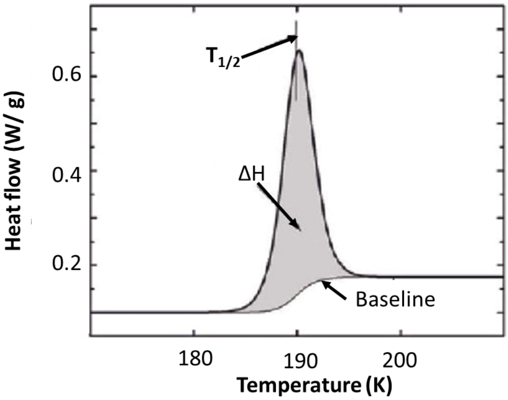

Figure 6.3: Schematic diagram of a peak in DSC data, depicting the baseline correction, the area under the peak (ΔH), and the transition temperature ($T_{1/2}$) [285, 286].

6.3 Powder diffraction data analysis

In order to determine the lattice parameters of polycrystalline samples of both polymorphs, Le Bail refinements [287] on the collected neutron and synchrotron X-ray powder patterns have been performed with the program *JANA2006* [288]. The Le Bail Method (Figure 6.4) is an iterative method and ideally suited to follow the change in lattice parameter as a function of thermodynamic variables like e.g. temperature or pressure [289, 290].

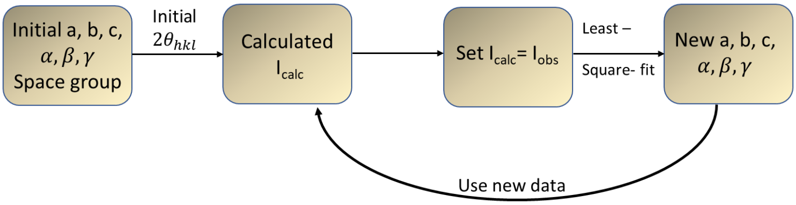

Figure 6.4: Illustration of the Le Bail refinement.

For the application of the Le Bail method, a pre-determined approximate lattice parameter, either from a structural model provided in the literature or deduced from indexing, must be available. Ideally, the space group of the crystal is also known. The lattice parameter in combination with the space group symmetry, define all possible $2\theta_{hkl}$ positions of reflections in a powder diffraction diagram [289].

The temperature-dependent powder patterns were refined using the following refinement strategy, and parameters:

- Background: The background was fitted by Legendre polynomials (10 polynomial coefficients) combined with 30-40 background points assigned manually.
- Zero shift: Zero shift describes an instrumental error (detector zero point error) which results in systematic shifts of the peak positions (2θ).
- Lattice parameter: The initial values were taken from single crystal data which were collected at BM01, SNBL/ESRF.
- Peak fitting: The peaks were fitted using a pseudo-Voigt profile function which combines a Lorentzian (L_Y) and an angle-dependent Gaussian (G_W) contribution: A simplified pseudo-Voigt function is used [291, 292]:

$$PV(H,x) = \zeta \left[\frac{2}{\pi b_L} \frac{1}{1 + \left(\frac{2x}{b_L}\right)^2} \right] + (1-\zeta) \left[\frac{1}{\sqrt{2\pi} b_G} e^{-x^2/(2b_G^2)} \right] \tag{6.8}$$

where $b_G^2 = H_G^2/(8ln2)$ and $b_L = H_L$. H_G and H_L describe the full widths at half maximum (FWHM), they are given by:

$$H_L = L_X \tan\theta + \frac{L_Y}{\cos\theta} \tag{6.9}$$

$$H_G = \sqrt{G_W + G_V \tan\theta + G_U \tan^2\theta} \tag{6.10}$$

> ζ is a mixing parameter, which defines the contribution of the Lorentzian and Gaussian parts to the total profile function. The actual value of ζ depends on the shape of the observed peaks and ranges from 0 to 1. L_X is directly proportional to crystallite size, whereas L_Y is connected with the microstrain on the sample. Equation 6.10 defines the half width of the Gaussian component. G_W is a constant, G_V and G_U are proportional to the diffraction angle.
>
> In addition, anisotropic stain broadening (*St400*, *St004*, and *St103*) was also taken into account while fitting the data [293].[1] Bérar's correction was applied to the standard uncertainties of all refined parameters (profile, elementary cell, and structure) [294] as it results in more realistic and larger standard deviation values.

Sequential Le Bail refinements were performed using the procedure available in the *JANA2006* software [288]. The sequential refinement process commences with the first data file, representing the highest temperature for cooling measurements or the lowest temperature for heating measurements. The parameter values for the second refinement are based on the results of the first convergence, and so on. The program also offers an option for the easy export of parameters for analysis.

For the le Bail fit of the neutron powder data from HRPT, the lattice parameters a, b, c, and β, the peak-shape parameters GW and LY, and the *Zero-shift* parameter were refined. The background was refined with about 30 manually set points and 5 refined Legendre polynomial terms. Bérar's correction [294] was applied to the estimated standard uncertainties.

6.4 Single crystal X-ray diffraction data analysis

6.4.1 Data pre-processing

For analyzing the single-crystal X-ray diffraction data (SCXRD) collected from BM01, ESRF, the data frames first needed to be converted to the Esperanto (**.par*) format. The Esperanto format is specifically designed to handle X-ray diffraction data and is recognized by *CrysAlis*^{Pro} as the preferred file format for analysis. The converted files were then further processed using the software *CrysAlis*^{Pro} [295].

For this first step, the files for data processing were prepared using the SNBL ToolBox [277] with the Crysis software. While converting from the Pilatus (**.cbf*) to the Esperanto format, the same experimental parameters were kept for all data sets using a calibration file obtained by measuring *Alaun* single crystal (see Section 5.4.3.3).

---

[1] P. W. Stephens [293] provided a phenomenological model of anisotropic broadening in powder diffraction, taking into account the distribution of lattice metric values within the sample. Each crystallite in this model is assumed to have its own lattice parameters, distributed in multidimensions throughout the powder sample. The width of each reflection can be expressed in terms of moments of this distribution, which leads to parameters that can be altered to obtain optimal fits. The anisotropic strain is described by a symmetrical 4^{th} order tensor.

The SC data obtained from the laboratory instrument were already in a format which could be processed using *CrysAlis*^{Pro}; no additional conversion was required.

6.4.2 Searching, indexing, integration and data reduction

Each frame was visually inspected to ensure no corrupted frames were included before the data processing began. The following is a general overview of the data processing steps using *CrysAlis*^{Pro} (v171.42.80A; Rigaku Oxford Diffraction, 2023):

1. Peak Search: The first step is "Peak hunting". *CrysAlis*^{Pro} uses a search algorithm in which the intensity of each pixel in the image is compared with the local background. Smart peak hunting has been used. At the end of this process, *CrysAlis*^{Pro} creates a "Peaktable file".

2. Peak Indexing: Peak indexing is the process of assigning Miller indices (h, k, l) to each of the diffraction peaks observed in the X-ray diffraction pattern. This step is necessary to determine the orientation of the unit cell. The orientation matrix relates the reciprocal axes of the crystal to the Cartesian reference system of the diffractometer [296]. The orientation matrix UB describes the relationship between the crystal vector h $=h\mathbf{a}^* + k\mathbf{b}^* + l\mathbf{c}^*$ and the instrument vector r_0 as follows:
$$r_0 = UBh \tag{6.11}$$

   The elements of the matrix contain information about the size and orientation of the unit cell of the crystal.

   CrysAlis^{Pro} includes an automated peak indexing routine that uses the measured peak positions to search for a consistent set of lattice parameters that match the observed diffraction pattern. The orientation matrix is used to predict the Bragg reflection position matching the lattice. The orientation is considered to be correct if a certain percentage of peak position matches the obtained orientation matrix, which can be a criterion to evaluate the indexing success.[1] Once the orientation matrix and the unit cell are assigned, a refinement is performed to optimize the fit between the observed and calculated peak positions.

3. Intensity Integration: After determining the orientation matrix, the next step is intensity integration. The program predicts the positions of the reflections based on the UB-matrix, and then reconstructs reflections with split profiles over several frames. The integrated intensity of each reflection is then deduced based on the reflection shape and the background. Each Bragg peak is integrated around the centroid of the predicted Bragg peak position, with specified radii for integration and the outer and inner radii of pixels surrounding the peak for a background estimate. It is worth noting that the integration mask can be adjusted. The background signal, which includes contributions from sources such as air scattering and detector noise, is approximated and subtracted from the observed reflections.

---

[1] The indexing percentage is defined as the number of indexed patterns over the number of initially identified diffraction peaks hunted.

4. Data Reduction: The final step in the X-ray diffraction data processing is data reduction, which involves scaling the intensity data from multiple diffraction runs to obtain a single dataset with an improved signal-to-noise ratio. It also involves applying a series of correction factors to the integrated intensities of the diffraction peaks. These factors are absorption, and Lorentz-polarization correction (see Section 6.4.3 for more details).

   In *CrysAlis*^{Pro}, the data finalization command applies a frame scaling and an empirical absorption correction to the intensities of the reflections and outputs the final corrected values in the *.hkl file. By default, an automatic procedure is performed after each data reduction. One can inspect the XRD data quality by merging the intensities of the symmetry -equivalent reflections [R_{sigma}, $I^2_{obs}/\sigma^2_{int}(I^2_{obs})$ and R_{int}]. The frame scaling factors can help in the detection of serious problems in the data. The R_{int} value indicates the overall quality of the data collection. The value of R_{int} is obtained by merging the intensities of certain groups of reflections, (those reflections which are symmetry-equivalent under the chosen Laue symmetry). R_{int} is defined as [297]:

$$R_{\text{int}} = \sum_j \left[\frac{\sum_i |I_{\text{obs}} - \langle I_{\text{obs}} \rangle|}{\sum_i \langle I_{\text{obs}} \rangle} \right] \tag{6.12}$$

   where I_{obs} stands for the intensity of a single reflection, and $\langle I^2_{\text{obs}} \rangle$ is the average intensity of a set of symmetry equivalent reflections. All independent reflections i are included in the inner summation, and all symmetry equivalent reflections j, which correspond to the i^{th} independent reflection, are covered in the outer summation. In other words, R_{int} represents the weighted difference between the average intensity and individual Bragg reflections. R_{sigma} is defined by the ratio:

$$R_{\text{sigma}} = \sum_j \left[\frac{\sum_i \sigma_{\text{int}}(I_{\text{obs}})}{\sum_i I_{\text{obs}}} \right] \tag{6.13}$$

   where the summation is as in Equation 6.12, and the $\sigma_{\text{int}}(I^2_{\text{obs}})$ is the calculated standard uncertainty of the intensity of the merged reflection, which is given by:

$$\sigma_{\text{int}}(F^2_{\text{obs}}) = \sqrt{\sum_i \frac{(I_{\text{obs}} - \langle I_{\text{obs}} \rangle)^2}{|N_{\text{red}}|}} \tag{6.14}$$

   where N_{red} is the number of redundant reflections. Note that only observed quantities are required to calculate R_{int} and σ_{int}. The higher the symmetry, the larger the number of merged reflections. This is represented by the "Redundancy," which is the average number of observed reflections merged into symmetry-independent reflections. By measuring reflections more than once, the redundancy can be enhanced. High redundancy helps in the detection of outliers. Insufficient intensities in a data set lead to poor $F^2_{obs}/\sigma_{int}(F^2_{obs})$ and high-R_{sigma} values (3 and $> 20\%$, respectively, for the outermost resolution d-shells), and consequently, high R_{int} values.

6.4.3 Structure solution and the phase problem

The process of determining the approximate crystal structure of a material from X-ray diffraction data is called structure determination. In this process, the goal is to determine the positions of all atoms in the unit cell of the crystal and their corresponding displacement parameters (isotropic or anisotropic parameters). The method is based on the expression for the intensity of a reflection, which can be given as:

$$I_{hkl} = k.L_p.AF^2_{(hkl)} \tag{6.15}$$

where k, L_P, and A are the scale, Lorentz-polarization correction, and the absorption factors, respectively. The polarization factor is given by [296]:

$$P = \frac{1 + A\cos^2(2\theta)}{1 + A} \tag{6.16}$$

where $A = \cos^2(2\theta_M)$ and θ_M is the Bragg angle of the monochromator crystal. The Lorentz factor (Equation 6.17) results from the fact that the time needed for a reciprocal lattice point to travel across the sphere of reflection is not constant but rather varies with its position in reciprocal space and the direction in which it approaches the sphere.

$$L = \frac{1}{sin2\theta} \tag{6.17}$$

Since both corrections (polarization and Lorentz factor) depend on the experimental conditions but not on the structural model, they are typically combined to provide a single correction factor, the so-called Lorentz-polarization correction, L_P, for a particular experimental geometry. The L_P factor is given by [296]:

$$L_P = \frac{1 + A\cos^2(2\theta)}{(1 + A)\sin(2\theta)} \tag{6.18}$$

Absorption effects in the integrated intensities are described by Beer-Lambert's law given by [296]:

$$I = I_0 e^{-\mu\tau} \tag{6.19}$$

where I_0 and I are the intensity of the incident and the attenuated beam, respectively, τ in the total beam path, and μ is the linear absorption coefficient. Spherical crystals have the advantage of having a more uniform absorption correction [296]. Several methods can be employed to correct absorption effects, among them empirical [298], semi-empirical (multiscan) [299] absorption correction derived from the reflection intensity, as well as numerical absorption correction [300] (Gaussian [301], spherical) based on the crystal shape.

The F term denotes the structure factor, which is defined as the sum of the contributions of all atoms in the unit cell to the amplitude and phase of the diffracted X-ray wave (Equation 6.20).

$$F_{(hkl)} = \sum_{i=1}^{N} f_i e^{-2\pi i(hx_i + ky_i + lz_i)} \tag{6.20}$$

where h, k, and l are the Miller indices of the reflection *(h,k,l)*, x, y, and z are the coordinates of the i^{th} atom in the unit cell, N is the total number of atoms in the unit cell, and f_i is the atomic scattering factor of the i^{th} atom. The scattering factor (f_0) represents the scattering power of a specific atom, quantified in relation to the scattering power of an equivalent number of electrons situated at the nucleus atomic position. The scattering factor of each atom is a function of the atom type and the scattering angle (sinθ/λ), as illustrated in Figure 6.5. f_0 reaches its maximum when (θ=0). Thus, f_0 is equal to the atomic number Z, and it decreases as a function of the angle of incidence.

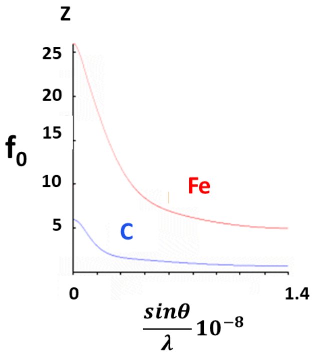

Figure 6.5: The scattering factor of different atoms plotted as a function of Bragg angle for incident X-ray of a specific wavelength [302].

Up to this point, the aforementioned equations have been formulated under the assumption of rigid atoms at an absolute temperature of 0 K. However, when the temperature increases ($T > 0$ K), the atoms start to vibrate around their equilibrium positions. These vibrations lead to a reduction in the intensity of the Bragg peaks as the scattering angle (θ) increases. This atomic vibration depends on the temperature and the mass of the atom. In general, the higher the temperature, the greater the vibration. The effect of the thermal motion is to spread an electron cloud over a larger volume and thus cause the scattering factor to fall down more rapidly. Thus, the real scattering factor is no longer the simple f_0, but rather the given combined expression:

$$f = f_0 e^{-B(\sin^2\theta)/\lambda^2} \tag{6.21}$$

where B-factor can be related to the mean displacement of a vibrating atom $\langle u \rangle$ by the Debye-Waller equation:

$$B = 8\pi^2 \langle u^2 \rangle \tag{6.22}$$

The correction of the thermal motion can be applied to the structure factor at two different approximations. The simplest assumption is the isotropic vibration, in which all the atoms vibrate in a spherical shape. The second assumption assumes anisotropic movement in which the single atomic thermal parameter is replaced by six atomic displacement parameters (ADPs) that describe the size and the orientation of the ellipsoid of vibration. They are represented by a 3 × 3 matrix:

$$U = \begin{pmatrix} U_{11} & U_{12} & U_{13} \\ U_{21} & U_{22} & U_{23} \\ U_{31} & U_{32} & U_{33} \end{pmatrix} \tag{6.23}$$

In the context of ADPs, the "diagonal elements" (U_{11}, U_{22}, U_{33}) represent the mean square displacement of an atom along the corresponding crystallographic principle axes. They characterize the atom's thermal vibrations in specific directions. On the other hand, the "off-diagonal elements" of the matrix (U_{12}, U_{13}, U_{21}, U_{23}, U_{31}, U_{32}) denote the correlation between the displacements along different axes. For isotropic vibrations, the ellipsoids have zero off-diagonal terms and identical diagonal terms, indicating that the thermal ellipsoids are spherical. It is worth noting that ADP values corresponding to the diagonals can not be negative.

The process of structure solution relies on the determination of the structure factor F from the observed experimental intensities (Equation 6.24).

$$\sqrt{I} = |F| e^{(i\phi_{hkl})} \tag{6.24}$$

In order to determine the electron density, both the amplitudes and the phases are needed. However, experimentally, it is only possible to measure the intensity of the reflections (I), which provides information about the amplitude of the structure factor, but not the phase. Therefore, it is required to recover the missing phases by providing a close enough "starting structure". For this structure solution step, there are several methods that can be used: Direct methods [303] e.g., with the program SIR92 [304], SHELXT [305] or charge flipping methods [306, 307] e.g., Superflip [308]. It is worth noting that the initial model for the crystal structure can be obtained from the literature.

6.4.4 Structure refinement

The crystal structure corresponding to the lowest temperature of the single crystal, which was collected at the SNBL beamline at ESRF, was solved via direct methods using the SHELXT software [305]. Structure refinement was performed using SHELXL [309]. Laboratory data were refined with the program *JANA2006* [288].

As the structure solution sometimes does not find all the atoms in the model, a difference Fourier synthesis is utilized to find the missing atoms which were not found at the solution stage. A difference Fourier synthesis uses the difference between the calculated structure factor F_{calc} and the observed structure factor F_{obs} ($|F_{calc}|$ - $|F_{obs}|$, as shown in Equation 6.25). The result is a residual electron density map that highlights discrepancies between the model and the observed data, thereby helping to identify missing or excess atoms within the crystal structure.

$$\Delta\rho(x,y,z) = \frac{1}{V} \sum_{hkl} \left(F_{hkl}^{\mathrm{calc}} - F_{hkl}^{\mathrm{obs}} \right) e^{-2\pi i(hx+ky+lz)} e^{i\Delta\phi_{hkl}} \tag{6.25}$$

We used the difference Fourier synthesis to locate all atoms apart from hydrogen atoms. Then the structural refinement was started with the atomic positions and the isotropic as well as anisotropic ADPs were subsequently refined, starting with the heaviest atoms (Fe, S, N, and C).

Finally, all hydrogen atoms were placed in calculated positions using the riding model[1] with C-H bond distances set to 0.93 Å. All non-hydrogen atoms were refined anisotropically.

As the anisotropic displacement parameters of one of the phenyl groups in the monoclinic polymorph were very large, this group was treated as disordered and splitted over two positions. The disordered phenyl group was treated as a rigid group with C-C and C-H bond distances set to 1.39 Å and 0.93 Å, respectively. The sum of the occupancies for the disordered phenyl group was restricted to be 1.

The basic principle of refinement is the statistical adjustment of atomic parameters in the model to fit the intensities of the diffraction data as well as possible. This is achieved by using least squares refinement [296] (see Appendix SectionC.1). Various mathematical parameters are used to assess the quality of the structure determination. The most important ones are the overall R-factor (Equation 6.26) and the weighted R-factor (Equation 6.27). They are generally based on the difference between the observed and calculated structure factors (F_{obs} and F_{calc}). The GOF (Goodness Of Fit), depends on the number of observations and parameters (n and p). The lower the value for these statistical measures, the better the fit of the calculated model to the observed data.

$$R = \sum_i \frac{|F_{obs}| - |F_{calc}|}{|F_{obs}|} \tag{6.26}$$

$$R_w = \sqrt{\frac{\sum_i w_i(|F_{obs}| - |F_{calc}|)^2}{\sum_i w_i|F_{obs}|}} \tag{6.27}$$

$$GOF = \sqrt{\frac{\sum w(|F_{obs}| - |F_{calc}|)^2}{(n-p)}} \tag{6.28}$$

where n is the number of independent reflections and p is the number of least-square refined parameters [288]. It should be noted that the Goodness of Fit is always based on refinements against F^2, in SHELX software [309].

$$GOF_{SHELX} = \sqrt{\frac{\sum w(|F_{obs}^2| - |F_{calc}^2|)^2}{(n-p)}} \tag{6.29}$$

6.4.5 Sequential processing of multiple temperature single crystal diffraction data set

Performing sequential data reduction for a large set of data points in CrysAlis can be efficiently done by utilizing the batch processing capabilities of CrysAlis software. The process is described in detail in Appendix Section C.2.1. When batch

---

[1] The riding model assumes that the hydrogen atom position is directly related to the position of the heavy atom it is bonded to. Also, it considers that the thermal displacement of the hydrogen atom as a fraction of thermal displacement of the heavy atom.

processing is run, sequential data reduction begins, where the initial orientation matrix of each dataset is the matrix from the prior one.

The sequential refinement of variable temperature diffraction data using SHELXL [309] and the *seq_ Shell* software involves several steps. Initially, the process begins with refining the lowest temperature data set using SHELXL to obtain an initial structural model. Subsequently, the *seq_ Shell* software is employed to perform batch refinement for each subsequent data set. This software copies the refined structural model from the previous temperature step as the starting point, executes SHELXL for refinement, and extracts relevant information. The entire procedure ensures a systematic and easy refinement process for temperature-dependent structural analysis (see Appendix Section C.2.2 for more details).

6.5 High pressure single crystal X-ray diffraction

6.5.1 Pre-Processing: Conversion of XRD images with *CrysAlis^{Pro}* software

The studies under high-pressure conditions were carried out at P24 beamline at Petra III in Hamburg, Germany (see Section 5.4.4 for experimental details). Therefore, the *.cbf had to be converted to the Esperanto format.

The detailed procedure for converting data into the *CrysAlis^{Pro}* format, ESPERANTO, is provided in Appendix Section C.3.1. A series of parameter settings are outlined in Appendix Figure C.1.

6.5.2 Peak search

The first step in the data analysis is the peak search, which has been discussed previously (in Section 6.4.2). Before starting the procedure, it was checked whether the first and last frames of an experiment contain of diffraction rings from the gasket, and if so, these frames were eliminated from peak hunting. A traditional peak hunting[1] with different thresholds and a 5 for 7 x 7 average was used to harvest reflections from the raw frame data. It should be noted that in the initial peak search process, some diamond peaks or reflections on powder rings (e.g., from the gasket) may be selected.

6.5.3 Indexing

The Ewald Explorer tool was utilized to clearly distinguish between the diffraction patterns originating from the diamond, the gasket, and those originating from the sample itself (see Appendix Section C.3.2 for details). Diamond peaks exhibit the highest intensities and the peaks on the powder rings occur manifest at specific

---

[1] *CrysAlis^{Pro}* employs two parameters to locate a peak for traditional peak hunting: threshold value and 7×7 average. First, only image pixels with an intensity greater than the selected threshold are considered for peak localization. When such a pixel is identified, sequence of neighborhood tests are conducted. Calculated are the average intensities of $I_{3\times3}$, $I_{5\times5}$, and $I_{7\times7}$ pixel areas. If $I_{3\times3} > I_{5\times5} > I_{7\times7}$, then the pixel in the center is a peak.

angles (corresponding to the same d-values). Based on these criteria, the peaks were excluded before starting the indexation. The indexing process was carried out by automatic indexing. In order to get an accurate orientation matrix, the lattice parameters were refined. Additionally, the parameters describing goniometer offsets were also refined. However, the sample to-detector distance d and the values of $x0$ and $y0$ describing the position of the primary beam were restricted. For higher pressure data points, the orientation matrix, which had been determined from the previous pressure point, was imported. For the data at higher pressure points, the refined instrument parameters obtained at lower pressure were kept fixed and used for all other pressure points. This is important to ensure consistency of the unit cell parameters at all pressures.

6.5.4 Intensity integration

Once the orientation matrix was refined, the data reduction for the two phi-runs together was performed (see Section 6.4.2). During the integration, a proper mask was applied to the beam stop, the detector stripes, and the regions of the deteriorated pixels on the detector. Regions shadowed by the body of the DAC were also excluded (Appendix Section C.3.3 for a detailed step-by-step manual).

The integrated data set may still contain outliers with falsified intensities, which were detected by comparing the intensities of symmetry-equivalent reflections. For the outlier rejection, the Laue symmetry mmm was chosen for the orthorhombic polymorph and $2/m$ with a b-unique axis for the monoclinic polymorph.

In the final data reduction stage, the output intensities were corrected for the Lorentz-polarization factor, and the absorption correction was applied empirically by the Scale3 Abspack program implemented in *CrysAlis*^{Pro} [295]. To reduce noise in the final dataset, we applied a resolution cutoff at the $\sin\theta/\lambda$ values, where 13% of the reflections had an intensity $> 3\sigma(\mathrm{I})$. Thus, only reflections which are within the specified value in the "2 Theta max threshold" are considered in the data reduction.

Reflections with falsified intensities (overlap with diamonds, in the shadowed region, lay on powder rings), which were not rejected during the integration procedure, were identified and removed at a later stage in the refinement process using the manual culling options based on the intensities of symmetry equivalent reflections, which is implemented in *JANA2006* [310]. To confirm that the reflection was an outlier, we cross-verified it against the original frame in *CrysAlis*^{Pro}.

6.5.5 Structure solution and refinement

In a high-pressure single-crystal X-ray diffraction experiment, the amount of symmetry independent reflections is low due to the limited opening angle of the DAC. As none of the samples investigated at high pressure had higher symmetry than orthorhombic, structural solution and refinement were complicated due to the low availability and completeness of the data.

In general, the structures at ambient conditions were used as starting points for the refinement of the high pressure data. The refined model from each pressure point was used as a starting model for the subsequent pressure points.

Due to the limited amount of data, the displacement parameters were modeled isotropically (U_{iso}) to improve the data-to-parameter ratio. For the monoclinic polymorph, restraints were applied to the atomic displacement parameters of the carbon atoms in the same aromatic ring (pyridine or biphenyl rings) and sulfur atoms to enforce identical values, again to improve the data-to-parameter ratio. Finally, all hydrogen atoms were placed in calculated positions using the riding model with C-H bond distances set to 0.93 Å.

Chapter 7

Results and Discussion

7.1 Magnetic properties: Effect of particle size and scan rate

The magnetic property measurements for both polymorphs were performed on a bunch of single crystals using a SQUID magnetometer. The cooling and heating cycles were recorded with a scanning rate of 0.5 K/min. The product of the molar magnetic susceptibility with temperature, $\chi_M T$, as a function of temperature, T is shown in Figure 7.1 for both polymorphs. The diamagnetic and paramagnetic corrections have been applied (see Section 6.1).

At room temperature, $\chi_M T$ is near $3.2\,\mathrm{cm^3\,K\,mol^{-1}}$, corresponding to what is expected for a triplet HS state (S=2) (Figure 7.1) [59]. Upon cooling, $\chi_M T$ decreases sharply for the orthorhombic polymorphs, while for the monoclinic polymorph, the magnetic signal decreases gradually. Below 120 K, the magnetic responses of both phases are almost zero, indicating the presence of a singlet LS state. In the heating cycle, $\chi_M T$ of the monoclinic polymorph increases smoothly, showing a gradual spin transition at $T_{1/2}$= 207 K, spanning a large transition region from 250 K to 150 K. In contrast, the orthorhombic polymorph exhibits an abrupt spin transition with transition temperatures of $T_{1/2\uparrow}$= 173 K and $T_{1/2\downarrow}$= 167 K, resulting in a thermal hysteresis width of 5 K. These results are in a good agreement with the magnetic properties recorded in the literature for these two polymorphs [33, 34, 206].

The measurements on polycrystalline samples of both polymorphs were conducted under comparable conditions (Figure 7.1). The measurements show that the polycrystalline sample of the monoclinic polymorph, exhibits a transition curve similar to the one of single crystal, while the orthorhombic polymorph, a two-step transition with an intermediate state is observed during the heating cycle between 179 K and 188 K (Figure 7.1), which was not observed for the single crystal.

Further studies of the magnetic properties have been performed on a bunch of single crystals and on polycrystalline material of both polymorphs at different scan rates (0.2 K/min, 0.5 K/min, 1 K/min, 2 K/min, 5 K/min, 8 K/min, and 10 K/min (see Section 5.2)). For single crystalline samples of both polymorphs, the shape of the transition is similar with different scan rates (Figure 7.2) and the thermal hysteresis width shows negligible dependence on the scan rate ($\approx 0.8\,\mathrm{K}$ for monoclinic; $\approx 6.5\,\mathrm{K}$ for orthorhombic, Figure 7.2(right)).

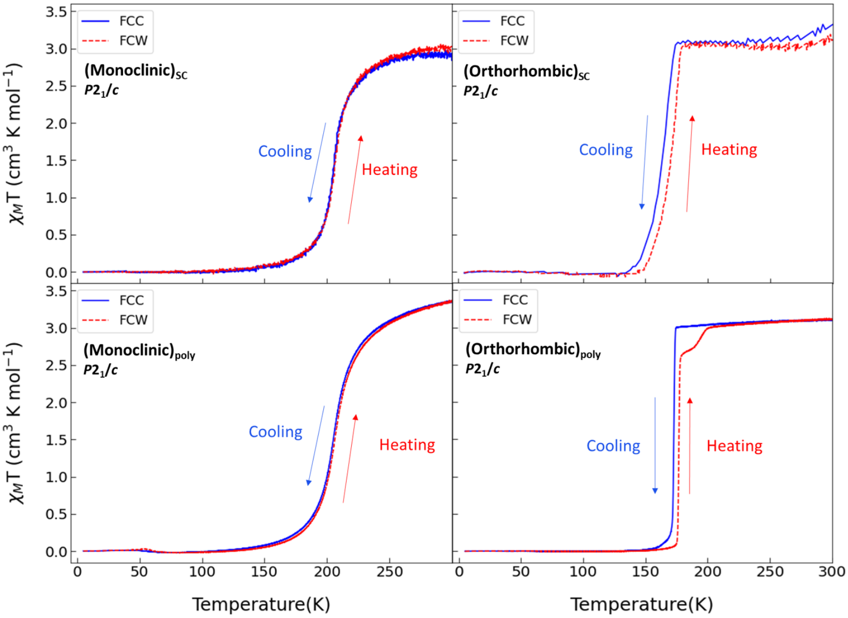

Figure 7.1: Product of magnetic molar susceptibility with temperature as a function of temperature ($\chi_M T$ vs. T) measured at a scan rate of 0.5 K/min with an applied field of $\mu_0 H = 2\mathrm{T}$. The measurements were performed on the monoclinic (left) and the orthorhombic polymorph (right). The abbreviations ‘poly’ and ‘SC’ stand for polycrystalline and single crystals, respectively. The solid blue and the dashed red lines correspond to the cooling and heating cycles, respectively. Diamagnetic and paramagnetic corrections were applied for the sample holder and the sample itself.

On the other hand, for the polycrystalline samples of both polymorphs, a remarkable scan rate dependence is revealed, in which the width of the hysteresis loop increases with increasing scan rate. For the monoclinic polymorph, the hysteresis width undergoes a monotonic increase from 0.6 K to 12.3 K ($\Delta T = 11.7\,\mathrm{K}$) (Figure 7.2 (right)), while for the orthorhombic polymorph, the hysteresis width increases from 3.2 K to 17.9 K ($\Delta T = 14.7\,\mathrm{K}$) (Figure 7.2).

The different scan rate dependencies of the thermal hysteresis width observed between single crystals and polycrystalline material can be explained by considering the kinetic properties of the surface-to-volume ratio [311]. This phenomenon suggests a complex interplay between grain size and the kinetics of the material (Appendix Section D.1).

It should be noted that for the orthorhombic polymorph, there is also a difference in transition temperatures between measurements conducted on powder and those on single crystals at the slowest scan rate. However, the hysteresis width is almost the same at the slowest scan rate (Figure 7.2).

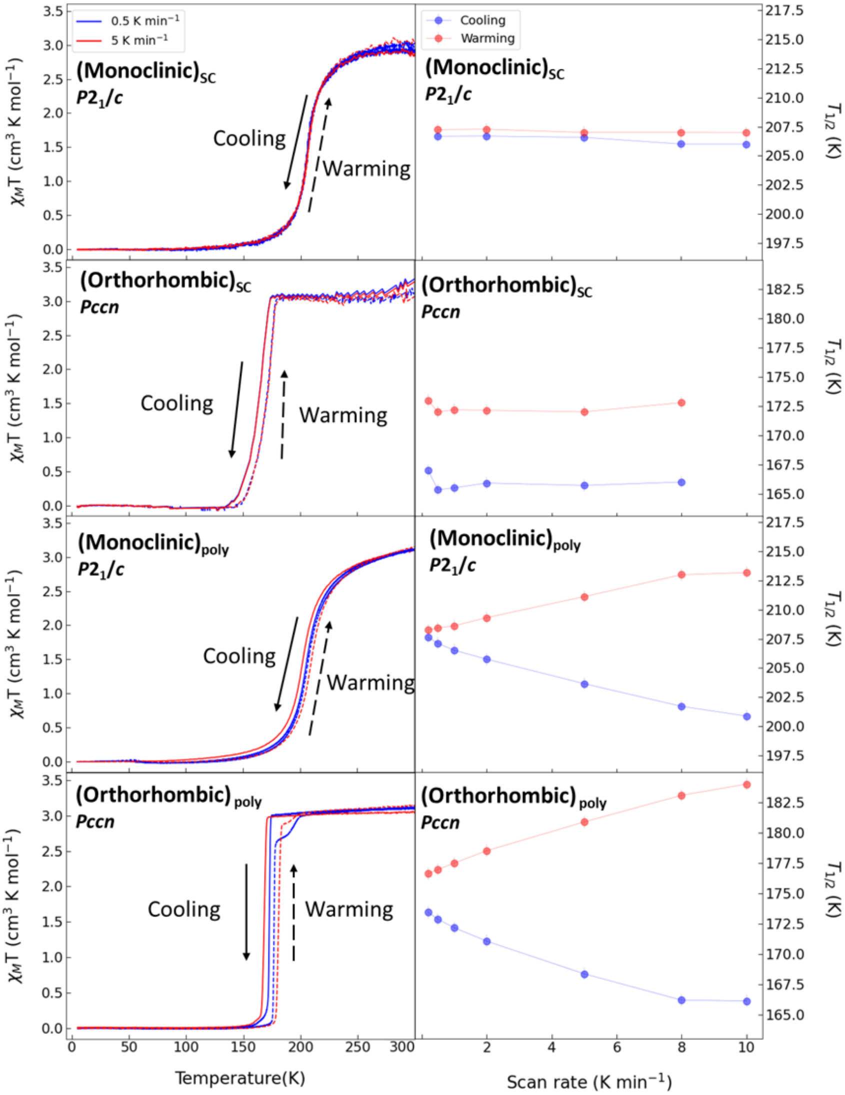

Figure 7.2: (Left) $\chi_M T$ as a function of temperature measured at two different scan rates at 0.5 K/min (blue) and 5 K/min (red) for both polymorphs. (Right) The observed $T_{1/2}$, while cooling (blue) and heating (red), as a function of the scan rate for both polymorphs. The abbreviations ‘poly’ and ‘SC’ stand for polycrystalline and single crystals, respectively. The solid and the dashed lines correspond to the cooling and cooling cycles, respectively.

The two-step transition which is observed on the polycrystalline sample of the orthorhombic polymorph corresponds to an intermediate state between the high and low spin states. It is exclusively observed during heating cycles (Figure 7.2 (bottom left)). The slower scan rates make the two-step nature of the transition more apparent and pronounced (Figure 7.3). Earlier investigations on the magnetic characteristics of the orthorhombic polymorph, which were conducted at faster scan rates, did not report this two-step behavior [33, 59, 60, 203]. However, interestingly, a similar two-step behavior has been reported in diffuse reflectivity measurements at high hydrostatic pressures, by Rotaru et al., [210] and was attributed to the existence of a new phase which was denoted as polymorph (III).

This intermediate state may arise due to the presence of energy barriers that need to be overcome for the complete transition between spin states. These barriers probably results from the existence of two crystallographically independent SCO Fe(II) sites with slightly different coordination environments, leading to dissimilar transition temperatures delimiting a plateau (or shoulder) [109]. When the orthorhombic polymorph is subjected to a faster scan rate, the transition process within each domain maintains its synchronization. As a result, the material tends to exhibit a direct transition from the LS-to-HS transition, leading to the disappearance of the intermediate state. Conversely, a slower scan rate results in effectively passing through the intermediate state with the existence of distinct domains. It is worth noting that it has been reported in the literature that the two-step spin transition was connected to a dramatic change in the hydrogen-bonding system [312].

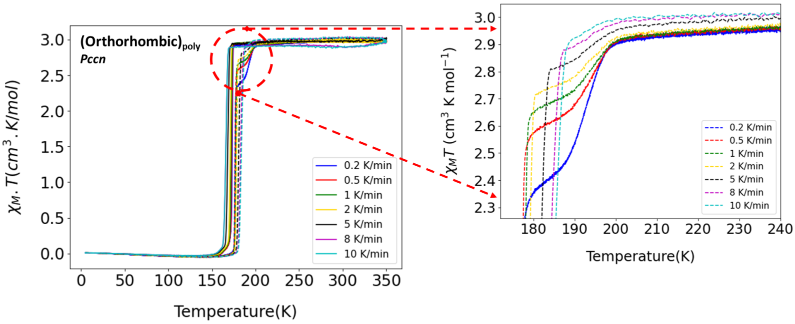

Figure 7.3: (Left) The magnetic susceptibility measurement on a polycrystalline sample of the orthorhombic polymorph at different scan rates ranging from 0.2 K/min to 10 K/min. (Right) Zoom into the stability region of the intermediate state which is observed only on heating, illustrating its evolution with different scan rates. The dashed and solid lines correspond to heating and cooling cycles, respectively.

To draw further conclusions on the nature of the intermediate phase, and in order to completely comprehend the relevance and consequence of this two-step behavior and its connection to a slow scan rate and pressure-induced phase transitions in the orthorhombic polymorph, it is essential to carry out additional single crystal diffraction investigations to elucidate the crystal structure. However, these studies are out of the scope of this thesis.

The stability and reproducibility of the magnetic behavior of both polymorphs were demonstrated by carrying out many heating cycles at the same scan rate (Appendix Figure E.1). Furthermore, additional measurements on both samples in different fields reveal no significant field effects, apart from small shifts in $T_{1/2}$ ($< 1\,\mathrm{K\,T^{-1}}$, Appendix Section E.2, Figures E.2 and E.3).

7.2 Differential scanning calorimetry

Differential scanning calorimetry (DSC) has been used to examine the thermal characteristics of the spin transition of the monoclinic polymorph of $\mathrm{Fe(PM\text{-}Bia)_2(NCS)_2}$ over the temperature range of 140 K- 310 K, in both warming and cooling modes, with a temperature scan rate of 10 K/min at ambient pressure. Figure 7.4 (left) shows the heat flow as a function of the temperature. The two broad peaks shown in the graph correspond to a gradual crossover transition. The peak observed during heating is an endothermic peak, representing the LS to HS transition (Table 7.1). The peak observed on cooling is an exothermic peak that corresponds to the HS to LS transitions. The two peaks are separated by a thermal hysteresis of 3.1(40) K, as detected by magnetization measurement at fast scan rate measurements (see Section 7.1). The spin transition is associated with a change of enthalpy ΔH. The change in entropy ΔS is calculated using the relation $\Delta S = \frac{\Delta H}{T_{1/2}}$ (see Section 4.4.1 for more details). Considering the fact that the electronic contribution is equal to R ln5 $=13.4\,\mathrm{J\,mol^{-1}\,K^{-1}}$ (for S_{HS}=2, S_{LS}=0) for iron(II) SCO compounds, the vibrational contribution to the entropy variation is calculated (Table 7.1).

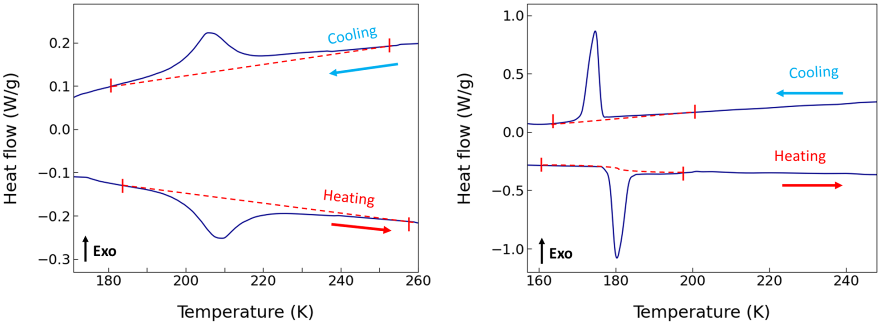

Figure 7.4: DSC curves of the monoclinic (left) and the orthorhombic (right) polymorph of $\mathrm{Fe(PM\text{-}Bia)_2(NCS)_2}$ recorded at 10 K/min upon heating and cooling.

The DSC study for the orthorhombic polymorph has been performed in the temperature range 120 K - 310 K, with a temperature scan rate of 10 K/min in both heating and cooling modes. The heat capacity as a function of temperature (Figure 7.4 (right)) shows sharp peaks, which are characteristics of a first-order phase transition as is the apparent hysteresis. The endothermic and exothermic peaks are observed on heating and cooling; the corresponding changes in enthalpy and entropy, are shown in Table 7.1.

The orthorhombic polymorph shows higher changes in enthalpy and entropy values than the monoclinic polymorph (Table 7.1), and a slightly larger value than the one reported in the literature (Δ S $= 59\,\mathrm{J\,mol^{-1}\,K^{-1}}$ [33]). Nevertheless, the obtained values of the change in enthalpy and entropy are in the same range as those reported in the literature for compounds of the same family or, more generally, compounds containing thiocyanate or selenocyanate groups (Table 3.2 in Section 3).

Table 7.1: Thermodynamic parameters obtained from differential scanning calorimetry measurements of both polymorphs of Fe(PM-Bia)$_2$(NCS)$_2$. Enthalpy (ΔH) is expressed $\mathrm{k\,J\,mol^{-1}}$, the transition temperature $T_{1/2}$ is given in K, and entropy (ΔS) is in $\mathrm{J\,mol^{-1}\,K^{-1}}$. **M** represents the monoclinic polymorph and **O** represents the orthorhombic polymorph. Symbols ↓ and ↑ indicate cooling and heating cycles, respectively.

	ΔH		$T_{1/2}$		ΔS		ΔS_{vib}	
	↓	↑	↓	↑	↓	↑	↓	↑
M	9.7(6)	10.0(9)	205.6(4)	208.7(3)	47.1(3)	48.0(4)	34.6(3)	35.6(4)
O	10.7(3)	11.5(2)	174.8(2)	180.3(2)	61.3(6)	63.7(7)	34.6(6)	35.6(7)

7.2.1 Effect of thermal history

To investigate the thermal behavior of both polymorphs and to explore their response to higher temperatures, DSC experiments were carried out by gradually increasing the final temperature from 300 K to 310 K, 320 K, 330 K, 340 K, 345 K, and up to 350 K (temperature scan rate of 10 K/min).

The results of the DSC experiments are presented in Figure 7.5, as a function of temperature for the monoclinic (left) and the orthorhombic (right) polymorphs. The measurements confirm that the spin transition occurs almost at the same temperature value regardless of the thermal history (Figure 7.5). Also, the enthalpy and the entropy changes are hardly influenced by the cooling and heating cycles with different maximum temperatures (Appendix Figure E.4).

Up to six successive thermal cycles, with a maximum temperature of 350 K, were performed on the monoclinic polymorph (scanning rate of 10 K/min) (Figure 7.6). They confirm that the thermal properties of this polymorph are hardly changed by cycling (Appendix Figure E.4). Also, the transition temperatures, entropy, and enthalpy changes mainly remained unchanged.

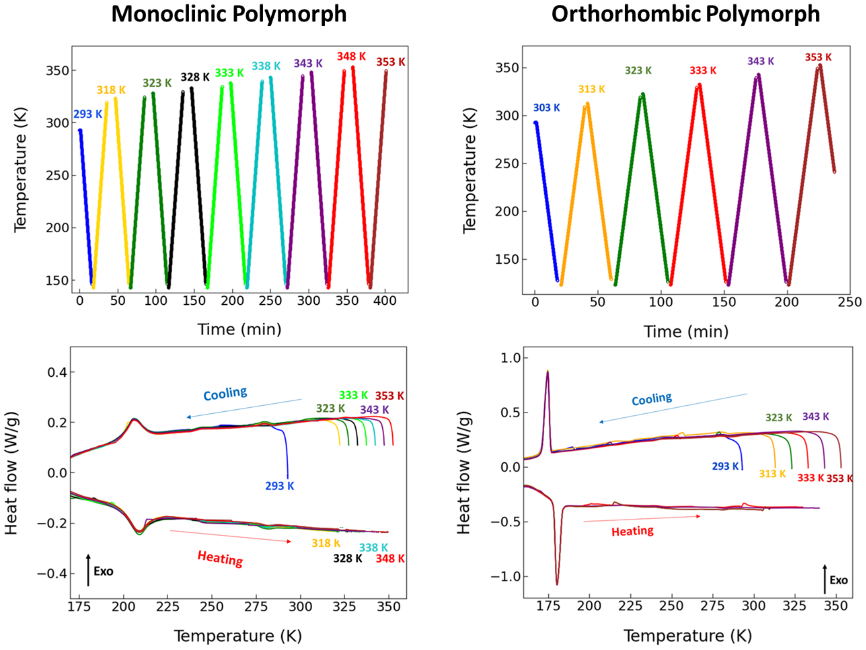

Figure 7.5: Change in the heat flow as a function of temperature with different maximum temperatures upon heating and cooling at a rate of 10 K/min for the monoclinic (left) and the orthorhombic (right) polymorph. Temperature profiles are shown on top.

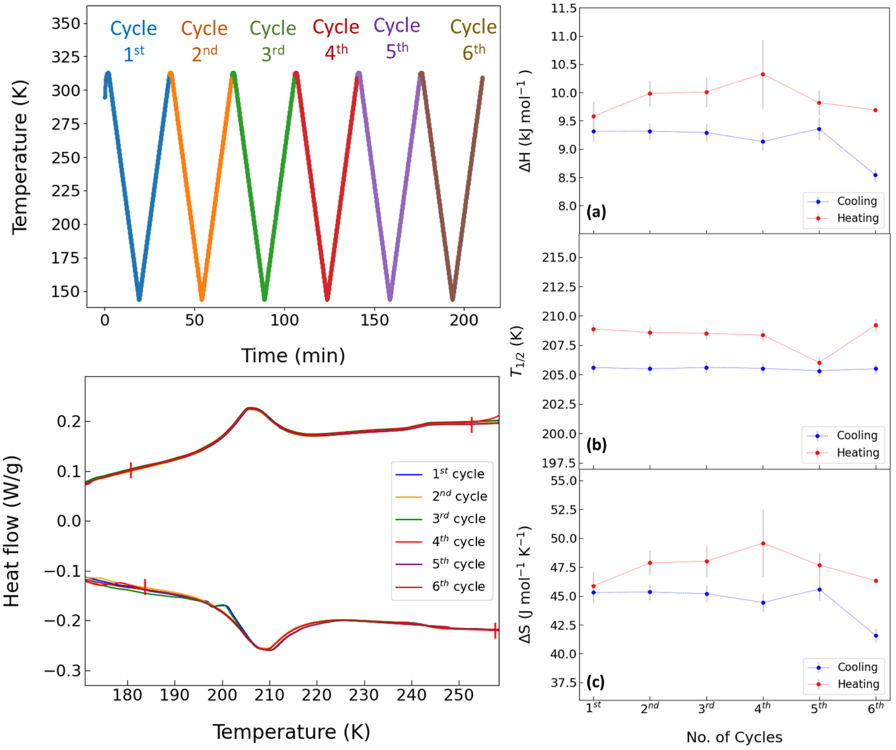

Figure 7.6: (Left) DSC measurement at a rate of 10 K/min illustrating the temperature change as a function of time during DSC experiments (top). (Bottom) shows the change in heat flow as a function of temperature upon several thermal cycles on cooling and heating for the monoclinic polymorphs. (Right) Enthalpy changes **(a)**, transition temperature **(b)**, and entropy changes **(c)** obtained upon six thermal cycles during cooling and heating.

7.2.2 Effect of scan rate

To map and obtain detailed information on the intermediate step observed in the magnetization data (see Section 7.1) of the orthorhombic polymorph, a DSC measurement has been carried out by following the protocol shown in Figure 7.7 (see also Section 5.3). Although different temperature endpoints were reached while cooling and subsequent heating of the sample at a rate of 0.2 K/min (without any measurement),[1] no significant effect on the enthalpy or transition temperature was observed during the heating process at a rate of 10 K/min.

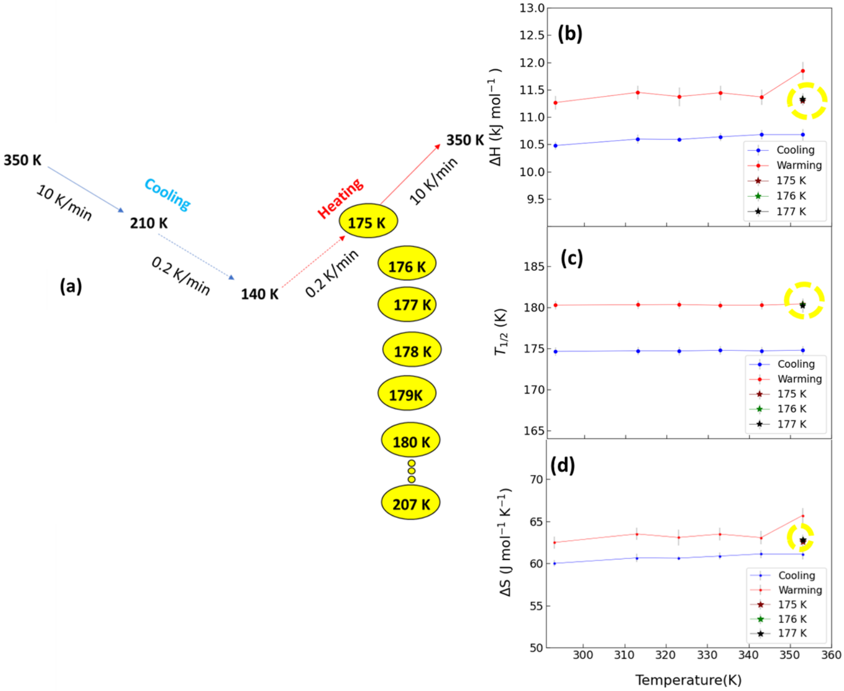

Figure 7.7: **(a)** Illustrates the protocol followed for the measurement of the orthorhombic polymorph. For a better comparison, the right figure mirrors Appendix Figure E.4 for the orthorhombic polymorph, with additional points highlighted in yellow circles (175 K, 176 K, and 177 K). Enthalpy changes **(b)**, transition temperature **(c)**, and entropy changes **(d)** values are indicated in yellow circles, were obtained with different temperature endpoints while cooling and heating the sample slowly.

Cooling the orthorhombic polymorph with varying scan rates and subsequently heating it up with the same scan rate of 10 K/min (for detailed measurement protocol, see Section 5.3) shows that the enthalpy and transition temperature observed

---

[1] The sample was cooled down and subsequently heated up with a rate of 0.2 K/min without any measurement during this heating phase. The measurement then started at different temperature points, as highlighted in yellow in Figure 7.7, and the heating rate was 10 K/min (see Section 5.3 for experimental details).

during the heating process remained unaffected by the different scan rates employed during cooling (Appendix Figure E.5).

7.3 Temperature-dependent powder X-ray diffraction

The evolution of the powder X-ray diffraction pattern with temperature for the orthorhombic and monoclinic polymorphs, respectively, in the temperature range from 250 K to 150 K are shown in Figures 7.8 and 7.9, respectively.

For the orthorhombic polymorph, the appearance of new diffraction peaks on cooling is evidence for the HS → LS phase transition between 170 K and 165 K.[1] These new peaks appear in low-temperature regions corresponding to the low spin state. This observation is in good agreement with the magnetic data, which show a transition from the high to the low spin state at $T_{1/2\downarrow} = 167\,\mathrm{K}$. It is worth noting that the positions of the characteristic peaks show minimal variation with temperature within the same spin state.

For the monoclinic polymorph, the evolution of the diffraction patterns shows a gradual shifting of the peak positions as a function of temperature (Figure 7.9). This behavior is consistent with the gradual nature of the spin transition of this polymorph.

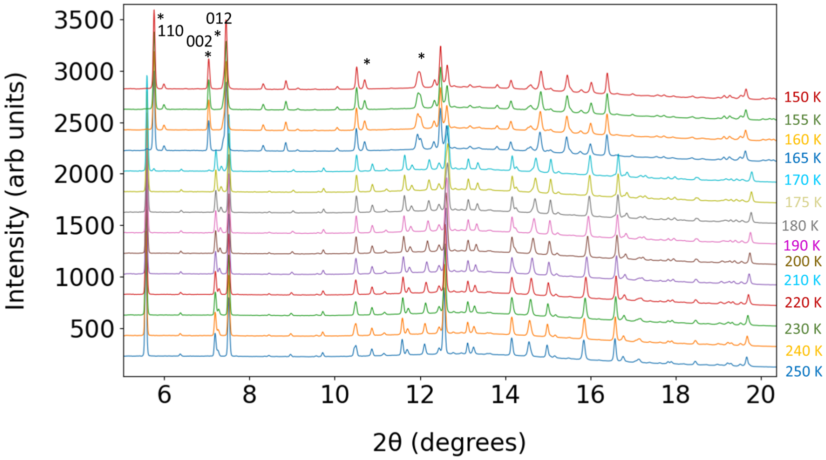

Figure 7.8: Thermal evolution of the XRD patterns of the orthorhombic polymorph as a function of the temperature. The asterisk (*) shows the positions of new peaks formed, which correspond to the LS state (the measurement has been performed while cooling at a rate of 6 K/min at the BM01 beamline at the ESRF synchrotron). Only selected temperatures are shown for clarity.

---

[1] While the characteristic HS phase peak, i.e., (110) and (002), starts to vanish at low temperatures, characteristic peaks corresponding to the LS state starts to appear.

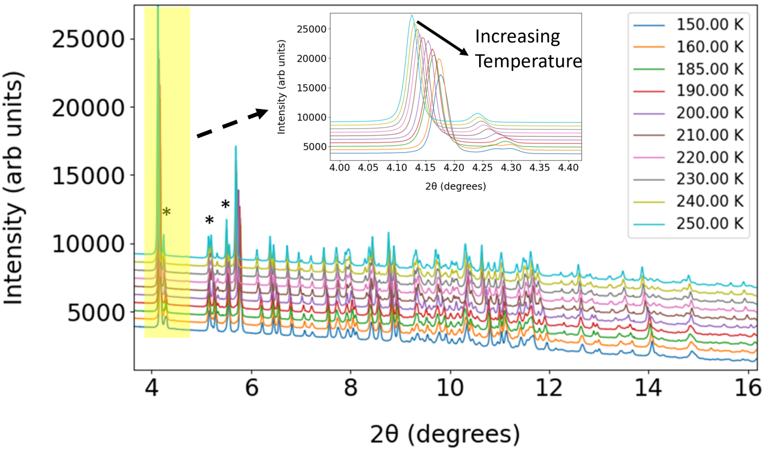

Figure 7.9: Thermal evolution of the XRD patterns of the monoclinic polymorph as a function of the temperature (the measurement has been performed during cooling at a rate of 6 K/min at PSI synchrotron). Only selected temperatures have been shown for clarity. The inset shows an enlargement for the yellow shaded peaks around 4.15°, for a better view of the shift of the peak positions.

7.4 Temperature-dependent single crystal X-ray diffraction

Obtaining high-quality crystal structures allows us to characterize the two spin states from three different aspects: the coordination sphere, the molecular arrangement, and finally, the crystal packing. Understanding how these crystal structures change with temperature sheds light on the behavior and mechanism of the spin crossover.

Experimental parameters for the structural refinement, as well as information about the crystal lattice, are summarized in Table 7.2 (for more details on the refinement process, see Section 6.4.4). Assuming the same $\sin\theta/\lambda$ limits, the overall agreement refinement factors are significantly better than those published in the literature [33, 37].

The SCO occurs in both polymorphs without a change in the space group symmetry. Figures 7.10 and 7.11 show the HS and the LS structures, respectively, for the monoclinic and orthorhombic polymorphs. These structures are made up of layers of molecular units arranged differently in each polymorph. In the case of the monoclinic polymorph, the molecular layers are arranged in the b, c plane, and stacked along the a-axis; neighboring layers, which are shifted by $\frac{1}{2}\vec{b}$, form the crystal stacking. For the orthorhombic polymorph, the molecular layers are arranged in the a, c plane, and stacked along the b axis; neighboring layers are shifted by $\frac{1}{2}\vec{a}$.

Table 7.2: Experimental Crystal Data for both polymorphs of Fe(PM-Bia)$_2$(NCS)$_2$ in the HS and LS states at selected temperatures.

	Monoclinic		Orthorhombic	
Chemical Formula	$FeN_6S_2C_{38}H_{28}$			
Temperature (K)	270	93	350	85
a (Å)	17.3421(2)	17.1496(2)	12.9662(8)	12.3332(2)
b (Å)	12.4836(10)	12.2625(10)	15.3404(8)	14.6757(2)
c (Å)	17.2399(2)	16.9243(2)	17.5869(8)	18.2772(2)
V (Å^3)	3361.96(7)	3202.98(7)	3498.2(3)	3308.14(8)
Density (g cm^{-1})	1.3606	1.428	1.308	1.383
μ (m m^{-1})	0.456	0.4695	0.439	0.454
Radiation type	Synchrotron			
λ (Å)	0.630(5)	0.630(5)	0.650(5)	0.650(5)
Diffractometer	Multipurpose PILATUS@SNBL diffractometer			
No. of measured	25238	23716	36859	34317
symmetry independent	7835	7435	6983	6472
observed [I>2σ(I)] reflections	6678	6986	2327	4872
Redundancy	3.79	3.39	15.8	7.5
R$_{int}$	0.0313	0.0351	0.1024	0.0703
(sinθ/λ)(Å^{-1})	0.67	0.67	0.84	0.83
No. of parameters	457	457	213	213
R[F^2>2σ(F^2)]	0.0393	0.0334	0.1137	0.0643
wR(F^2)	0.1137	0.0937	0.1938	0.118

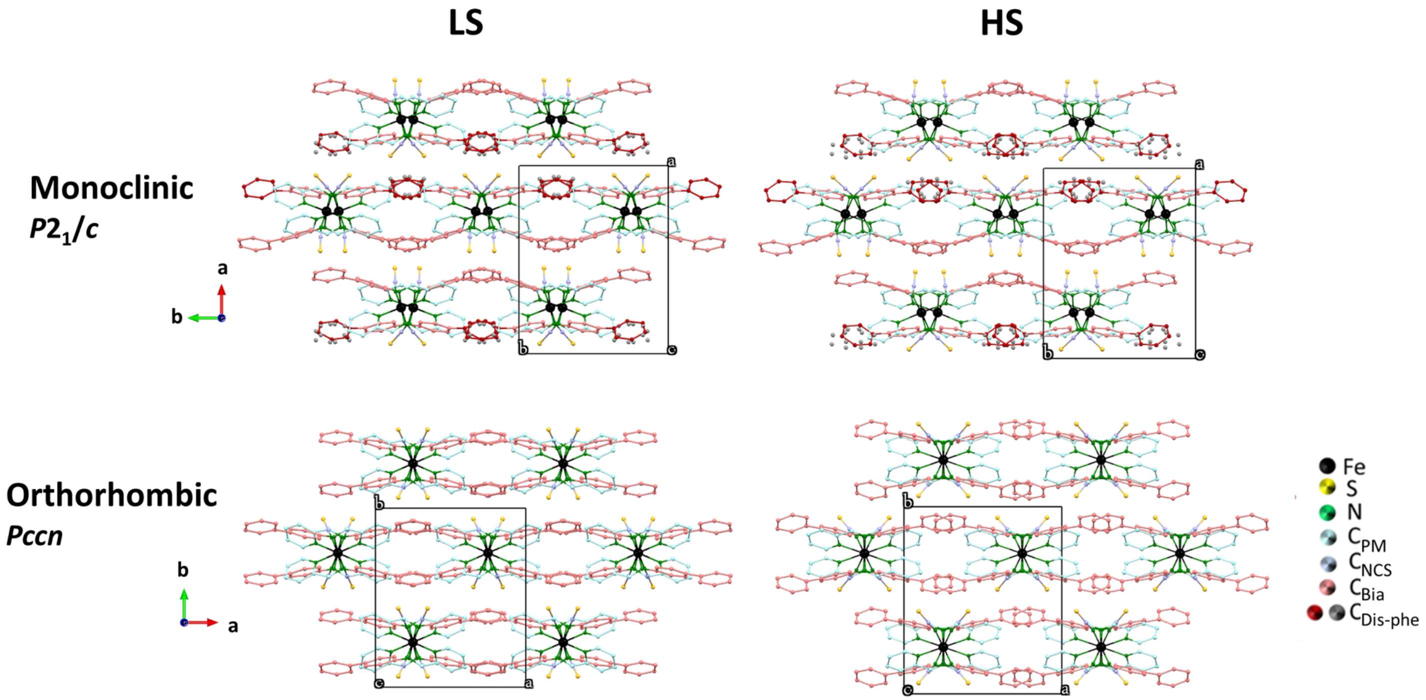

Figure 7.10: Crystal structure of the HS (right) and the LS (left) of the two polymorphs of [Fe(PM–Bia)$_2$(NCS)$_2$]. Projection along the *c*-axis for both polymorphs, monoclinic (top) and orthorhombic (bottom). For clarity, hydrogen atoms have been omitted.

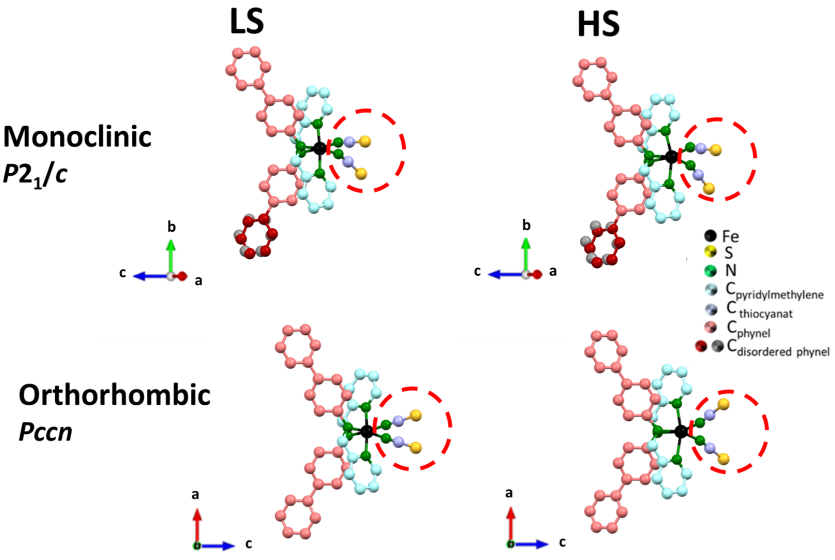

Figure 7.11: Individual molecules of the monoclinic (top) and orthorhombic (bottom) polymorphs, in high spin (right) and low spin (left). For clarity, hydrogen atoms are omitted. The dotted red circles highlight the changes in the NCS^- branches.

A striking difference is the disorder present in one of the external phenyl rings, which is exclusively observed in the monoclinic polymorph and not present in the orthorhombic one (Figure 7.11). This disorder persists over the whole temperature range. The occupation probabilities of the two positions of the disordered phenyl ring also show a remarkable trend: while in the HS state the two positions have within error constant occupation probabilities, in the LS state, one of the two positions becomes dominant (Figure 7.12).

According to [313], the corresponding configurational entropy for a two-configurational structural model (config. A and config. B) with respective populations $\rho_{config.A}$ and $\rho_{config.B}$ can be calculated as $S = -k_B \Sigma \rho_j \ln(\rho_j)$, taking into account the various thermally accessible configuration states. This implies that the entropy changes obtained during the spin transition may be partially attributed to configurational disorder (Appendix Figure E.6). However, the contribution is less than 1.2% of the total entropy change.

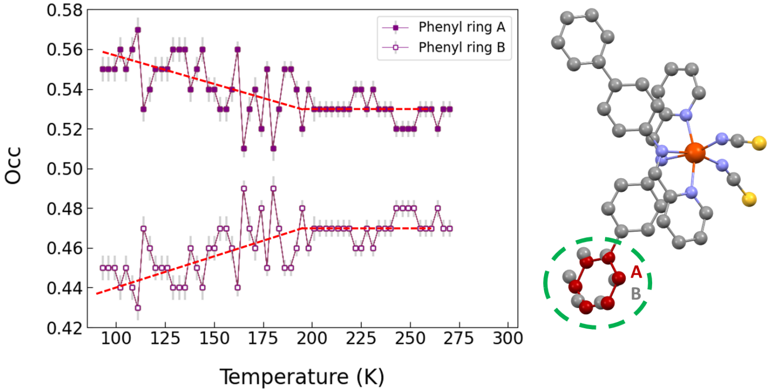

Figure 7.12: (Left) Temperature evolution of the occupation probability of the two disordered sites of the phenyl group in the monoclinic polymorph. (Right) A structural diagram of the monoclinic polymorph illustrating the disorder exhibited over two distinct sites, denoted as **A** and **B**.

7.4.1 Unit cell volume and lattice parameters

By tracking how the lattice parameters change with temperature, one gets an overview of the different behavior of both polymorphs during the spin crossover transition. For both polymorphs, the evolution of the normalized lattice parameters and the unit cell volume is monitored over the entire temperature range from 93 K to 270 K and 85 K to 350 K for the monoclinic and the orthorhombic polymorph, respectively. The normalized lattice parameters exhibit distinct behavior for each polymorph and show excellent agreement with literature data (Figure 7.13) and with the temperature-dependent PXRD results (Appendix Figure E.7).

The lattice parameters of the orthorhombic phase undergo sudden changes within a very small temperature range, reflecting the abrupt behavior of the transition. The discontinuous change in the lattice parameter is an indication of a first-order phase transition. In contrast, the monoclinic polymorph exhibits smoother variations in lattice parameters over a wider temperature range, indicating a gradual crossover.

During the spin transition, the unit cell volume of both polymorphs decreasess. However, the decrease is significantly larger for the monoclinic polymorph, with -4.92% (-4.65%) of single crystalline (polycrystalline) material, compared to the orthorhombic polymorph, with a decrease of -3.97% (-3.26%).

A highly anisotropic behavior of the lattice parameters, in particular around the phase transition temperature, is observed (Table 7.3).[1] The lattice param-

---

[1] The difference in percentage values for the single crystal and powder samples, despite exhibiting the same trend of increasing or decreasing, may be attributed partially to differences in the nature of these two samples (single crystal and polycrystalline). In addition, it should be noted that the measurements were carried out using different synchrotron facilities and even different rates of temperature change.

eter aligned with the stacking direction of the sheets (a in monoclinic and b in orthorhombic) shows different behavior. Notably, the a lattice parameter in the monoclinic polymorph shows an anomaly around the transition temperature (Figure 7.13), and the a-axis increases by +0.97% (+0.31%) for single crystal (powder) material. Conversely, the b-axis in the orthorhombic polymorph decreases by -0.6% (-1.26%), during the HS-LS transition.

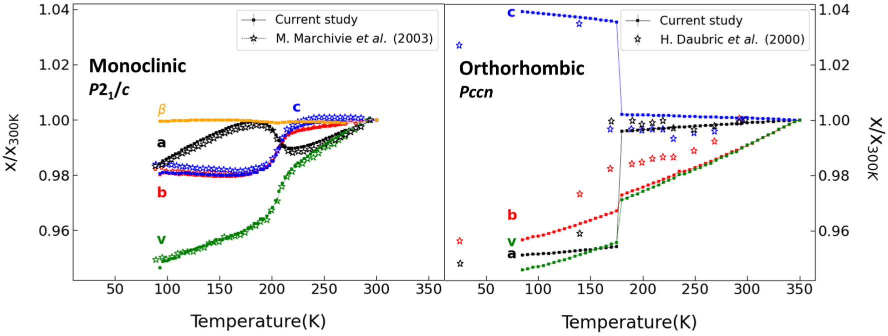

Figure 7.13: The normalized unit cell parameters and unit cell volume (normalized to the values at 300 K) as a function of temperature for both polymorphs; monoclinic (left) and orthorhombic (right) polymorphs. Filled symbols in black, red, and blue, represent data from the current study. Open stars are from references [37, 314].

Table 7.3: Changes of the lattice parameter for both polymorphs in percent around their corresponding transition temperatures. The calculated values correspond to the range from 220 K to 180 K for the monoclinic polymorph and from 180 K to 170 K for the orthorhombic polymorph.

	Single crystal			**Polycrystalline**		
	a	**b**	**c**	**a**	**b**	**c**
Monoclinic	+0.97%	-1.53%	-1.53%	+0.31%	-1.11%	-1.1%
Orthorhombic	-4.1%	-0.6%	+3.2%	-4.6%	-1.26%	+4.3%

Within the molecular plane of both polymorphs, the c lattice parameter in the monoclinic polymorph is reduced by -1.53% (-1.1%), while in the orthorhombic polymorph around the transition, it sharply increases by +3.2% (+4.3%). The third direction (b in monoclinic and a in orthorhombic) decreases in both polymorphs, but with different magnitudes. The monoclinic polymorph shows a decrease of -1.53% (-1.1%). On the other hand, the orthorhombic polymorph exhibits a significant decrease of -4.1% (-4.6%).

From the evolution of the lattice parameters, the thermal expansion tensors can be calculated for both spin states, HS and LS (Table 7.4). These calculations were carried out with the PASCal program (Principal Axis Strain Calculator) [315] in the temperature ranges far from the transition. For the HS state, the calculations spanned from 185 K to 350 K and from 250 K to 270 K for the orthorhombic and monoclinic polymorphs, respectively. In the LS state, the temperature ranges were 85 K to 170 K and 93 K to 150 K for the orthorhombic and monoclinic polymorphs, respectively. The expansion axes X_1, X_2, and X_3 correspond to the three crystallographic axes [315]. Positive values indicate that the crystal lattice is expanding along the corresponding direction, while negative values correspond to contraction as the temperature increases.

Table 7.4: Principal axes and coefficients of thermal expansion with their components along the three crystallographic axes and the coefficient of volume thermal expansion. The correspondence HS state values are calculated from the lattice parameters of the orthorhombic polymorph (185 K and 350 K) and the monoclinic polymorph (250 K and 270 K). The correspondence LS state values are calculated from the lattice parameters of the orthorhombic polymorph (85 K and 170 K) and monoclinic polymorph (93 K and 150 K). Note the re-definition of the principle axis for the monoclinic phase in the HS and LS states.

Orthorhombic			
HS		**LS**	
Axes	α **(MK^{-1})**	**Axes**	α **(MK^{-1})**
$X_1 = \vec{c}$	-11.4(7)	$X_1 = \vec{c}$	-38.0(7)
$X_2 = \vec{a}$	24.1(10)	$X_2 = \vec{a}$	35.4(9)
$X_3 = \vec{b}$	163.6(23)	$X_3 = \vec{b}$	120(2)
V	177.0(26)	V	118(2)
Monoclinic			
HS		**LS**	
Axes	α **(MK^{-1})**	**Axes**	α **(MK^{-1})**
$X_1 = -0.1258\ \vec{a} - 0.9921\ \vec{c}$	8.7(1.7)	$X_1 = 0.2499\vec{a} + 9683\ \vec{c}$	-31(2)
$X_2 = \vec{b}$	46.0(3)	$X_2 = \vec{b}$	-20(3)
$X_3 = -0.9506\ \vec{a} - 0.3105\ \vec{c}$	157(7)	$X_3 = -0.9808\ \vec{a} - 0.1953\ \vec{c}$	213(4)
V	212(5)	V	167(10)

In the high-spin phase of both polymorphs, the direction with the highest thermal expansion is the direction of molecular stacking, the *b*- and the *a*- direction for orthorhombic and monoclinic polymorph, respectively. On the other hand, the *c*-direction within the molecular plane, exhibits similar behavior of negative thermal expansion for both polymorphs (Table 7.4). The other directions within the molecular plane (*a*- and *b*- directions for orthorhombic and monoclinic polymorph) exhibit similar thermal expansion; however, the *b* direction for monoclinic has a higher value.

In the low-spin state for the orthorhombic polymorph, the *c*-axis still shows negative expansion, while the *a*-axis has larger thermal expansion compared to the HS state, and the *b*-axis exhibits less thermal expansion than in the HS state (Table 7.4). In the low-spin state for the monoclinic polymorph, both the *c* and *b*-axes exhibit negative expansion, and the *a*-axis continues to show the highest thermal expansion. It is worth noting that the volume expansion coefficient for the monoclinic polymorph has a lower thermal expansion coefficient in the LS state when compared to the HS state. For the orthorhombic polymorph, the volume thermal expansion remains nearly constant in the HS and LS states. Thus, the direction of the molecular stacking and the orientation of the thiocyanate group plays a crucial role in influencing the thermal expansion characteristics of both polymorphs in the HS state.

7.4.2 Intramolecular geometry

The FeN_6 octahedron undergoes the most substantial structural changes during the spin transition. Three pairs of nitrogen atoms from three distinct ligands surround the Fe^{2+} ion (the inset in Figure 7.14); the pyridylmethylene ligand (N_{PM}), the aminobiphenyl ligand (N_{Bia}), and the thiocyanate ligand (N_{CS}). As mentioned in Section 4.1, the $Fe-N$ distances in the HS state are longer than those in the LS state. During the high-spin to low-spin (HS-LS) transition, the $Fe-N$ distances in both compounds are shortened by approximately 0.2 Å (Figure 7.14). These $Fe-N$ distances are consistent with the limited data available in the literature [33, 37, 38].

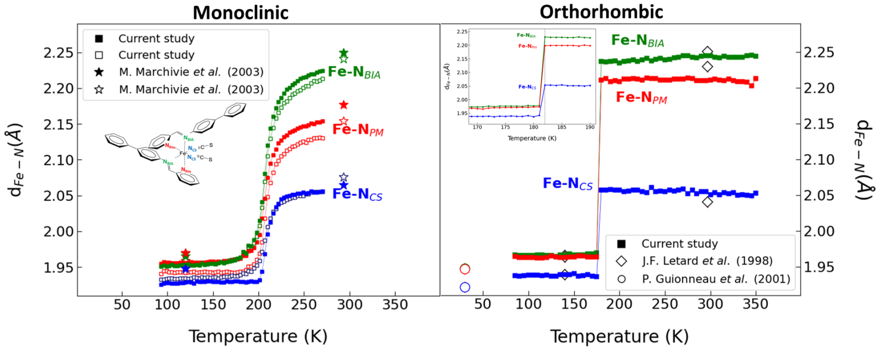

Figure 7.14: $Fe-N$ bond length evolution as a function of temperature for monoclinic (left) and orthorhombic polymorph (right). The squares and the filled circles (green, red, and blue) represent data from our study. Stars, diamonds, and open circles correspond to two data points from references [33, 37, 38]. The inset shows the schematic diagram of the Fe(PM-Bia)$_2$(NCS)$_2$ and the temperature-dependence of the $Fe-N$ bond length of the orthorhombic polymorph at the spin transition (between 169 K and 190 K, with 1 K temperature step). Lines are guides for the eyes. Error bars are the same size or smaller than the symbols.

The fine temperature steps that have been chosen in our X-ray diffraction (XRD) measurements enables us to monitor the temperature evolution of the transition and clearly demonstrates the differences between the two polymorphs in their transition nature.

In the orthorhombic polymorph, a sharp change in the $Fe-N$ distances occurs within a very narrow temperature range of about 1 K difference, between 177 K and 178 K (see inset in Figure 7.14). In contrast, the changes in $Fe - N$ bond lengths in the monoclinic polymorph are more gradual, spanning a broad temperature range from 250 K to 150 K.

The spin transition also induces changes in the $N - Fe - N$ angles. In particular, the $N_{PM} - Fe - N_{PM}$ and $N_{Bia} - Fe - N_{CS}$ angles (Figure 7.15(top)), show striking structural changes in both polymorphs during the spin transition. The $N_{PM} - Fe - N_{PM}$ and $N_{Bia} - Fe - N_{CS}$ angles display an increased linearity in the low spin state, indicating more symmetric configuration of the coordination sphere around the central metal ion.

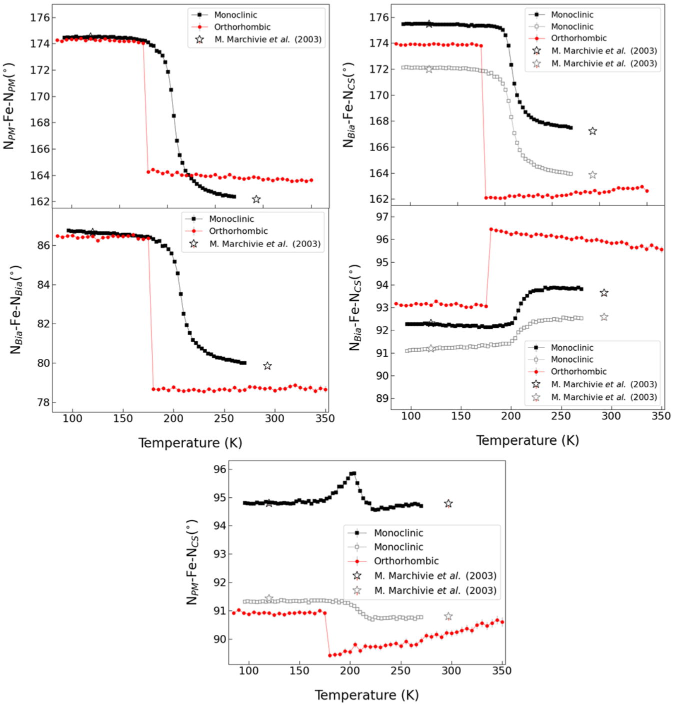

Figure 7.15: Temperature dependence of angles; (Top) $N_{Pm} - Fe - N_{Pm}$ (left) and $N_{Bia} - Fe - N_{NCS}$ (right), (middle) $N_{Bia} - Fe - N_{Bia}$ (left) and $N_{Bia} - Fe - N_{NCS}$ (right), and (bottom) $N_{Pm} - Fe - N_{CS}$. Results from this study are shown in full red circles (orthorhombic) and black and gray squares (monoclinic). Open black and gray stars are from reference [37]. Lines are guides to the eyes. Error bars are the same size or smaller than the symbols.

Furthermore, in the low spin state, the $N_{Bia} - Fe - N_{Bia}$ and $N_{Bia} - Fe - N_{CS}$ angles tend to approach the ideal value of 90° (Figure 7.15(middle)). The $N_{PM} - Fe - N_{CS}$ branches related to the disordered phenyl rings in the monoclinic polymorph exhibit significant anomalies around the transition temperature (Figure 7.15(bottom)).

To quantify the degree of distortion in the octahedral coordination, several key parameters have been proposed, such as ζ (bond length distortion) [103], Σ (angular distortion) [37], and Θ (the deviation from a perfectly octahedral geometry, O_h, towards a trigonal prismatic structure) (see Section 2.3.2 for more details) [37, 316]. Our calculations reveal a higher distortion of the orthorhombic polymorph as compared to the monoclinic polymorph in the high spin state (see Figure 7.16), with the difference being maximum for the parameter Θ. The values of parameters Σ, ζ, and Θ are consistent with those reported in the literature for the same family of compounds [316, 317]. During the spin state transition for both polymorphs, the maximum relative change is observed in $\Delta\zeta_{HL}{}^{1}$ (84%). For the monoclinic polymorph, $\Delta\Sigma_{HL}$ exhibits a higher value than $\Delta\Theta_{HL}$. However, due to the higher distortion of the orthorhombic polymorph, the relationship between $\Delta\Sigma_{HL}$ and $\Delta\Theta_{HL}$ changes. In the orthorhombic case, $\Delta\Theta_{HL}$ exhibits a higher value than $\Delta\Sigma_{HL}$, reversing the relationship between these two parameters compared to the monoclinic polymorph. In the low spin state, the values of all the distortion parameters converge towards the ideal values of an octahedron, creating a more symmetrical surrounding of Fe.

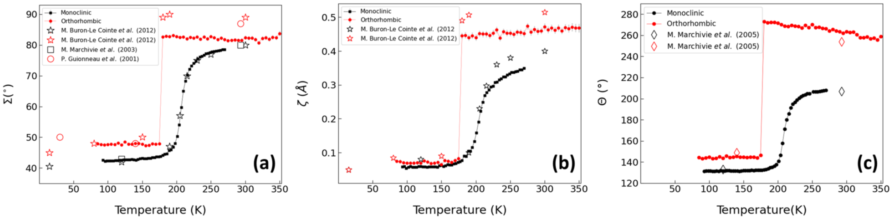

Figure 7.16: **(a)** Angular distortion parameter (Σ) representing the deviations of the 12 N-Fe-N bond angles from 90°. **(b)** Bond length distortion parameter (ζ) indicating deviation in bond lengths from the average value. **(c)** Deviation parameter (Θ) illustrating the deviation from ideal octahedral to trigonal prismatic coordination. Data from this study are represented by the black and red circles (monoclinic and orthorhombic, respectively). Open red and black stars are from reference [103]. Open red circles and open black squares are from reference [37]; open red and black diamonds are from reference [316]. Lines are provided as guides to the eyes. Error bars are the same size or smaller than the symbols.

The $N_{CS} - Fe - N_{CS}$ angles of the two thiocyanates (Figure 7.11) are decreased at the HS⟶LS transition, particularly in the orthorhombic polymorph, forming a scissor-like closing effect in the molecule (Figure 7.17). As a consequence of this scissor-like mechanism, the material shows a negative thermal expansion, and the orthorhombic polymorph expands with decreasing temperature along the *c*-axis (see Section 7.4.1).

During the HS⟶LS transition, the $\mathrm{N} \equiv \mathrm{C} - S$ triple bonds undergo noticeable increases with decreasing temperature (Figure 7.11). Figure 7.18 (left) demonstrates

---

[1] $\Delta\zeta_{HL}$, $\Delta\Sigma_{HL}$, and $\Delta\Theta_{HL}$, denote transitions from the high-spin (HS) states (ζ_{HS}, Σ_{HS}, Θ_{HS}) to low-spin (LS) states (ζ_{LS}, Σ_{LS}, Θ_{LS}).

that one of the NCS^- branches in the monoclinic phase undergoes an unusually abrupt and pronounced change during the transition. Also, the $C-S$ bond lengths of the thiocyanate ligands get longer at the HS⟶LS transition in both polymorphs, but the changes are much more pronounced in the orthorhombic polymorph (Figure 7.18 (right)). In fact, the increased back bonding within the LS state is responsible for the lengthening of the $\mathrm{N} \equiv \mathrm{C}$ bond length during the HS⟶LS transition. The back bonding is explained by the fact that the metal ion donates electrons to the ligand, and as a consequence, the bonds in its vicinity are weakened [126].

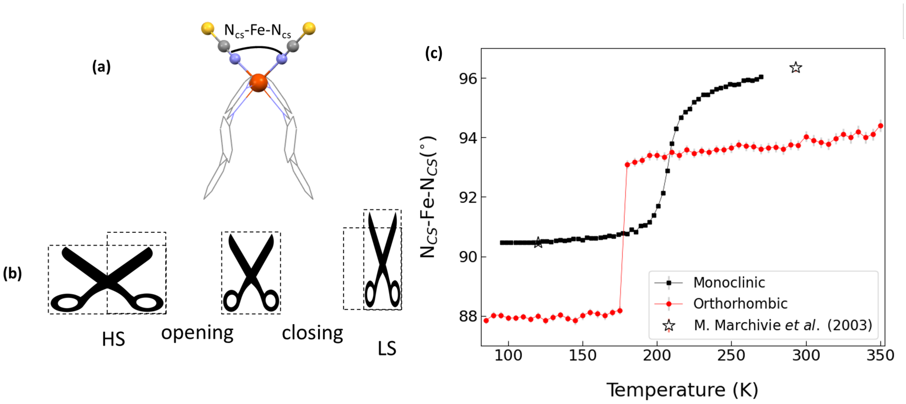

Figure 7.17: **(a)** View in the *bc* plane of the orthorhombic polymorph at room temperature indicating the angle presented in **(c)**. **(b)** Illustration of the "scissor-like" geometric mechanism in the HS to LS transition. Closing is observed upon decreasing temperature; opening is associated with LS to HS transition. **(c)** The N_{CS}-Fe-N_{CS} angle as a function of temperature. The red circles correspond to the orthorhombic polymorph and the black squares correspond to the monoclinic polymorph. Filled symbols are obtained from the current study. Open star symbols are obtained from reference [37]. Lines are guides to the eyes. Error bars are the same size or smaller than the symbols.

In both polymorphs, the $\mathrm{Fe}-\mathrm{N} \equiv \mathrm{C}(S)$ angles show a deviation from linearity (Figure 7.19 (left)). This deviation from linearity is less pronounced in the low-spin state than in the high-spin state. In the case of the orthorhombic polymorph, the degree of linearity in the thiocyanate group (NCS^-) is only slightly decreased at the HS to LS transition. However, in the monoclinic polymorph, more significant changes in the $\mathrm{Fe}-\mathrm{N} \equiv \mathrm{C}(S)$ angles are observed during the HS to LS transition, as one of the branches of the thiocyanate group becomes significantly less linear in the LS state (Figure 7.19 (right)). Consequently, this alteration brings the sulfur atom in this branch more closer to the carbon atoms in the phenyl rings associated in the nearest neighboring molecular unit.[1] On the other hand, the second branch exhibits an anomalous change around the transition region (Figure 7.19 (right)).

---

[1] This lead to the formation of H-bonds (discussed later in Section 7.4.3).

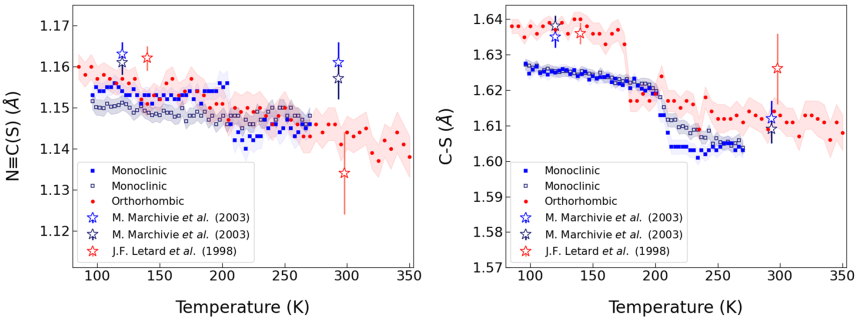

Figure 7.18: Temperature dependence of the $\mathrm{N} \equiv \mathrm{C}(S)$ bond length (left) and $\mathrm{C}-\mathrm{S}$ bond length (right) for both polymorphs. Filled blue and open dark blue squares (monoclinic), and red circles (orthorhombic), are from this study. The two colors are utilized to distinguish the two (NCS^{-}) branches. Open blue and dark blue stars are from reference [37]. Open red stars are from reference [33]. The shaded area indicates the standard deviations.

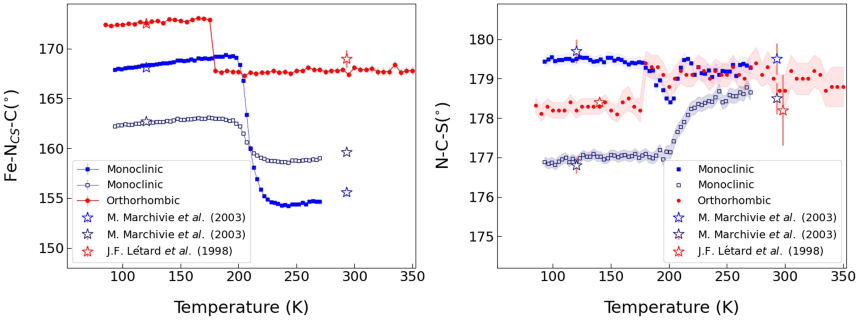

Figure 7.19: Temperature dependence of the $\mathrm{Fe}-\mathrm{N} \equiv \mathrm{C}(S)$ angle (left), $\mathrm{N} \equiv \mathrm{C}-\mathrm{S}$ angle (right) for both polymorphs. Filled blue and open dark blue squares (monoclinic), and the red circles (orthorhombic), are from this study. The two colors are utilized to distinguish the two (NCS^{-}) branches. Open blue and dark blue stars are from reference [37]. Open red stars are from reference [33]. The standard deviations are indicated by the shaded area. Lines are guides to the eyes.

The spin transition has almost no effect on the intramolecular distances in the pyridine and phenylene rings, which tend to stay mainly constant (Appendix Figure E.9) or only slightly increase as the temperature decreases (see Appendix Figure E.10). However, a notable exception is observed in the monoclinic polymorph, where the $C-C$ bond lengths in one of the pyridine ring (linked to the disordered phenylene ring) show significant anomalies around the transition temperature (Appendix Figure E.10).

A noticeable difference between the two polymorphs is observed for the intramolecular torsion angle of the biphenyl rings (as defined in Figure 7.20), which exhibits distinct behaviors during the spin transition in each polymorph. In the orthorhombic polymorph, the intramolecular torsion angle of the biphenyl rings experiences a strong and abrupt decrease upon the HS to LS transition, following a pattern similar to the abrupt changes observed in the $Fe-N$ distances (Figure 7.14). However, the monoclinic polymorph behaves differently: the intramolecular torsion angle of both biphenyl ligands gradually increases (Figure 7.20) at the HS to LS transition. Moreover, within the monoclinic polymorph, the torsion angle of the disordered biphenyl ring that is influenced by the disorder is found to be larger than the angle for the ordered biphenyl ligand. This difference in the torsion angles contributes to the asymmetry between the two branches of the molecule in the monoclinic polymorph.

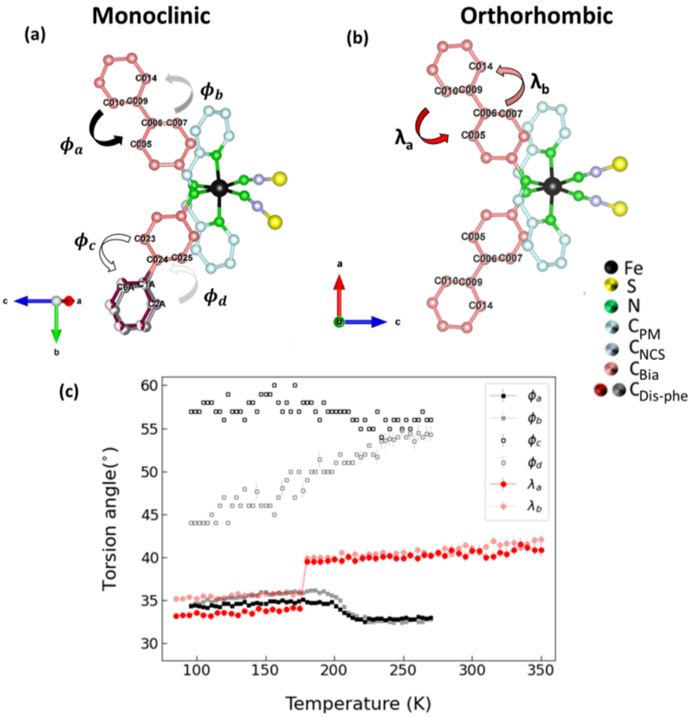

Figure 7.20: The torsion angles of the monoclinic **(a)** and the orthorhombic **(b)** polymorph. **(c)** Torsion angles of the two biphenyl rings for the two polymorphs as a function of temperature (black symbols: monoclinic; red symbols: orthorhombic). The lines are guides to the eyes. Error bars are the same size or smaller than the symbols.

7.4.3 Intermolecular contacts

Earlier studies on spin-crossover compounds have indicated that the strength of cooperativity is directly related to several factors, amongst which the strength of

π-π interactions [95, 205], the van der Waals forces [93, 103, 318], and the H-bonding within the system [96, 97] are the most relevant (see Section 1.5 for more details).

7.4.3.1 π - π interactions

On the basis of our data, we investigated the strength of intermolecular interactions in these two polymorphs with the Mercury program [319].[1] The contrasting behavior of π- π interactions between the two polymorphs sheds light on their distinct roles in the spin-crossover behavior. In the case of the orthorhombic polymorph, no strong π- π interactions between the phenyl rings were observed in either spin state (HS or LS). On the other hand, for the monoclinic polymorph, the investigation revealed the presence of several strong π- π interactions between two phenyl rings, and these interactions exhibit a similar strength in both the LS and HS states, indicating that π- π interactions persist across the spin-crossover transition in the monoclinic polymorph (Figure 7.21). It is worth noting that in the transition region around 225 K, some of the moderate π- π interactions in the monoclinic polymorph become stronger, however; in the low spin state, these π- π interactions return to their moderate strength (Table 7.5).

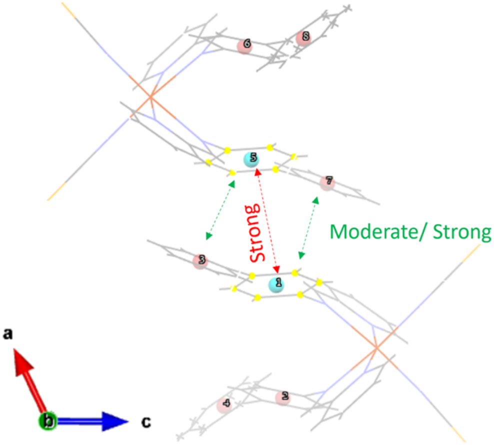

Figure 7.21: Illustration of the 3D packing of the monoclinic polymorph showing the shortest contacts between phenyl rings. The strength of the $\pi - \pi$ interactions depends on the distance between the two centroids and the angle between the normal vectors of the two centroids (see Section 1.5.3 for more details). The interaction between the inner phenyl rings (centroid 1 and centroid 5) is strong at all temperature points; however, centroid 7 and centroid 1, and centroid 3 and centroid 5, have moderate strengths in the HS state. At 225 K, $\pi - \pi$ interactions become strong and in the LS state, they restore their moderate strength.

---

[1] Mercury software utilizes the ‘UNI Intermolecular Potentials’ [320, 321] for force-field intermolecular energy calculations [319].

Table 7.5: π-π interactions of the two polymorphs as identified using the Mercury software [319]. The table includes centroid to centroid distances (D) and their relative orientation angle of ($\measuredangle$). The table also indicates the intermediate temperatures corresponding to 180 K (orthorhombic) and 225 K (monoclinic), and corresponding to 170 K (orthorhombic) and 180 K (monoclinic). The term "No." indicates the number of π-π interactions in each case.

	Strong											
	HS			180 K ($Pccn$) 225 K ($P2_1/c$)			170 K ($Pccn$) 180 K ($P2_1/c$)			LS		
	No.	**D** (Å)	$\measuredangle$ (°)	**No.**	**D** (Å)	$\measuredangle$ (°)	**No.**	**D** (Å)	$\measuredangle$ (°)	**No.**	**D** (Å)	$\measuredangle$ (°)
$Pccn$	–	–	–	–	–	–	–	–	–	–	–	–
$P2_1/c$	1	4.11	0	2	4.09 4.83	0 33.1	1	4.2	0	1	4.13	0
	Moderate											
$Pccn$	2	5.18 5.1	35.47 58.27	2	5.16 4.95	34.24 56.71	3	5.51 4.96 4.35	18.26 33.27 42.58	3	5.45 4.95 4.29	17.22 32.86 41.5
$P2_1/c$	5	4.84 5.56 5.07 6.48 4.71	32.97 46.15 49.72 18.39 59.57	3	5.48 5.04 6.41	44.31 48.65 17.94	4	4.87 5.49 5.01 6.16	35.79 40.6 48.14 20.36	4	5.33 4.84 5 6.14	38.02 34.8 46.61 18.37

7.4.3.2 Van der Waals interactions

Intermolecular interactions in the studied polymorphs can be classified into two main categories: intrasheet contacts, occurring within the molecular plane, and intersheet contacts, involving molecular units from different sheets (Figure 7.10). Both polymorphs, exhibit van der Waals interactions with $C \cdots\cdot C$ contacts with distances less than 3.4 Å, smaller than the sum of van der Waals radii [322]. The changes in various intra- and intersheet contacts during the transition to LS state, show different trends, with some contacts decreasing through the HS-LS transition while others increase (Figure 7.22).

The monoclinic polymorph in the HS state displays the shortest $C \cdots\cdot C$ contacts, with a distance of 3.326(11) Å, which persists even in the LS state (Figure 7.22, Appendix Figure E.11). It should be noted that the $C_{2A} \cdots\cdot C_{14}$ shortest contact in the intrasheet layers shows a similar change in its trend similar to the anomaly observed in the a lattice parameter (as shown in Figure 7.13). In contrast, the orthorhombic polymorph exhibits fewer $C \cdots\cdot C$ contacts and these interactions are weaker in the HS state compared to those observed in the monoclinic polymorph, with a distance of 3.429(9) Å (Figure 7.22, Appendix Figure E.12). Part of these $C \cdots\cdot C$ contacts (e.g., $C_{14} \cdots C_{14}$), exhibits a significant decrease (becomes stronger) during the transition to the LS state (Figure 7.22, Appendix Figure E.12). However, one of these contacts ($C_{11} \cdots\cdot C_1$) in the orthorhombic polymorph exhibits a sharp increase around the transition to the LS state which is similar to the abrupt increase observed in the c lattice parameter during the transition to LS state (Figure 7.13).[1]

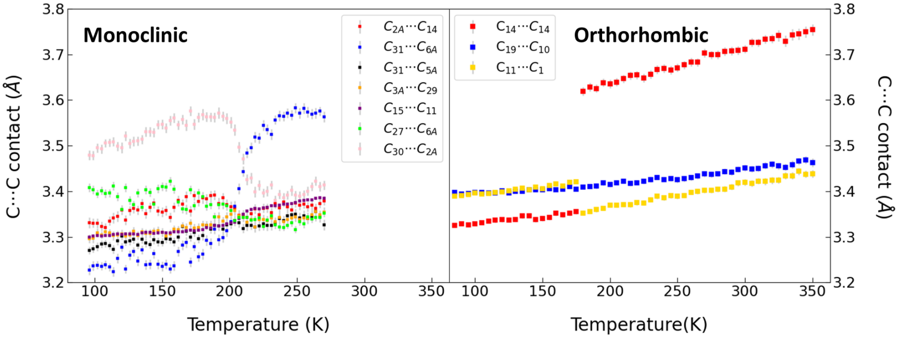

Figure 7.22: **(a)** The shortest $C \cdots\cdot C$ intermolecular distances as a function of temperature in the monoclinic polymorph (see Appendix Figure E.11). $C_{2A} \cdots\cdot C_{30}$ shortest contact in the intrasheet layers shows a similar change in its trend similar to the anomaly observed in a lattice parameter (as shown in Figure 7.13). **(b)** The shortest $C \cdots\cdot C$ intermolecular distances as a function of temperature in the orthorhombic polymorph (see Appendix Figure E.12).

---

[1] It is not surprising as the $C_{11} \cdots\cdot C_1$ contact aligns in the direction of the c lattice parameter.

7.4.3.3 Hydrogen bonds

Another critical interaction that influences the cooperativity in these spin-crossover complexes is the intermolecular hydrogen bonding involving the sulfur atoms of the NCS^- branches with the closest -C atom in one of the internal biphenyl rings (Figure 7.23). In the case of the orthorhombic polymorph, a short $S \cdot \cdot \cdot \cdot (H) - C$ contact is present in the HS state, with a distance less than 3.5 Å [322]. Conversely, for the monoclinic polymorph, the shortest $S \cdot \cdot \cdot \cdot (H) - C$ contact in the HS state exceeds 3.5 Å, and a value smaller than 3.5 Å is only attained at lower temperatures during the spin-crossover process (Figure 7.24 and Figure 7.25).

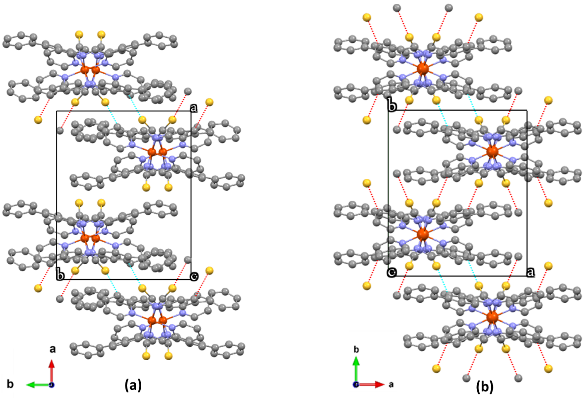

Figure 7.23: Crystal packing in the LS of the monoclinic **(a)**, and orthorhombic **(b)** showing H-bonding. The red and the cyan dashed line highlights the interaction of the $S \cdot \cdot \cdot \cdot C$ contacts. The evolution of these $S \cdot \cdot \cdot \cdot C$ contacts as a function of temperature is shown in Figure 7.24.

It is worth noting, that the $S \cdot \cdot \cdot \cdot (H) - C$ intermolecular contacts in both polymorphs, become almost identical in the LS state due to an increase in this distance when the orthorhombic polymorph undergoes the HS to LS transition (Figure 7.24). This indicates a significant structural reconfiguration associated with the LS state.

For hydrogen bonding, the ideal the $S \cdot \cdot \cdot \cdot (H) - C$ angle should be 180° (see Section 1.5.1). However, in the orthorhombic polymorph, in the high-spin state, this angle is smaller than 120°, and in the low-spin state, it is more than 125°. On the other hand, for the monoclinic polymorph, the $S \cdot \cdot \cdot \cdot (H) - C$ angle as a function of temperature shows a similar anomaly as observed in the a lattice parameter (Figure 7.13). In both polymorphs, the H-bond angle in the low-spin state is larger than in the high-spin state.

As a summary, one can say that in the HS state, the monoclinic polymorph shows a number of intrasheet and intersheet contacts, which correspond to van der Waals and π- π interactions, whereas the orthorhombic polymorph in the HS state, does not show any intrasheet contact, but it shows only one intersheet contact corresponding to hydrogen bonding. Upon transition to the low spin state the intersheet contacts in both polymorphs, are formed by hydrogen bonding, while the intrasheet contacts are in the form of van der Waals interactions in the orthorhombic polymorph.

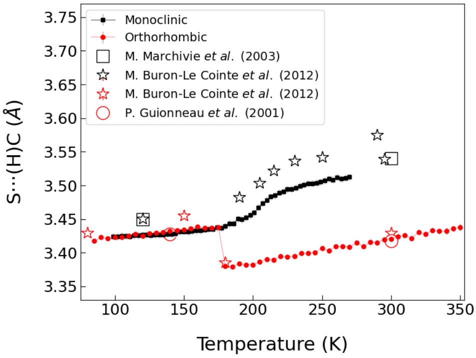

Figure 7.24: The change in the shortest $S\cdots\cdot(H)-C$ contacts as a function of temperature for the orthorhombic polymorph (small filled red circles) and the monoclinic polymorph (black squares). Open large symbols are from references [37, 38, 103]. Lines are guides to the eyes. Error bars are the same size or smaller than the symbols.

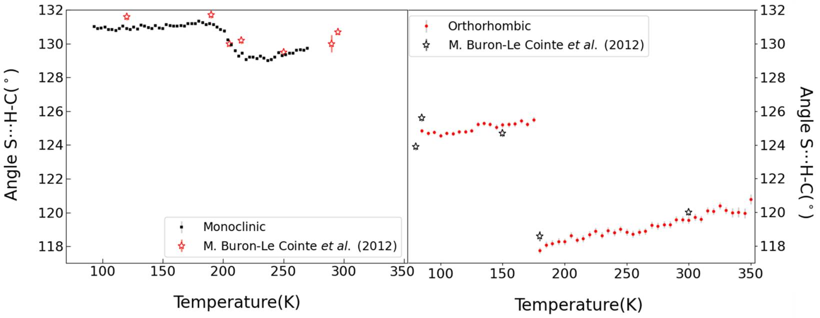

Figure 7.25: The evolution of the $S\cdots\cdot(H)-C$ angles for the monoclinic polymorph (left) and the orthorhombic polymorph (right). Open stars are from reference [103]. Error bars are the same size or smaller than the symbols.

7.4.4 Intra and intermolecular changes impacting the lattice parameters anomalies

An anomalous behavior in the lattice parameter within the transition region is observed only in the *a* direction in the monoclinic polymorph[1] (Figure 7.13). A closer

---

[1] In the monoclinic polymorph, the *a*-axis is in the direction of molecular packing.

examination reveals clear connections between this anomaly and intra and intermolecular changes during the HS-LS transition (Figure 7.26).

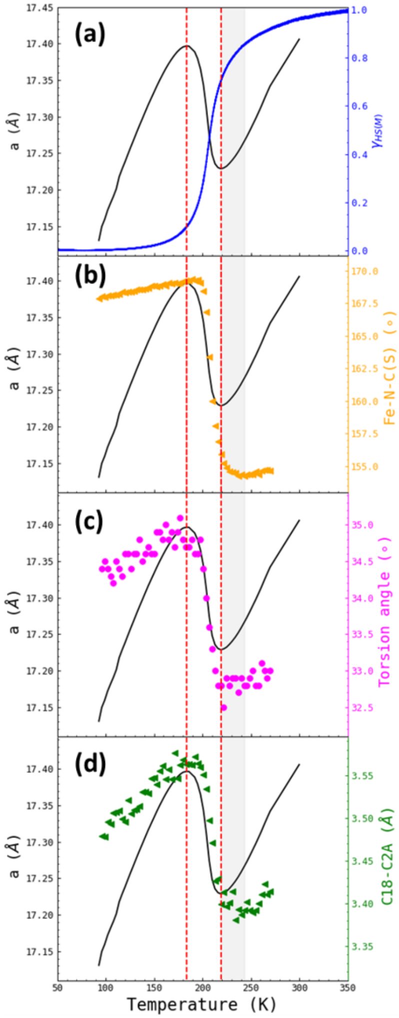

Figure 7.26: A comparison of the evolution a-lattice parameter of the monoclinic polymorph with different parameters. **(a)** Comparison to the high spin fraction calculated from magnetization measurements. **(b)** Comparison to the angle formed by the $Fe-N-C$ atoms in the thiocyanate branch. **(a)** Comparison with the torsion angle formed by two biphenyl rings.**(c)** Comparison of the van der Waals contact of two carbon atoms. Two temperatures (219 K and 183 K) were depicted by two red dashed lines, which emphasize a change in the a-lattice behavior trend. The temperature range (243 K to 219 K), where some of the $\pi-\pi$ interactions are changing their strength from moderate to strong is shown by the gray shaded patches.

For instance, during the HS to LS transition, the intramolecular $\mathrm{Fe} - \mathrm{N} \equiv \mathrm{C}(S)$ angle in one of the branches of the thiocyanate group exhibits an anomalous change mirroring the behavior of the a-lattice parameter around the transition region (Figure 7.26 **(b)**). Furthermore, the intramolecular torsion angle of both biphenyl ligands exhibits a gradual increase during the HS to LS transitions which aligns with the anomalous behavior of the a-lattice parameter, as shown in Figure 7.26 **(c)**. The intermolecular interactions probably also contribute to the anomalous behavior of the a- lattice parameter. In the transition region around 225 K, some of the moderate $\pi - \pi$ interactions become stronger. Intriguingly, these $\pi - \pi$ interactions restore their moderate strength in the low-spin state (Table 7.5). In addition, some van der Waals interactions, such as the $C_{2A} \cdots \cdot C_{14}$ shortest contact within the intrasheet layers, exhibit a similar change in response to temperature variations, to the behavior observed for the a-lattice parameter (Figure 7.26 **(d)**).

7.5 Mechanism of transition (Formation of domains)

The extent and nature of domain formation will influence properties such as hysteresis and reproducibility, which are important for potential applications. Therefore, understanding how different polymorphs exhibit varying domain formation is crucial in tailoring spin-crossover materials for specific uses. To investigate the transition mechanism, we examined the evolution of the Bragg peaks as a function of temperature for both polymorphs from the reconstructions of reciprocal space (Figure 7.27). For the orthorhombic polymorph, a splitting in the Bragg peaks is seen in the region where the transition takes place. As seen in the reciprocal reconstruction of the $h0l$ plane (Figure 7.27**(a)**), the splitting of the peaks is observed at 177 K on cooling and at 182 K on heating (Figure 7.27**(b)**). The resulting diffraction pattern can be indexed by the superposition of two distinct reciprocal lattices with cell parameters corresponding to a purely HS state and a purely LS state.[1]

As the transition progresses, part of the crystal collectively undergoes the spin transition. This cooperative behavior leads to the formation of HS and LS domains. The coexistence of HS and LS domains is a further sign of a first-order transition (the presence of hysteresis is support this observation, see Sections 7.1 and 7.2). The Braggs peaks corresponding to both HS and LS states are comparatively sharp, indicating large domain sizes. However, the experimental resolution during this experiment does not make it possible to investigate the sizes precisely. It is worth noting that even after 4 thermal cycles (as depicted in Figure 7.27), the splitting of the Bragg peak is still observed, evidence of the reproducibility of the domain formation.

In the case of the monoclinic polymorph, the Bragg peaks show a different behavior compared to the orthorhombic polymorph. The positions of the Bragg peaks continuously shift with temperature (Figure 7.27**(c)**), reflecting the gradual spin

---

[1] For the data sets which show peak splitting (177 K on cooling and 182 K on heating), the peak integration procedure was carried out by integrating only the higher peak intensity; whereas the lower intensity peaks were rejected.

transition nature, and unlike for the orthorhombic phase, there is no splitting of the Bragg peaks. This continuous shift of the Bragg peak positions can be understood assuming that the HS and LS molecules are randomly distributed throughout the crystal lattice. In other words, the HS and LS states are not organized into clearly separated domains (Figure 1.2).

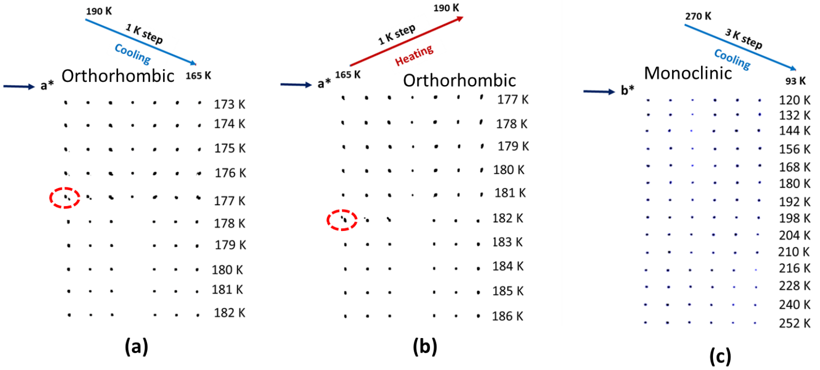

Figure 7.27: Line of diffraction spots as a function of temperature and its evolution from HS to LS for orthorhombic polymorph while cooling **(a)** and heating **(b)** in the (h, 0, -2) where -3 $< h <$ 3, and the monoclinic polymorph **(c)** in the (0, k, -2) where 7 $< k <$ 12. Note the different temperature scales.

To further explore and understand the mechanism of the spin transition, we investigated the atomic displacement parameters (ADP), which are derived from the anisotropical structure refinements. The schematic representation of the anisotropic thermal parameters of the nitrogen atoms within the coordination sphere of the Fe in the monoclinic polymorph at 210 K is shown in Figure 7.28. The figure clearly shows that the ADPs of the nitrogen atoms exhibit remarkably elongated shapes, indicating either significant thermal motion or static disorder.

The comparison of the temperature dependence of the ADPs for the six nitrogen atoms coordinating Fe for the monoclinic and the orthorhombic polymorphs shows clear differences (Figure 7.29). For the monoclinic polymorph, the temperature evolution clearly demonstrates two distinct regimes; one close to the SCO temperature and the other outside the transition range. When the sample is purely HS or purely LS, the ADPs parameters decrease with temperature, as expected. However, around the spin transition ($T_{1/2}$), a clear λ-type anomaly is observed in the U_{22} component of the ADP for two of the nitrogen atoms attached to the two thiocyanate groups. This anomaly indicates a significant change in the motion of the nitrogen atom in a direction perpendicular to the $Fe - N$ bond. We assume that this anomaly results from the disorder at $T_{1/2}$, where 50% of the Fe^{2+} ions are in the high spin state and the other 50% are in the low spin state. The instrumental resolution in the diffraction experiment is only 0.8 Å, making it impossible to resolve the disorder clearly; instead, it is modeled in terms of the average between the HS and LS positions, and the atomic displacement parameters try to approximate the electron density corresponding to both states [108].

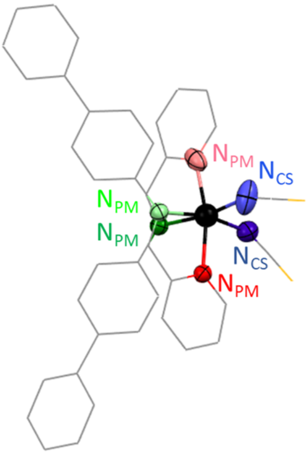

Figure 7.28: Schematic representation of the monoclinic polymorph at 210 K with anisotropic atomic displacement parameters at a 50% probability level.

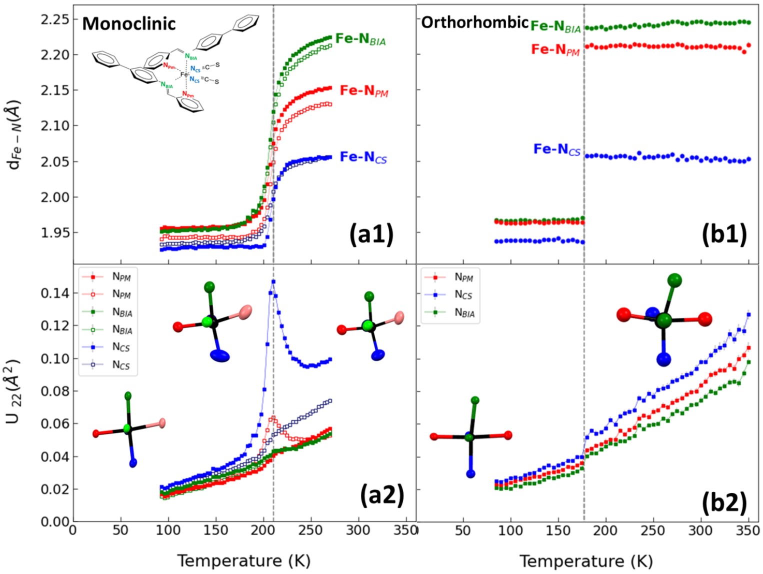

Figure 7.29: The evolution of U_{22} of the N atoms as a function of temperature for the monoclinic **(a)** and orthorhombic **(b)** polymorphs. The grey dashed line indicates the transition temperature. The inset shows a schematic diagram illustrating the associated ADPs of the N atoms surrounding the Fe atom.

A similar anomaly is not observed around $T_{1/2}$ for the orthorhombic compound (Figure 7.29**(b2)**) when measuring with a temperature step of 5 K. However, a measurement with a finer temperature step of 1 K clearly shows increased ADP parameters resulting from the superposition of the two spin states for the Fe atom. This is particularly seen in U_{11} and can be related to the significant increase in the x-coordinate of Fe across the spin crossover (Figure 7.30). For the lighter atoms, this effect is not visible, due to the larger standard deviations of the ADPs.

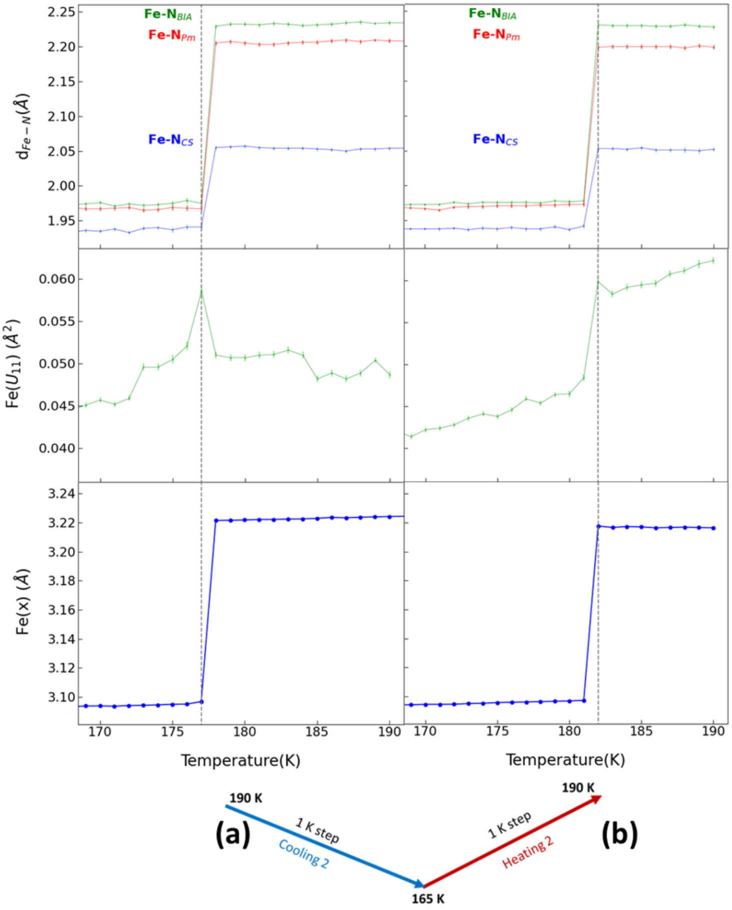

Figure 7.30: Temperature dependence of Fe-N distances, $Fe(U_{11})$, and $Fe(x)$ for the orthorhombic polymorph during the second cooling **(a)** and heating **(b)** cycles covering the SCO transition with 1 K temperature step between 169 K and 190 K.

7.6 Pressure-dependent crystal structure

High-pressure single-crystal X-ray diffraction measurements were conducted using DACs, on both polymorphs under hydrostatic pressure ranging between 0.33 GPa and 2.02 GPa (see Section 5.4.4). Experimental data for measurements under pressure for both compounds are summarized in Appendix Tables E.1 and E.2.

7.6.1 Equation of state and anisotropic compressibility

By applying pressure on the monoclinic polymorph, the structure maintains the monoclinic $P2_1/c$ symmetry across the range of pressures measured. The same is true for the orthorhombic polymorph, which remains orthorhombic (space group $Pccn$), but only up to 1.36 GPa. At a higher pressure of approximately 2.02 GPa, we observe the emergence of a superstructure characterized by a doubling of the c-axis.

The bulk modulus, derived from the unit cell volume as a function of pressure, yields values of 3.26(22) GPa and 6(1) GPa for the orthorhombic[1] and monoclinic polymorphs, respectively (Figure 7.31). These values are obtained through fitting using the third-order Birch–Murnaghan equation of state[2] [242, 243] (see Section 4.3.3, Equation 4.24 for more details).

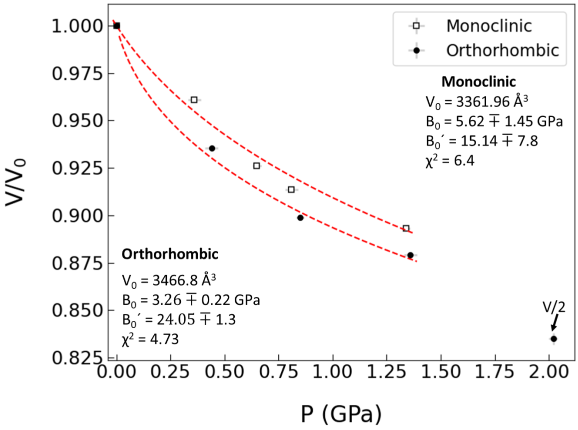

Figure 7.31: Normalized unit cell volume with respect to the ambient pressure HS volume, as a function of pressure. Results are shown for the monoclinic polymorph (open black squares) and the orthorhombic polymorph (filled black circles). The red line represents the fit of the third-order Birch–Murnaghan equation of state to the data.

The obtained values are comparable to those reported in the literature for other SCO materials [249]. The low bulk modulus of both polymorphs reflects the significantly stronger compressibility of Fe(Pm-Bia)$_2$(NCS)$_2$ compared to the other compounds [324]. In general, the bulk moduli of SCO compounds range from 4 GPa to 13 GPa [324]. The monoclinic polymorph, having a larger bulk modulus, is less compressible than the orthorhombic polymorph. In other words, the crystal lattice of the monoclinic structure is more rigid and resistant to volume changes

---

[1] Only in the HS phase.

[2] Program EoS-Fit V5.2 [323]. The experimental value for unit-cell volume at ambient pressure is $V_0 = 3468.8(1)$ Å^3 and $V_0 = 3361.9(1)$ Å^3 for orthorhombic and monoclinic, respectively. The fitted values of the first pressure derivative of the bulk modulus $B_0' = 24(1)$ and 15(7) for orthorhombic and monoclinic, respectively (Figure 7.31).

under external pressure. Conversely, the orthorhombic polymorph with a lower bulk modulus and a high compressibility of the HS molecular lattice has a crystal lattice that is more flexible, allowing for more substantial volume adjustments. It is worth noting that the LS materials are found to be relatively stiffer [188, 325].

The evolution of unit cell volume and lattice parameters of the monoclinic polymorph, as a function of pressure at ambient temperature, in the pressure interval 0.36 GPa $<$ P $<$ 1.34 GPa is shown in Figure 7.32. All the unit cell parameters decrease as a function of pressure, leading to an isotropic compression. At 1.34 GPa, the unit cell volume is approximately 11.95% smaller than the ambient pressure value, with the a, b, and c-axes shortening by -2.9%, -2.8%, and -5.6%, respectively. The β angle changes by less than 0.1° across the investigated pressure range.

For the orthorhombic polymorph, the variation of unit cell volume and lattice parameters as a function of pressure is illustrated in Figure 7.32 for pressures between 0.44 GPa and 2.02 GPa. All unit cell parameters are isotropically compressed, with the lattice parameters a, b, and c-axes decreased by -2.1%, -11.4%, and -0.03%, respectively, up to 1.36 GPa. The compressed unit cell volume at 1.36 GPa is approximately 13.7% smaller than the volume at ambient pressure. Interestingly, from 1.36 GPa to 2.02 GPa, the unit cell parameters exhibit anisotropic responses to the pressure, in which the a lattice parameter decreases by -4.8%, the b-axis increases by +2.5%, and the c-axis decreases by -2.9% (referring to $c/2$). This response to pressure is reflected in decreasing the unit cell volume by -5% (referring to v/2) at 2.02 GPa.

7.6.2 Presence/Absence of HS-LS transition

The evolution of unit cell volume and lattice parameters for the monoclinic polymorph as a function of pressure, indicates a spin transition to the LS state in the pressure range between 0.36 GPa and 1.33 GPa (Figure 7.32).

However, the best criteria to figure out whether a pressure-induced spin transition takes place, is to compare the change in $Fe - N$ bond lengths under pressure to those at ambient pressure at high and low temperatures.

From the decrease of the $Fe - N$ bond lengths (Figure 7.33),[1] one can deduce that the monoclinic polymorph undergoes a HS-to-LS transition below 0.81 GPa.[2] This transition seems to be gradual in the pressure range of atmospheric pressure to 0.81 GPa. As the bond lengths do not decrease further with pressure above 0.81 GPa, the HS to LS transition is either fully completed or a further completion is hindered at this pressure. At a pressure of 1.36 GPa, a minimal amount of approximately 10(5)% remains in the HS state. The evidence that the spin transition might not

---

[1] The decrease for the $Fe - N_{Bia}$ is less pronounced than for $Fe - N_{CS}$ and $Fe - N_{Pm}$.

[2] It is noteworthy that the pressure point at 0.81 GPa for the monoclinic polymorph exhibits a less satisfactory R_{int} value and consequently not a satisfactory structural refinement. This observation can be attributed to the fact that the pressure point, 0.81 GPa, is in the vicinity of the spin transition.

be fully completed at the final pressure comes from the superimposed figures of the crystal structures (Appendix Figure E.13).[1]

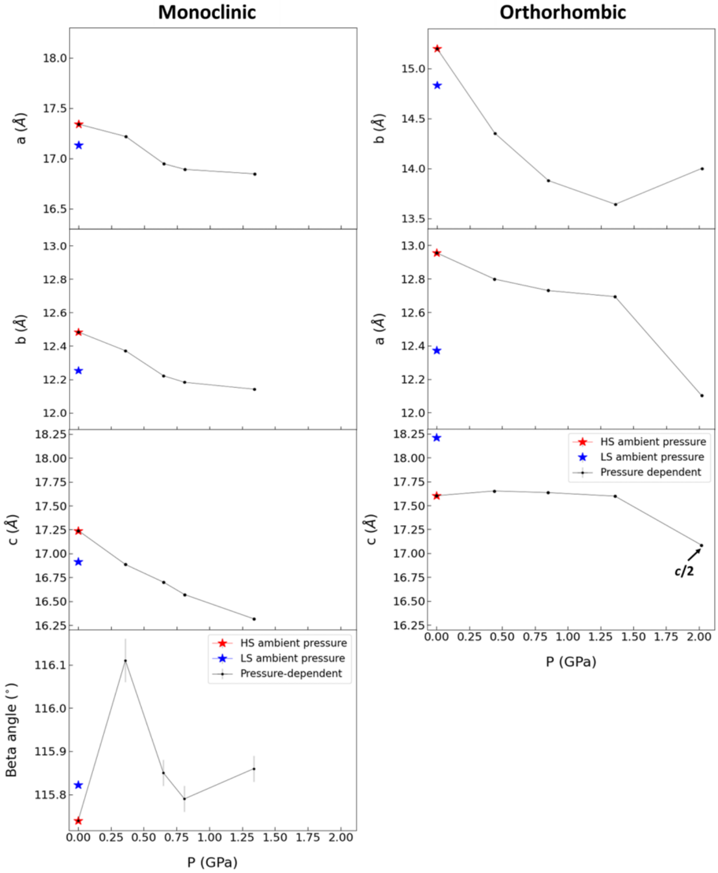

Figure 7.32: Pressure dependence of the unit-cell parameters and unit-cell volume of of the monoclinic polymorph (left) and the orthorhombic polymorph (right) at ambient temperature. At 2.02 GPa, the lattice parameters for the orthorhombic polymorph correspond to the superstructure; displayed values of the volume V and the c- lattice parameter correspond to $V/2$ and $c/2$. The lattice parameters of the two polymorphs are shown in pairs that reflect the crystal packing (see Section 7.4). The black circles represent data obtained from pressure-dependent measurements. The red and blue stars represent values in the HS (300 K and 270 K for the orthorhombic and the monoclinic polymorph, respectively) and in the LS state (95 K and 93 K for the orthorhombic and the monoclinic polymorph, respectively) at ambient pressure, respectively. Lines are guides to the eyes. Error bars are smaller than symbols.

---

[1] Figure E.13 shows the differences between the crystal structures with applied pressure and the LS/HS crystal structures at ambient pressure.

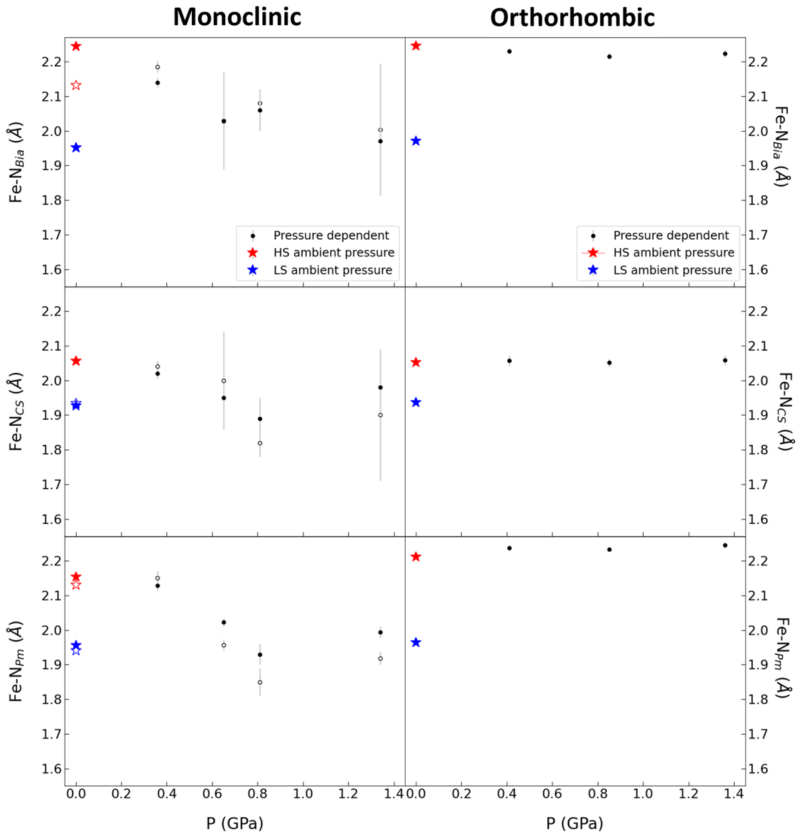

Figure 7.33: Change in $Fe-N$ bond length as a function of pressure for the monoclinic polymorph (left) and the orthorhombic polymorph (right). The red and blue star symbols represent values in the HS and LS at ambient pressure, respectively. Error bars are smaller than the symbols.

Apart from the change in the $Fe-N$ bond length, a reduction in the distortion parameter (Σ) is commonly observed for spin crossover compounds when undergoing a HS-LS transition. For the monoclinic phase, the distortion parameter Σ is in fact reduced as a function of pressure, in accordance with the assumption of a pressure-induced HS to LS transition (Figure 7.34).

A thorough comparison of the bond lengths and bond angles obtained under pressure with those observed previously at room temperature and ambient pressure reveals differences. The most noticeable changes affect the thiocyanate NCS^- group in the monoclinic polymorph (as shown clearly in Appendix Figure E.13), in which the shortening of the $Fe-N_{CS}$ bond length is observed indicating the transition to the LS state. All the $C-S$ bond lengths of the thiocyanate ligands show an apparent increase with applying pressure for the monoclinic polymorph (Figure 7.35), similar to the behavior observed during the thermal-induced spin transition to the LS state.

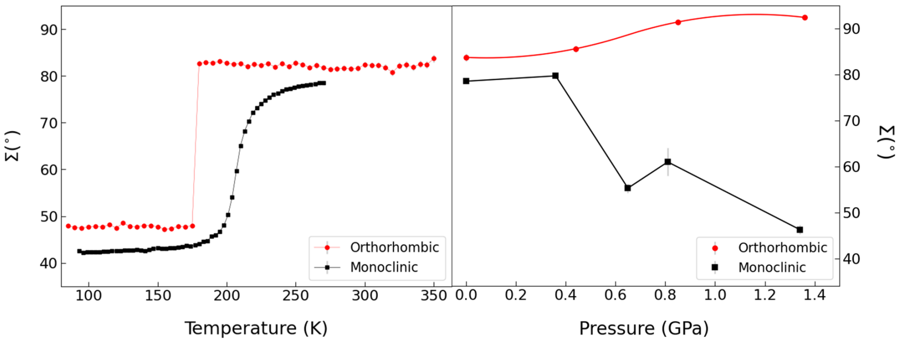

Figure 7.34: The evolution of the angular distortion parameter (denoted as Σ) as a function of temperature at ambient pressure (left) and as a function of pressure at ambient temperature (right) for both the orthorhombic (red circles) and monoclinic (black squares) polymorphs.

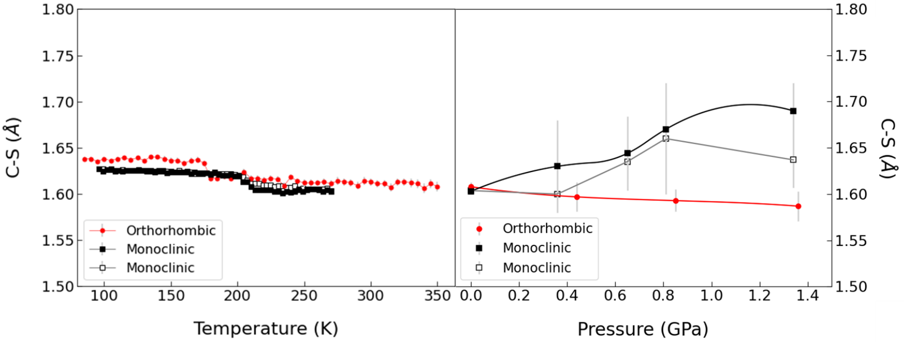

Figure 7.35: The $C-S$ bond length (corresponds to the NSC^{-} group) as a function of temperature (left) and pressure (right). Red circles correspond to the orthorhombic polymorph, and the full and open black squares correspond to the monoclinic polymorph. Lines are guides to the eyes.

Further structural changes corresponding to the thiocyanate NCS^{-} group are presented in Figures 7.36 and 7.37, illustrating the changes in the $Fe-\mathrm{N}\equiv\mathrm{C}$, and the $\mathrm{N}\equiv\mathrm{C}-S$ bond angles, respectively. In the monoclinic polymorph, one of the two NCS^{-} branches exhibits a tendency toward linearity with increasing pressure (similar behavior as the thermal induced LS state) (Figure 7.36). On the other hand, the other branch behaves differently from the thermal-induced LS state by becoming less linear as pressure increases. The $\mathrm{N}\equiv\mathrm{C}-S$ bond angle (Figure 7.37) exhibits deviation from linearity with applying pressure.This behavior is similar to the temperature-induced LS transition.[1]

---

[1] It is worth noting that in the monoclinic phase, for the thermal-induced spin transition, one of the two branches exhibits an anomaly around the transition temperature, as previously discussed in Section 7.4.

In the monoclinic polymorph, the structural properties associated with the pressure induced LS structure spin state are comparable to those related to the thermal induced LS structure, with the exception that the bond lengths and distortion parameters are slightly larger than those observed at 93 K.

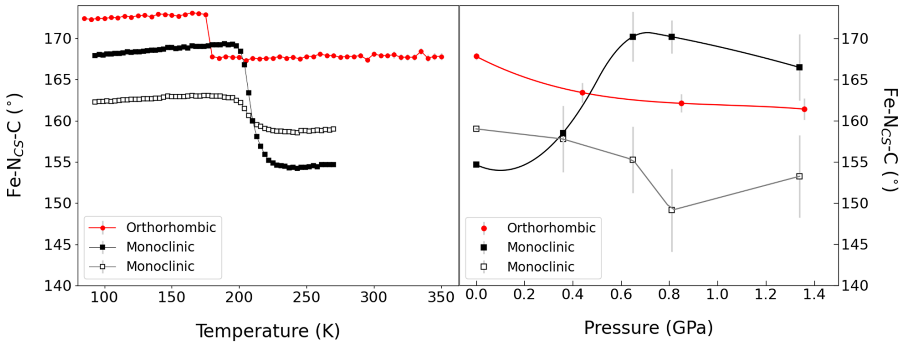

Figure 7.36: The $Fe - \mathrm{N} \equiv \mathrm{C(S)}$ angle (corresponds to NSC^{-} group) as a function of temperature (left) and pressure (right). Red circles correspond to the orthorhombic polymorph and the full and open black squares correspond to the monoclinic polymorph. Lines are guides to the eyes.

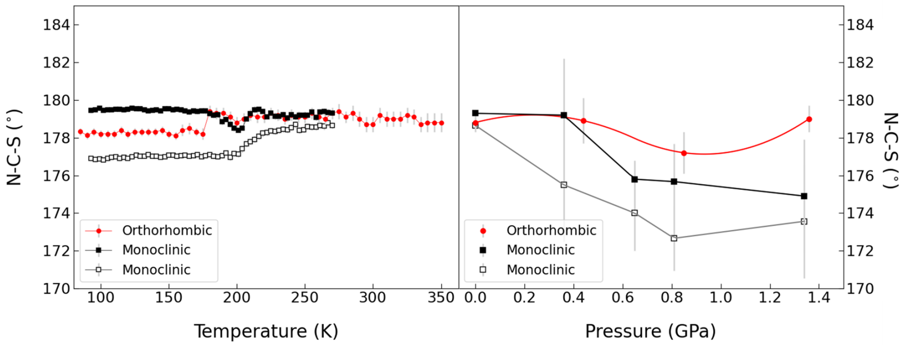

Figure 7.37: The $\mathrm{N} \equiv \mathrm{C} - \mathrm{S}$ angle (corresponds to NSC^{-} group) as a function of temperature (left) and pressure (right). Red circles correspond to the orthorhombic polymorph and the full and open black squares correspond to the monoclinic polymorph. Lines are guides to the eyes.

In the case of the orthorhombic polymorph, in the temperature-dependent study, the sharp spin transition that occurs at $T_{1/2} = 175\,\mathrm{K}$, was related to a sharp increase of the unit cell parameter c with decreasing temperature (see Figure 7.13). Thus, it seems reasonable to consider that change in the same parameter c has to be related to the HS to LS transition induced by applying pressure.

However, the true evidence of spin transition can be observed from $Fe-N$ bond lengths in the orthorhombic polymorph, which are basically not influenced by the application of pressure up to 1.36 GPa (Figure 7.33). They persist at values corresponding to $Fe-N$ bond lengths observed in the HS state at ambient pressure (Figure 7.33)[1] indicating that the HS state is maintained up to 1.36 GPa.

By comparing superimposed crystal structure figures (Appendix Figure E.14), one can observe that the crystal structure of the orthorhombic polymorph remains similar to the HS-ambient pressure crystal structure, and with applying pressure, it does not exhibit signatures of a HS to LS transition.

Furthermore, the distortion parameter for the orthorhombic polymorph is not much influenced by pressure, indicating again that it remains in the high spin state and does not undergo any spin transition (Figure 7.34).

The intramolecular distances and angles, within the standard deviation, remain almost constant with applying pressure for the orthorhombic polymorph. For example, the $C-S$ bond lengths and the $Fe-\mathrm{N}\equiv\mathrm{C}$, and the $\mathrm{N}\equiv\mathrm{C}-S$ bond angles of the thiocyanate ligands (Figures 7.35, 7.36 and 7.37) are hardly influenced by applying pressure.

7.6.3 High pressure in orthorhombic polymorph

A doubling of the *c*-axis ($a \times b \times 2c$) was observed at hydrostatic pressure of 2.02 GPa, demonstrated by the appearance of supercell reflections at (h, k, l $\pm$ 1/2) relative to the lattice at ambient pressure and temperature (Figure 7.38).

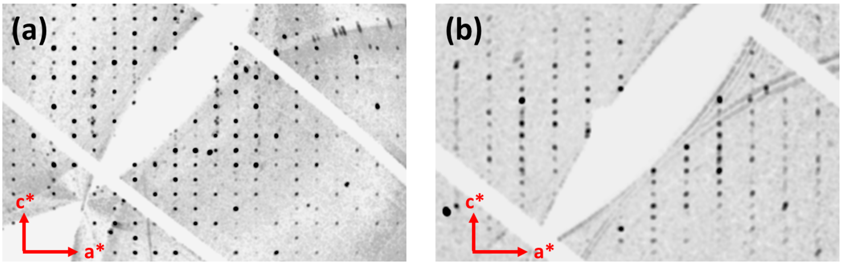

Figure 7.38: The reconstruction of reciprocal space in the $h1l$ plane for the orthorhombic polymorph, at two different pressure points **(a)** 0.85 GPa and (b) 2.02 GPa at room temperature.

Careful analysis of the extinction rules shows that in the $hk0$ plane $h+k \neq even$, which indicates that the n-glide plane does not exist anymore. The systematic absences are an indication of a change in the original space group $Pccn$. Also it worth noting that α, β, γ angles slightly deviate from 90° (α, β, γ = 89.97(3)°,

---

[1] At 2.02 GPa the crystal structure is not solved yet.

90.12(5)°, 89.88(5)°, respectively). Importantly, these structural changes do not align with the HS state of the monoclinic polymorph.

Due to the low symmetry of the structure and the limited coverage of reciprocal space (not unusual for high-pressure single crystal data, due to the limited opening angle of the DAC cells), we encountered severe problems in solving the crystal structure. Neither Charge Flipping nor Direct Methods led to an acceptable solution that would yield an appropriate initial model. Starting the refinement from a derived model from the low-pressure structures, also did not allow for a satisfactory refinement of the data. This serves as evidence that the atomic arrangement has undergone significant changes with respect to the ambient pressure structure. The crystal structure above 2.02 GPa could thus not be solved with the available data.

7.6.4 Comparative analysis with previous studies

The stabilization of the orthorhombic polymorph in the high spin state up to 1.36 GPa at ambient temperature without undergoing a spin transition[1] is in good agreement with the reported magnetic measurements under pressure (Figure 3.5) [34], which show that at room temperature the orthorhombic phase remains in the high spin state up to 1.36 GPa. On the other hand, this observation contradicts the findings reported in the literature based on neutron powder diffraction at room temperature. Legrand et al., [211] assume that the orthorhombic polymorph remains in the high spin state up to 0.84 GPa at 260 K and that at a higher pressure of 1.07 GPa, the orthorhombic polymorph transforms from the HS spin orthorhombic to the HS monoclinic polymorph. A change of symmetry from the orthorhombic to the monoclinic polymorph should be clearly visible in the reconstruction of reciprocal space, and we do not observe this (see Section 7.6.3). Furthermore, the fact that the monoclinic polymorph is already in the low spin state at 1.07 GPa makes it highly unlikely that the HS state is formed from the orthorhombic polymorph at this pressure. The discrepancies between our observations and Legrand [211] might be attributed to the lack of hydrostaticity conditions associated with the use of powder diffraction, and also powder diffraction offers limited information about the crystal structure.

Rotaru et al. [210] employed diffuse reflectivity to investigate the effect of hydrostatic pressure up to 0.18 GPa on the thermal spin transition of orthorhombic polymorph. They showed that the orthorhombic polymorph undergoes a structural phase transition to a new phase. As the diffuse reflectance feature of this new phase is different from the ones of monoclinic and orthorhombic polymorph, they labeled the new structural phase as polymorph (III). It is worth noting that the surface behavior probed by diffuse reflectance may significantly differ from that of the bulk, which we are studying in our case.

---

[1] It is worth noting that, in rare cases, stabilization of the HS state under pressure has also been reported [38, 54, 150, 326, 327]. One of the examples is the SCO compound [Fe(btre)$_2$(NCS)$_2$] with btre=1,2-bis(1,2,4-triazol-4-yl)ethane remains HS even at 1.2 GPa [327]. It has also been reported that increasing pressure leads to a shift of the transition to lower temperatures, equivalent to a stabilization of the HS state [34].

7.6.5 The role of intermolecular interaction for stiffness, compressibility, and transition

The crystal packing as a function of pressure is shown in Figures 7.39 and 7.40 (also Appendix Figures E.15 and E.16), for the monoclinic and the orthorhombic polymorph, respectively.[1] Molecular units are arranged as layers within the b, c-plane for monoclinic polymorphs and the a, c-molecular plane for orthorhombic polymorphs (as previously discussed in Section 7.4).

The observed strong enhancement of stiffness in the HS and LS networks of the monoclinic polymorph (see Section 7.6.1) is probably a result of the differences in intermolecular interactions that emerge in response to applying pressure. The monoclinic polymorph forms additional strong intermolecular contacts via $\pi - \pi$ stacking (see Appendix Table E.3). Furthermore, in both polymorphs, many van der Waals $C \cdot \cdot \cdot \cdot C$ shortest contacts are observed between neighboring molecules within the intrasheet and with the intersheet with increasing pressure (see Figures 7.41, 7.42, and 7.43, also for a clear view of these short structural contacts, see Appendix Figures E.20, E.21, and E.22).

Differences are seen with respect to the hydrogen bonding $S \cdots\cdot (H) - C$, which is established between the sulfur atom of the NCS^- branches and a carbon atom in one of the internal phenyl rings in both polymorphs. While the orthorhombic polymorph shows the formation of two hydrogen bonds with applying pressure (Figure 7.44, see Appendix Figure E.23 for more detail of the structural H-bonding), the monoclinic polymorph shows the development of four hydrogen bonds with applying pressure (Figure 7.44, see Appendix Figure E.24 for more detail of the structural H-bonding).

Furthermore, it can be seen visually that the orthorhombic and the monoclinic polymorphs behave differently (Figures 7.39 and 7.40). A significant anisotropic compressibility is observed in both polymorphs (Figure 7.32). For instance, within the molecular plane, the thiocyanate groups align along the c-direction for both polymorphs. With applying pressure, in the case of the monoclinic polymorph, the c-axis is the most compressible direction (-5.6%). In contrast, the orthorhombic polymorph maintains the c-axis as the least compressible direction, exhibiting a minimal decrease of -0.03% at 1.36 GPa. This can be explained by the fact that the packing of the HS orthorhombic phase is locked by strong intermolecular interaction, namely the $S \cdots \cdot (H) - C$ contacts. These contacts predominantly occur in the c-direction, and their influence most likely prevents the compound from being compressed effectively in this particular direction. Probably, one can speculate that a pressure of 2.02 GPa is incompatible with the H-bonding, prompting a significant rearrangement of atoms, leading to the transition and formation of the superstructure.

---

[1] Appendix Figures E.17 and E.18 show the differences between the crystal packing with applied pressure and the LS/HS crystal structures at ambient pressure.

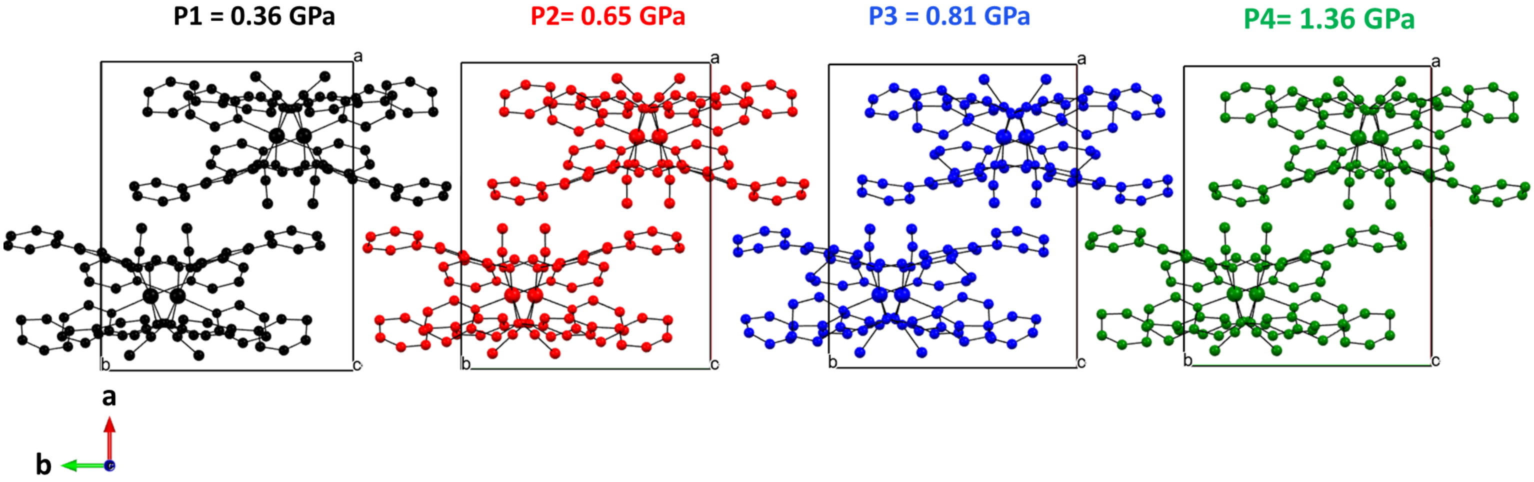

Figure 7.39: An illustration of the monoclinic polymorph of [Fe(PM–Bia)$_2$(NCS)$_2$] projected along the *c*-direction, showing the impact of applied pressure on the crystal packing (P1 in black, P2 in red, P3 in blue, and P4 in green). Atoms of hydrogen are left out for clarity.

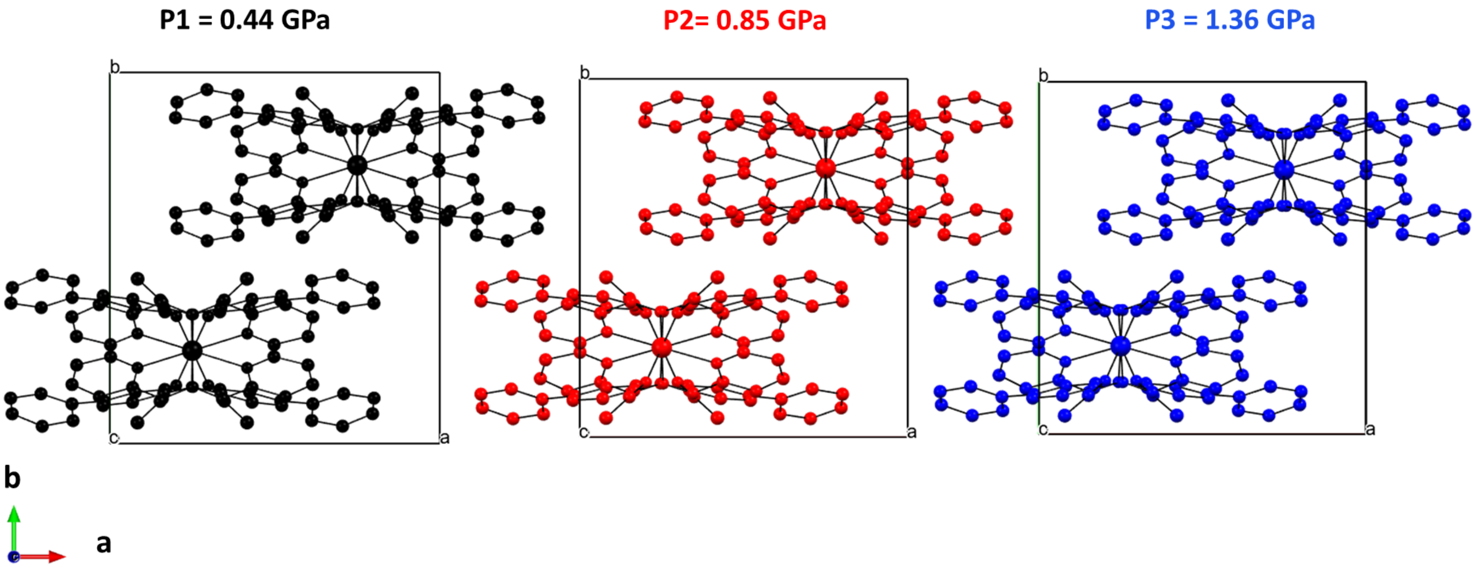

Figure 7.40: An illustration of the orthorhombic polymorph of [Fe(PM–Bia)$_2$(NCS)$_2$] projected along the *c*-direction, showing the impact of applied pressure on the crystal packing (P1 in black, P2 in red, and P3 in blue). Hydrogen atoms are omitted for clarity.

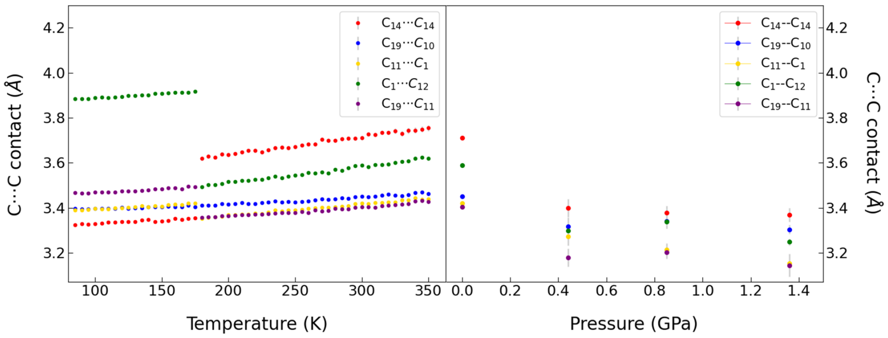

Figure 7.41: Evolution of the shortest intermolecular distance $C\cdots\cdot C$ for the orthorhombic polymorph as a function of temperature (left) and pressure (right). $C_{11}\cdots\cdot C_1$ and $C_{12}\cdots\cdot C_1$ are the shortest contact in the intersheet layers. $C_{14}\cdots\cdot C_{14}$, $C_{19}\cdots\cdot C_{10}$, and $C_{19}\cdots\cdot C_{11}$ are shortest contact in the intrasheet layers.

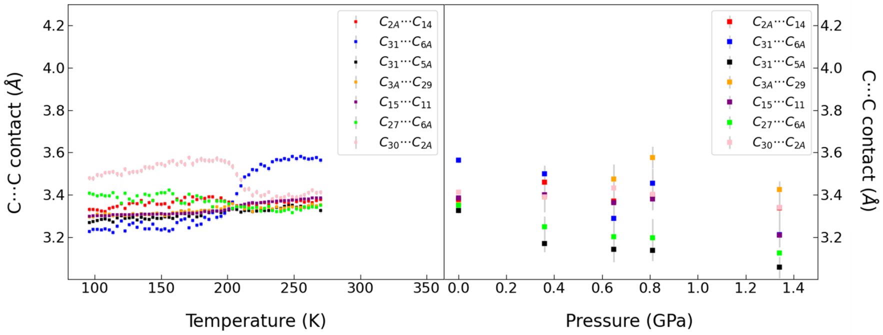

Figure 7.42: Evolution of the shortest intermolecular distance $C\cdots\cdot C$ for the monoclinic polymorph as a function of temperature (left) and pressure (right). $C_{15}\cdots\cdot C_{11}$ and $C_{27}\cdots\cdot C_{6A}$ are the shortest contact in the intersheet layers. $C_{31}\cdots\cdot C_{6A}$, $C_{2A}\cdots\cdot C_{14}$, $C_{3A}\cdots\cdot C_{29}$, and $C_{19}\cdots\cdot C_{10}$ are shortest contact in the intrasheet layers.

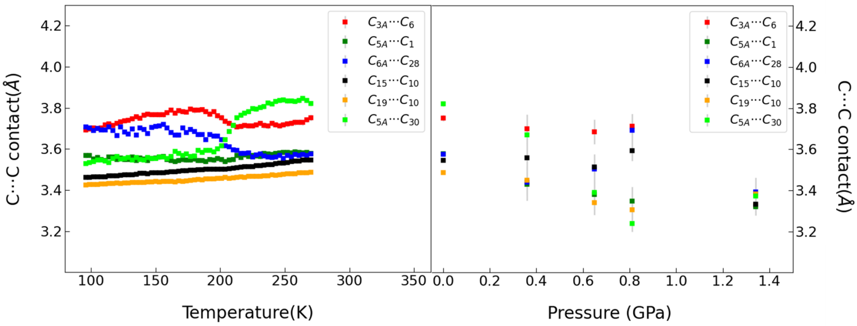

Figure 7.43: Evolution of the shortest intermolecular distance $C\cdots\cdot C$ observed only under applying pressure for the monoclinic polymorph as a function of temperature (left) and pressure (right). $C_{5A}\cdots\cdot C_1$, $C_{15}\cdots\cdot C_{10}$, and $C_{6A}\cdots\cdot C_{28}$, are the shortest contact in the intersheet layers. $C_{3A}\cdots\cdot C_6$, $C_{19}\cdots\cdot C_{10}$, and $C_{5A}\cdots\cdot C_{30}$ are shortest contact in the intrasheet layers.

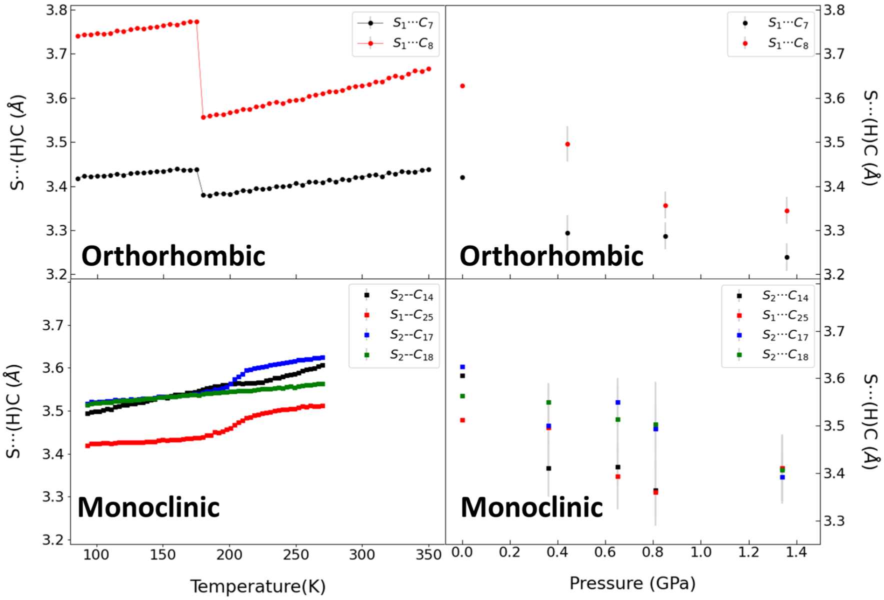

Figure 7.44: The variation in the shortest intermolecular $S\cdots\cdot(H)-C$ distance for the orthorhombic (top) and monoclinic (bottom) polymorph as a function of temperature and as a function of pressure.

Concerning the other perpendicular direction within the molecular layer, the *b*-direction in the monoclinic polymorph is the stiffest direction which decreases by -2.8%; similarly, the *a*-direction for the orthorhombic polymorph at 1.36 GPa, decreases by -2.1%. However, between 1.36 GPa to 2.02 GPa the *a*-axis of the orthorhombic polymorph undergoes a more pronounced reduction of -4.9%.

The lattice parameter associated with the stacking direction of the sheets reveals further differences. The *b*-axis in the orthorhombic polymorph is the most substantial compressible one by -11.4% (at 1.36 GPa) which decreases faster in comparison with the *a*-direction in the monoclinic polymorph, which decreases by -2.9%. A plausible explanation for this dissimilarity lies in the distinct arrangements of the NCS^- groups along the stacking direction (Figures 7.39 and 7.40). In the monoclinic polymorph, the linear alignment of NCS^- groups along the *a*-direction possibly hinders compression in the stacking direction. However, the orthorhombic polymorph presents a different scenario with the NCS^- groups not linearly oriented along the stacking direction (*b*-direction); consequently, the stacking direction of the orthorhombic polymorph undergoes more pronounced compression behavior. This is in line with the presence of weak intersheet interactions along this direction, compared to stronger intrasheet interactions in the *ac*-plane.

7.6.6 Comparison of high-pressure and low-temperature crystal packing

The HS-to-LS transition increases the density of the crystal structure. It has been assumed that the occurrence of cooperative SCO behavior can be thought of in terms of internal pressure [326], that induces the HS to LS transition. The orthorhombic polymorph undergoes the spin transition after a contraction of the unit cell with decreasing temperature at a unit cell volume of 3343.6(9) Å (-3.97%, compared to room temperature). However, the high-pressure unit-cell volume at 1.36 GPa is 3048(2) Å which is much smaller than the low-temperature LS unit cell volume at 85 K and the spin transition to the LS state is still not observed (Figure 7.45). From ambient pressure up to 1.36 GPa the unit-cell volume decreases by $\Delta V = 418.8(3)$ Å^3 compared to a temperature-induced decrease of $\Delta V = 123.2(2)$ Å^3, and still no HS-LS transition is triggered.

For the orthorhombic polymorph, a linear decrease in lattice parameters with volume is observed in pressure-dependent measurements (Figure 7.45). On the other hand, for the monoclinic polymorph, which undergoes a spin transition in both pressure-dependent and temperature-dependent measurements, it is difficult to judge whether the lattice parameters from pressure-dependent and temperature-dependent measurements follow the same trend due to the limited data points available in the pressure dataset (Figure 7.45).

While it is often assumed that cooperativity increases with stronger and more numerous intermolecular interactions, the reality is far more intricate. A striking example of this complexity can be observed when comparing the thermal transition of the two polymorphs (see Section 7.4.3 for more details).

The cooperative thermal behavior of SCO materials could arise from strong interactions, like hydrogen bonding, between neighboring molecules. These interactions promote simultaneous alignment and switching between the spin states. It is believed that, as a result, the spin transition is cooperative and leads to an abrupt transition. In the absence of strong interaction, the individual molecules may switch their spin states more independently, leading to a gradual spin transition.

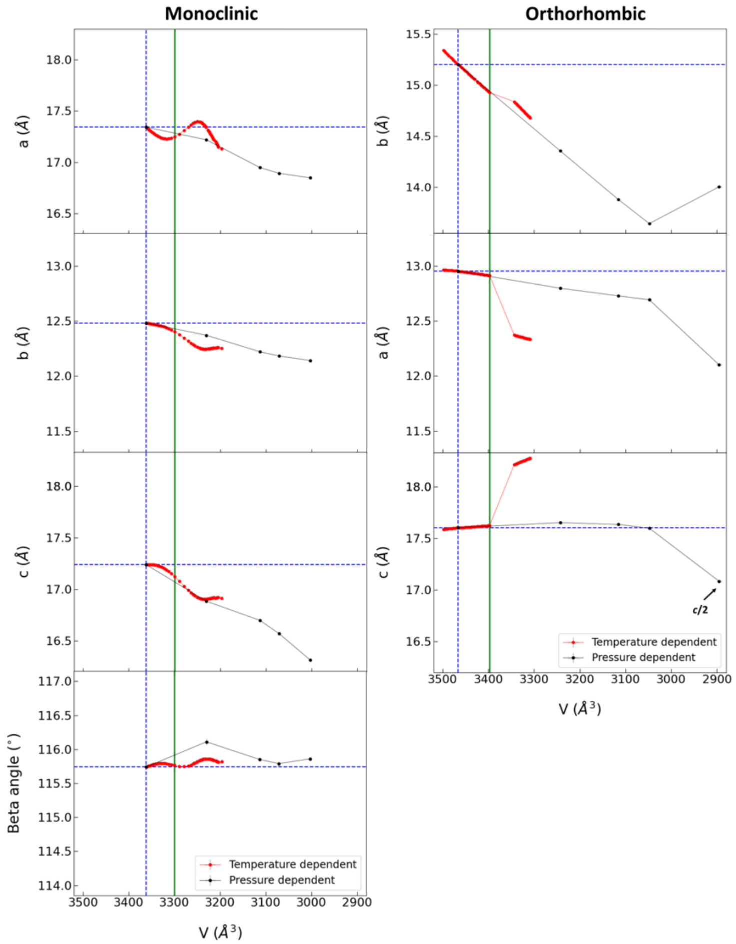

Figure 7.45: The lattice parameter as a function of unit cell volume: Depicted for both the monoclinic polymorph (left) and orthorhombic polymorph (right). The red and black symbols are obtained from temperature and pressure studies, respectively. At 2.02 GPa, the lattice parameters for the orthorhombic polymorph correspond to the superstructure, where the displayed values of the volume V and the c- lattice parameter correspond to $V/2$ and $c/2$. The lattice parameters of the two polymorphs are ordered in a way similar to the crystal packing, for easier comparison. The vertical green line represents the unit cell volume corresponding to the transition temperature ($T_{1/2}$ = 210 K and 177 K for the monoclinic and the orthorhombic polymorph, respectively) at ambient pressure. The horizontal and vertical dashed blue lines represent the values of the lattice parameters and unit cell volume at ambient pressure at 300 K. Lines are guides to the eyes. Error bars are smaller than the symbols.

We believe that in the case of the orthorhombic polymorph, the presence of the H-bonding facilitates the cooperative change of spin states in adjacent molecules (Figure 7.24). H-bonding leads to synchronized behavior, which can be considered a domino-like effect where one molecule spin transition triggers the neighboring molecules to follow, resulting in an abrupt, cooperative spin transition across the crystal lattice. The H-bond network could be assumed to be a "glue", which holds the spin-crossover units together and ensures their simultaneous thermal switching.

On the other hand, in the monoclinic polymorph, the absence of a strong H-bonding "glue" between molecules and the presence of several van der Waals and $\pi - \pi$ interactions result in smearing out the transition over a wide range of temperatures. Different parts of the lattice could have different degrees of the $\pi - \pi$ and van der Waals interactions. As a consequence, individual molecules or smaller groups within the crystal switch their spin states more independently.

The application of pressure strongly influences the intermolecular interactions. In the orthorhombic polymorph, at elevated pressures, the hydrogen bonding intensifies through the formation of more hydrogen bonds (Figure 7.44) and becomes stronger than the ones observed during HS-LS transitions at ambient pressure. As a consequence, this intensified hydrogen bonds probably hinders the transition to the low-spin state due to the fact the twofold decrease of the volume related to the HS-LS transition is not compatible with the space requirements of the hydrogen bonds. Moreover, an increase in the number and strength of van der Waals contacts is observed (Figure 7.41). Some of these pressure-induced intermolecular contacts were not observed in the LS state at low temperatures as shown in Figure 7.41. Strikingly, $\pi - \pi$ interactions are not observed neither as a function of temperature or pressure (Appendix Table E.3).

Conversely, for the monoclinic polymorph, it is worth noting that strong $\pi - \pi$ interactions are observed at ambient conditions (see Section 7.4.3 for more details), and the number of observed $\pi - \pi$ interactions under pressure is similar to what is observed at temperatures around 225 K during the thermal transition. This observation indicates that $\pi - \pi$ interactions might in this case play a role in facilitating the spin transition. In addition, with applying pressure additional hydrogen bonds are formed (Figure 7.44) and the number of van der Waals interactions increases (Figures 7.42 and 7.43).

In conclusion, cooperativity is a complex phenomenon which is not solely determined by a single factor, like one particular type of intermolecular interaction. The specific behavior of cooperativity can vary significantly from one SCO material to another, and it is influenced by a complex interplay of factors and their response to external stimuli like temperature or pressure.

7.7 Thermal cycling

Given the importance of reproducibility for potential applications, we conducted consecutive cooling and heating cycles, utilizing DSC, magnetization (see Section 7.2.1 and Appendix Section E.1) and X-ray diffraction techniques, to investigate whether the observed spin crossover phenomena is reproducible.

The unit cell parameters and unit cell volume of the monoclinic polymorph upon consecutive thermal cycling (Figure 7.46) show that the changes in the volume with cycling are not reproducible: with respect to the initial value[1]; the volume in the LS state increases by 0.42%, while in the HS state, it increases by 0.22%. We attribute the increase of the unit cell volume on cycling to radiation damage. The spin crossover process seems to be affected by the accumulated radiation exposure, which favors the stabilization of the high spin state. This in turn leads to shifting the transition temperature to lower temperatures, reducing it from 210.6 K to 208.8 K. Radiation damage possibly decreases the cooperativity of spin crossover compounds by introducing defects that disrupt the regularity of the crystal lattice, leading to increases in the width (a decrease in the steepness) of the spin transition at the transition temperature.

Moreover, the individual lattice parameters of the monoclinic polymorph, are also not fully reproducible and show different deviations in the LS state and HS state from the initial value. The a parameter increases by 0.23% and 0.5% in the LS and HS states, respectively, whereas the b and c parameters slightly increase in the LS state by 0.085% and 0.053%, and exhibit a decrease in the HS state by 0.088% and 0.32%.

In contrast, the unit cell volume of the orthorhombic polymorph is perfectly reproduced in all measured cycles using X-ray diffraction (cooling down two times and warming up two times), although the same is not true for the behavior of the individual lattice parameters (Figure 7.46). While in the first cooling and warming cycle, all the lattice parameters are fully reproducible in the LS state, lattice parameters on cooling and heating in the HS state are different: the a lattice parameter is slightly smaller than its initial value (0.23%), the b lattice parameter is slightly larger (0.35%), and the c lattice parameter remains unchanged. These discrepancies between initial and reproduced values get even larger for the second cooling/warming cycle: the a lattice still remains unchanged in the LS state but decreases even more in the HS state (0.37%). The b lattice parameter exhibits a larger value in both the LS and HS states during the second cycle (0.22%), and the c lattice parameter has a significantly smaller value in the LS state (0.24%) and a slightly larger value in the HS state (0.2%).

Nevertheless, it is worthwhile to delve into the examination of crystalline mosaicity[2] concerning cycling. The evolution of mosaicity values e1, e2, and e3 obtained from *CrysAlis*^{Pro} software [295], is shown in Figure 7.47. Even after four cycles, the mosaicity values are found to be reproducible. The mosaicity only increases at temperatures where both phases coexist in a mixed HS/LS state (as expected). We deduce from these observations that, despite the abruptness of the transition of the

---

[1] It is worth noting that the calculation in Figure 7.46 employs the expression $^{*}x_{normalized} = \frac{x(LS)cycle1-x(T)}{x(LS)cycle1-x(HS)cycle1}$, where x is the lattice parameter or the unit cell volume.

[2] The concept of "mosaicity" introduced by Bragg et al., in 1926, which defined the crystals as a mosaic of blocks (known as domains), each differing slightly in orientation [328].

orthorhombic polymorph, the crystal maintains its quality throughout the cycling process. This exceptional robustness can be attributed to the strong intermolecular interactions, particularly the H-bonds.

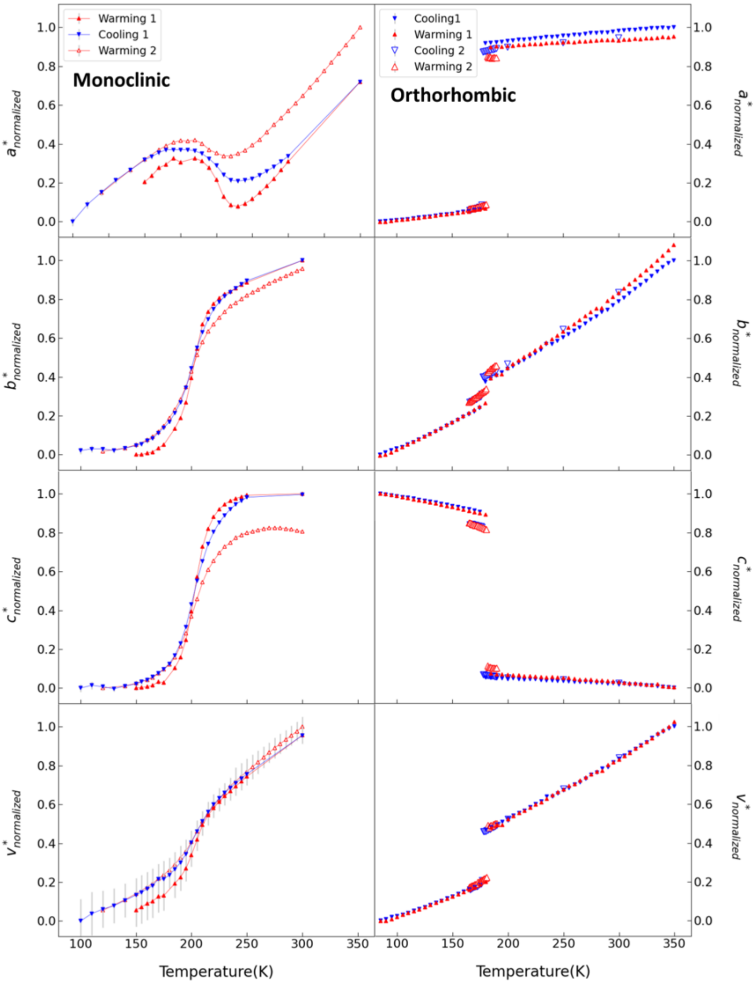

Figure 7.46: Evolution of the relative change in the normalized lattice parameters and unit cell volume (see text for the expression), during consecutive thermal cycles for the orthorhombic and the monoclinic polymorph. The filled blue and red triangle symbols represent the values obtained from the first cooling and first warming, respectively. The open blue and red triangles correspond to the second cooling and second warming, respectively. Lines are guides to the eyes. Error bars are the same size or smaller than the symbols.

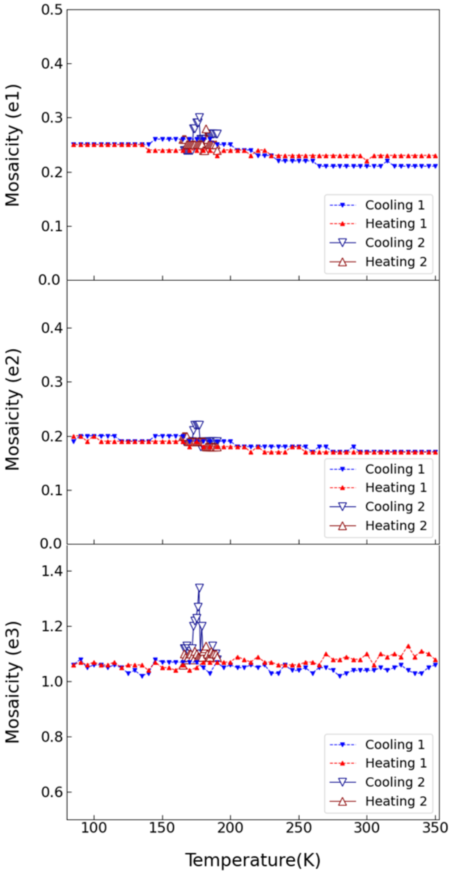

Figure 7.47: During thermal cycle measurements, the mosaicity evolution of the orthorhombic polymorph. Crystal mosaicity is measured by the e1, e2, and e3 values that are derived from the *CrysAlis*^{Pro} software [295].

For the orthorhombic polymorph where cycling was also carried out during the single crystal measurements, we also inspected the intra- and intermolecular changes. No significant change was observed when taking into account the standard deviations (see Figure 7.48). Therefore, the overall change in the lattice parameters during the cyclic measurements must be induced from a collection of several small changes across the lattice, as depicted in the plots of the structural features (bond length and angles) and intermolecular contacts (H-bonding and VdW contacts, Figures 7.48 **(a)**&**(b)**).

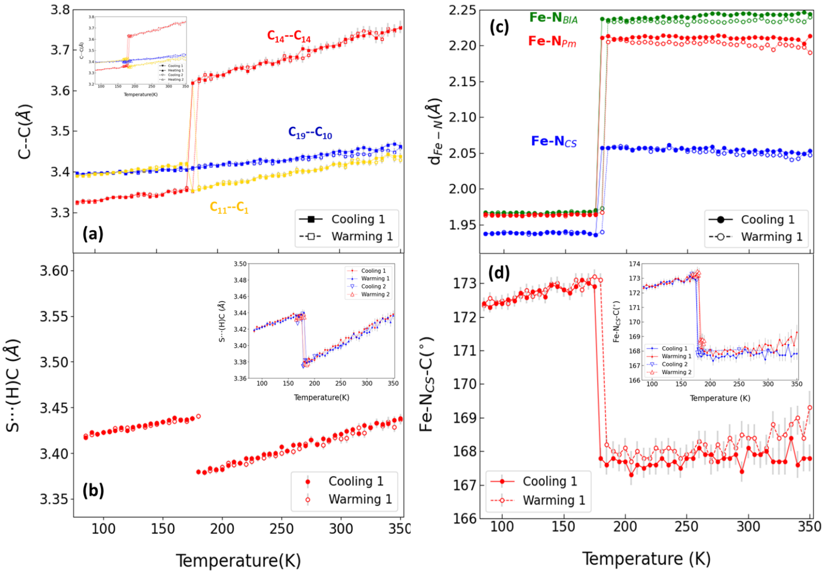

Figure 7.48: Evolution of the intermolecular contacts: van der Waals interaction **(a)**, and hydrogen bonding **(b)** in the orthorhombic polymorph. Changes in $Fe - N$ bond lengths and $Fe - N - C(S)$ bond angle, upon consecutive thermal cycles, are shown in **(c)** and **(d)**. Lines are guides to the eyes. Error bars are the same size or smaller than the symbols.

7.8 Effect of scan rate and intermediate state

The appearance of an intermediate state during the heating cycles with a slow scan rate in the magnetization measurement (see Section 7.1) of the orthorhombic polymorph prompted further investigation. To explore this phenomenon, we performed powder X-ray diffraction with two different scan rates on cooling and heating cycles (see Section 7.8 for experimental details). At a temperature corresponding to the intermediate state, with a fast scan rate of 6 K/min, the cooling and heating patterns coincide (Figure 7.49 (left)). However, at a slower scan rate of 0.2 K/min, additional peaks are observed during the heating cycle, as shown in Figure 7.49 (right). It is remarkable that these additional peaks are not observed in the corresponding cooling cycle. The difference in heating cycles is clearly visible if one overlays the collected powder patterns measured with different scan rates (Figure 7.50). The additional peaks which appear in the heating cycles with the slow scan rate can be indexed with a supercell in which the *c*-lattice parameter is doubled ($a = 13.00(4)$ Å, $b = 14.87(7)$ Å, $c = 33.81(8)$ Å; space group $= P1$).

It is noteworthy that the observed intermediate state, which is indexed with a supercell with a doubled *c*- lattice parameter, is surprisingly similar to the supercell which has been observed under pressure of 2.02 GPa.

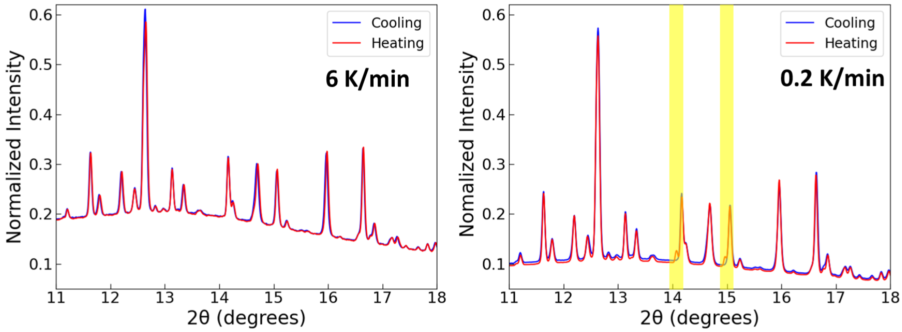

Figure 7.49: Powder patterns of the orthorhombic polymorph measured at two different scan rates 6 K/min (left) and 0.2 K/min (right) at the intermediate temperature of 185 K while heating (red line) and cooling (blue line). The yellow-shaded areas highlight the additional peaks.

Figure 7.51 (right) illustrates the evolution of the unit cell parameters with temperature upon cooling and heating cycle a scan rate 6 K/min. As expected, the evolution of the unit cell parameters reveals a thermal hysteresis about 10 K with this fast scan rate.[1]

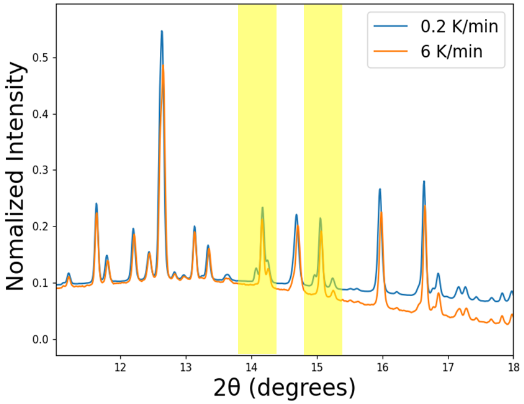

Figure 7.50: Overlay of the powder patterns of the orthorhombic polymorph at 185 K for two different scan rates 6 K/min (blue) and 0.2 K/min (orange) while heating. The yellow-shaded area highlights the additional peaks.

---

[1] The data set collected upon cooling with a rate of 6 K/min shows three different regions (Figure 7.51 (right)). The first region, covering from 250 K to 170 K represents the high spin state. The second region, ranging from 170 K to 161 K, is found to be a mixture of the high and low spin phases. The third region, extending from 160 K to 150 K, represents a pure low spin state. In the heating cycle at the same rate of 6 K/min, three distinct regions are observed. The first region, spanning from 150 K to 174 K, is characterized by a pure low spin state. The second region, covering temperatures from 174 K to 179 K displays a mixture of both high and low spin states. The third region, ranging from 180 K and 250 K, is purely in the high spin state.

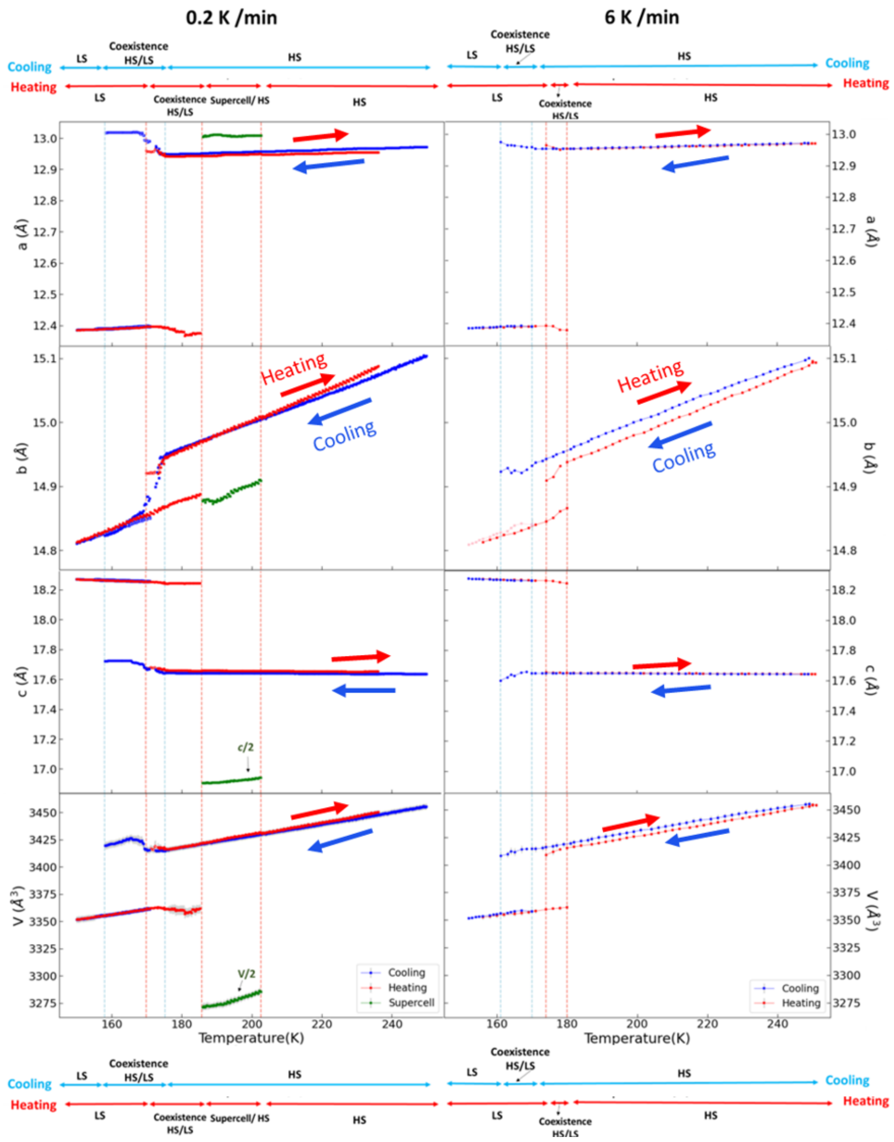

Figure 7.51: Evolution of the lattice parameters and unit cell volume, during the cooling and heating cycle for the orthorhombic polymorph at a rate of 6 K (right) and 0.2 K (left). The blue and red symbols represent the values obtained from the cooling and heating, respectively. The green squares (left, at 0.2 K) correspond to the superstructure, where the displayed values of the volume V and the c- lattice parameter correspond to $V/2$ and $c/2$. The vertical dashed light blue and red lines divide the region of the spin state during cooling and heating respectively. Lines are guides to the eyes.

Figure 7.51 shows a comparison of the lattice parameters derived from the data measured at the two different scan rates. The evolution of the unit cell parameters reveal a thermal hysteresis of about 5.2 K with the slow scan rate. During the cooling cycle, three distinct temperature regions (HS: 250 K - 175.2 K, HS + LS: 175.1 K - 158.6 K, and LS: 158.5 K to 150 K) are observed similar to the fast scan rate of 6 K/min. However, for the heating cycle four regions can be distinguished (Table 7.6).

Table 7.6: Temperature regions and corresponding spin states for the heating cycle with a scan rate of 0.2 K/min.

Temperature Range	**Spin state**
150 K - 169.8 K	Pure low spin state
169.9 K - 185 K	Mixture of high spin and low spin states
185 K - 202 K	Mixture of supercell and high spin state
202 K - 236 K	Pure high spin state

The observed coexistence of the HS and LS phases is an indicator of formation of LS and HS domains. The domain behavior observed in the PXRD is consistent with the domain formation observed in the single crystal diffraction data (see Section 7.5).

In summary, the choice of the scan rate during heating and cooling plays a pivotal role in the formation or disappearance of intermediate states in polycrystalline SCO materials.

7.9 Analysis of cooperativity and entropy change with Slichter and Drickamer model

In order to acquire an estimation of the thermodynamic parameters ΔH and ΔS and to get an idea about cooperativity associated with the spin conversion, we employed the Slichter and Drickamer model [191] by utilizing both magnetic and structural studies. This model reproduces different forms of SCO curves following the Equation 4.51.

γ_{HS} has been calculated at each temperature from the magnetic susceptibility data using the relation:

$$\gamma_{HS}^{M} = \frac{(\chi_M T(LS) - \chi_M T(T))}{(\chi_M T(LS) - \chi_M T(HS))} \tag{7.1}$$

where $\chi_M T$(LS) and ($\chi_M T$(HS) are the values of $\chi_M T$ in the LS and HS states, respectively.[1]

Additionally, the γ_{HS} was deduced from the structural data by using the relation:

$$\gamma_{HS}^{XRD} = \frac{(d_{Fe-N}(LS) - d_{Fe-N}(T))}{(d_{Fe-N}(LS) - d_{Fe-N}(HS))} \tag{7.2}$$

---

[1] Values of $\chi_M T$ for the pure high-spin ($\chi_M T$ (HS)) and pure low spin ($\chi_M T$(LS)) forms are directly obtained from the magnetic susceptibility data in the temperature intervals corresponding to pure HS and LS states.

where d_{Fe-N}(LS) and d_{Fe-N}(HS) are the $Fe - N$ bond lengths in the LS and HS states, respectively. At the equilibrium temperature $T_{1/2}$, where $\gamma_{HS} = 0.5$ [329], the enthalpy change ΔH in equation (4.51) can be related to the change in entropy using the relation $\Delta H = \Delta S T_{1/2}$. By substituting this relation into equation (4.51), the modified Equation 7.3 is obtained.

$$T = \frac{\Delta S T_{1/2} + \Gamma(1 - 2\gamma_{HS})}{R\ ln(\frac{1-\gamma_{HS}}{\gamma_{HS}}) + \Delta S} \tag{7.3}$$

To obtain the best fit, the parameters ΔS and Γ were chosen as variables. Figures 7.52 and 7.53 show the resulting fit for both polymorphs.

DSC measurements have been used to further verify the value of cooperativity (Γ) derived from the single crystal structure and magnetization data. In order to do this, the value of ΔS obtained from the DSC measurement was used to fit γ_{HS} acquired from the $Fe - N$ bond lengths (Figure 7.54). The value obtained by this fit is found to be in excellent agreement with the one obtained by treating both ΔS and Γ as free parameters (Table 7.7).

Equation 7.3 is a continuous mathematical equation. Therefore, in the case of the monoclinic polymorph, which exhibits a gradual transition, the fitting of the data is straightforward; however, this is not the case for the orthorhombic polymorph, which exhibits an abrupt and discontinuous transition. As a consequence, a fit using both ΔS and Γ as free parameters cannot be performed. To address this issue, the value of ΔS was fixed to the reported value deduced from previous DSC measurements [33]. With ΔS fixed, the only variable parameter left in Equation 7.3 for the orthorhombic polymorph is then the cooperativity Γ.

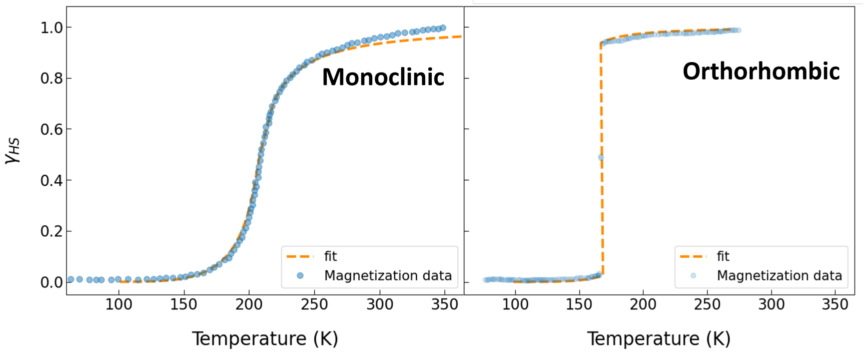

Figure 7.52: Temperature dependence of the γ_{HS} fraction, calculated from the magnetic susceptibility measurement for the monoclinic **(a)** and the orthorhombic **(b)** polymorph. The experimental magnetization data are shown in blue circles. The dashed orange line represents the fit according to the Slichter and Drickamer model (Equation 7.3).

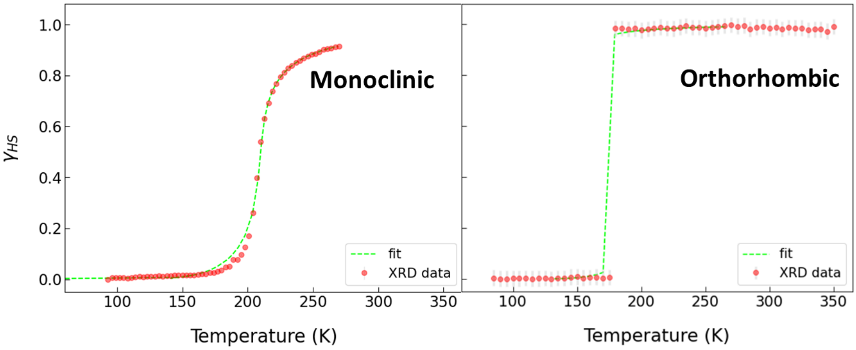

Figure 7.53: Temperature dependence of the γ_{HS} fraction, calculated from the $Fe-N$ bond lengths for the monoclinic **(a)** and orthorhombic **(b)** polymorphs. The data derived from the synchrotron single crystal structure data are shown by red circles. The dashed line line represents the fit corresponding to the Slichter and Drickamer model (Equation 7.3).

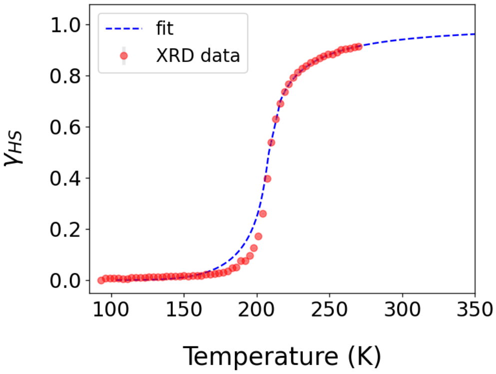

Figure 7.54: Temperature dependence of the γ_{HS} fraction, derived from the crystal structure data for the monoclinic polymorph, fitted with the Slichter and Drickamer model. The ΔS value was fixed to the values obtained from the DSC measurements.

The resulting parameters estimated from the Slichter and Drickamer model are summarized in Table 7.7. Estimated values for the entropy and enthalpy change are in good agreement with the values obtained from the DSC measurements. As expected, ΔS for both polymorphs is significantly larger than the entropy change resulting from the change in electronic entropy $\Delta S = \mathrm{Rln}[(2\mathrm{S}_{HS}+1)/(2\mathrm{S}_{LS}+1)] = 13.4\,\mathrm{J\,mol^{-1}\,K^{-1}}$ (for $S_{HS} = 2$, and $S_{LS} = 0$). The excess of entropy corresponds mainly to the vibrational, configurational, and rotational entropy changes [255].

According to the classification given by comparison of Γ with $2RT_{1/2}$ (see Section 4.5.3 for more details), the values of Γ and $T_{1/2}$ for the monoclinic and orthorhombic fall within the respective ranges, which indicate the nature of the spin crossover transitions. In the monoclinic polymorph, Γ is less than $2RT_{1/2}$ ($3.1\,\mathrm{k\,J\,mol^{-1}} < 3.46\,\mathrm{k\,J\,mol^{-1}}$), in which the gradual transition is consistent with weak cooperative interactions. On the other hand, for the orthorhombic polymorph, the abrupt transition aligns with strong cooperative interactions, as Γ is greater than $2RT_{1/2}$ ($5.01\,\mathrm{k\,J\,mol^{-1}} > 2.94\,\mathrm{k\,J\,mol^{-1}}$).

Table 7.7: $T_{1/2}$ (transition temperature) and thermodynamic parameters (ΔS, ΔH, Γ, and $2RT_{1/2}$) for the monoclinic and orthorhombic polymorphs as derived from crystal structure data, magnetization data, and DSC calorimetry measurements by fitting the data to the Slichter–Drickamer model.

	Thermodynamics values	ΔS ($\mathrm{J\,mol^{-1}\,K^{-1}}$)	ΔH ($\mathrm{k\,J\,mol^{-1}}$)	$T_{1/2}$ (K)	Γ ($\mathrm{k\,J\,mol^{-1}}$)	$2\mathrm{R}T_{1/2}$ ($\mathrm{k\,J\,mol^{-1}}$)
Monoclinic	Magnetization	47.3(1)	9.9(1)	208.3(9)	2.6(3)	3.46(9)
	DSC	48(3)	10.2(9)	208.5(5)	2.85(2)	
	Crystal Structure	46.3(5)	9.7(7)	209.8(2)	3.1(2)	
Orthorhombic	Crystal Structure	59 [33]	10 [33]	177.0(5)	5.01 (1)	2.94(5)

Chapter 8

Conclusion and Outlook

The main findings of this thesis, which are based on diffraction measurements, measurement of magnetic properties, and DSC investigations on both polymorphs of the [Fe(Pm-Bia)$_2$(NCS)$_2$], are:

- The orthorhombic polymorph exhibits a sharp temperature-induced HS-LS transition in a very narrow temperature interval of 1 K. Upon applying pressure at room temperature, it does not experience any spin transition to the LS state, yet at 2.02 GPa, a superstructure emerges. The pressure-induced superstructure does not appear to be a simple modified structure of the orthorhombic polymorph. The monoclinic polymorph exhibits a gradual temperature-induced HS-LS transition over a wide temperature interval (100 K). Upon applying pressure up to 1.36 GPa at room temperature, it shows an incomplete HS-LS transition.

- The monoclinic polymorph exhibits several anomalies (in e.g., lattice parameters, torsion angles, $C \cdots C$ bond lengths, and ADP's) in the temperature range of the HS-LS transition, which are absent in the orthorhombic polymorph.

- Both polymorphs show reproducible transitions in their magnetic and thermal properties. Structural investigations on cycling show excellent reproducibility for the orthorhombic polymorph. However, the monoclinic polymorph shows clear signs of radiation damage up on cycling in the scattering experiments.

- The behaviour of the thermal hysteresis upon varying the scan rate depends on the grain size (polycrystalline versus single crystal). A novel scan rate-dependent intermediate state of the orthorhombic polymorph for polycrystalline sample on heating is visible in the magnetization data.

- Diffraction experiments show that the intermediate state observed with slow scan rates and the superstucture observed under pressure for the orthorhombic polymorph can both be indexed as supercells with a doubled c-lattice parameter. It can thus be speculated that the orthorhombic polymorph has a similar structural transformation in response to the slow scan rates and to pressure.

- The microstructure within the abrupt transition of the orthorhombic polymorph is characterized by the formation and coexistence of domains in the HS- and LS- states. On the other hand, the gradual transition of the monoclinic polymorph is most probably due to a random distribution of HS and LS Fe centers throughout the lattice.

- In the thermally induced spin transition of the monoclinic polymorph, $\pi - \pi$ interactions are present in both spin states, while H-bonding is observed only in the low spin state. In the orthorhombic polymorph, H-bonding is present both in the HS and in the LS states. Under pressure, for the monoclinic polymorph, $\pi - \pi$ interactions persist, and H-bonding starts to form at a pressure of 0.36 GPa. In the orthorhombic polymorph, no $\pi - \pi$ interactions are observed under pressure, and only H-bonding is present.
- We attribute the resilience of the orthorhombic polymorph to radiation exposure and the formation of HS and LS domains in the thermal transition to the H-bonding network. The absence of these strong interactions in the monoclinic polymorph results in radiation damage and in random HS/LS entities.
- We assume the following relation between intermolecular interactions and the cooperativity which determines the nature of the HS-LS transition: in the monoclinic polymorph, the presence of $\pi - \pi$ interactions leads to smearing out the transition over a wide range of temperatures. The $\pi - \pi$ interaction effect persists under pressure, helping the system to undergo a spin transition to the low spin state. However, the emergence of H-bonding under pressure presumably hinders the completion of the spin transition to the LS state. For the orthorhombic polymorph, the presence of H-bonds triggers the sharp temperature-induced HS-LS transition. However, we believe that at high pressures, (where the volume is compressed and less space is available), the H-bonds sterically hinder the HS-LS transition, which would limit the available space even more. At a critical pressure of 2.02 GPa, a severe modification occurs in the H-bonding, resulting in the formation of a superstructure.
- Entropy and enthalpy change, as well as cooperativity, Γ, for the temperature-induced HS-LS transition in both polymorphs were obtained within the framework of Slichter and Drickamer model. The values of ΔS are significantly larger than the entropy variation resulting from the change of spin state. Obtained values for cooperativity reflect the relationship, small $\Gamma \longleftrightarrow$ weak interactions, $\longleftrightarrow$ gradual transition, and large $\Gamma \longleftrightarrow$ strong interactions, $\longleftrightarrow$ abrupt transition, respectively.
- The monoclinic polymorph might be a potential candidate for barocaloric application as it shows a transition to the LS state at room temperature by applying relatively low pressure, albeit only incomplete. The orthorhombic polymorph, on the other hand, does not seem to be suitable as up to 2 GPa, the HS-LS transition is not observed.

Based on our findings, several approaches for further investigation are suggested:

▻ **Determination of the superstructure(s):**
The pressure and scan rate-induced superstructures of the orthorhombic polymorph have to be determined to gain insight on the behaviour of the crystal structures and, in particular, the role of the H-bonding in the transition to the superstructure.

- ▻ **Structure - Property - dynamic relation:**
  The investigations presented here are focused on the relation between the structures and properties of the two polymorphs and neglect the role of dynamics. To elucidate the dynamic of the system, vibrational spectroscopy experiments (which would also elucidate the contribution of the vibrational entropy) and inelastic scattering experiments are warranted.

- ▻ **Verification of H-bonding hypothesis:**
  The utilization of deuterated samples would lead to an expansion of the lattice due to the larger size of deuterium in comparison to hydrogen. This expansion would provide additional space in the structure and could drastically change the behaviour observed under pressure. Substituting sulfur within the thiocayanate group with larger atoms like selenium could have similar effects.

Reflecting on our findings and our (hypothetical) interpretation of them, we suggest to look for potential SCO candidates for barocaloric applications that combine strong intermolecular interactions (as they lead to large cooperativity and sharp transitions) with open structures so that the volume change produced by pressure and the HS/LS spin transition can be accommodated and the pressure-induced transition is not hindered by space restrictions.

Bibliography

[1] International Energy Agency (IEA). The Future of Cooling - Analysis and key findings. A report by the International Energy Agency. `https://www.iea.org/reports/thefuture-of-cooling`, May 2018. Accessed Sep. 10, 2023.

[2] M. Santamouris. Cooling the buildings – past, present and future. *Energy and Buildings*, 128:617–638, 2016. `https://doi.org/10.1016/j.enbuild.2016.07.034`.

[3] W. Goetzler, R. Shandross, J. Young, O. Petritchenko, D. Ringo, and S. McClive. Energy savings potential and RD&D opportunities for commercial building HVAC systems. Technical report, Navigant Consulting, Burlington, MA (United States), 2017.

[4] S. Qian, D. Nasuta, A. Rhoads, Y. Wang, Y. Geng, Y. Hwang, R. Radermacher, and I. Takeuchi. Not-in-kind cooling technologies: A quantitative comparison of refrigerants and system performance. *International Journal of Refrigeration*, 62:177–192, 2016. `https://doi.org/10.1016/j.ijrefrig.2015.10.019`.

[5] X. Moya, S. Kar-Narayan, and N.D. Mathur. Caloric materials near ferroic phase transitions. *Nature Materials*, 13(5):439–450, 2014. `https://doi.org/10.1038/nmat3951`.

[6] S. Fähler, U.K. Rößler, O. Kastner, J. Eckert, G. Eggeler, H. Emmerich, P. Entel, S. Müller, E. Quandt, and K. Albe. Caloric effects in ferroic materials: new concepts for cooling. *Advanced Engineering Materials*, 14(1-2):10–19, 2012. `https://doi.org/10.1002/ente.201800201`.

[7] V.K. Pecharsky and K.A Gschneidner. Giant magnetocaloric effect in $Gd_5(Si_2Ge_2)$. *Physical Review Letters*, 78(23):4494, 1997. `https://doi.org/10.1103/PhysRevLett.78.4494`.

[8] A.S. Mischenko, Q. Zhang, J.F Scott, R.W. Whatmore, and N.D. Mathur. Giant electrocaloric effect in thin-film $PbZr_{0.95}Ti_{0.05}O_3$. *Science*, 311(5765):1270–1271, 2006. `https://doi.org/10.1126/science.1123811`.

[9] E. Bonnot, R. Romero, L. Mañosa, E. Vives, and A. Planes. Elastocaloric effect associated with the martensitic transition in shape-memory alloys. *Physical Review Letters*, 100(12):125901, 2008. `https://doi.org/10.1103/PhysRevLett.100.125901`.

[10] T. Strässle, A. Furrer, P. Lacorre, and L.A. Müller. A novel principle for

cooling by adiabatic pressure application in rare-earth compounds. *Journal of Alloys and Compounds*, 303:228–231, 2000. `https://doi.org/10.1016/S0925-8388(00)00662-9`.

[11] L. Mañosa and A. Planes. Materials with giant mechanocaloric effects: cooling by strength. *Advanced Materials*, 29(11):1603607, 2017. `https://doi.org/10.1002/adma.201603607`.

[12] I.A. Stepanov. Entropy change in materials under compression and expansion. *Materials Letters*, 234:38–39, 2019. `https://doi.org/10.1016/j.matlet.2018.09.052`.

[13] K.A. Müller, F. Fauth, S. Fischer, M. Koch, A. Furrer, and P. Lacorre. Cooling by adiabatic pressure application in $Pr_{1-x}La_xNiO_3$. *Applied Physics Letters*, 73 (8):1056–1058, 1998. `https://doi.org/10.1016/S0921-4526(99)01288-0`.

[14] H. Yamada, K. Fukamichi, and T. Goto. Itinerant-electron metamagnetism and strong pressure dependence of the Curie temperature. *Physical Review B*, 65(2):024413, 2001. `https://doi.org/10.1103/PhysRevB.65.024413`.

[15] S. Gama, A.A. Coelho, A. de Campos, A.M.G. Carvalho, F.C.G. Gandra, P.J. Von Ranke, and N.A. de Oliveira. Pressure-induced colossal magnetocaloric effect in MnAs. *Physical Review Letters*, 93(23):237202, 2004. `https://doi.org/10.1103/PhysRevLett.93.237202`.

[16] L. Morellon, Z. Arnold, C. Magen, C. Ritter, O. Prokhnenko, Y. Skorokhod, P.A. Algarabel, M.R. Ibarra, and J. Kamarad. Pressure Enhancement of the Giant Magnetocaloric Effect in $Tb_5Si_2Ge_2$. *Physical Review Letters*, 93(13): 137201, 2004. `https://doi.org/10.1103/PhysRevLett.93.137201`.

[17] L. Mañosa, D. González-Alonso, A. Planes, E. Bonnot, M. Barrio, J.L. Tamarit, S. Aksoy, and M. Acet. Giant solid-state barocaloric effect in the Ni-Mn-In magnetic shape-memory alloy. *Nature Materials*, 9(6):478–481, 2010. `https://doi.org/10.1038/nmat2731`.

[18] S. Yuce, M. Barrio, B. Emre, E. Stern-Taulats, A. Planes, J.L. Tamarit, Y. Mudryk, K.A. Gschneidner, V.K. Pecharsky, and L. Mañosa. Barocaloric effect in the magnetocaloric prototype $Gd_5Si_2Ge_2$. *Applied Physics Letters*, 101(7), 2012. `https://doi.org/10.1063/1.4745920`.

[19] L. Mañosa, D. Gonzalez-Alonso, A. Planes, M. Barrio, J.L. Tamarit, I.S. Titov, M. Acet, A. Bhattacharyya, and S. Majumdar. Inverse barocaloric effect in the giant magnetocaloric La-Fe-Si-Co compound. *Nature Communications*, 2 (1):595, 2011. `https://doi.org/10.1038/ncomms1606`.

[20] B. Li, Y. Kawakita, S. Ohira-Kawamura, T. Sugahara, H. Wang, J. Wang, Y. Chen, S.I. Kawaguchi, S. Kawaguchi, and K. Ohara. Colossal barocaloric effects in plastic crystals. *Nature*, 567(7749):506–510, 2019. `https://doi.org/10.1038/s41586-019-1042-5`.

[21] J. Li, D. Dunstan, X. Lou, A. Planes, L. Mañosa, M. Barrio, J.L. Tamarit, and P. Lloveras. Reversible barocaloric effects over a large temperature span

in fullerite C_{60}. *Journal of Materials Chemistry A*, 8(39):20354–20362, 2020. `https://doi.org/10.1039/D0TA05399F`.

[22] A. Aznar, P. Lloveras, M. Romanini, M. Barrio, J.L. Tamarit, C. Cazorla, D. Errandonea, N.D. Mathur, A. Planes, and X. Moya. Giant barocaloric effects over a wide temperature range in superionic conductor AgI. *Nature Communications*, 8(1):1851, 2017. `https://doi.org/10.1038/s41467-017-01898-2`.

[23] P. Lloveras, E. Stern-Taulats, M. Barrio, J.L. Tamarit, S. Crossley, W. Li, V. Pomjakushin, A. Planes, L. Mañosa, and N.D. Mathur. Giant barocaloric effects at low pressure in ferrielectric ammonium sulphate. *Nature Communications*, 6(1):8801, 2015. `https://doi.org/10.1038/ncomms9801`.

[24] J.M. Bermúdez-García, M. Sánchez-Andújar, S. Castro-García, J. López-Beceiro, R. Artiaga, and M.A. Señarís-Rodríguez. Giant barocaloric effect in the ferroic organic-inorganic hybrid [TPrA][Mn(dca)$_3$] perovskite under easily accessible pressures. *Nature Communications*, 8(1):15715, 2017. `https://doi.org/10.1038/ncomms15715`.

[25] A.M.G. Carvalho, W. Imamura, E.O. Usuda, and N.M. Bom. Giant room-temperature barocaloric effects in PDMS rubber at low pressures. *European Polymer Journal*, 99:212–221, 2018. `https://doi.org/10.1016/j.eurpolymj.2017.12.007`.

[26] N.M. Bom, W. Imamura, E.O. Usuda, L.S. Paixão, and A.M.G. Carvalho. Giant barocaloric effects in natural rubber: a relevant step toward solid-state cooling. *ACS Macro Letters*, 7(1):31–36, 2018. `https://doi.org/10.1021/acsmacrolett.7b00744`.

[27] A. Aznar, P. Lloveras, M. Barrio, P. Negrier, A. Planes, L. Mañosa, N.D. Mathur, X. Moya, and J.L. Tamarit. Reversible and irreversible colossal barocaloric effects in plastic crystals. *Journal of Materials Chemistry A*, 8 (2):639–647, 2020. `https://doi.org/10.1039/C9TA10947A`.

[28] K.G. Sandeman. Research Update: The mechanocaloric potential of spin crossover compounds. *APL Materials*, 4(11), 2016. `https://doi.org/10.1063/1.4967282`.

[29] S.P. Vallone, N. Anthony A. Tantillo, A.M. Dos Santos, J.J. Molaison, R. Kulmaczewski, A. Chapoy, P. Ahmadi, M.A. Halcrow, and K.G. Sandeman. Giant barocaloric effect at the spin crossover transition of a molecular crystal. *Advanced Materials*, 31(23):1807334, 2019. `https://doi.org/10.1002/adma.201807334`.

[30] P.J. Von Ranke. A microscopic refrigeration process triggered through spin-crossover mechanism. *Applied Physics Letters*, 110(18), 2017. `https://doi.org/10.1063/1.4982792`.

[31] P.J. Von Ranke, B.P. Alho, and P.O. Ribeiro. First indirect experimental evidence and theoretical discussion of giant refrigeration capacity through the reversible pressure induced spin-crossover phase transition. *Journal of Alloys*

and Compounds, 749:556–560, 2018. `https://doi.org/10.1016/j.jallcom.2018.03.315`.

[32] Y. Otsuki, S. Kimura, S. Awaji, and M. Nakano. Magnetocapacitance effect and magnetostriction by the field-induced spin-crossover in [MnIII (taa)]. *AIP Advances*, 9(8), 2019. `https://doi.org/10.1063/1.5097891`.

[33] J.F. Létard, P. Guionneau, L. Rabardel, J.A.K. Howard, A.E. Goeta, D. Chasseau, and O. Kahn. Structural, magnetic, and photomagnetic studies of a mononuclear iron (II) derivative exhibiting an exceptionally abrupt spin transition. Light-induced thermal hysteresis phenomenon. *Inorganic Chemistry*, 37(17):4432–4441, 1998. `https://doi.org/10.1021/ic980107b`.

[34] V. Ksenofontov, G. Levchenko, H. Spiering, P. Gütlich, J.F. Létard, Y. Bouhedja, and O. Kahn. Spin crossover behavior under pressure of Fe (PM-L)$_2$ (NCS)$_2$ compounds with substituted 2′-pyridylmethylene 4-anilino ligands. *Chemical Physics Letters*, 294(6):545–553, 1998. `https://doi.org/10.1016/S0009-2614(98)00901-4`.

[35] H.J. Shepherd, I.A. Gural'skiy, C.M. Quintero, S. Tricard, L. Salmon, G. Molnár, and A. Bousseksou. Molecular actuators driven by cooperative spin-state switching. *Nature Communications*, 4(1):2607, 2013. `https://doi.org/10.1038/ncomms3607`.

[36] P. Gütlich, Y. Garcia, and H.A. Goodwin. Spin crossover phenomena in Fe (ii) complexes. *Chemical Society Reviews*, 29(6):419–427, 2000. `https://doi.org/10.1039/B003504L`.

[37] M. Marchivie, P. Guionneau, J.F. Létard, and D. Chasseau. Towards direct correlations between spin-crossover and structural features in iron (II) complexes. *Acta Crystallographica Section B: Structural Science, Crystal Engineering and Materials*, 59(4):479–486, 2003. `https://doi.org/10.1107/S0108768103011200`.

[38] P. Guionneau, C. Brigouleix, Y. Barrans, A.E. Goeta, J.F. Létard, J.A.K. Howard, J. Gaultier, and D. Chasseau. High pressure and very low temperature effects on the crystal structures of some iron (II) complexes. *Comptes Rendus de l'Académie des Sciences-Series IIC-Chemistry*, 4(2):161–171, 2001. `https://doi.org/10.1016/S1387-1609(00)01193-2`.

[39] L. Cambi and L. Szegö. Über die magnetische Susceptibilität der komplexen Verbindungen. *Berichte der Deutschen Chemischen Gesellschaft (A and B Series)*, 64(10):2591–2598, 1931. `https://doi.org/10.1002/cber.19310641002`.

[40] L. Cambi and L. Szegö. Über die magnetische Susceptibilität der komplexen Verbindungen (II. mitteil.). *Berichte der Deutschen Chemischen Gesellschaft (A and B Series)*, 66(5):656–661, 1933. `https://doi.org/10.1002/cber.19330660508`.

[41] L. Cambi and L. Malatesta. Magnetismus und Polymorphie innerer Kom-

plexsalze: Eisensalze der Dithiocarbamidsäuren. *Berichte der Deutschen Chemischen Gesellschaft (A and B Series)*, 70(10):2067–2078, 1937. `https://doi.org/10.1002/cber.19370701006`.

[42] A.H. White, R. Roper, E. Kokot, H. Waterman, and R.L. Martin. The anomalous paramagnetism of iron (III) NN-dialkyldithiocarbamates. *Australian Journal of Chemistry*, 17(3):294–303, 1964. `https://doi.org/10.1071/CH9640294`.

[43] J. Baker and H.M. Bobonich. Magnetic properties of some high-spin complexes of iron (II). *Inorganic Chemistry*, 3(8):1184–1188, 1964. `https://doi.org/10.1021/ic50018a027`.

[44] E. König and K. Madeja. Unusual magnetic behaviour of some iron (II)–bis-(1, 10-phenanthroline) complexes. *Chemical Communications*, 9(3):61–62, 1966. `https://doi.org/10.1039/C19660000061`.

[45] K. Madeja and E. König. Zur Frage der Bindungsverhältnise in Komplexverbindungen des Eisen (II) mit 1, 10-phenanthrolin. *Journal of Inorganic and Nuclear Chemistry*, 25(4):377–385, 1963. `https://doi.org/10.1016/0022-1902(63)80188-8`.

[46] E. König, S. Hüfner, E. Steichele, and K. Madeja. Mössbauer effect studies on iron(II) bis(α-diimine) complexes. *Journal for Natural Research A*, 22(10):1543–1550, 1967. `https://doi.org/10.1515/zna-1967-1013`.

[47] E. König and S. Kremer. Exact spin-pairing energies at the crossovers in octahedral d^4, d^5, d^6, and d^7 transition metal complexes. *Theoretica Chimica Acta*, 23(1):12–20, 1971. `https://doi.org/10.1007/BF00530196`.

[48] P. Gütlich, H.A. Goodwin, A. Bousseksou, F. Varret, M. Goiran, K. Boukheddaden, and J.P. Tuchagues. The spin crossover phenomenon under high magnetic field. Spin Crossover in Transition Metal Compounds III. *Topics in Current Chemistry*, 235:65–84, 2004.

[49] P. Gütlich, P.J. Koningsbruggen, and F. Renz. Recent Advances of Spin Crossover Research. In T. Schönherr, editor, *Optical Spectra and Chemical Bonding in Transition Metal Complexes*. Springer Berlin Heidelberg, 2004. ISBN 978-3-540-36571-6.

[50] O. Kahn. Spin-crossover molecular materials. *Current Opinion in Solid State and Materials Science*, 1(4):547–554, 1996. `https://doi.org/10.1016/S1359-0286(96)80070-2`.

[51] P. Gütlich and H.A. Goodwin. *Spin crossover in transition metal compounds I*, volume 233. Springer Science & Business Media, 2004. ISBN 978-3-540-40395-1.

[52] M.A. Halcrow. *Spin-crossover materials: properties and applications, 1st ed.* John Wiley & Sons, 2013. ISBN 1-119-99867-0.

[53] P. Gütlich, V. Ksenofontov, and A.B. Gaspar. Pressure effect studies on spin

crossover systems. *Coordination Chemistry Reviews*, 249(17-18):1811–1829, 2005. `https://doi.org/10.1016/j.ccr.2005.01.022`.

[54] V. Ksenofontov, A.B. Gaspar, and P. Gütlich. Pressure effect studies on spin crossover and valence tautomeric systems, Spin Crossover in Transition Metal Compounds III. *Topics in Current Chemistry*, 235:23–64, 2004.

[55] S. Decurtins, P. Gütlich, C.P. Köhler, H. Spiering, and A. Hauser. Light-induced excited spin state trapping in a transition-metal complex: The hexa-1-propyltetrazole-iron (II) tetrafluoroborate spin-crossover system. *Chemical Physics Letters*, 105(1):1–4, 1984. `https://doi.org/10.1016/0009-2614(84)80403-0`.

[56] N. Baadji, M. Piacenza, T. Tugsuz, F.D. Salaand G. Maruccio, and S. Sanvito. Electrostatic spin crossover effect in polar magnetic molecules. *Nature Materials*, 8(10):813–817, 2009. `https://doi.org/10.1038/nmat2525`.

[57] O. Kahn, J. Kröber, and C. Jay. Spin transition molecular materials for displays and data recording. *Advanced Materials*, 4(11):718–728, 1992. `https://doi.org/10.1002/adma.19920041103`.

[58] O. Kahn and C.J. Martinez. Spin-transition polymers: from molecular materials toward memory devices. *Science*, 279(5347):44–48, 1998. `https://doi.org/10.1126/science.279.5347.44`.

[59] J.F. Létard, G. Chastanet, O. Nguyen, S. Marcén, M. Marchivie, P. Guionneau, D. Chasseau, and P. Gütlich. Spin crossover properties of the [Fe (PM-BiA)$_2$ (NCS)$_2$] complex–Phases I and II. *Monatshefte für Chemie/Chemical Monthly*, 134(2):165–182, 2003. `https://doi.org/10.1007/s00706-002-0537-0`.

[60] V. Ksenofontov, A.B. Gaspar, G. Levchenko, B. Fitzsimmons, and P. Gütlich. Pressure effect on spin crossover in [Fe (phen)$_2$ (NCS)$_2$] and [CrI$_2$ (depe)$_2$]. *The Journal of Physical Chemistry B*, 108(23):7723–7727, 2004. `https://doi.org/10.1021/jp049512g`.

[61] A. Hauser. Ligand field theoretical considerations. Spin Crossover in Transition Metal Compounds I. *Topics in Current Chemistry*, 233:49–58, 2004.

[62] R.G. Miller, S. Narayanaswamy, J.L. Tallon, and S. Brooker. Spin crossover with thermal hysteresis in cobalt (II) complexes and the importance of scan rate. *New Journal of Chemistry*, 38(5):1932–1941, 2014. `https://doi.org/10.1039/C3NJ01451G`.

[63] P. Gütlich, M.J. Clarke, J.B. Goodenough, P. Hemmerich, J.A. Ibers, C.K. Jörgensen, J. B. Neilands, D. Reinen, R. Weiss, and R.J.P. Williams. *Spin crossover in iron (II)-complexes. Structure Bonding*, volume 44. Springer, 1981. ISBN 978-3-540-38499-1.

[64] W. Klaeui, W. Eberspach, and P. Gütlich. Spin-crossover cobalt (III) complexes: steric and electronic control of spin state. *Inorganic Chemistry*, 26 (24):3977–3982, 1987. `https://doi.org/10.1021/ic00271a004`.

[65] D.M. Halepoto, D.G.L. Holt, L.F. Larkworthy, G.J. Leigh, D.C. Povey, and G.W. Smith. Spin crossover in chromium (II) complexes and the crystal and molecular structure of the high spin form of bis [1, 2-bis (diethylphosphino) ethane] di-iodochromium (II). *Journal of the Chemical Society, Chemical Communications*, 5(18):1322–1323, 1989. `https://doi.org/10.1039/C39890001322`.

[66] P. Gütlich, B.R. McGarvey, and W. Klaeui. Temperature-dependent $^5T_2$ (O_h) $\leftrightarrow$ 1^A_1 (O_h) spin equilibrium in a six-coordinate cobalt (III) complex. Investigation by phosphorus-31 NMR in solution. *Inorganic Chemistry*, 19(12): 3704–3706, 1980. `https://doi.org/10.1021/ic50214a026`.

[67] J.H. Ammeter, R. Bucher, and N. Oswald. High-spin-low-spin equilibrium of manganocene and dimethylmanganocene. *Journal of the American Chemical Society*, 96(25):7833–7835, 1974. `https://doi.org/10.1021/ja00832a049`.

[68] P. Gütlich, H.A. Goodwin, Y. Garcia, and P. Gütlich. Thermal Spin Crossover in Mn(II), Mn(II), Cr(II) and Co(II) Coordination Compounds. Spin Crossover in Transition Metal Compounds II. *Topics in Current Chemistry*, 234:49–62, 2004.

[69] M.A. Robinson, J.D. Curry, and D.H. Busch. Complexes Derived from Strong Field Ligands. XVII. Electronic Spectra of Octahedral Nickel (II) Complexes with Ligands of the α-Diimine and Closely Related Classes. *Inorganic Chemistry*, 2(6):1178–1181, 1963. `https://doi.org/10.1021/ic50010a021`.

[70] M.H. Chisholm, E.M. Kober, D.J. Ironmonger, and P. Thornton. Bis (2, 2'-bipyridyl) diisopropoxomolybdenum (II): a spin-state equilibrium for a complex of a second-row transition element. *Polyhedron*, 4(11):1869–1874, 1985. `https://doi.org/10.1016/S0277-5387(00)86703-0`.

[71] P. Gütlich, H.A. Goodwin, A. Bousseksou, F. Varret, M. Goiran, K. Boukheddaden, and J.P. Tuchagues. Bipyrimidine-bridged dinuclear iron (II) spin crossover compounds. Spin Crossover in Transition Metal Compounds I. *Topics in Current Chemistry*, 233:1869–1874, 2004.

[72] A. Bousseksou, G. Molnár, J.A. Real, and K. Tanaka. Spin crossover and photomagnetism in dinuclear iron (II) compounds. *Coordination Chemistry Reviews*, 251(13-14):1822–1833, 2007. `https://doi.org/10.1016/j.ccr.2007.02.023`.

[73] R. Clerac, F.A. Cotton, L.M. Daniels, K.R. Dunbar, C.A. Murillo, and X. Wang. Tuning the Metal- Metal Bonds in the Linear Tricobalt Compound Co_3 $(dpa)_4Cl_2$: Bond-Stretch and Spin-State Isomers. *Inorganic Chemistry*, 40(6):1256–1264, 2001. `https://doi.org/10.1021/ic001068i`.

[74] M. Ruben, E. Breuning, J.-M.Lehn, V. Ksenofontov, F. Renz, P. Gütlich, and G.BM. Vaughan. Supramolecular spintronic devices: spin transitions and magnetostructural correlations in $[Fe^{II}_4L_4]^{8+}$[2× 2]-grid-type complexes. *Chemistry–A European Journal*, 9(18):4422–4429, 2003. `https://doi.org/10.1002/chem.200304933`.

[75] M.C. Mũnoz and J.A. Real. Thermo-, piezo-, photo-and chemo-switchable spin crossover iron (II)-metallocyanate based coordination polymers. *Coordination Chemistry Reviews*, 255(17-18):2068–2093, 2011. `https://doi.org/10.1016/j.ccr.2011.02.004`.

[76] J.D. Dunitz and J. Bernstein. Disappearing polymorphs. *Accounts of Chemical Research*, 28(4):193–200, 1995. `https://doi.org/10.1021/ar00052a005`.

[77] J. Bernstein. *Polymorphism in Molecular Crystals 2e*, volume 30. International Union of Crystallography, 2020. ISBN 978-0-19-965544-1.

[78] D. Pogoda, J. Janczak, and V. Videnova-Adrabinska. New polymorphs of an old drug: Conformational and synthon polymorphism of 5-nitrofurazone. *Acta Crystallographica Section B: Structural Science, Crystal Engineering and Materials*, 72(2):263–273, 2016. `https://doi.org/10.1107/S2052520615024956`.

[79] S.A. Moggach, S. Parson, and P.A. Wood. High-pressure polymorphism in amino acids. *Crystallography Reviews*, 14(2):143–184, 2008. `https://doi.org/10.1080/08893110802037945`.

[80] A.V. Trask, W.D. S. Motherwell, and W. Jones. Solvent-drop grinding: green polymorph control of cocrystallisation. *Chemical Communications*, 7(2):890–891, 2004. `https://doi.org/10.1039/B400978A`.

[81] B.A. Zakharov, E.A. Losev, and E.V. Boldyreva. Polymorphism of “glycine–glutaric acid” co-crystals: the same phase at low temperatures and high pressures. *CrystEngComm*, 15(9):1693–1697, 2013. `https://doi.org/10.1039/C3CE27013K`.

[82] L.H. Thomas, C. Wales, L. Zhao, and C.C. Wilson. Paracetamol form I: an elusive polymorph through facile multicomponent crystallization routes. *Crystal Growth and Design*, 11(5):1450–1452, 2011. `https://doi.org/10.1021/cg2002018`.

[83] J. Bauer, S. Spanton, R. Henry, J. Quick, W. Dziki, W.Porter, and J. Morris. Ritonavir: an extraordinary example of conformational polymorphism. *Pharmaceutical Research*, 18:859–866, 2001. `https://doi.org/10.1023/A:1011052932607`.

[84] S.Aitipamula, P.S. Chow, and R.B.H. Tan. Polymorphism in cocrystals: a review and assessment of its significance. *CrystEngComm*, 16(17):3451–3465, 2014. `https://doi.org/10.1039/C3CE42008F`.

[85] A. Nangia and G. Desiraju. Supramolecular structures–reason and imagination. *Acta Crystallographica Section A: Foundations of Crystallography*, 54(6):934–944, 1998. `https://doi.org/10.1107/S0108767398008551`.

[86] A.D. Bond, D.A. Haynes, C.M. Pask, and J.M. Rawson. Concomitant polymorphs: structural studies on the trimorphic dithiadiazolyl radical, ClCNSSN. *Dalton Transactions*, 12:2522–2531, 2002. `https://doi.org/10.1039/B110922G`.

[87] E. König and K.Madeja. $^5T_2$-$^1A_1$ Equilibriums in some iron (II)-bis (1, 10-phenanthroline) complexes. *Inorganic Chemistry*, 6(1):48–55, 1967. `https://doi.org/10.1021/ic50047a011`.

[88] E. König, K. Madeja, and K.J. Watson. Reversible quintet-singlet transition in dithiocyanato-bis (2, 2'-dipyridyl) iron (II). *Journal of the American Chemical Society*, 90(5):1146–1153, 1968. `https://doi.org/10.1021/ja01007a010`.

[89] R.J. Wei, B. Li, J. Tao, R.B. Huang, L.S. Zheng, and Z. Zheng. Making spin-crossover crystals by successive polymorphic transformations. *Inorganic Chemistry*, 50(4):1170–1172, 2011. `https://doi.org/10.1021/ic102231j`.

[90] C.F. Sheu, K. Chen, S.M. Chen, Y.S. Wen, G.H. Lee, J.M Chen, J.F. Lee, B.M. Cheng, H.S. Sheu, and N. Yasuda. Structure and electronic configuration of an iron (II) complex in a LIESST state: a pump and probe method. *Chemistry–A European Journal*, 15(10):2384–2393, 2009. `https://doi.org/10.1002/chem.200802279`.

[91] D.L. Reger, J.R. Gardinier, M.D. Smith, A.M. Shahin, L.G. Long, L. Rebbouh, and F. Grandjean. Polymorphism in Fe [(p-IC$_6$H$_4$) B (3-Mepz)$_3$]$_2$ (pz= Pyrazolyl): Impact of Supramolecular Structure on an Iron (II) Electronic Spin-State Crossover. *Inorganic Chemistry*, 44(6):1852–1866, 2005. `https://doi.org/10.1021/ic048406q`.

[92] A.B. Gaspar, M. Carmen Muñoz, N. Moline, V. Ksenofontov, G. Levchenko, P. Gütlich, and J.A. Real. Polymorphism and pressure driven thermal spin crossover phenomenon in [Fe(abpt)$_2$ (NCX)$_2$](X= S, and Se): Synthesis, structure and magnetic properties. *Monatshefte für Chemie/Chemical Monthly*, 134:285–294, 2003. `https://doi.org/10.1039/C1CS15136C`.

[93] B. Weber, E. Kaps, C. Desplanches, and J.F. Létard. Quenching the hysteresis in single crystals of a 1D chain iron (II) spin crossover complex. *European Journal of Inorganic Chemistry*, 19:2963–2966, 2008. `https://doi.org/10.1002/ejic.200800391`.

[94] K. Takahashi, M. Okai, T. Mochida, T. Sakurai, H. Ohta, T. Yamamoto, Y. Einaga, Y. Shiota, K. Yoshizawa, and H. Konaka. Contribution of Coulomb Interactions to a Two-Step Crystal Structure Phase Transformation Coupled with a Significant Change in Spin Crossover Behavior for a Series of Charged Fe^{II} Complexes from 2, 6-Bis (2-methylthiazol-4-yl) pyridine. *Inorganic Chemistry*, 57(3):1277–1287, 2018. `https://doi.org/10.1021/acs.inorgchem.7b02721`.

[95] P. Guionneau, J.F. Létard, D.S. Yufit, D. Chasseau, G. Bravic, A.E. Goeta, J.A.K. Howard, and O. Kahn. Structural approach of the features of the spin crossover transition in iron (II) compounds. *Journal of Materials Chemistry*, 9(4):985–994, 1999. `https://doi.org/10.1039/A808075E`.

[96] J.A. Real, A.B. Gaspar, V. Niel, and M.C. Muñoz. Communication between iron (II) building blocks in cooperative spin transition phenomena. *Coordination Chemistry Reviews*, 236(1-2):121–141, 2003. `https://doi.org/10.1016/S0010-8545(02)00220-5`.

[97] F.X. Shen, Q. Pi, L. Shi, D. Shao, H.Q. Li, Y.C. Sun, and X.Y. Wang. Spin crossover in hydrogen-bonded frameworks of Fe II complexes with organodisulfonate anions. *Dalton Transactions*, 48(24):8815–8825, 2019. `https://doi.org/10.1039/C9DT01326A`.

[98] N. Willenbacher and H. Spiering. The elastic interaction of high-spin and low-spin complex molecules in spin-crossover compounds. *Journal of Physics C: Solid State Physics*, 21(8):1423, 1988. `https://doi.org/10.1088/0022-3719/21/8/017`.

[99] H. Spiering, E. Meissner, H. Köppen, E.W. Müller, and P. Gütlich. The effect of the lattice expansion on high spin $\Longleftrightarrow$ low spin transitions. *Chemical Physics*, 68(1-2):65–71, 1982. `https://doi.org/10.1016/0301-0104(82)85080-5`.

[100] M. Nishino, C. Enachescu, and S. Miyashita. Multistep spin-crossover transitions induced by the interplay between short-and long-range interactions with frustration on a triangular lattice. *Physical Review B*, 100(13):134414, 2019. `https://doi.org/10.1103/PhysRevB.100.134414`.

[101] H. Spiering and N. Willenbacher. Elastic interaction of high-spin and low-spin complex molecules in spin-crossover compounds. II. *Journal of Physics: Condensed Matter*, 1(50):10089, 1989. `https://doi.org/10.1088/0953-8984/1/50/011`.

[102] S. Lakhloufi, M. Lemée-Cailleau, G. Chastanet, P. Rosa, N. Daro, and P. Guionneau. Structural movies of the gradual spin-crossover in a molecular complex at various physical scales. *Physical Chemistry Chemical Physics*, 18 (40):28307–28315, 2016. `https://doi.org/10.1039/C6CP04987G`.

[103] M. Buron-Le Cointe, J. Hebert, C. Baldé, N. Moisan, L. Toupet, P. Guionneau, J.F. Letard, E. Freysz, H. Cailleau, and E. Collet. Intermolecular control of thermoswitching and photoswitching phenomena in two spin-crossover polymorphs. *Physical Review B*, 85(6):064114, 2012. `https://doi.org/10.1103/PhysRevB.85.064114`.

[104] V. Legrand, C. Carbonera, S. Pillet, M. Souhassou, J.F. Létard, P. Guionneau, and C. Lecomte. Photo-crystallography: from the structure towards the electron density of metastable states. In *Journal of Physics: Conference Series*, volume 21, page 73. IOP Publishing, 2005. `https://doi.org/10.1088/1742-6596/21/1/012`.

[105] P. Guionneau, F. Le Gac, S. Lakhoufi, A. Kaiba, D. Chasseau, F.J. Létard, P. Négrier, D. Mondieig, J.A.K. Howard, and J.M. Léger. X-ray diffraction investigation of a spin crossover hysteresis loop. *Journal of Physics: Condensed Matter*, 19(32):326211, 2007. `https://doi.org/10.1088/0953-8984/19/32/326211`.

[106] S. Pillet, J. Hubsch, and C. Lecomte. Single crystal diffraction analysis of the thermal spin conversion in [Fe $(\mathrm{btr})_2(\mathrm{NCS})_2](\mathrm{H}_2\mathrm{O})$: evidence for spin-like domain formation. *The European Physical Journal B-Condensed Matter and*

Complex Systems, 38(4):541–552, 2004. `https://doi.org/10.1140/epjb/e2004-00150-9`.

[107] K. Ichiyanagi, J. Hebert, L. Toupet, H. Cailleau, P. Guionneau, J.F. Létard, and E. Collet. Nature and mechanism of the photoinduced spin transition in [Fe(PM-BiA)$_2$ (NCS)$_2$]. *Physical Review B*, 73(6):060408, 2006. `https://doi.org/10.1103/PhysRevB.73.060408`.

[108] D. Chernyshov, M. Hostettler, K.W. Törnroos, and H.B. Bürgi. Ordering Phenomena and Phase Transitions in a Spin-Crossover Compound—Uncovering the Nature of the Intermediate Phase of [Fe (2-pic)$_3$] Cl$_2$ EtOH. *Angewandte Chemie International Edition*, 42(32):3825–3830, 2003. `https://doi.org/10.1002/anie.200351834`.

[109] S. Pillet, Sébastien, E.E. Bendeif, S. Bonnet, H. J. Shepherd, and P. Guionneau. Multimetastability, phototrapping, and thermal trapping of a metastable commensurate superstructure in a Fe^{II} spin-crossover compound. *Physical Review B*, 86(6):064106, 2012. `https://doi.org/10.1103/PhysRevB.86.064106`.

[110] A.B. Gaspar, G. Molnár, A. Rotaru, and H.J. Shepherd. Pressure effect investigations on spin-crossover coordination compounds. *Comptes Rendus Chimie*, 21(12):1095–1120, 2018. `https://doi.org/10.1016/j.crci.2018.07.010`.

[111] G. Fogarasi and P. Pulay. Ab initio calculation of force fields and vibrational spectra. *Vibrational spectra and structure*, 14:125–219, 1985. `https://doi.org/10.1146/annurev.pc.35.100184.001203`.

[112] A.P. Scott and L. Radom. Harmonic vibrational frequencies: an evaluation of Hartree- Fock, Møller- Plesset, quadratic configuration interaction, density functional theory, and semiempirical scale factors. *The Journal of Physical Chemistry*, 100(41):16502–16513, 1996. `https://doi.org/10.1021/JP960976R`.

[113] K. Ishii and M. Kato. *Soft Crystals: Flexible Response Systems with High Structural Order*. Springer Nature Singapore Singapore, 2023. ISBN 978-981-99-0259-0.

[114] L. Pauling. The nature of the chemical bond—1992. *Journal of Chemical Education*, 69(7):519, 1992. `https://doi.org/10.1021/ed069p519`.

[115] G.R. Desiraju. Hydrogen bridges in crystal engineering: interactions without borders. *Accounts of chemical research*, 35(7):565–573, 2002. `https://doi.org/10.1021/ar010054t`.

[116] G.R. Desiraju. A bond by any other name. *Angewandte Chemie International Edition*, 50(1):52–59, 2011. `https://doi.org/10.1002/anie.201002960`.

[117] E. Arunan, G.R. Desiraju, R.A. Klein, J. Sadlej, S. Scheiner, I. Alkorta, D.C. Clary, R.H. Crabtree, J.J. Dannenberg, and P. Hobza. Defining the hydrogen bond: An account (IUPAC Technical Report). *Pure and Applied Chemistry*, 83(8):1619–1636, 2011. `https://doi.org/10.1351/PAC-REP-10-01-01`.

[118] S.J. Grabowski. Analysis of hydrogen bonds in crystals. *Crystals*, 6(5):59, 2016. `https://doi.org/10.3390/cryst6050059`.

[119] G. Gilli and P. Gilli. *The Nature of the Hydrogen Bond: Outline of a Comprehensive Hydrogen Bond Theory*, volume 23. International Union of Crystallography, Oxford University Press: Oxford, UK, 2009. ISBN 978-019955-896-4.

[120] P. Schuster and P. Wolschann. *Hydrogen bonding: from small clusters to biopolymers*. Springer, 1999. ISBN 978-3-7091-6419-8.

[121] G.A. Jeffrey and G.A. Jeffrey. *An introduction to hydrogen bonding*, volume 12. Oxford University Press: Oxford, UK, 1997. ISBN 978-019509-549-4.

[122] S. Scheiner. *Hydrogen bonding: A Theoretical Perspective*. Oxford University Press: Oxford, U.K., 1997. ISBN 0-19-509011-X.

[123] G.R. Desiraju and T. Steiner. *The weak hydrogen bond: in structural chemistry and biology*, volume 9. IUCr Monographs on Crystallography; Oxford, Oxford University Press/ International Union of Crystallography, 2001. ISBN 0-19-850970-7.

[124] S.J. Grabowski. *Hydrogen bonding: new insights, 1st eds.*, volume 3. Springer: Heidelberg, 2006. ISBN 1-40-204852-1.

[125] J. Joseph and E.D. Jemmis. Red-, blue-, or no-shift in hydrogen bonds: a unified explanation. *Journal of the American Chemical Society*, 129(15):4620–4632, 2007. `https://doi.org/10.1021/ja067545z`.

[126] J.W. Steed and J.L. Atwood. *Supramolecular Chemistry, 2nd ed.* John Wiley & Sons: Chichester, UK, 2022. ISBN 978-1-119-58251-9.

[127] T. Steiner. The hydrogen bond in the solid state. *Angewandte Chemie International Edition*, 41(1):48–76, 2002. `https://doi.org/10.1002/1521-3773(20020104)41:1<48::AID-ANIE48>3.0.CO;2-U`.

[128] E. Weber, Y. Aoyama, M.R. Caira, G.R. Desiraju, J.P. Glusker, A.D. Hamilton, R.E. Melèndez, and A. Nangia. Design of Organic Solids. *Topics in Current Chemistry*, 198:15–20, 1998.

[129] C.B. Aakeröy and K.R. Seddon. The hydrogen bond and crystal engineering. *Chemical Society Reviews*, 22(6):397–407, 1993. `https://doi.org/10.1039/CS9932200397`.

[130] A. Bondi. Van der Waals volumes and radii. *The Journal of Physical Chemistry*, 68(3):441–451, 1964. `https://doi.org/10.1021/j100785a001`.

[131] K. Tashiro, M. Hanesaka, T. Ohhara, T. Ozeki, T. Kitano, T. Nishu, K. Kurihara, T. Tamada, R. Kuroki, and S. Fujiwara. Structural refinement and extraction of hydrogen atomic positions in polyoxymethylene crystal based on the first successful measurements of 2-dimensional high-energy synchrotron X-ray diffraction and wide-angle neutron diffraction patterns of hydrogenated and deuterated species. *Polymer Journal*, 39(12):1253–1273, 2007. `https://doi.org/10.1295/polymj.PJ2007076`.

[132] Y. Nishiyama, P. Langan, and H. Chanzy. Crystal structure and hydrogen-bonding system in cellulose Iβ from synchrotron X-ray and neutron fiber diffraction. *Journal of the American Chemical Society*, 124(31):9074–9082, 2002. `https://doi.org/10.1021/ja0257319`.

[133] M.V. Lützow, I. Kögel-Knabner, K. Ekschmitt, E. Matzner, G. Guggenberger, B. Marschner, and H. Flessa. Stabilization of organic matter in temperate soils: mechanisms and their relevance under different soil conditions–a review. *European Journal of Soil Science*, 57(4):426–445, 2006. `https://doi.org/10.1111/j.1365-2389.2006.00809.x`.

[134] L.F. Lindoy and I.M. Atkinson. *Self-assembly in supramolecular systems*, volume 7. Royal Society of Chemistry: Cambridge, U.K, 2000. ISBN 0-85404-512-0.

[135] I.E. Dzyaloshinskii, E.M. Lifshitz, and L.P. Pitaevskii. The general theory of van der Waals forces. *Advances in Physics*, 10(38):165–209, 1961. `https://doi.org/10.1080/00018736100101281`.

[136] P. Bhattacharya, R. Fornari, and H. Kamimura. *Comprehensive Semiconductor Science and Technology, 1st ed.* Elsevier Science, 2011. ISBN 978-0-444-53153-7.

[137] G. Birnbaum. *Phenomena induced by intermolecular interactions*, volume 127. Springer Science & Business Media, 2013. ISBN 1-4612-9518-1.

[138] J. Ángyán, J. Dobson, G. Jansen, and T. Gould. *London Dispersion Forces in Molecules, Solids and Nano-structures: An Introduction to Physical Models and Computational Methods, 1st ed.* Royal Society of Chemistry, 2020. ISBN 978-1-78262-045-7.

[139] C.R. Groom, I.J. Bruno, M.P. Lightfoot, and S.C Ward. The Cambridge structural database. *Acta Crystallographica Section B: Structural Science, Crystal Engineering and Materials*, 72(2):171–179, 2016. `https://doi.org/10.1107/S2052520616003954`.

[140] M. Carini, M.P. Ruiz, I. Usabiaga, J.A. Fernández, E. J. Cocinero, M. Melle-Franco, I. Diez-Perez, and A. Mateo-Alonso. High conductance values in π-folded molecular junctions. *Nature Communications*, 8(1):15195, 2017. `https://doi.org/10.1038/ncomms15195`.

[141] R.R. Choudhury and R. Chitra. Stacking interaction between homostacks of simple aromatics and the factors influencing these interactions. *CrystEngComm*, 12(7):2113–2121, 2010. `https://doi.org/10.1039/B919793A`.

[142] C. Janiak. A critical account on π–π stacking in metal complexes with aromatic nitrogen-containing ligands. *Dalton Transactions*, 21:3885–3896, 2000. `https://doi.org/10.1039/B0030100`.

[143] C.A. Hunter and J.KM. Sanders. The nature of π - π interactions. *Journal of the American Chemical Society*, 112(14):5525–5534, 1990. `https://doi.org/10.1021/JA00170A016`.

[144] M. Kertesz. Pancake bonding: An unusual Pi-stacking interaction. *Chemistry–A European Journal*, 25(2):400–416, 2019. `https://doi.org/10.1002/chem.201802385`.

[145] X. Ye, Z.H. Li, W. Wang, K. Fan, W. Xu, and Z. Hua. The parallel π–π stacking: a model study with MP2 and DFT methods. *Chemical Physics Letters*, 397(1-3):56–61, 2004. `https://doi.org/10.1016/j.cplett.2004.07.115`.

[146] S. Tsuzuki, K. Honda, T. Uchimaru, M. Mikami, and K. Tanabe. Origin of attraction and directionality of the π/π interaction: model chemistry calculations of benzene dimer interaction. *Journal of the American Chemical Society*, 124(1):104–112, 2002. `https://doi.org/10.1021/ja0105212`.

[147] M. O. Sinnokrot, E.F. Valeev, and C.D. Sherrill. Estimates of the ab initio limit for π- π interactions: The benzene dimer. *Journal of the American Chemical Society*, 124(36):10887–10893, 2002. `https://doi.org/10.1021/ja025896h`.

[148] N. Moliner, M. Carmen Muñoz, S. Létard, J.F. Létard, X. Solans, R. Burriel, M. Castro, O. Kahn, and J.A. Real. Spin-crossover in the [Fe (abpt)$_2$ (NCX)$_2$](X= S, Se) system: structural, magnetic, calorimetric and photomagnetic studies. *Inorganica Chimica Acta*, 291(1-2):279–288, 1999. `https://doi.org/10.1016/S0020-1693(99)00128-0`.

[149] C. F. Sheu, S. Pillet, Y.C. Lin, S.M. Chen, I.J. Hsu, C. Lecomte, and Y. Wang. Magnetostructural Relationship in the Spin-Crossover Complex t-Fe(abpt)$_2$[N(CN)$_2$]$_2$: Polymorphism and Disorder Phenomenon. *Inorganic Chemistry*, 47(23):10866–10874, 2008. `https://doi.org/10.1021/ic800879c`.

[150] A. Galet, A.B. Gaspar, M.C. Muñoz, G. Levchenko, and J.A. Real. Pressure Effect and Crystal Structure Reinvestigations on the Spin Crossover System:[Fe (bt)$_2$ (NCS)$_2$](bt= 2, 2′-Bithiazoline) Polymorphs A and B. *Inorganic Chemistry*, 45(24):9670–9679, 2006. `https://doi.org/10.1021/ic060729u`.

[151] A. Ozarowski, B.R. McGarvey, A.B Sarkar, and J.E. Drake. EPR study of manganese (II) in two crystalline forms of bis (2, 2'-bi-2-thiazoline) bis (thiocyanato) iron and the high-spin-low-spin transition that occurs in only one form. X-ray structure determination of both forms. *Inorganic Chemistry*, 27 (4):628–635, 1988. `https://doi.org/10.1021/ic00277a012`.

[152] T.M. Pfaffeneder, S. Thallmair, W. Bauer, and B. Weber. Complete and incomplete spin transitions in 1D chain iron (II) compounds. *New Journal of Chemistry*, 35(3):691–700, 2011. `https://doi.org/10.1039/C0NJ00750A`.

[153] B. Weber, W. Bauer, and J. Obel. An iron (II) spin-crossover complex with a 70 K wide thermal hysteresis loop. *Angewandte Chemie International Edition*, 47(52):10098–10101, 2008. `https://doi.org/10.1002/anie.200802806`.

[154] M.A. Halcrow. Structure: Function relationships in molecular spin-crossover materials. *Spin-Crossover Materials: Properties and Applications*, pages 147–169, 2013. `https://doi.org/10.1002/9781118519301.ch5`.

[155] J. Tang, Jinkui, J. Sánchez Costa, S. Smulders, G. Moloár, A. Bousseksou, S.J. Teat, Y. Li, G.A. van Albada, P. Gamez, and J. Reedijk. Two-step spin-transition iron (III) compound with a wide [high spin-low spin] plateau. *Inorganic Chemistry*, 48(5):2128–2135, 2009. `https://doi.org/10.1021/ic801973x`.

[156] D. Boinnard, A. Bousseksou, A. Dworkin, J.M. Savariault, F. Varret, and J. Tuchagues. Two-Step Spin Conversion of [Fe^{II} (5-NO$_2$-sal-N (1, 4, 7, 10))]: 292, 153, and 103 K X-ray Crystal and Molecular Structure, Infrared, Magnetic, Mössbauer, Calorimetric, and Theoretical Studies. *Inorganic Chemistry*, 33(2):271–281, 1994. `https://doi.org/10.1021/ic00080a015`.

[157] L. Salmon, A. Boussekso, B. Donnadieu, and J.P. Tuchagues. Two novel iron (II) materials based on dianionic N$_4$O$_2$ Schiff bases: Structural properties and spin-crossover characteristics in the series [Fe (3-X, 5-NO$_2$-sal-N (1, 4, 7, 10)](X= H, 3-MeO, 3-EtO). *Inorganic Chemistry*, 44(6):1763–1773, 2005. `https://doi.org/10.1021/ic048387k`.

[158] K.S. Min, K. Swierczek, A.G. DiPasquale, A.L. Rheingold, W.M. Reiff, A.M. Arif, and J.S. Miller. A dinuclear iron(II) complex,[(TPyA)Fe^{II} (THBQ $^{2-}$) Fe^{II} (TPyA)](BF$_4$)$_2$ [TPyA= tris (2-pyridylmethyl) amine; THBQ $^{2-}$= 2, 3, 5, 6-tetrahydroxy-1, 4-benzoquinonate] exhibiting both spin crossover with hysteresis and ferromagnetic exchange. *Chemical Communications*, 3:317–319, 2008. `https://doi.org/10.1039/B715271J`.

[159] M. Hostettler, K.W. Törnroos, D. Chernyshov, B. Vangdal, and H.B. Bürgi. Challenges in engineering spin crossover: structures and magnetic properties of six alcohol solvates of iron (II) tris (2-picolylamine) dichloride. *Angewandte Chemie International Edition*, 43(35):4589–4594, 2004. `https://doi.org/10.1002/anie.200460736`.

[160] G.S. Matouzenko, D. Luneau, G. Molnár, N. Ould-Moussa, S. Zein, S.A. Borshch, A. Bousseksou, and F. Averseng. A Two-Step Spin Transition and Order–Disorder Phenomena in the Mononuclear Compound [Fe (Hpy-DAPP)](BF$_4$)$_2$. *European Journal of Inorganic Chemistry*, 13:2671–2682, 2006. `https://doi.org/10.1002/ejic.200600068`.

[161] K.W. Törnroos, M. Hostettler, D. Chernyshov, B. Vangdal, and H.B. Bürgi. Interplay of spin conversion and structural phase transformations: re-entrant phase transitions in the 2-propanol solvate of tris (2-picolylamine) iron (II) dichloride. *Chemistry–A European Journal*, 12(24):6207–6215, 2006. `https://doi.org/10.1002/chem.200600547`.

[162] H.Z. Lazar, T. Forestier, S.A. Barrett, C.A. Kilner, J.F. Létard, and M.A. Halcrow. Thermal and light-induced spin-crossover in salts of the heptadentate complex [tris (4-{pyrazol-3-yl}-3-aza-3-butenyl) amine] iron (II). *Dalton Transactions*, 38:4276–4285, 2007. `https://doi.org/10.1039/B708971F`.

[163] V.A. Money, J. Elhaïk, I.R. Evans, M.A. Halcrow, and JA. A. Howard. A study of the thermal and light induced spin transition in [FeL$_2$](BF$_4$)$_2$ and [FeL$_2$](ClO$_4$)$_2$ L= 2, 6-di (3-methylpyrazol-1-yl) pyrazine. *Dalton Transactions*, 1:65–69, 2004. `https://doi.org/10.1039/B311262B`.

[164] Y. Garcia, P. Guionneau, G. Bravic, D. Chasseau, J.AK. Howard, O. Kahn, V. Ksenofontov, S. Reiman, and P. Gütlich. Synthesis, crystal structure, magnetic properties and ^{57}Fe Mössbauer spectroscopy of the new trinuclear [Fe_3 (4-(2′-hydroxyethyl)-1, 2, 4-triazole)$_6$ (H_2O)$_6$](CF_3SO_3)$_6$ spin crossover compound. *European Journal of Inorganic Chemistry*, 2000(7):1531–1538, 2000. `http://hdl.handle.net/2078/92643`.

[165] G.S. Matouzenko, J.F. Létard, S. Lecocq, A. Bousseksou, L. Capes, L. Salmon, M. Perrin, O. Kahn, and A. Collet. Two-Step Spin Crossover in a Mononuclear Compound [Fe (DPEA)(bim)](ClO_4) 2· 0.5 H_2O [DPEA=(2-Aminoethyl) bis (2-pyridylmethyl) amine, bim= 2, 2-Bisimidazole]- Crystal Structure, Magnetic Properties, Mössbauer Spectroscopy, and Photomagnetic Effects. *European Journal of Inorganic Chemistry*, 2001(11): 2935–2945, 2001. `https://doi.org/10.1002/1099-0682(200111)2001:11<2935::AID-EJIC2935>3.0.CO;2-D`.

[166] S. Hayami, K. Hiki, T. Kawahara, Y. Maeda, D. Urakami, K. Inoue, M. Ohama, S. Kawata, and O. Sato. Photo-induced spin transition of iron (III) compounds with π–π intermolecular interactions. *Chemistry–A European Journal*, 15(14):3497–3508, 2009. `https://doi.org/10.1002/chem.200802395`.

[167] Philipp Gütlich, Ana B Gaspar, and Yann Garcia. Spin state switching in iron coordination compounds. *Beilstein Journal of Organic Chemistry*, 9(1): 342–391, 2013. `https://doi.org/10.3762/bjoc.9.39`.

[168] A. Arroyave, A. Lennartson, A. Dragulescu-Andrasi, K.S. Pedersen, S. Piligkos, S.A. Stoian, S.M. Greer, C. Pak, O. Hietsoi, and H. Phan. Spin crossover in Fe (II) complexes with N_4S_2 coordination. *Inorganic Chemistry*, 55(12):5904–5913, 2016. `https://doi.org/10.1021/acs.inorgchem.6b00246`.

[169] M.S. Sylla, C. Baldé, N. Daro, C. Desplanches, M. Marchivie, and G. Chastanet. On the Effect of the Internal Pressure on the Photoinduced Spin-Crossover Behavior of [Fe_xM_{1-x} (1, 10-phenanthroline)$_2$(NCS)$_2$] Solid Solutions (M= Ni^{II}, Zn^{II} and Cd^{II}). *European Journal of Inorganic Chemistry*, 2018(3-4):297–304, 2018. `https://doi.org/10.1002/ejic.20170`.

[170] P. Guionneau. Crystallography and spin-crossover. A view of breathing materials. *Dalton Transactions*, 43(2):382–393, 2014. `https://doi.org/10.1039/C3DT52520A`.

[171] S. Hayami, R. Kawajiri, G. Juhász, T. Kawahara, K. Hashiguchi, O. Sato, K. Inoue, and Y. Maeda. Study of intermolecular interaction for the spin-crossover iron (II) compounds. *Bulletin of the Chemical Society of Japan*, 76 (6):1207–1213, 2003. `https://doi.org/10.1246/bcsj.76.1207`.

[172] G. Molnár, T. Guillon, N.O. Moussa, L. Rechignat, T. Kitazawa, M. Nardone, and A. Bousseksou. Two-step spin-crossover phenomenon under high pressure in the coordination polymer Fe (3-methylpyridine)$_2$ [Ni (CN)$_4$]. *Chemical Physics Letters*, 423(1-3):152–156, 2006. `https://doi.org/10.1016/j.cplett.2006.03.053`.

[173] J.F. Létard. Photomagnetism of iron (II) spin crossover complexes—the T (LIESST) approach. *Journal of Materials Chemistry*, 16(26):2550–2559, 2006. `https://doi.org/10.1039/B603473J`.

[174] G. Vankó, F. Renz, G. Molnár, T. Neisius, and S. Kárpáti. Hard-X-ray-induced excited-spin-state trapping. *Angewandte Chemie International Edition*, 46 (28):5306–5309, 2007. `https://doi.org/10.1002/anie.200604432`.

[175] A. Bousseksou, F. Varret, M. Goiran, K. Boukheddaden, and J.P. Tuchagues. The spin crossover phenomenon under high magnetic field, Spin Crossover in Transition Metal Compounds III. *Topics in Current Chemistry*, 235:65–84, 2004.

[176] P.J. van Koningsbruggen, Y. Garcia, E. Codjovi, R. Lapouyade, O. Kahn, L. Fournes, and L. Rabardel. Non-classical Fe^{II} spin-crossover behaviour in polymeric iron (II) compounds of formula [Fe (NH_2 trz)$_3$] X_2.xH_2O (NH_2 trz= 4-amino-1, 2, 4-triazole; X= derivatives of naphthalene sulfonate). *Journal of Materials Chemistry*, 7(10):2069–2075, 1997. `https://doi.org/10.1039/A702690K`.

[177] R. Kulmaczewski, J. Olguín, J.A. Kitchen, H.L.C. Feltham, G.N. Jameson, J.L Tallon, and S. Brooker. Remarkable scan rate dependence for a highly constrained dinuclear iron (II) spin crossover complex with a wide thermal hysteresis loop. *Journal of the American Chemical Society*, 136(3):878–881, 2014. `https://doi.org/10.1021/ja411563x`.

[178] A.J. Fitzpatrick, P.N. Martinho, B.J. Gildea, J.D. Holbrey, and G.G. Morgan. Robust room temperature hysteresis in an Fe^{III} spin crossover metallomesogen. *European Journal of Inorganic Chemistry*, 2016(13-14):2025–2029, 2016. `https://doi.org/10.1002/ejic.201501335`.

[179] P. Chakraborty, C. Enachescu, C. Walder, R. Bronisz, and A. Hauser. Thermal and Light-Induced Spin Switching Dynamics in the 2D Coordination Network of $\{[Zn_{1-x}Fe_x\ (bbtr)_3](ClO_4)_2\ \}$: The Role of Cooperative Effects. *Inorganic Chemistry*, 51(18):9714–9722, 2012. `https://doi.org/10.1016/j.ijheatmasstransfer.2013.08.099`.

[180] P. Chakraborty, C. Enachescu, and A. Hauser. Analysis of the Experimental Data for Pure and Diluted $[Fe_xZn_{1-x}(bbtr)_3](ClO_4)_2$ Spin-Crossover Solids in the Framework of a Mechanoelastic Model. *European Journal of Inorganic Chemistry*, 2013(5-6):770–780, 2013. `https://doi.org/10.1002/ejic.201201193`.

[181] A.J. Fitzpatrick, E. Trzop, H. Müller-Bunz, M.M. Dîrtu, Y. Garcia, E. Collet, and G.G. Morgan. Electronic vs. structural ordering in a manganese (III) spin crossover complex. *Chemical Communications*, 51(99):17540–17543, 2015. `https://doi.org/10.1039/C5CC05129K`.

[182] S. Brooker. Spin crossover with thermal hysteresis: Practicalities and lessons learnt. *Chemical Society Reviews*, 44(10):2880–2892, 2015. `https://doi.org/10.1039/C4CS00376D`.

[183] O. Roubeau, M. Castro, R. Burriel, J.G. Haasnoot, and J. Reedijk. Calorimetric investigation of triazole-bridged Fe (II) spin-crossover one-dimensional materials: measuring the cooperativity. *The Journal of Physical Chemistry B*, 115(12):3003–3012, 2011. `https://doi.org/10.1021/jp109489g`.

[184] M. Seredyuk, M.C. Muñoz, M. Castro, T. Romero-Morcillo, A.B. Gaspar, and J.A. Real. Unprecedented Multi-Stable Spin Crossover Molecular Material with Two Thermal Memory Channels. *Chemistry–A European Journal*, 19 (21):6591–6596, 2013. `https://doi.org/10.1002/chem.201300394`.

[185] S. Usha, R. Srinivasan, and C. Rao. High-pressure magnetic susceptibility studies of spin-state transition in Fe (II) complexes. *Chemical Physics*, 100 (3):447–455, 1985. `https://doi.org/10.1016/0301-0104(85)87069-5`.

[186] C. Roux, J. Zarembowitch, J.P. Itié, A. Polian, and M. Verdaguer. Pressure-Induced Spin-State Crossovers in Six-Coordinate $Fe^{II}L_n$ L'_m $(NCS)_2$ Complexes with L= L′ and L≠L′: A XANES Investigation. *Inorganic Chemistry*, 35(3):574–580, 1996. `https://doi.org/10.1021/ic951080o`.

[187] T. Granier, B. Gallois, J. Gaultier, J.A. Real, and J. Zarembowitch. High-pressure single-crystal x-ray diffraction study of two spin-crossover iron (II) complexes: Fe $(Phen)_2$ $(NCS)_2$ and Fe $(Btz)_2$ $(NCS)_2$. *Inorganic Chemistry*, 32(23):5305–5312, 1993. `https://doi.org/10.1021/ic00075a058`.

[188] H.J. Shepherd, T. Palamarciuc, P. Rosa, P. Guionneau, G. Molnár, J.F. Létard, and A. Bousseksou. Antagonism between extreme negative linear compression and spin crossover in $[Fe(dpp)_2$ $(NCS)_2]$ py. *Angewandte Chemie-International Edition*, 51(16):3910, 2012. `https://doi.org/10.1002/anie.201108919`.

[189] J. Jeftić and A. Hauser. Pressure Study of the Thermal Spin Transition and the High-Spin→ Low-Spin Relaxation in the $R\overline{3}$ and $P\overline{1}$ Crystallographic Phases of $[Zn_{1-x}$ Fe_x $(ptz)_6$ $](BF_4)_2$ Single Crystals (x= 0.1, 0.32, and 1; ptz= 1-n-propyltetrazole). *The Journal of Physical Chemistry B*, 101(49):10262–10270, 1997. `https://doi.org/10.1021/jp972083k`.

[190] P. Gütlich, A.B. Gaspar, Y. Garcia, and V. Ksenofontov. Pressure effect studies in molecular magnetism. *Comptes Rendus Chimie*, 10(1-2):21–36, 2007. `https://doi.org/10.1016/j.crci.2006.09.011`.

[191] C.P. Slichter and H.G. Drickamer. Pressure-induced electronic changes in compounds of iron. *The Journal of Chemical Physics*, 56(5):2142–2160, 1972. `https://doi.org/10.1063/1.1677511`.

[192] E. Meissner, H. Köppen, H. Spiering, and P. Gütlich. The effect of low pressure on a high-spin—low-spin transition. *Chemical Physics Letters*, 95(2):163–166, 1983. `https://doi.org/10.1016/0009-2614(83)85088-X`.

[193] P. Adler, L. Wiehl, E. Meibner, C.P. Köhler, H. Spiering, and P. Gütlich. The influence of the lattice on the spin transition in solids. Investigations of the high spin a_g low spin transition in mixed crystals of $[Fe_xM1-x$ (2- pic$)_3]$

Cl_2· MeOH. *Journal of Physics and Chemistry of Solids*, 48(6):517–525, 1987. `https://doi.org/10.1016/0022-3697(87)90046-1`.

[194] H. Köppen, E. Meissner, L. Wiehl, H. Spiering, and P. Gütlich. Quadrupole splitting of Fe (II) spin crossover compounds study of temperature and pressure dependence and the implication for the interaction mechanism. *Hyperfine Interactions*, 52:29–45, 1989. `https://doi.org/10.1007/BF02609561`.

[195] Y. Konishi, H. Tokoro, M. Nishino, and S. Miyashita. Monte Carlo simulation of pressure-induced phase transitions in spin-crossover materials. *Physical Review Letters*, 100(6):067206, 2008. `https://doi.org/10.1103/PhysRevLett.100.067206`.

[196] Y. Qi, EW. Müller, H. Spiering, and P. Gütlich. The effect of a magnetic field on the high-spin α low-spin transition in $[Fe(phen)_2(NCS)_2]$. *Chemical Physics Letters*, 101(4):503–505, 1983. `https://doi.org/10.1016/0009-2614(83)87521-6`.

[197] J.A. Real, A.B. Gaspar, and M.C. Muñoz. Thermal, pressure and light switchable spin-crossover materials. *Dalton Transactions*, 1(12):2062–2079, 2005. `https://doi.org/10.1039/B501491C`.

[198] M. Marchivie, P. Guionneau, J.AK. Howard, G. Chastanet, J.F. Létard, A.E. Goeta, and D. Chasseau. Structural characterization of a photoinduced molecular switch. *Journal of the American Chemical Society*, 124(2):194–195, 2002. `https://doi.org/10.1021/ja016980k`.

[199] S. Alvarez. Relationships between temperature, magnetic moment, and continuous symmetry measures in spin crossover complexes. *Journal of the American Chemical Society*, 125(22):6795–6802, 2003. `https://doi.org/10.1021/ja0283450`.

[200] J.H. Takemoto, B. Streusand, and B. Hutchinson. Far-infrared spectra of some $Fe(1, 10\text{-phenanthroline})_2X_2$ complexes. *Spectrochimica Acta Part A: Molecular Spectroscopy*, 30(3):827–834, 1974. `https://doi.org/10.1016/0584-8539(74)80199-6`.

[201] P. Gütlich, A. Hauser, and H. Spiering. Thermal and optical switching of iron (II) complexes. *Angewandte Chemie International Edition in English*, 33(20): 2024–2054, 1994. `https://doi.org/10.1002/anie.199420241`.

[202] E. Tailleur, M. Marchivie, P. Negrier, D. Denux, S. Massip, D. Mondieig, G. Chastanet, and P. Guionneau. Using polymorphism to master the spin crossover mechanism in $[Fe\ (PM\text{-}PeA)_2\ (NCSe)_2]$. *CrystEngComm*, 21(41): 6246–6251, 2019. `https://doi.org/10.1039/C9CE01137D`.

[203] L. Capes, J.F. Létard, and O. Kahn. Photomagnetic properties in a series of spin crossover compounds $[Fe\ (PM\text{-}L)_2\ (NCX)_2]$(X= S, Se) with substituted 2′-pyridylmethylene-4-amino ligands. *Chemistry–A European Journal*, 6 (12):2246–2255, 2000. `https://doi.org/10.1002/1521-3765(20000616)6:12<2246::AID-CHEM2246>3.0.CO;2-X`.

[204] E. König, G. Ritter, and R. Schnakig. Thermally induced incomplete high-spin ($^5T_2$) $\Longleftrightarrow$ low-spin (^1A_J) transition in dithiocy anatobis (n-phenyl-2-pyridinaldimine) iron (II). *Chemical Physics Letters*, 27(1):23–26, 1974. `https://doi.org/10.1016/0009-2614(74)80436-7`.

[205] J.F. Létard, P. Guionneau, E. Codjovi, O. Lavastre, G. Bravic, D. Chasseau, and O. Kahn. Wide Thermal Hysteresis for the Mononuclear Spin-Crossover Compound cis-Bis (thiocyanato) bis [N-(2'-pyridylmethylene)-4-(phenylethynyl) anilino] iron (II). *Journal of the American Chemical Society*, 119(44):10861–10862, 1997. `https://doi.org/10.1021/ja972441x`.

[206] J.F. Létard, S. Montant, P. Guionneau, P. Martin, A. Le Calvez, E. Freysz, D. Chasseau, R. Lapouyade, and O. Kahn. Large negative cubic hyperpolarizability for the spin-crossover compound cis-bis (thiocyanato) bis [N-(2-pyridylmethylene) aminobiph enyl] iron (ii). *Chemical Communications*, 8: 745–746, 1997. `https://doi.org/10.1039/A700019G`.

[207] N. Paradis, F. Le Gac, P. Guionneau, A. Largeteau, D.S. Yufit, P. Rosa, J.F. Létard, and G. Chastanet. Effects of Internal and External Pressure on the [Fe (PM-PEA)$_2$ (NCS)$_2$] Spin-Crossover Compound (with PM-PEA= N-(2′-pyridylmethylene)-4-(phenylethynyl) aniline). *Magnetochemistry*, 2(1):15, 2016. `https://doi.org/10.3390/magnetochemistry2010015`.

[208] S. Zheng, M.A. Siegler, O. Roubeau, and S. Bonnet. Influence of selenocyanate ligands on the transition temperature and cooperativity of bapbpy-based Fe (II) spin-crossover compounds. *Inorganic Chemistry*, 53(24):13162–13173, 2014. `https://doi.org/10.1021/ic502381m`.

[209] M. Sorai and S. Seki. Phonon coupled cooperative low-spin $^1A_1$high-spin $^5T_2$ transition in [Fe (phen)$_2$ (NCS)$_2$] and [Fe (phen)$_2$(NCSe)$_2$] crystals. *Journal of Physics and Chemistry of Solids*, 35(4):555–570, 1974. `https://doi.org/10.1016/S0022-3697(74)80010-7`.

[210] A. Rotaru, F. Varret, E. Codjovi, K. Boukheddaden, J. Linares, A. Stancu, P. Guionneau, and J.F. Létard. Hydrostatic pressure investigation of the spin crossover compound [Fe (PM- BiA)$_2$ (NCS)$_2$] polymorph I using reflectance detection. *Journal of Applied Physics*, 106(5):053515, 2009. `https://doi.org/10.1063/1.3202385`.

[211] V. Legrand, S. Pechev, J.F. Létard, and P. Guionneau. Synergy between polymorphism, pressure, spin-crossover and temperature in [Fe (PM-BiA)$_2$ (NCS)$_2$: A neutron powder diffraction investigation. *Physical Chemistry Chemical Physics*, 15(33):13872–13880, 2013. `https://doi.org/10.1039/C3CP51444G`.

[212] V. Legrand, F. Le Gac, P. Guionneau, and J.F. Létard. Neutron powder diffraction studies of two spin transition Fe^{II} complexes under pressure. *Journal of Applied Crystallography*, 41(3):637–640, 2008. `https://doi.org/10.1107/S0021889808006481`.

[213] A. Marbeuf, S.F. Matar, P. Négrier, L. Kabalan, J.F. Létard, and P. Guion-

neau. Molecular dynamics of spin crossover: The (P, T) phase diagram of [Fe (PM-BIA)$_2$ (NCS)$_2$]. *Chemical Physics*, 420:25–34, 2013. `https://doi.org/10.48550/arXiv.1301.4568`.

[214] A. Tissot, H.J. Shepherd, L. Toupet, E. Collet, J. Sainton, G. Molnár, P. Guionneau, and M.L. Boillot. Temperature-and Pressure-Induced Switching of the Molecular Spin State of an Orthorhombic Iron (III) Spin-Crossover Salt. *European Journal of Inorganic Chemistry*, 2013(5-6):1001–1008, 2013. `https://doi.org/10.1002/ejic.201201059`.

[215] R.C. Johnson. A simple approach to crystal field theory. *Journal of Chemical Education*, 42(3):147, 1965. `https://doi.org/10.1021/ed042p147`.

[216] J.S. Griffith and L.E. Orgel. Ligand-field theory. *Quarterly Reviews, Chemical Society*, 11(4):381–393, 1957. `https://doi.org/10.1039/QR9571100381`.

[217] J.H. Van Vleck. Theory of the variations in paramagnetic anisotropy among different salts of the iron group. *Physical Review*, 41(2):208, 1932. `https://doi.org/10.1103/PhysRev.41.208`.

[218] J.R. Jiménez, B. Doistau, M. Poncet, and C. Piguet. Heteroleptic trivalent chromium in coordination chemistry: Novel building blocks for addressing old challenges in multimetallic luminescent complexes. *Coordination Chemistry Reviews*, 434:213750, 2021. `https://doi.org/10.1016/j.ccr.2020.213750`.

[219] R. Chang. *Physical Chemistry for the Biosciences*. University Science Books, 2005. ISBN 978-1891389337.

[220] L.E. Orgel. Spectra of transition-metal complexes. *The Journal of Chemical Physics*, 23(6):1004–1014, 1955. `https://doi.org/10.1063/1.1742182`.

[221] L.E. Sutton. Some recent developments in the theory of bonding in complex compounds of the transition metals. *Journal of Chemical Education*, 37(10): 498, 1960. `https://doi.org/10.1021/ed037p498`.

[222] P. Gütlich and H.A. Goodwin. Spin crossover in cobalt (II) systems, Spin Crossover in Transition Metal Compounds II. *Topics in Current Chemistry*, 234:23–47, 2004.

[223] Y. Tanabe and S. Sugano. On the absorption spectra of complex ions II. *Journal of the Physical Society of Japan*, 9(5):766–779, 1954. `https://doi.org/10.1143/JPSJ.9.766`.

[224] H.L. Schläfer and G. Gliemann. *Einführung in die Ligandenfeldtheorie*, volume 462. Akademische Verlagsgesellschaft: Wiesbaden, Germany, 1967.

[225] C. Kittel and P. McEuen. *Introduction to Solid State Physics*. John Wiley & Sons, 2018. ISBN 978-1-119-45416-8. pp. 136–140.

[226] B. Fultz. Vibrational thermodynamics of materials. *Progress in Materials Science*, 55(4):247–352, 2010. `https://doi.org/10.1016/j.pmatsci.2009.05.002`.

[227] C. Enachescu and W. Nicolazzi. Elastic models, lattice dynamics and finite size effects in molecular spin crossover systems. *Comptes Rendus Chimie*, 21 (12):1179–1195, 2018. `https://doi.org/10.1016/j.crci.2018.02.004`.

[228] M. Varón, M. Beleggia, T. Kasama, R.J. Harrison, R.E. Dunin-Borkowski, F. Víctor Puntes, and C. Frandsen. Dipolar magnetism in ordered and disordered low-dimensional nanoparticle assemblies. *Scientific Reports*, 3(1):1234, 2013. `https://doi.org/10.1038/srep01234`.

[229] J.S. Zhou, H.Q. Yin, and J.B. Goodenough. Vibronic superexchange in single-crystal $\mathrm{LaMn}_{1-x}\mathrm{Ga}_x\mathrm{O}_3$. *Physical Review B*, 63(18):184423, 2001. `https://doi.org/10.1103/PhysRevB.63.184423`.

[230] Á. Martín, M. Dolores Bermejo, and M. Jose Cocero. Recent developments of supercritical water oxidation: a patents review. *Recent Patents on Chemical Engineering*, 4(3):219–230, 2011. `https://doi.org/10.2174/1874478811104030219`.

[231] E. Machlin. *An introduction to aspects of thermodynamics and kinetics relevant to materials science, 3rd ed.*, volume 3. Elsevier, Oxford, UK, 2010. ISBN 978-0-08-046615-6.

[232] J. Anwar and D. Zahn. Polymorphic phase transitions: Macroscopic theory and molecular simulation. *Advanced Drug Delivery Reviews*, 117:47–70, 2017. `https://doi.org/10.1016/j.addr.2017.09.017`.

[233] E. König and K. Madeja. Novel series of six-coordinated iron (II) diimine complexes with half-quenched spin. *Inorganic Chemistry*, 7(9):1848–1855, 1968. `https://doi.org/10.1021/ic50067a030`.

[234] M. Sorai and S. Seki. Magnetic heat capacity due to cooperative low-spin (remark: graphics omitted.) $^5\mathrm{T}_2$ transition in Fe (phen)$_2$ (NCS)$_2$ crystal. *Journal of the Physical Society of Japan*, 33(2):575–575, 1972. `https://doi.org/10.1143/JPSJ.33.575`.

[235] E. Collet, M.L. Boillot, J. Hebert, N. Moisan, M. Servol, M. Lorenc, L. Toupet, B.L. Cointe, A. Tissot, and J. Sainton. Polymorphism in the spin-crossover ferric complexes [(TPA) Fe^{III} (TCC)] PF_6. *Acta Crystallographica Section B: Structural Science, Crystal Engineering and Materials*, 65(4):474–480, 2009. `https://doi.org/10.1107/S0108768109021508`.

[236] D. Chernyshov, N. Klinduhov, K.W. Törnroos, M. Hostettler, B. Vangdal, and H.B. Bürgi. Coupling between spin conversion and solvent disorder in spin crossover solids. *Physical Review B*, 76(1):014406, 2007. `https://doi.org/10.1103/PhysRevB.76.014406`.

[237] N.F. Sciortino, K.R. Scherl-Gruenwald, G. Chastanet, G.J. Halder, K.W. Chapman, J.F. Létard, and C.J. Kepert. Hysteretic Three-Step Spin Crossover in a Thermo-and Photochromic 3D Pillared Hofmann-type Metal–Organic Framework. *Angewandte Chemie International Edition*, 51(40):10154–10158, 2012. `https://doi.org/10.1002/anie.201204387`.

[238] G. Agustí, A.B. Gaspar, M.C. Mũnoz, and J.A. Real. [Thermal-and pressure-induced cooperative spin transition in the 2D and 3D coordination polymers {Fe (5-Br-pmd)$_z$ [M (CN)$_x$]$_y$}(M= AgI, AuI, NiII, PdII, PtII). *Inorganic Chemistry*, 46(23):9646–9654, 2007. `https://doi.org/10.1021/ic700993s`.

[239] I. Šalitroš, O. Fuhr, A. Eichhöfer, R. Kruk, J. Pavlik, L. Dlháň, R. Boča, and M. Ruben. The interplay of iron (II) spin transition and polymorphism. *Dalton Transactions*, 41(17):5163–5171, 2012. `https://doi.org/10.1039/C2DT11906D`.

[240] K. Ridier, G. Molnár, L. Salmon, W. Nicolazzi, and A. Bousseksou. Hysteresis, nucleation and growth phenomena in spin-crossover solids. *Solid State Sciences*, 74:A1–A22, 2017. `https://doi.org/10.1016/j.solidstatesciences.2017.10.014`.

[241] R.M. Hazen, R.T. Downs, and C.T. Prewitt. Principles of comparative crystal chemistry. *Reviews in Mineralogy and Geochemistry*, 41(1):1–33, 2000. `https://doi.org/10.2138/rmg.2000.41.1`.

[242] F. Birch. Finite Elastic Strain of Cubic Crystals. *Physical Review B*, 71(11):809–824, 1947. `https://doi.org/10.1103/PhysRev.71.80`.

[243] F.D. Murnaghan. The compressibility of media under extreme pressures. *Proceedings of the National Academy of Sciences*, 30(9):244–247, 1944. `https://doi.org/10.1073/pnas.30.9.244`.

[244] R.J. Angel. Equations of state. *Reviews in Mineralogy and Geochemistry*, 41 (1):35–59, 2000. `https://doi.org/10.2138/rmg.2000.41.2`.

[245] R. Clausius. *The Mechanical Theory of Heat: With Its Applications to the Steam-Engine and To the Physical Properties of Bodies*. Macmillan, 1867. ISBN 0-35-393784-3.

[246] R. Boča. *Theoretical Foundations of Molecular Magnetism, 1st ed.*, volume 1. Elsevier, Amsterdam, The Netherlands, 1999. ISBN 0-444-50229-7.

[247] A. Bousseksou, G. Molnár, and G. Matouzenko. Switching of molecular spin states in inorganic complexes by temperature, pressure, magnetic field and light: towards molecular devices. *European Journal of Inorganic Chemistry*, 2004(22):4353–4369, 2004. `https://doi.org/10.1002/ejic.200400571`.

[248] E. König, G. Ritter, and S.K. Kulshreshtha. The Nature of Spin-State Transitions in Solid Complexes of Iron (II) and the Interpretation of Some Associated Phenomena. *Chemical Reviews*, 85(3):219–234, 1985. `https://doi.org/10.1021/cr00067a003`.

[249] G. Molnár, M. Mikolasek, K. Ridier, A. Fahs, W. Nicolazzi, and A. Bousseksou. Molecular spin crossover materials: Review of the lattice dynamical properties. *Annalen der Physik*, 531(10):1900076, 2019. `https://doi.org/10.1002/andp.201900076`.

[250] A. Bousseksou, H. Constant-Machado, and F. Varret. A simple ising-like model

for spin conversion including molecular vibrations. *Journal de Physique I*, 5 (6):747–760, 1995. `https://doi.org/10.1051/jp1:1995165`.

[251] A. Bousseksou, J.J. McGarvey, F. Varret, J.A. Real, J.P. Tuchagues, A.C. Dennis, and M.L. Boillot. Raman spectroscopy of the high-and low-spin states of the spin crossover complex Fe (phen)$_2$ (NCS)$_2$: an initial approach to estimation of vibrational contributions to the associated entropy change. *Chemical Physics Letters*, 318(4-5):409–416, 2000. `https://doi.org/10.1016/S0009-2614(00)00063-4`.

[252] S.K. Kulshreshtha and R.M. Iyer. Nature of the high-spin ($^5T_2$) ↔ low-spin ($^1A_1$) transition in [Fe (bipy)$_2$(NCS)$_2$]. *Chemical Physics Letters*, 108(5):501–504, 1984. `https://doi.org/10.1016/0009-2614(84)85188-X`.

[253] S.K. Kulshreshtha, R.M. Iyer, E. König, and G. Ritter. The nature of spin-state transitions in Fe (II) complexes. *Chemical Physics Letters*, 110(2):201–204, 1984. `https://doi.org/10.1016/0009-2614(84)80175-X`.

[254] N. Moliner, L. Salmon, L. Capes, M. Carmen Muñoz, J.F. Létard, A. Bousseksou, J.P. Tuchagues, J.J. McGarvey, A.C. Dennis, and M. Castro. Thermal and optical switching of molecular spin states in the {[FeL [H$_2$B (pz)$_2$]$_2$ } spin-crossover system (L= bpy, phen). *The Journal of Physical Chemistry B*, 106 (16):4276–4283, 2002. `https://doi.org/10.1021/jp013872b`.

[255] G. Molnár, V. Niel, A.B. Gaspar, J.A. Real, A. Zwick, A. Bousseksou, and J.J. McGarvey. Vibrational spectroscopy of cyanide-bridged, iron (ii) spin-crossover coordination polymers: Estimation of vibrational contributions to the entropy change associated with the spin transition. *The Journal of Physical Chemistry B*, 106(38):9701–9707, 2002. `https://doi.org/10.1021/jp025678a`.

[256] Y. Miyazaki, T. Nakamoto, S. Ikeuchi, K. Saito, A. Inaba, M. Sorai, T. Tojo, T. Atake, G.S. Matouzenko, and S. Zein. Spin Crossover Phenomenon Accompanying Order- Disorder Phase Transition in the Ligand of [Fe^{II} (DAPP)(abpt)](ClO$_4$)$_2$ Compound (DAPP= Bis (3-aminopropyl)(2-pyridylmethyl) amine, abpt= 4-Amino-3, 5-bis (pyridin-2-yl)-1, 2, 4-triazole) and Its Successive Self-Grinding Effect. *The Journal of Physical Chemistry B*, 111(43):12508–12517, 2007. `https://doi.org/10.1021/jp0730287`.

[257] V.A. Money, I.R. Evans, M.A. Halcrow, A.E. Goeta, and J.A.K. Howard. Light induced excited high spin-state trapping in [FeL$_2$](BF$_4$)$_2$ (L= 2, 6-di (pyrazol-1-yl) pyridine). *Chemical Communications*, 33(1):158–159, 2003. `https://doi.org/10.1039/B210146G`.

[258] C.P. Köhler, R. Jakobi, E. Meissner, L. Wiehl, H. Spiering, and P. Gütlich. Nature of the phase transition in spin crossover compounds. *Journal of Physics and Chemistry of Solids*, 51(3):239–247, 1990. `https://doi.org/10.1016/0022-3697(90)90052-H`.

[259] H. Spiering, Th. Kohlhaas, H. Romstedt, A. Hauser, C. Bruns-Yilmaz, J. Kusz, and P. Gütlich. Correlations of the distribution of spin states in spin

crossover compounds. *Coordination Chemistry Reviews*, 190:629–647, 1999. `https://doi.org/10.1016/S0010-8545(99)00109-5`.

[260] A. Hauser, J. Jeftić, H. Romstedt, R. Hinek, and H. Spiering. Cooperative phenomena and light-induced bistability in iron (II) spin-crossover compounds. *Coordination Chemistry Reviews*, 190:471–491, 1999. `https://doi.org/10.1016/S0010-8545(99)00111-3`.

[261] R. Zimmermann. A model for high-spin/low-spin transitions with an interpretation of thermal hysteresis effects. *Journal of Physics and Chemistry of Solids*, 44(2):151–158, 1983. `https://doi.org/10.1016/0022-3697(83)90164-6`.

[262] P.S. Rao, P. Ganguli, and B.R. McGarvey. Proton NMR study of the high-spin-low-spin transition in Fe $(phen)_2$ $(NCS)_2$ and Fe (pic) $3Cl_2$.(EtOH or MeOH). *Inorganic Chemistry*, 20(11):3682–3688, 1981. `https://doi.org/10.1021/ic50225a020`.

[263] R Zimmermann and E König. A model for high-spin/low-spin transitions in solids including the effect of lattice vibrations. *Journal of Physics and Chemistry of Solids*, 38(7):779–788, 1977. `https://doi.org/10.1016/0022-3697(77)90072-5`.

[264] R. Boča and W. Linert. Is there a need for new models of the spin crossover? *Monatshefte für Chemie/Chemical Monthly*, 134:83—100, 2003. `https://doi.org/10.1007/s00706-002-0489-4`.

[265] P. Gütlich, Y. Garcia, and H. Spiering. *In Magnetism: Molecules to Materials IV: Nanosized Magnetic Materials*, volume 8. Wiley Online Library, 2003. ISBN 978-352760-069-4.

[266] M. Sorai. *Comprehensive Handbook of Calorimetry and Thermal Analysis*. John Wiley & Sons Oxford, UK, 2004. ISBN 978-0-470-85152-4.

[267] K.F. Purcell and M.P. Edwards. Cooperativity in thermally induced intersystem crossing in solids: Fe $(phen)_2$ $(NCR)_2$, R= BH_3, BPh_3, S, Se. *Inorganic Chemistry*, 23(17):2620–2625, 1984. `https://doi.org/10.1021/ic00185a016`.

[268] A. Kraft, C. Rupprecht, and Y.C. Yam. Superconducting Quantum Interference Device (SQUID). UBC Phys, 2017. URL `https://phas.ubc.ca/~berciu/TEACHING/PHYS502/PROJECTS/17SQUID.pdf`. Accessed on 3 May 2023.

[269] Inc. Quantum Design. *PPMS DynaCool – Product Description*, 2019.

[270] Inc. Quantum Design. *Vibrating Sample Magnetometer (VSM) Option User's Manual*, 2011.

[271] P. Fischer, G. Frey, M. Koch, M. Könnecke, V. Pomjakushin, J. Schefer, R. Thut, N. Schlumpf, R. Bürge, U. Greuter, S. Bondt, and E. Berruyer. High-Resolution Powder Diffractomter HRPT for Thermal Neutrons at SINQ. *Physica B*, 276–278:146–147, 2000. `https://doi.org/10.1016/S0921-4526(99)01399-X`.

[272] P. Fischer, J. Schefer, L. Keller, O. Zaharko, V. Pomjakushin, D. Sheptyakov, N. Aliouane, and M. Frontzek. 50 Years of Swiss Neutron Diffraction Instrumentation. *Swiss Neutron News*, 42:4–15, 2013.

[273] HUBER Diffraktionstechnik GmbH & Co. KG. *Guinier Imaging Plate Camera G670*, 2006.

[274] P.R. Willmott, D. Meister, S.J. Leake, M. Lange, A. Bergamaschi, M. Böge, M. Calvi, C. Cancellieri, N. Casati, and A. Cervellino. The materials science beamline upgrade at the swiss light source. *Journal of synchrotron radiation*, 20(5):667–682, 2013. `https://doi.org/10.1107/S0909049513018475`.

[275] Agilent Technologies XRD Products, Ltd. *SuperNova – X-ray Diffractometer System*, 2014.

[276] ESRF SNBL. Esrf bm01 beamline, 2020. `https://www.esrf.fr/UsersAndScience/Experiments/CRG/BM01/bm01-a`.

[277] V. Dyadkin, P. Pattison, V. Dmitriev, and D. Chernyshov. A new multipurpose diffractometer PILATUS SNBL. *Journal of Synchrotron Radiation*, 23 (3):825–829, 2016. `https://doi.org/10.1107/S1600577516002411`.

[278] R. Boehler. New diamond cell for single-crystal x-ray diffraction. *Review of Scientific Instruments*, 77(11):115103, 2006. `https://doi.org/10.1063/1.2372734`.

[279] Q. Ma and D.R. Clarke. Piezospectroscopic Determination of Residual Stresses in Polycrystalline Alumina. *Journal of the American Ceramic Society*, 77(2): 298–302, 1994. `https://doi.org/10.1016/0956-7151(94)90377-8`.

[280] K. Syassen. Ruby under pressure. *High Pressure Research*, 28(2):75–126, 2008. `https://doi.org/10.1080/08957950802235640`.

[281] G. Shen, Y. Wang, A. Dewaele, C. Wu, D.E. Fratanduono, J. Eggert, S. Klotz, K.F. Dziubek, P. Loubeyre, O.V. Fat'yanov, P.D. Asimow, T. Mashimo, R.M.M. Wentzcovitch, and other members of the IPPS task group. Toward an International Practical Pressure Scale: A Proposal for an IPPS Ruby Gauge (IPPS-Ruby2020). *High Pressure Research*, 40(3):299–314, 2020. `https://doi.org/10.1080/08957959.2020.1791107`.

[282] M. Tolkiehn, H. Schulze-Ritter, W. Drube, C. Paulmann, A. Berghäuser, and D. Ropers. Beamline P24 – Chemical Crystallography. Technical Report, DESY, 06 2014.

[283] A. Hofmann. *The Physics of Synchrotron Radiation.* Cambridge University Press, New York, 2004. ISBN 978-0-511-19200-5.

[284] G.A. Bain and J.F. Berry. Diamagnetic corrections and Pascal's constants. *Journal of Chemical Education*, 85(4):532, 2008. `https://doi.org/10.1021/ed085p532`.

[285] W.P. Brennan, B. Miller, and J.C. Whitwell. Improved method of ana-

lyzing curves in differential scanning calorimetry. *Industrial & Engineering Chemistry Fundamentals*, 8(2):314–318, 1969. `https://doi.org/10.1021/i160030a021`.

[286] G.W.H. Höhne, W.F. Hemminger, and H.-J. Flammersheim. *Applications of Differential Scanning Calorimetry.* Springer Berlin Heidelberg, Berlin, 2003. ISBN 978-3-662-06710-9.

[287] A. Le Bail, H. Duroy, and J.L. Fouquet. Ab-Initio Structure Determination of $LiSbWO_6$ by X-ray Powder Diffraction. *Materials Research Bulletin*, 23(3): 447–452, 1988. `https://doi.org/10.1016/0025-5408(88)90019-0`.

[288] V. Petříček, M. Dušek, and L. Palatinus. Crystallographic Computing System JANA2006: General Features. *Zeitschrift für Kristallographie-Crystalline Materials*, 229(5):345–352, 2014. `https://doi.org/10.1515/zkri-2014-1737`.

[289] V.K. Peterson. Lattice parameter measurement using Le Bail versus structural (Rietveld) refinement: A caution for complex, low symmetry systems. *Powder Diffraction*, 20(1):14–17, 2005. `https://doi.org/10.1154/1.1810156`.

[290] G. Fiquet, A. Dewaele, D. Andrault, M. Kunz, and T. Le Bihan. Thermoelastic properties and crystal structure of $MgSiO_3$ perovskite at lower mantle pressure and temperature conditions. *Geophysical Research Letters*, 27(1):21–24, 2000. `https://doi.org/10.1029/1999GL008397`.

[291] W.I.F David. Powder diffraction peak shapes. Parameterization of the pseudo-Voigt as a Voigt function. *Journal of Applied Crystallography*, 19(1):63–64, 1986. `https://doi.org/10.1107/S0021889886089999`.

[292] A. Albinati and B.T.M Willis. The rietveld method in neutron and x-ray powder diffraction. *Journal of Applied Crystallography*, 15(4):361–374, 1982. `https://doi.org/10.1107/S0021889882012187`.

[293] P.W. Stephens. Phenomenolgical Model of Anisotropic Peak Broadening in Powder Diffraction. *Journal of Applied Crystallography*, 32(2):281–289, 1999. `https://doi.org/10.1107/S0021889898006001`.

[294] J.-F. Bérar and P. Lelann. E.S.D.'s and Estimated Probable Error Obtained in Rietveld Refinements with Local Correlations. *Journal of Applied Crystallography*, 24(1):1–5, 1991. `https://doi.org/10.1107/S0021889890008391`.

[295] CrysAlisPro Agilent. Software System, Version 1.171. 36.28, 2013.

[296] G.H. Stout and L.H. Jensen. *X-ray structure determination: a practical guide, 2nd ed.* John Wiley & Sons, 1989. ISBN 978-0-471-60711-3.

[297] M.S. Weiss and R. Hilgenfeld. On the use of the merging R factor as a quality indicator for X-ray data. *Journal of Applied Crystallography*, 30(2):203–205, 1997. `https://doi.org/10.1107/S0021889897003907`.

[298] N. Walker and D. Stuart. An empirical method for correcting diffractometer data for absorption effects. *Acta Crystallographica Section A: Foundations of Crystallography*, 39(1):158–166, 1983. `https://doi.org/10.1107/S0108767383000252`.

[299] R.H. Blessing. An empirical correction for absorption anisotropy. *Acta Crystallographica Section A: Foundations of Crystallography*, 51(1):33–38, 1995. `https://doi.org/10.1107/S0108767394005726`.

[300] J.T. de Meulenaer and H. Tompa. The absorption correction in crystal structure analysis. *Acta Crystallographica*, 19(6):1014–1018, 1965. `https://doi.org/10.1107/S0365110X65004802`.

[301] F. R. Ahmed, S. R. Hall, and C. P. Huber. *Crystallographic Computing: Proceedings of an International Summer School Organized by The Commission on Crystallographic Computing of the International Union of Crystallography*, volume 1. Munksgaard, 1970. ISBN 9788716001795.

[302] E.A. Preoteasa, E.S. Preoteasa, I. Suciu, and R.N. Bartok. Atomic and nuclear surface analysis methods for dental materials: A review. *AIMS Materials Science*, 5(4):781–844, 2018. `https://doi.org/10.3934/matersci.2018.4.781`.

[303] H. Schenk. *An introduction to direct methods: the most important phase relationships and their application in solving the phase problem.* International Union of Crystallography, University College Cardiff Press, Cardiff, Wales, 1984. ISBN 0-906449-71-5.

[304] A. Altomare, G. Cascarano, C. Giacovazzo, A. Guagliardi, M.C. Burla, G. Polidori, and M. Camalli. SIRPOW. 92–a program for automatic solution of crystal structures by direct methods optimized for powder data. *Journal of Applied Crystallography*, 27(3):435–436, 1994. `https://doi.org/10.1107/S0021889894000221`.

[305] G.M. Sheldrick. SHELXT–Integrated space-group and crystal-structure determination. *Acta Crystallographica Section A: Foundations and Advances*, 71 (1):3–8, 2015. `https://doi.org/10.1107/S2053273314026370`.

[306] G. Oszlányi and A. Sütő. The charge flipping algorithm. *Acta Crystallographica Section A: Foundations of Crystallography*, 64(1):123–134, 2008. `https://doi.org/10.1107/S0108767307046028`.

[307] G.Oszlányi and A. Sütő. Ab initio structure solution by charge flipping. *Acta Crystallographica Section A: Foundations of Crystallography*, 60(2):134–141, 2004. `https://doi.org/10.1107/S0108767303027569`.

[308] L. Palatinus and G. Chapuis. SUPERFLIP – A Computer Program for the Solution of Crystal Structures by Charge Flipping in Arbitrary Dimensions. *Journal of Applied Crystallography*, 40(4):786–790, 2007. `https://doi.org/10.1107/S0021889807029238`.

[309] G.M. Sheldrick. Crystal structure refinement with SHELXL. *Acta Crystallographica Section C: Structural Chemistry*, 71(1):3–8, 2015. `https://doi.org/10.1107/S2053229614024218`.

[310] K. Friese, A. Grzechnik, J.M. Posse, and V. Petříček. Refinement of High Pressure Single-Crystal Diffraction Data using Jana2006. *High Pressure Research*, 33(1):196–201, 2013. `https://doi.org/10.1080/08957959.2012.758723`.

[311] K. Ridier, S. Rat, L. Salmon, W. Nicolazzi, G. Molnár, and A. Bousseksou. Scan-rate and vacuum pressure dependence of the nucleation and growth dynamics in a spin-crossover single crystal: the role of latent heat. *Physical Chemistry Chemical Physics*, 20(14):9139–9145, 2018. `https://doi.org/10.1039/C7CP08522B`.

[312] J. Kusz, M. Nowak, and P. Gütlich. Crystal-Structure Studies of Mononuclear Iron (II) Complexes with Two-Step Spin Crossover:[Fe {5-NO_2-sal-N (1, 4, 7, 10)}] Revisited. *European Journal of Inorganic Chemistry*, 2013(5-6):832–842, 2013. `https://doi.org/10.1002/ejic.201201467`.

[313] S. Pillet. Spin-crossover materials: Getting the most from X-ray crystallography. *Journal of Applied Physics*, 129(18), 2021. `https://doi.org/10.1063/5.0047681`.

[314] H. Daubric, J. Kliava, P. Guionneau, D. Chasseau, J.F. Létard, and O. Kahn. Spin transition in [Fe $(PM\text{-}BiA)_2$ $(NCS)_2$] studied by the electron paramagnetic resonance of the Mn^{2+} ion. *Journal of Physics: Condensed Matter*, 12(25):5481–5494, 2000. `https://api.semanticscholar.org/CorpusID:250785194`.

[315] M.J. Cliffe and A.L. Goodwin. PASCal: a principal axis strain calculator for thermal expansion and compressibility determination. *Journal of Applied Crystallography*, 45(6):1321–1329, 2012. `https://doi.org/10.1107/S0021889812043026`.

[316] M. Marchivie, P. Guionneau, J.F. Létard, and D. Chasseau. Photo-induced spin-transition: the role of the iron (II) environment distortion. *Acta Crystallographica Section B: Structural Science, Crystal Engineering and Materials*, 61(1):25–28, 2005. `https://doi.org/10.1107/S0108768104029751`.

[317] P. Guionneau, M. Marchivie, G. Bravic, J.-F. Létard, and D. Chasseau. Co(II) Molecular Complexes as a Reference for the Spin Crossover in Fe(II) Analogues. *Journal of Materials Chemistry*, 12(8):2546–2551, 2002. `https://doi.org/10.1039/b202610d`.

[318] C.R. Martinez and B.L. Iverson. Rethinking the term “pi-stacking”. *Chemical Science*, 3(7):2191–2201, 2012. `https://doi.org/10.1039/C2SC20045G`.

[319] C.F. Macrae, I. Sovago, S.J. Cottrell, P.TA. Galek, P. McCabe, E. Pidcock, M. Platings, G.P. Shields, J.S. Stevens, and M. Towler. Mercury 4.0: From visualization to analysis, design and prediction. *Journal of Applied Crystallography*, 53(1):226–235, 2020. `https://doi.org/10.1107/S1600576719014092`.

[320] A. Gavezzotti and G. Filippini. Geometry of the intermolecular X-H$\cdot\cdot\cdot Y(X, Y = N, O)$ hydrogen bond and the calibration of empirical hydrogen-bond potentials. *The Journal of Physical Chemistry*, 98(18):4831–4837, 1994. `https://doi.org/10.1021/j100069a010`.

[321] A. Gavezzotti. Are crystal structures predictable? *Accounts of Chemical Research*, 27(10):309–314, 1994. `https://doi.org/10.1021/ar00046a004`.

[322] S.S. Batsanov. Van der Waals radii of elements. *Inorganic Materials*, 37(9): 871–885, 2001. `https://doi.org/10.1023/A:1011625728803`.

[323] R.J. Angel, R.T Downs, and L.W. Finger. High-Temperature–High-Pressure Diffractometry. *Reviews in Mineralogy and Geochemistry*, 41(1):559–597, 2000. `https://doi.org/10.2138/rmg.2000.41.16`.

[324] M. Mikolasek, M.D. Manrique-Juarez, H.J. Shepherd, K. Ridier, S. Rat, V. Shalabaevaand A.-C. Bas, I.E. Collings, F. Mathieu, and J. Cacheux. Complete set of elastic moduli of a spin-crossover solid: Spin-state dependence and mechanical actuation. *Journal of the American Chemical Society*, 140(28): 8970–8979, 2018. `https://doi.org/10.1021/jacs.8b05347`.

[325] J. Laisney, H.J. Shepherd, L. Rechignat, G. Molnár, E. Rivière, and M.L. Boillot. Pressure-induced switching properties of the iron (III) spin-transition complex [Fe^{III} (3-OMeSalEen)$_2$] PF_6. *Physical Chemistry Chemical Physics*, 20(23):15951–15959, 2018. `https://doi.org/10.1039/C8CP02376J`.

[326] P. Guionneau, M. Marchivie, Y. Garcia, J.A.K. Howard, and D. Chasseau. Spin crossover in [Mn^{III}(pyrol)$_3$tren] probed by high-pressure and low-temperature x-ray diffraction. *Physical Review B*, 72(21):214408, 2005. `https://doi.org/10.1103/PhysRevB.72.214408`.

[327] Y. Garcia, V. Ksenofontov, G. Levchenko, G. Schmitt, and P. Gütlich. Pressure-Induced High Spin State in [Fe (btr)$_2$ (NCS)$_2$]. H_2O (btr= 4, 4'-bis-1, 2, 4-triazole). *The Journal of Physical Chemistry B*, 104(21):5045–5048, 2000. `https://doi.org/10.1021/jp0004922`.

[328] W.L. Bragg, C.G. Darwin, and R.W. James. The intensity of reflexion of X-rays by crystals. *Philosophical Magazine and Journal of Science*, 1(5):897–922, 1926. `https://doi.org/10.1107/S0567739469000039`.

[329] W. Nicolazzi and A. Bousseksou. Thermodynamical aspects of the spin crossover phenomenon. *Comptes Rendus Chimie*, 21(12):1060–1074, 2018. `https://doi.org/10.1016/j.crci.2018.10.003`.

[330] P. Müller, R. Herbst-Irmer, A. Spek, T. Schneider, and M. Sawaya. *Crystal Structure Refinement: A Crystallographer's Guide to SHELXL*, volume 8. Oxford University Press, Oxford, UK, 2006. ISBN 978-0-19-857076-9.

[331] D. Chernyshov, V. Dyadkin, and K.W. Törnroos. Sequential SHELXL refinement of consecutive data sets: a tool to probe dynamically evolving single-crystal structures. *Acta Crystallographica Section A: Foundations of Crystallography*, 75:e678, 2019.

[332] K. Boukheddaden, I. Shteto, B. Hôo, and F. Varret. Dynamical model for spin-crossover solids. I. Relaxation effects in the mean-field approach. *Physical Review B*, 62(22):14796, 2000. `https://doi.org/10.1103/PhysRevB.62.14796`.

[333] N. Klinduhov, D. Chernyshov, and K. Boukheddaden. Choice of dynamics for spin-crossover systems. *Physical Review B*, 81(9):094408, 2010. `https://doi.org/10.1103/PhysRevB.81.094408`.

List of Figures

List of Tables

Acknowledgments

In my three years as a PhD, I have encountered many people. There isn't one person on this journey that I haven't learnt something from and for that, I owe a thank you to everyone who has been with me over the years. I would like to express my gratitude to a few particular people.

To my supervisor, **Apl. Prof. Dr. Karen Friese**, I don't think I ever really thanked you for taking me under your wing and offering me this PhD position to start with, so I can thank you now. I can only hope you haven't regretted it. For the last three years, you have been really patient with me and you have taught me a lot. I have done my best to hold on to every word of wisdom you have imparted. Every thesis probably has this same line about you, and whilst it sounds generic, there are no better words; thank you for being the best supervisor anyone could ask for, for your advice and guidance throughout. For being on the other side of a door-knock or the other end of an email, regardless of the day or time. For never underestimating me and mostly, for getting me to this point where I can say I have a PhD. Needless to say, it couldn't have been done without you. Thank you for this PhD. It has been an honor to work with you.

Prof. Dr. Thomas Brückel for giving me the opportunity to work at his institute.

Prof. Dr. Georg Roth for agreeing to be the second reviewer of my thesis.

I extend my heartfelt gratitude to **Dr. Andrzej Grzechnik**, for his invaluable support in preparing DACs, assisting with experimental and analytical tasks, and actively participating in all my beamtimes. I am also grateful to you for generously opening your home to me and my family and hosting parties.

My deepest gratitude goes to the beamline scientist **Dr. Dmitry Chernyshov**, who not only provided support during our beamtimes but followed our work closely, always contributing significantly to its enrichment.

My very sincere thanks go to **Prof. Dr. Manuel Angst** for consistently offering his time and understanding to engage in fruitful discussions, correcting my thesis, and participating in beamtime.

To **Dr. Pulkit Parkash**, there's a long list of all that I'm thankful for to you, a few lines can't possibly summarise it. Thank you for training me on drilling and loading DACs, for the beamtimes at the ESRF and Karlsruher, and for all your continuous advice and feedback, physics-related and other. For helping me with a problem related to my research projects and my personal life when I was stuck.

My sincere thanks are extended to members of the spin crossover group **Dr. Jörg**

Voigt, **Dr. Ji Qi**, **Jörg Perßon**, and previous members **Dr. Neetika Sharma** for their support, valuable contributions, and engaging discussions during our weekly meetings.

My past and present colleagues at JCNS-2, especially **Dr. Andreas Eich** for helping me get started at the Forschungszentrum, for training me on the X-ray diffractometer, gluing and mounting crystals, for all the general lab advice, for participating in our beam at the PSI Synchrotron, **Viliam Hakala** and **Yifan Xu** for making sharing an office for so long a pleasant experience. In addition, colleagues from RWTH Aachen **Sophia Kurig** and **Katharina Eickmeier** for participating in P24, DESY beamtime.

I would also like to thank **Prof. Michael Ohl** from JCNS-1 for carrying out the calorimetric measurements.

Prof. Karl Wilhelm Törnroos, for his keen interest in our research. I am particularly thankful for his generous offer to measure our samples during his beamtimes, which proved to be unintentionally crucial for this thesis.

Dr. Carsten Paulmann, **Dr. Denis Sheptyakov**, and **Antonio Cervellino** for their support during my beamtimes at P24 (DESY), HRPT (PSI), and X04SA-MS (PSI), respectively.

I am sincerely thankful to **Dr. Dmitry Chernyshov** (who gets a double mention), **Dr. Vadim Diadkin**, **Dr. Charlie McMonagle**, and all the SNBL staff for their kind support during the measurements conducted at the SNBL, ESRF, Grenoble.

I extend special thanks to our collaborator at RWTH Aachen University, **Prof. Ulli Englert**, and express gratitude to **Dr. Hans Gildenast** for their valuable contribution to the synthesis of the samples.

To **Mrs. Barbara Daegener**, our secretary, who has diligently managed all the paperwork with unwavering dedication. **Berthold Schmitz** and **Micha Hölzle** for their help with various technical issues, often on very short notice.

Prof. Shibabrata Nandi and **Dr. Oleg Petracic** for helping with the work on the DynaCool and MPMS instruments. I am grateful to **Dr. Emmanuel Kentzinger** for giving me the opportunity to contribute to organizing the JCNS-2 seminar. Additionally, to **Dr. Paul Zakalek** and **Dr. Connie Bednarski-Meinke**, for their help and assistance.

It is my deepest gratitude to **Prof. Ghaleb Natour**, who has been responsible for the establishment of the Palestinian German Science Bridge (PGSB) and the scholarship which has allowed me to pursue my PhD. His unwavering commitment to fostering scientific collaboration has not only provided financial support but has also been a cornerstone in shaping the future of aspiring researchers like myself, and I am sincerely thankful for the opportunities he has facilitated. Additionally, I would like to express my heartfelt appreciation to **Dr. Cate Morgan**, whose assistance has been invaluable in various aspects of my journey.

To my Palestinian supervisor, **Prof. Ghassan Saffarini**, it was because of my master's project under your supervision that I decided to embark upon this PhD, so thank you for that motivation.

I particularly would like to thank my dear friend **Asma** for her special friendship; my life in Jülich would not have been that colorful without her. My friends, **Mai**, **Neetika** (beyond her role as a postdoctoral researcher), **Nandan**, **Ronja**, **Jörgen**, **Natacha**, and **Max**, you are an important part of my life. I am very grateful for your help in getting me through the difficult times and for all the emotional support and care you have provided.

I would like to express my deepest gratitude to my dearest **Mutaz**. I wholeheartedly acknowledge that this thesis would not have been possible without you. I admit that the accomplishment of this thesis is not just mine but a shared achievement, and I am immensely grateful for the significant role you played in making it a reality. Without you, I would not be where I am today.

Finally, a special thought for the ones that were always there by my side. Dad, thank you for your support over these years and for being my source of motivation. I know things haven't been easy, but things always worked out for the better in the end. Through thick and thin, Allah has always been with us. I hope you are proud! To my mom and my brother, I cannot thank you enough. To my little man, **Danial**, you have motivated me to achieve my goals, so I dedicate this thesis to you.

Thanks to all the people I have met who have offered me even a smile to brighten my day.

List of Publications

- **H. Shahed**, N. Sharma, M. Angst, J. Voigt, J. Perßon, P. Prakash, K. W. Törnroos, D. Chernyshov, H. Gildenast, M. Ohl, G. Saffarini, A. Grzechnik and K. Friese. Structural insight into the cooperativity of spin crossover compounds. *Acta Cryst. B* **B79**:354–367, **2023**.
- A. Eich, A. Grzechnik, S. Yixi, B. Ouladdiaf, D. Sheptyakov, T. Wolf, V. Petricek, **H. Shahed** and K. Friese. Incommensurate magnetic structure of CrAs at low temperatures and high pressures. *Acta Cryst. B* **B79**(6):473–481, **2023**.
- A. Grzechnik, V. Dmitriev, M. Hanfland, T. Geise, **H. Shahed** and K. Friese. Anti-isostructural phase transition and twinning in CrAs at low temperatures and high pressures. *Chem. Solids* **180**:111436, **2023**.
- A. Grzechnik, V. Petříček, D. Chernyshov, C. McMonagle, T. Geise, **H. Shahed** and K. Friese. Incommensurate structures and radiation damage in $Rb_2V_3O_8$ and $K_2V_3O_8$ mixed-valence vanadate fresnoites. *Acta Cryst. B* **B79**:104–113, **2023**.

Appendix A

Theory

The Brillouin function $B_J(x)$ is defined by:

$$B_J(x) = \frac{2J+1}{2J}\coth\left(\frac{2J+1}{2J}x\right) - \frac{1}{2J}\coth\left(\frac{x}{2J}\right) \tag{A.1}$$

with

$$x = \frac{g_J \mu_B B}{k_B T} J \tag{A.2}$$

where , k_B is the Boltzmann's constant, and B is the magnetic field.

Weiss proposed the concept of the molecular field (B_{mf}). Each individual moment will experience an effective field that is a superposition of the effects of its interactions with all of the other moments that are present in the material. Weiss hypothesized that the strength of this "effective field" is directly related to the magnetization of the material. Thus, the net field experienced by a moment is the result of the applied field B_0 and the molecular field B_{mf}, where:

$$B_{mf} = \lambda M_s \tag{A.3}$$

Furthermore, constant λ is called the molecular field constant or the Weiss field constant.

$$B_{tot} = B_0 + \lambda M_s \tag{A.4}$$

Here, B_0 is the external magnetic field. To obtain the spontaneous magnetization, B_0 is set to be zero.

Thus, Equation A.2 can be written as:

$$x = \frac{g_J \mu_B \lambda M}{K_B T} J \tag{A.5}$$

Therefore,

$$M = \frac{K_B T}{g_J \mu_B \lambda J} x \tag{A.6}$$

By combining Equation 4.12 and Equation 4.13, the magnetization of the material can be expressed as follows:

$$M = n g_J \mu_B J \; B_J(x) \tag{A.7}$$

The solution M is obtained by the intersection of the M versus x curves of both Equations A.6 and A.7. As depicted in Figure 4.7, M takes a non-zero value below the critical temperature, denoted as T_C, where the tangent line of the Brillouin function coincides with the slope of the linear line of $M = \frac{K_B T}{g_J \mu_B \lambda J} x$.

The Taylor expansion of the Brillouin function is expressed as the following:

$$B_J(x) = \frac{2J+1}{3J} x - \frac{[(1+J)^2 + J^2](J+1)}{90J^3} x^3 \tag{A.8}$$

For small x (small B, high T), we see that $B_J(x) \approx \frac{(J+1)}{3J} x$. Consequently, for simplicity, the first term is retained only.

$$M = n g_J \mu_B J \; B_J(x) = n g_J \mu_B J \times \frac{1+J}{3J} \times \frac{J g_J \mu_B B}{K_B T} = \frac{n g_J^2 \mu_B^2 J(J+1) B}{3 K_B T} \tag{A.9}$$

Therefore, at the critical temperature (T_C) the two slops are equal, and thus:

$$\frac{K_B}{g_J \mu_B \lambda J} T_C = n g_J \mu_B J \frac{(1+J)}{3J} \tag{A.10}$$

The critical temperature (T_C) is so-called the Curie temperature.

$$T_C = \frac{n (g_J \mu_B J)^2 \lambda}{K_B} \frac{(1+J)}{3J} \tag{A.11}$$

Using Equation A.9 (recall that $B = \mu_0 H$, where μ_0 is the permeability of free space), the magnetic susceptibility is given as:

$$\chi = \frac{n \mu_0 g_J^2 \mu_B^2 J(J+1)}{3 K_B T} = \frac{C}{T} \tag{A.12}$$

We see that in the small-field, high-temperature regime, the susceptibility is independent of the field and is inversely proportional to the temperature. Equation A.13 is called Curie's law. The constant of proportionality C is called Curie's constant and is given by:

$$C = \frac{n \mu_0 g_J^2 \mu_B^2 J(J+1)}{3 K_B} \tag{A.13}$$

Figure 4.8 shows a schematic plot of $1/\chi$ vs. T, with a straight line through the origin. Curie's constant can be determined from its slope. This may be rewritten by introducing the effective magnetic moment of an atom, which is characterized by total-angular-momentum quantum number J.

$$\mu_{eff} = g \mu_B \sqrt{J(J+1)} \tag{A.14}$$

Thus, Curie's constant can be expressed as:

$$C = \frac{N_A g^2 \mu_B^2}{3 k_B} J(J+1) \tag{A.15}$$

$$\Longrightarrow C = \frac{N_A}{3 k_B} \mu_{eff}^2 \tag{A.16}$$

According to Equations A.13 and A.14, this leads to:

$$\mu_{eff} = \sqrt{\frac{3k_B}{N_A}}\sqrt{C} = 2.828\sqrt{C} \tag{A.17}$$

Appendix B

Measurement and Refinement Details

Table B.1: Experimental parameters for monoclinic polymorph and orthorhombic polymorph (first and second run) carried out at the SNBL at ESRF.

	Monoclinic	Orthorhombic
Scan rate (K/min)	6	6
ω-scan range (°)	0-360	0-360
Scan width (°)	0.5	1
Exposure time (s)	0.5	0.5
Waiting time (min)	1.5	2
Temperature steps (K)	3	5

Table B.2: List of the experimental parameters used for the scans in the pressure-dependent synchrotron X-ray single-crystal measurements for the monoclinic (denoted as "**M**") and the orthorhombic polymorph (denoted as "**O**") at P24, PETRA III, DESY, using the Boehler-Almax type DAC. The only difference between runs of the two polymorphs is the exposure time: 12 s for the monoclinic polymorph 8 s for the orthorhombic one. respectively.

	scan									
No.	angle	start	end	width	**M** t_{exp}	**O** t_{exp}	2θ	χ	ω	κ
#1	ϕ	48°	132°	0.5°	12 s	8 s	0°	0°	90°	0°
#2	ϕ	228°	312°	0.5°	12 s	8 s	0°	0°	90°	0°

No.	angle	start	end	width	**M** t_{exp}	**O** t_{exp}	2θ	χ	ϕ	κ
#3	ω	−42°	42°	0.5°	12 s	8 s	0°	90°	0°	109.47°
#4	ω	−42°	42°	0.5°	12 s	8 s	0°	90°	180°	109.47°

Appendix C

Data processing

C.1 Least square approach

Based on the atomic model, Fourier transformation is used to calculate the structure factors. By comparing the calculated intensities with the measured intensities, the best model is determined as the one that provides the minimum value for the minimization function M [330].

$$M = \sum w(F_o^2 - F_c^2)^2 \tag{C.1}$$

or

$$M = \sum w(|F_o|^2 - |F_c|^2)^2 \tag{C.2}$$

F_o and F_c are the observed and calculated structure factors, and w is the weighting factor related to the standard deviation σ.

It is worth noting that weak reflections might be assigned negative intensity due to a high background during data integration. Consequently, refining against F might be problematic since F incorporates the square root of negative intensity. To address this, negative intensities should be set to zero or assigned a very small arbitrary value. Weak reflections do carry information, and discarding them can influence the crystal structure.

The refinement against F introduces another problem. Due to the high sensitivity of least square refinement to reflection weights (Equations C.1 and C.2), any uncertainty in σ(F) estimation can create inaccuracies in refinement. The difficulty arises from estimating σ(F) from $\sigma(\mathrm{F}^2)$. $\sigma(\mathrm{F}^2)$ is determined during data reduction.

C.2 Processing of temperature-dependent single crystal x-ray data

C.2.1 Integration methodology for multiple data set

Here is a step-by-step guide on how to perform sequential data reduction with a large data set using *CrysAlis*^{Pro}:

- Import Data: From the multiple data sets, select "the lowest temperature file".
- Define Data Processing Parameters: Once the first data is imported, the "Data integration" should be carried out (see Section 6.4.2) with adjusting parameters according to the specific experimental setup and requirements. This should be followed by data reduction, where scaling and absorption correction is applied.
- Set up Batch Processing: Once the lowest temperature data set is integrated, typing the command **xx proffitbatch** in the command shell will open a new window with a file named "**proffitbatch.mac**" where the output directories for all data sets can be specified.
- Run Batch Processing: Type in the command shell **script** then select the file which has created in the previous stage (**proffitbatch.mac**). This initiates the sequential data reduction process. A batch file is created which can read in experimental data, and processes the data sequentially, with the orientation matrix for the second dataset based on the orientation matrix of the first dataset, and so on. (The orientation matrix is refined at every point and transferred to the next temperature). This batch processing can be monitored with viewing any error messages which might arise.
- Export Processed Data: Once satisfied with the processed data sets, they can be exported for further analysis or structure determination.
- Extracting Data: The *seq shel* software can be used to extract the unit cell information versus temperature for tables or plots.

C.2.2 Sequential refinement of variable temperature diffraction data using SHELXL and seq_Shell Software

The sequential refinement of large amounts of temperature dependent diffraction data using SHELXL [309] with the seq_Shell software [331] involves the following steps:

- Initial Refinement: The refinement process starts with the most appropriate starting data set, typically the one obtained at the lowest temperature. This data set is refined using SHELXL to obtain an initial refined structural model.
- Batch refinement: The command prompt is used to initiate the seq_shel software for a sequential refinement of each subsequent data set in the series. The seq_shel software works via the following steps:

1. Copy ***.res** to ***.ins**: The structure file (***.res**) is copied as the input file (*.ins) for the next temperature data set. This ensures that the structural model from the previous refinement is used as the starting point for the next refinement.
2. Update Unit Cell Dimensions: The unit cell dimensions are updated in the newly created *.ins file. The updated unit cell dimensions are obtained from the *CrysAlis*^{Pro}***.par** file.
3. Run ShelXL: The ShelXL software is executed using the updated ***.ins** file as input. ShelXL performs the refinement based on the specified parameters and generates refined structural models.
4. Repeat Steps 1-4: The refinement process is repeated for each subsequent temperature data set. The output from each refinement is saved for further analysis.
5. Data extraction: seq_shel software can extract numerical information or any parameter from any specific line of the CIFs for tables or graphs.

C.3 Processing of pressure dependent single crystal x-ray data

C.3.1 Conversion of XRD Images with the CrysAlisPro Software

For data from P24, from EH1

The red rectangles in the Figure C.1 represent the steps and parameters that have to be set up in a proper configuration for importing and processing Pilatus 1M frames (*.cbf) with *CrysAlis*^{Pro}. For this, open *CrysAlis*^{Pro} and load any *.par file. By following these steps:

1. Choose an input image format with the appropriate configuration, in this case "Sapphire 2048 × 20248 1 × 1 binning."
2. On the left side toolbar, click the "Image Import" icon.
3. Choose "Import" option.
4. Select the Multi-settings option. Then, OK.
5. Choose the image format. It could be cetrian MAR images, Bruker SAXI, ESPERANTO, etc. Select "DECTRIS/PILATUS" from the drop-down menu.
6. Click on "Add N Runs" and enter the location of the experiment's first and last frames. A new window will open for each run list, and one should proceed following steps (7-10) for each run.
7. Set alpha and Beta [deg] to 90 and 0. This simulates a theoretical Eulerian diffractometer.
8. Enable "Scan info" and select the proper Scan type. For example, use the "Phi" scan and provide the values for "omega", "Theta", and "Kappa" (all should refer Eulerian geometry).
9. Provide the starting angle, the step size and the exposure time of the scan.
10. Then press OK!
11. For "Esperanto output". Select 90 for "Rotation [deg]".
12. Enable "Flip horizontal (square with value -1)".
13. For "Detector info and Auto-gap detection". Enter the detector's pixel size in mm (0.172).
14. Provide the parameters of the Beamstop x_0=x_0 + 32 (520) and y_0=y_0 (533).
15. Check the "overflow" box and set it to be larger than (20000).
16. Check "Use the auto-gap detection" with value -1.

17. For the "Instrument common info". Enable "synchrotron" for the instrument type and provide the x-ray wavelength.
18. Set "Gain" to 1.
19. Select "Mirror/SYNCHROTRON/MICRO_ED" from the drop down menu of the Monochromator.
20. Set "Polfact" the polarization factor to 0.02.
21. Provide the sample to detector distance in mm.
22. Check "HPAD, module thickness" and set it to 1.
23. Check for "CdTe" detector.
24. Start the conversion procedure.

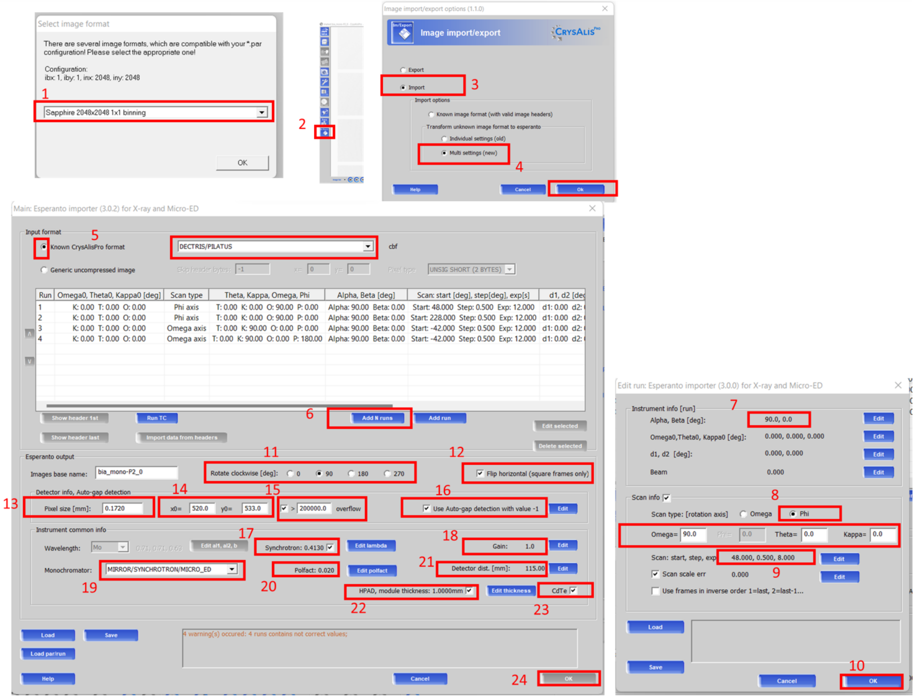

Select image format

There are several image formats, which are compatible with your *.par configuration! Please select the appropriate one!

Configuration:
ibx: 1, iby: 1, inx: 2048, iny: 2048

1 Sapphire 2048x2048 1x1 binning

Image import/export options (1.1.0)

○ Export
3 ● Import

Import options
○ Known image format (with valid image headers)
Transform unknown image format to esperanto
○ Individual settings (old)
4 ● Multi settings (new)

Main: Esperanto importer (3.0.2) for X-ray and Micro-ED

Input format
5 ● Known CrysAlisPro format — DECTRIS/PILATUS — cbf
○ Generic uncompressed image — Skip header bytes: -1 — x= 0 — y= 0 — Pixel type: UNSIG SHORT (2 BYTES)

Run	Omega0, Theta0, Kappa0 [deg]	Scan type	Theta, Kappa, Omega, Phi	Alpha, Beta [deg]	Scan: start [deg], step[deg], exp[s]	d1, d2 [deg
1	K: 0.00 T: 0.00 O: 0.00	Phi axis	T: 0.00 K: 0.00 O: 90.00 P: 0.00	Alpha: 90.00 Beta: 0.00	Start: 48.000 Step: 0.500 Exp: 12.000	d1: 0.00 d2:
2	K: 0.00 T: 0.00 O: 0.00	Phi axis	T: 0.00 K: 0.00 O: 90.00 P: 0.00	Alpha: 90.00 Beta: 0.00	Start: 228.000 Step: 0.500 Exp: 12.000	d1: 0.00 d2:
3	K: 0.00 T: 0.00 O: 0.00	Omega axis	T: 0.00 K: 90.00 O: 0.00 P: 0.00	Alpha: 90.00 Beta: 0.00	Start: -42.000 Step: 0.500 Exp: 12.000	d1: 0.00 d2:
4	K: 0.00 T: 0.00 O: 0.00	Omega axis	T: 0.00 K: 90.00 O: 0.00 P: 180.00	Alpha: 90.00 Beta: 0.00	Start: -42.000 Step: 0.500 Exp: 12.000	d1: 0.00 d2:

Esperanto output
Images base name: bia_mono-P2_0
11 Rotate clockwise [deg]: ○ 0 ● 90 ○ 180 ○ 270
12 ☑ Flip horizontal (square frames only)

Detector info, Auto-gap detection
13 Pixel size [mm]: 0.1720
14 x0= 520.0 y0= 533.0
15 ☑ > 200000.0 overflow
16 ☑ Use Auto-gap detection with value -1

Instrument common info
Wavelength: Mo 0.71 0.71 0.63
17 Synchrotron: 0.4130 ☑
18 Gain: 1.0
19 Monochromator: MIRROR/SYNCHROTRON/MICRO_ED
20 Polfact: 0.020
21 Detector dist. [mm]: 115.00
22 HPAD, module thickness: 1.0000mm ☑
23 CdTe ☑

4 warning(s) occured: 4 runs contains not correct values;

Edit run: Esperanto importer (3.0.0) for X-ray and Micro-ED

Instrument info [run]
7 Alpha, Beta [deg]: 90.0, 0.0
Omega0,Theta0, Kappa0 [deg]: 0.000, 0.000, 0.000
d1, d2 [deg]: 0.000, 0.000
Beam 0.000

Scan info ☑
8 Scan type: [rotation axis] ○ Omega ● Phi
Omega= 90.0 Phi= 0.0 Theta= 0.0 Kappa= 0.0
9 Scan: start, step, exp 48.000, 0.500, 8.000
☑ Scan scale err 0.000
☐ Use frames in inverse order 1=last, 2=last-1...

Figure C.1: A dialog for converting XRD images collected on the P24 beamline, at PETRA III synchrotron to ESPERANTO *CrysAlis*^{Pro} format. Red rectangles show the parameters which one has to set up for the appropriate conversion.

C.3.2 Peak indexing for high pressure data

There are several options for indexing:

- Automatic indexing that considers all detected peaks.
- Search for a known unit cell while taking into account all identified peaks.
- Automatic indexing after excluding the diamond and ruby reflection from the peaks table.
- Setting the orientation matrix manually (for example, if the prior pressure point is known).
- Manual unit cell selection using **Ewald Explorer**.

If automated indexing fails but the approximate lattice parameters are known, the command **um searchcell** can be used to search for the known unit cell.

If the search for a known cell fails to produce a reasonable result (due to a large number of peaks that do not belong to the sample) or if the lattice parameters are unknown, the user should determine which peaks belong to a diamond or ruby and eliminate them first. For this, it is practical to examine the peak table by typing **pt e** in *Command Shell.* Typically, diamond peaks have the highest intensities and they can be removed using intensity filter.

Ewald Explorer is a very useful tool for distinguishing sample peaks from diamond and ruby peaks; it is activated by entering **pt ewald**. Initially, it is necessary to investigate histograms displaying the distributions of intensities and d-values(Figure C.2). Consequently, the cluster of extremely intense reflections in the upper histogram of Figure C.2 corresponds probably to diamond peaks, whereas the numerous peaks at specific d-values (lower histogram of Figure C.2) are frequently contributions of the powder rings of the gasket (appearing at fixed angle), which produces numerous and intense reflections at the characteristic d-values.

By dragging the mouse on the corresponding histograms, reflections can be omitted. Since many peaks constituting the arcs have same d-values, they are not effectively cleaned using the distribution histograms, and should be removed by hand. The most convenient option for this is to use Ewald Explorer. The reciprocal space can be rotated in a way that one can see the rows of sample peaks. Then unwanted peaks can be skipped. Peaks flagged skip will not be considered for the unit cell findings.

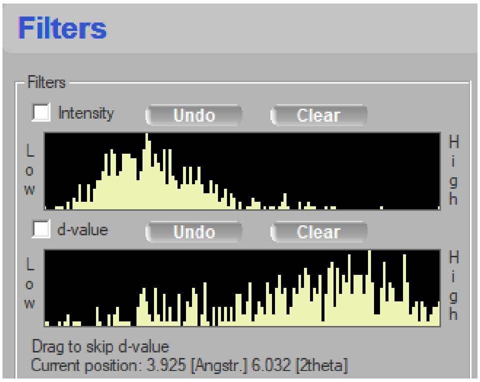

Drag to skip d-value
Current position: 3.925 [Angstr.] 6.032 [2theta]

Figure C.2: Histograms displaying the distribution of intensities and d-values.

To copy the orientation matrix from a previous pressure point the command **ty u** is used to print the orientation matrix, the command **um s** is used to set the orientation matrix for the data set. The matrix can then be refined by the command **um i**.

C.3.3 Data integration

During the integration process, the **Edit DAC angle** command is used to set the DAC opening angle. For the Boehler-Almax DAC, the value 40-45 is employed and for the YaoDAC, the value 53-60 is utilized. Nevertheless, one should take care of numerous things before the final integration:

- Skip areas shaded by additional equipment (e.g. burned areas of the detector).
- Set up the beamstop mask correctly.
- Ensure that the integration parameters are the most appropriate for the current data.

The command **script**, can be used to skip the undesired regions. Click **Options RED** in *CMD*, choose the tab **Beam stop**, and turn on **Put beam stop overlay** to define the beam stop. Using the tabs in the same window, change the orientation and size of the beam stop.

C.3.4 Background evaluation

The procedure of determining the average background in *CrysAlis*^{Pro} is governed by two parameters: the evaluation range **Re** and the repeat frequency **Fr**. The evaluation range determines the number of frames used to compute a single background image, whereas the repeat frequency indicates the number of times the procedure is repeated. By default, **Re**=**Fr** equals 25. Typically, for high-pressure data, these values must be substantially lower. In the case of high-pressure data collection relatively stable background, Re=Fr=5 has proved to be useful.

C.3.5 Outlier rejection

Although high-pressure data are typically not very redundant, it is still possible to apply outlier rejection in the case of high symmetry structures. Identifying and rejecting these outlying intensities is crucial for a successful structure solution and high pressure data refinement. This option can be selected during the data integration procedure. Click **Use outlier rejection** and the Laue group. If one is uncertain about the precise symmetry, one should not select this option.

C.3.6 Data Reduction

In general, **dc proffit** executes fully automated data reduction procedures, which involves frame scaling. Nevertheless, *CrysAlis*^{Pro} comes with a data finalization tool that one can use to modify certain parameters, carry out numerical absorption correction, and filter the data. The data finalization window has to be activated. This window displays all necessary information on data coverage, completeness, detected outliers, absorption correction model, and any errors and warnings that happened during the data integration, in addition to R_{int} and R_σ. In the **Sample** group, the chemical formula as well as the number of formula units can be set. The absorption correction can be performed by choosing either the "Empirical correction" or "Numerical correction" option under the **Correction** tap. The latter one can be used when crystal faces are determined while the former provides an "Automatic" and a "Manual" correction option. The "Automatic" option employs *SCALE3 ABSPACK* while when using the advanced option in "Manual correction" one can control individual parameter.

Appendix D

Non-equilibrium kinetics for SCO

D.1 Non-isothermal kinetics of spin conversion

The system approaches equilibrium faster than temperature variation if the rate of temperature change is slow. As a result, it is possible to quantify the equilibrium percentage of HS states or $\gamma_{eq}(T)$. When the rate of temperature variation exceeds the system's ability to return to equilibrium, a non-equilibrium fraction of HS states denoted as $\gamma_{ne}(T)$, is measured.

At room temperature ($T_0 = 300\,\mathrm{K}$) a pure HS state ($\gamma_{eq}(T_0) = 1$) is present. After cooling using the ramp rate β, the HS fraction is measured instantaneously. We propose a normalized measurement of spin conversion, which is as follows:

$$\alpha = \frac{1-\gamma}{1-\gamma_{eq}} \tag{D.1}$$

Spin conversion is occurring at the following rate:

$$\frac{d\alpha}{dt} = \frac{d\alpha}{dT}\frac{dT}{dt} = \beta\frac{d\alpha}{dT} = Ae^{\left[-\frac{E_a}{T}(1-\alpha)\right]} \tag{D.2}$$

and

$$\frac{d\alpha}{dT} = \beta\frac{d\alpha}{dT} = \frac{A}{B}e^{\left[-\frac{E_a}{T}(1-\alpha)\right]} \tag{D.3}$$

As equilibrium is reached, (1-α) guarantees that kinetics stops. The expression for a non-isothermal measure of spin conversion obtained by separating variables and integrating is as follows:

$$\int_0^a \frac{d\alpha}{(1-\alpha)} = \frac{A}{\beta}\int_T^{T_0} e^{\frac{-E_a}{T}}\,dT \tag{D.4}$$

Using $I(T, T_0, E_a)$ to represent integral on the right side and considering:

$$\int_0^a \frac{d\alpha}{(1-\alpha)} = -\ln(1-\alpha) \tag{D.5}$$

$$\alpha = 1 - e^{-\frac{A}{\beta}I(T,T_0,E_a)} \tag{D.6}$$

The non-equilibrium proportion of the high-state (HS) as a function of temperature, as determined during cooling, is as follows:

$$\gamma_{ne}^{\uparrow}(T) = \gamma_{eq}(T) + e^{-\frac{A}{\beta}I(T,T_0,E_a)}\left(1 - \gamma_{eq}(T)\right) \tag{D.7}$$

or,

$$\gamma_{ne}^{\downarrow}(T) = e^{-\frac{A}{\beta}I(T,T_0,E_a)} + \gamma_{eq}(T)\left(1 - e^{-\frac{A}{\beta}I(T,T_0,E_a)}\right) \tag{D.8}$$

For a heating branch; we begin with the pure LS condition;

$$\alpha = \frac{\gamma}{\gamma_{eq}} \tag{D.9}$$

As a result, a non-equilibrium fraction of the HS state during heating as a function of temperature is obtained;

$$\gamma_{ne}^{\uparrow}(T) = \gamma_{eq}(T)\left(1 - e^{-\frac{A}{\beta}I(T,T_0,E_a)}\right) \tag{D.10}$$

It is evident that the cooling and heating branches converge on the equilibrium curve with extremely slow ramp rates. It should be noted that the equations above are derived under the assumption that A is independent of both temperature and spin fraction. Boukheddaden et al. [332] assumed that cooperativity is ignored.

Figure D.1 provides an illustration of Equations D.9 and D.10, showing how the cooling curve overlaps the equilibrium and demonstrating the difference in kinetics between the heating and cooling systems, which must begin at distinct temperatures. As a result, one must assume a temperature dependence for A, that is, an unknown function summing up contributions for phonon modes interacting with spin states [332, 333]. The simple model presented above cannot thus fully explain a symmetric expansion of the apparent hysteresis observed experimentally (Figure 7.1). Experimentally, its explicit form can be determined by monitoring the relaxation kinetics of thermally quenched HS states within the spin crossover temperature range.

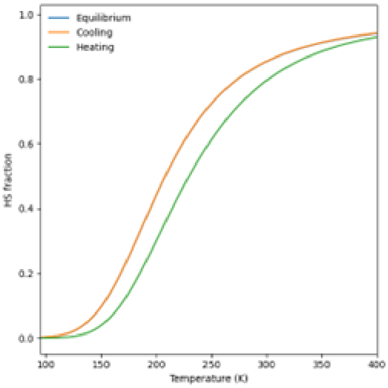

Figure D.1: A spin crossover transition with a low degree of cooperativity with apparent hysteresis (difference between cooling and heating regimes), with parameters taken from Table 7.7 (crystal structure data), A/β 0.025 and $E_a \approx 1000$.

Appendix E

E.1 Effect of thermal cycling

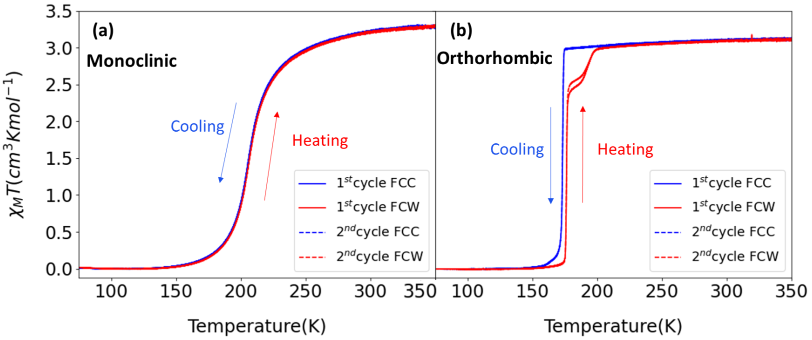

Figure E.1: $\chi_M T$ versus T measured on polycrystalline samples at the scan rate of 0.2 K/min in two consecutive cycles. The measurements were performed with applying a field of $\mu_0 H = 50\,\mathrm{mT}$ in a temperature range between 5 K- 350 K on both polymorphs (monoclinic **(a)** and the orthorhombic **(b)**). The solid blue and the dashed red lines correspond to the cooling and heating cycles, respectively. Diamagnetic and paramagnetic corrections have been applied.

E.2 Effect of different magnetic field

Magnetization measurements were conducted on both the monoclinic and orthorhombic polymorphs under various external magnetic fields. The results are presented in Figures E.2 and E.3 for the monoclinic and orthorhombic polymorphs, respectively. These figures demonstrate that the change in transition temperature ($\Delta T_{1/2}$) in response to the magnetic field (ΔB) is small for both polymorphs: the value of $\Delta T_{1/2}/\Delta B$ for the orthorhombic polymorph is approximately $0.9\,\mathrm{K\,T^{-1}}$, for the monoclinic polymorph, $\Delta T_{1/2}/\Delta B$ is approximately $0.16\,\mathrm{K\,T^{-1}}$.

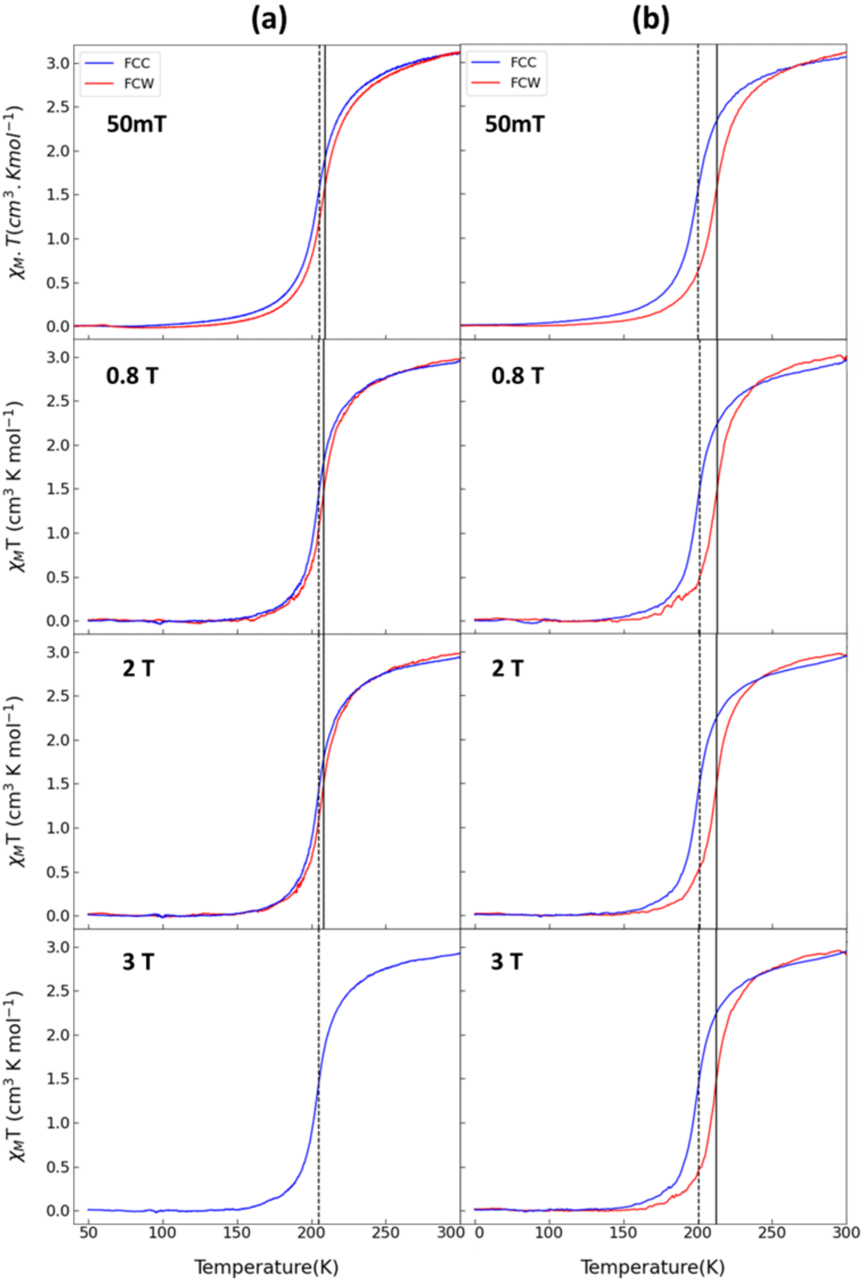

Figure E.2: $\chi_M T$ versus T for a polycrystalline sample of the monoclinic polymorph in different fields 50 mT, 0.8 T, 2 T and 3 T measured with different scan rates **(a)** 2 K/min, **(b)** 10 K/min in both cooling (blue-line) and heating modes (red-line). The dashed and the solid black lines pass through $T_{1/2}$ while cooling and heating, respectively.

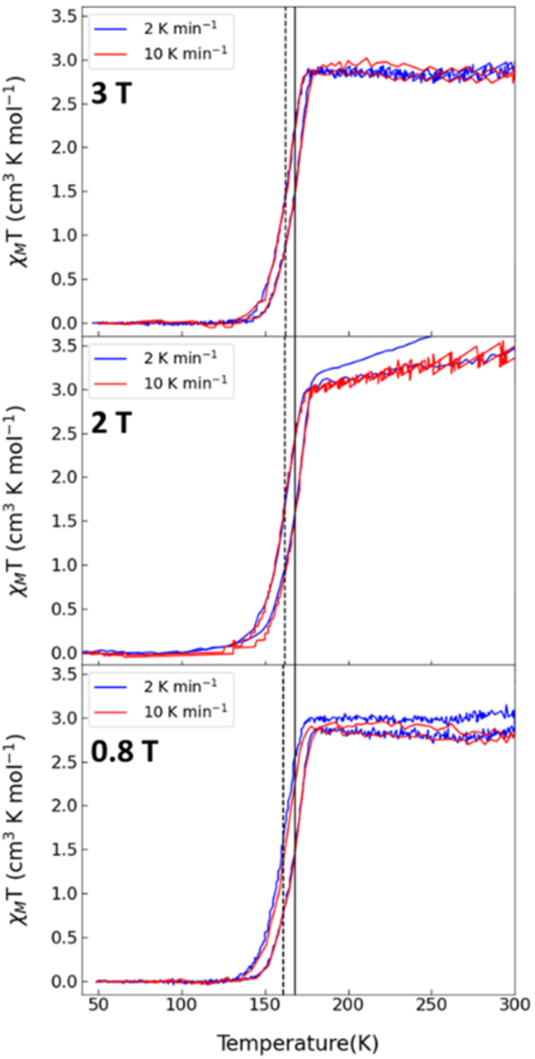

Figure E.3: $\chi_M T$ versus T for a bunch of single crystals of the orthorhombic polymorph in different fields 3 T (top), 2 T (middle), and 0.8T (bottom) measured with different scan rates 2 K/min (blue-line) 10 K/min (red-line) in both cooling and warming modes in blue and red, respectively. The dashed and the solid black lines pass through the $T_{1/2}$ while cooling and heating, respectively.

E.3 DSC measurements

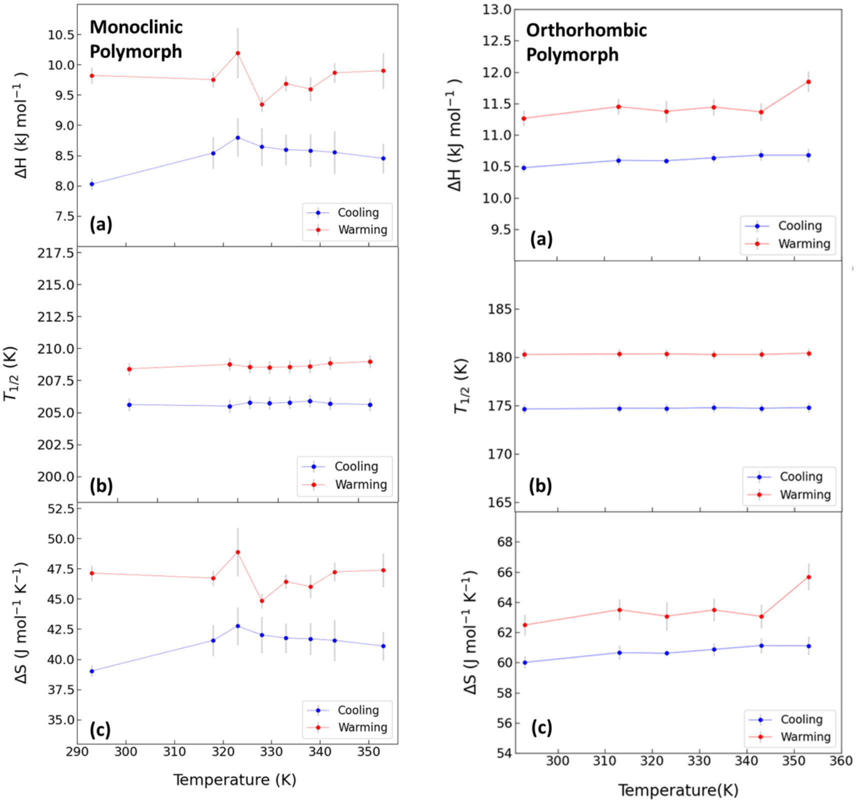

Figure E.4: Enthalpy changes (ΔH) **(a)**, transition temperatures ($T_{1/2}$) **(b)**, and entropy changes (ΔS) **(c)** values obtained during cooling and heating cycles with different maximum temperatures for the monoclinic (left) and the orthorhombic (right) polymorph.

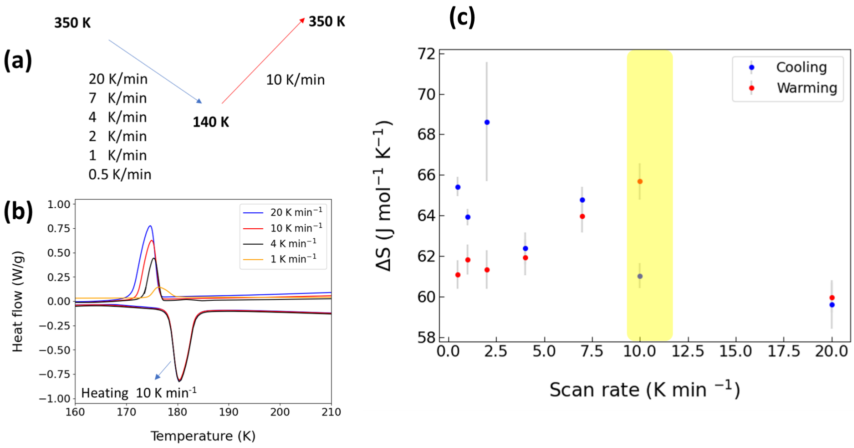

Figure E.5: **(a)** Illustrates the protocol followed in the orthorhombic polymorph measurement. The sample was cooled down with different scan rate of 20 K/min, 7 K/min, 4 K/min, 2 K/min, 1 K/min, and 0.5 K/min and subsequently heated up with a constant rate of 10 K/min. **(b)** Heat flow as a function of temperature depicted for different scan rates during cooling. **(c)** Entropy changes with different scan rates during cooling. The yellow shaded rectangle in **(c)**, represents the results from previous measurements (section 7.2.1) during cooling and heating at a rate of 10 K/min.

E.4 Temperature-dependent crystal structure

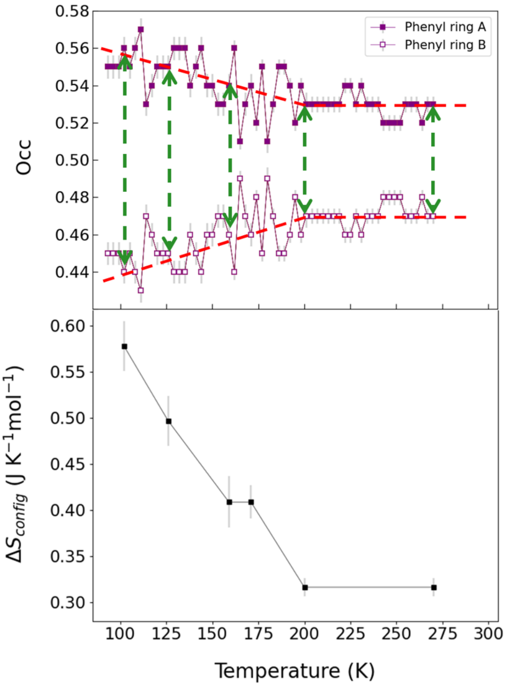

Figure E.6: (Top) Temperature evolution of the occupation probability of the two disordered sites of the phenyl group in the monoclinic polymorph. (Bottom) The change in the configuration entropy ΔS_{config} obtained from the disorder of the two positions of the phenyl rings A and B. It is worth noting that a selected set of points has been calculated for the sake of figure clarity.

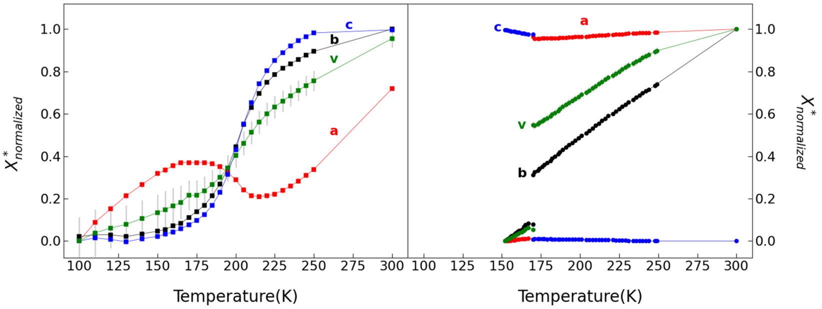

Figure E.7: Evolution of the relative change in the normalized lattice parameters and unit cell volume for the monoclinic (left) and the orthorhombic (right) polymorph. The calculation employs the expression $^*X_{normalized} = \frac{x(LS)-x(T)}{x(LS)-x(HS)}$, where x is the lattice parameters or the unit cell volume. Lines are guides to the eyes. Error bars are the same size or smaller than the symbols.

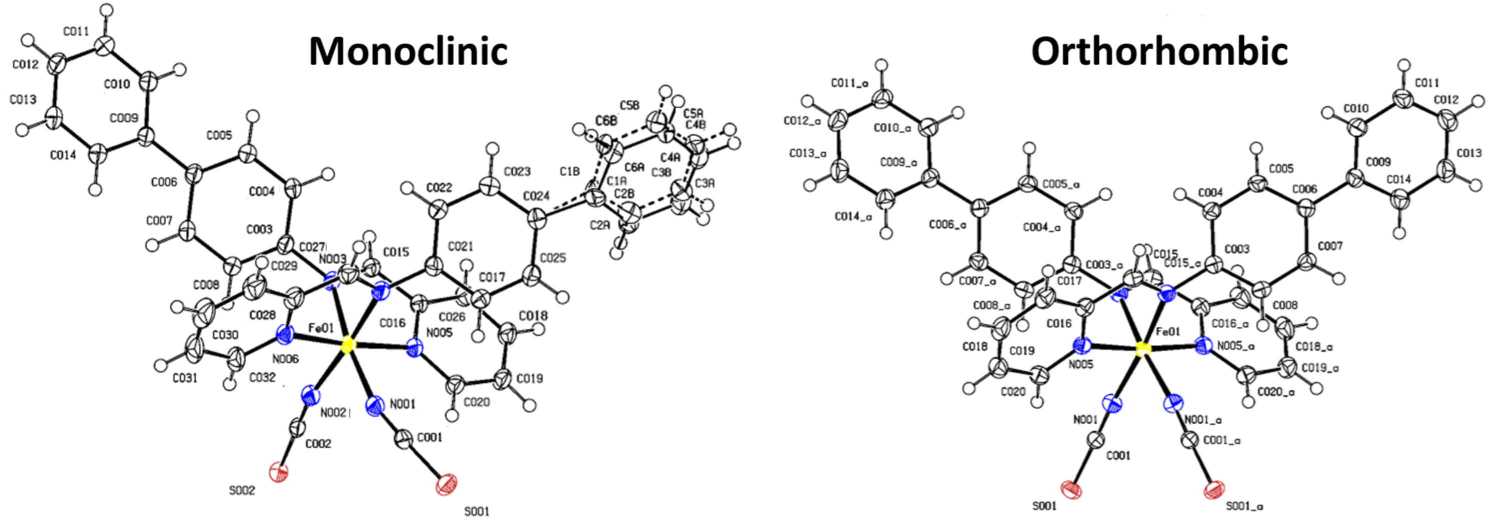

Figure E.8: Schematic diagram of the molecular unit in [Fe(PM-Bia)$_2$(NCS)$_2$]: Monoclinic polymorph (left) and orthorhombic polymorph (right) at a 50% probability level. Thermal ellipsoids are drawn.

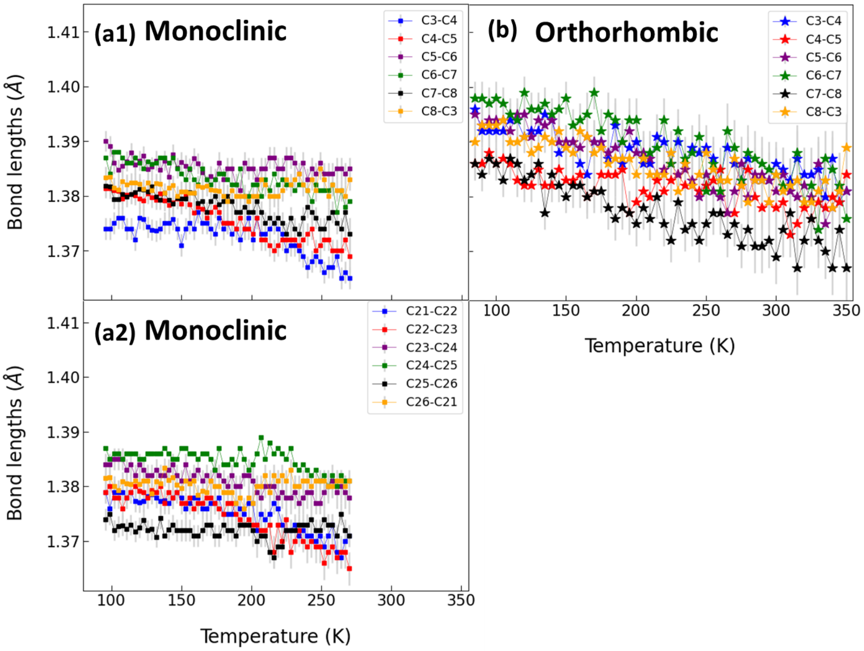

Figure E.9: Temperature dependence of the C-C bond length in the phenyl rings. **(a1)** & **(a2)** monoclinic,**(b)** orthorhombic. Lines are guides to the eyes. See Appendix Figure E.8 for atom labeling.

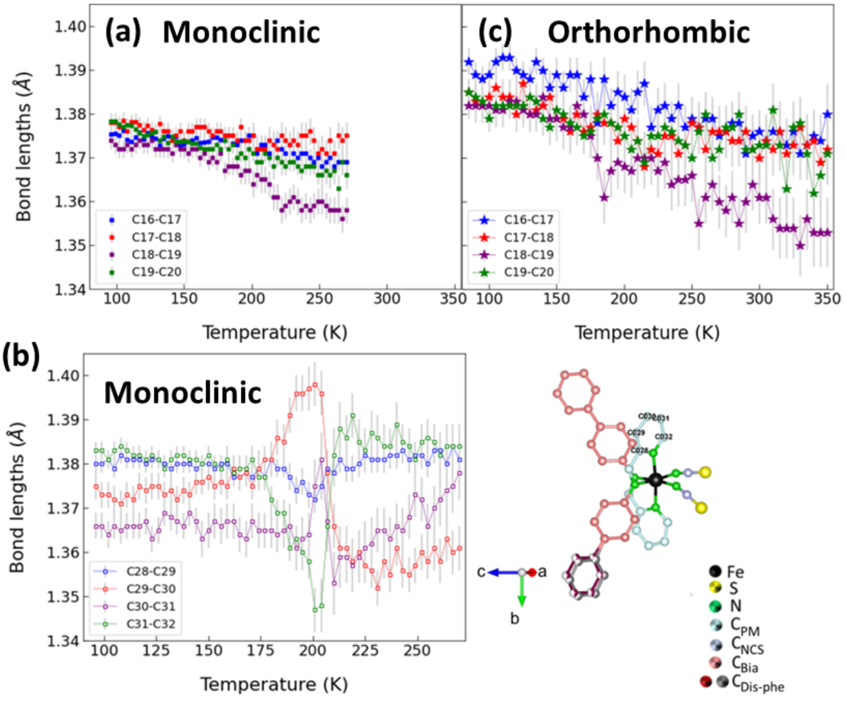

Figure E.10: Temperature-dependence changes of the *C–C* bond length in one pyridine ring **(a)**, **(b)** in the second pyridine ring (linked to the disordered phenyl ring) in the monoclinic polymorph, and **(c)** in the orthorhombic polymorph. Lines are guides to the eyes. See Appendix Figure E.8 for atom labeling.

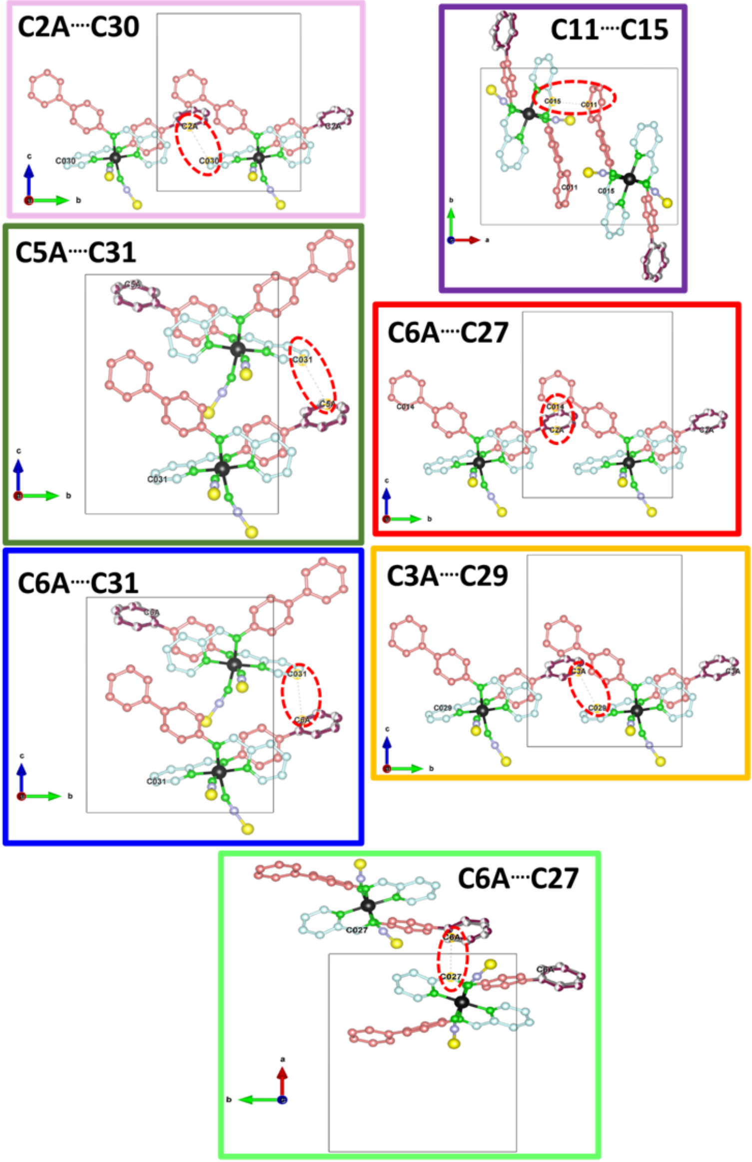

C2A····C30

C11····C15

C5A····C31

C6A····C27

C6A····C31

C3A····C29

C6A····C27

Figure E.11: The shortest $C \cdots\cdot C$ intermolecular distances in the monoclinic polymorph. Contacts are considered short if $C \cdots\cdot C < 3.5$ Å. $C_{27} \cdots\cdot C_{6A}$ and $C_{15} \cdots\cdot C_{11}$ are the shortest contacts in the intersheet layers. $C_{31} \cdots\cdot C_{6A}$, $C_{2A} \cdots\cdot C_{14}$, $C_{3A} \cdots\cdot C_{29}$, $C_{19} \cdots\cdot C_{10}$ are shortest contacts in the intrasheet layers. The evolution of these $C \cdots\cdot C$ contacts as a function of temperature is shown in Figure 7.22.

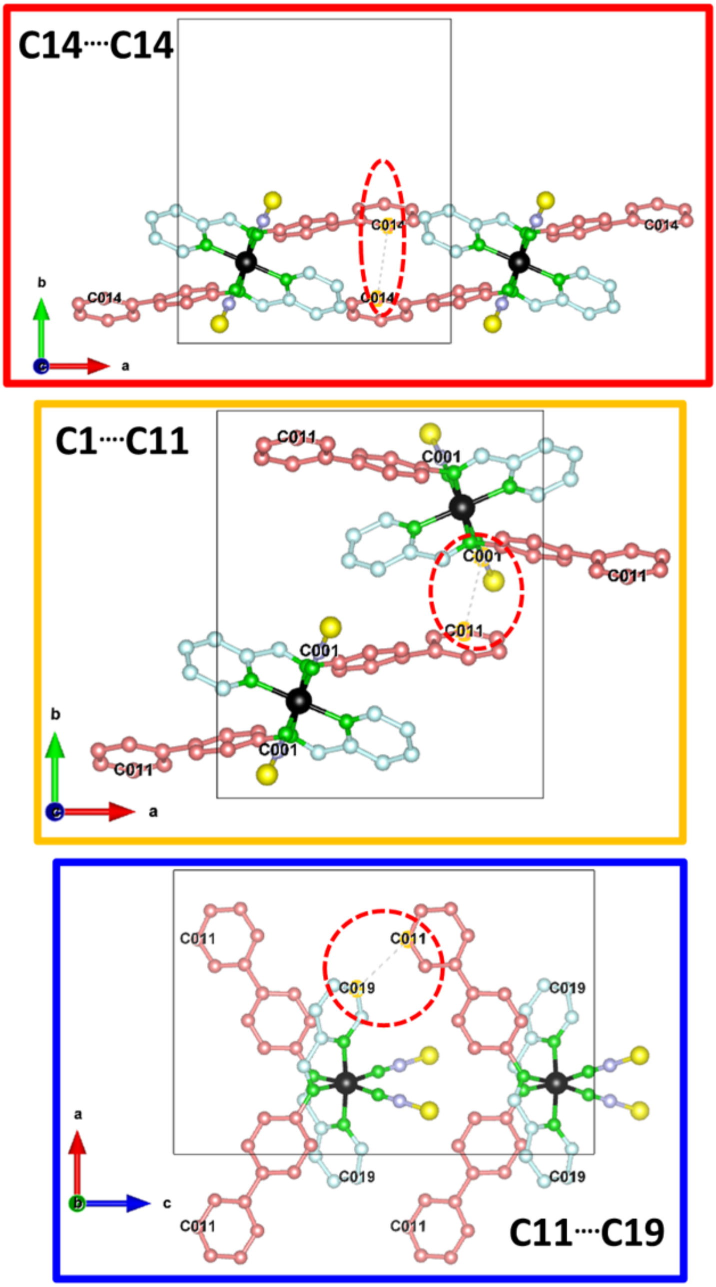

Figure E.12: The shortest $C \cdots C$ intermolecular distances in the orthorhombic polymorph. Contacts are considered short if $C \cdots C < 3.5\,\text{Å}$. $C_{14} \cdots C_{14}$ and $C_{11} \cdots C_{1}$ are the shortest contact in the intersheet layers. $C_{19} \cdots C_{10}$ is the shortest intrasheet contact. The evolution of these $C \cdots C$ contacts as a function of temperature is shown in Figure 7.22.

E.5 Pressure-dependent crystal structure

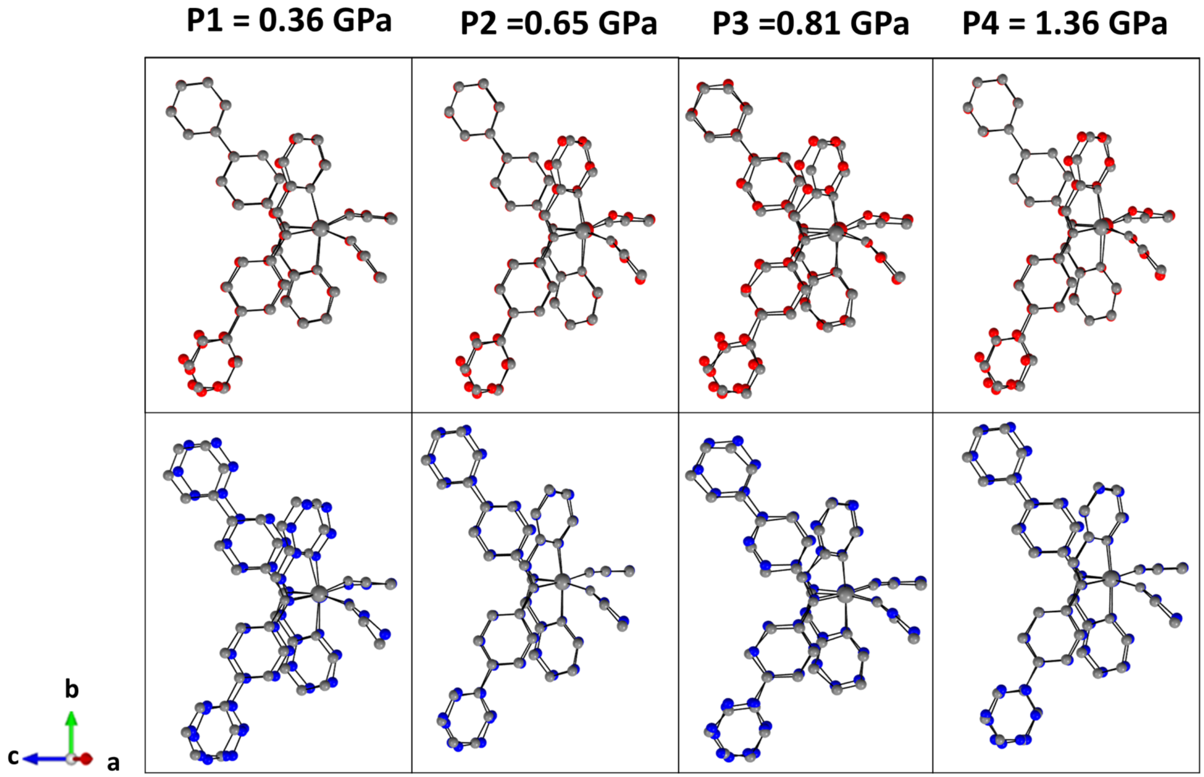

Figure E.13: Overlay of the molecular unit of the HS (red) and LS (blue) states at ambient pressure and with applied pressure (gray) for the monoclinic polymorph. Hydrogen atoms are left out for clarity.

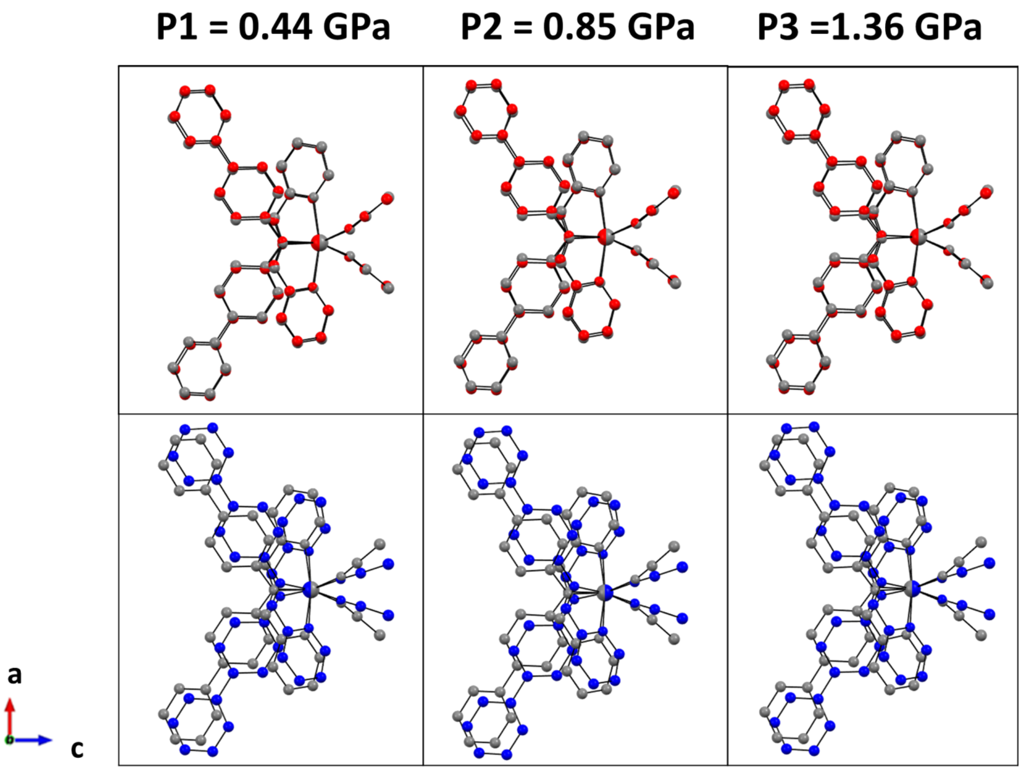

Figure E.14: Overlay of the molecular unit of the HS (red) and LS (blue) states at ambient pressure and with applied pressure (gray) for the orthorhombic polymorph. Hydrogen atoms are left out for clarity.

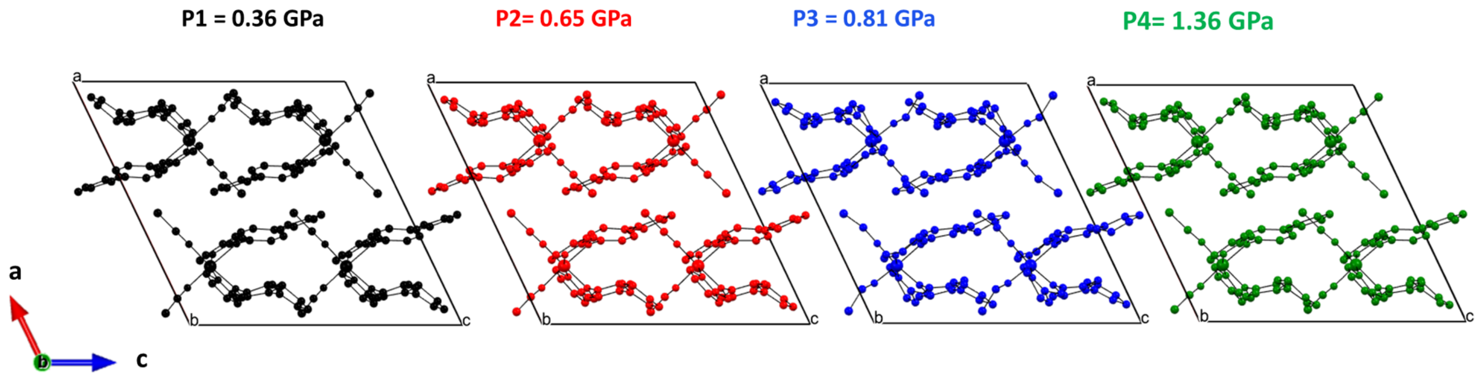

Figure E.15: An illustration of the monoclinic polymorph of [Fe(PM–Bia)$_2$(NCS)$_2$] projected along the *b*-direction, showing the impact of applied pressure on the crystal packing (P1 in black, P2 in red, P3 in blue, and P4 in green). Atoms of hydrogen are left out for clarity.

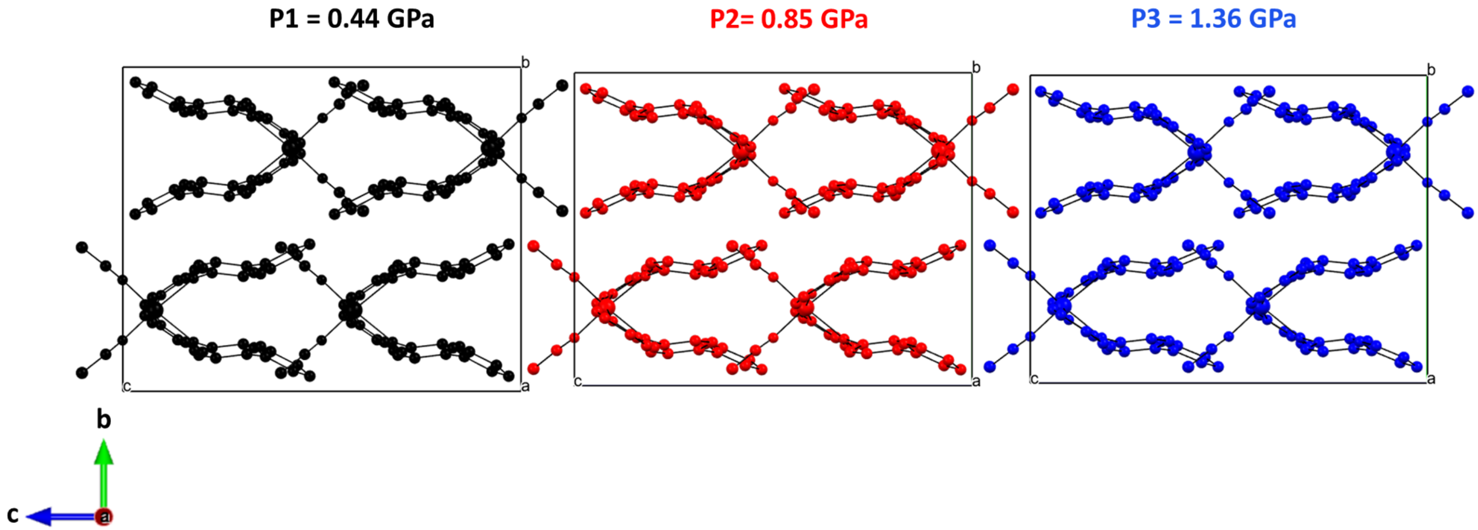

Figure E.16: An illustration of the orthorhombic polymorph of [Fe(PM–Bia)$_2$(NCS)$_2$] projected along the *a*-direction, showing the impact of applied pressure on the crystal packing (P1 in black, P2 in red, and P3 in blue). Hydrogen atoms are omitted for clarity.

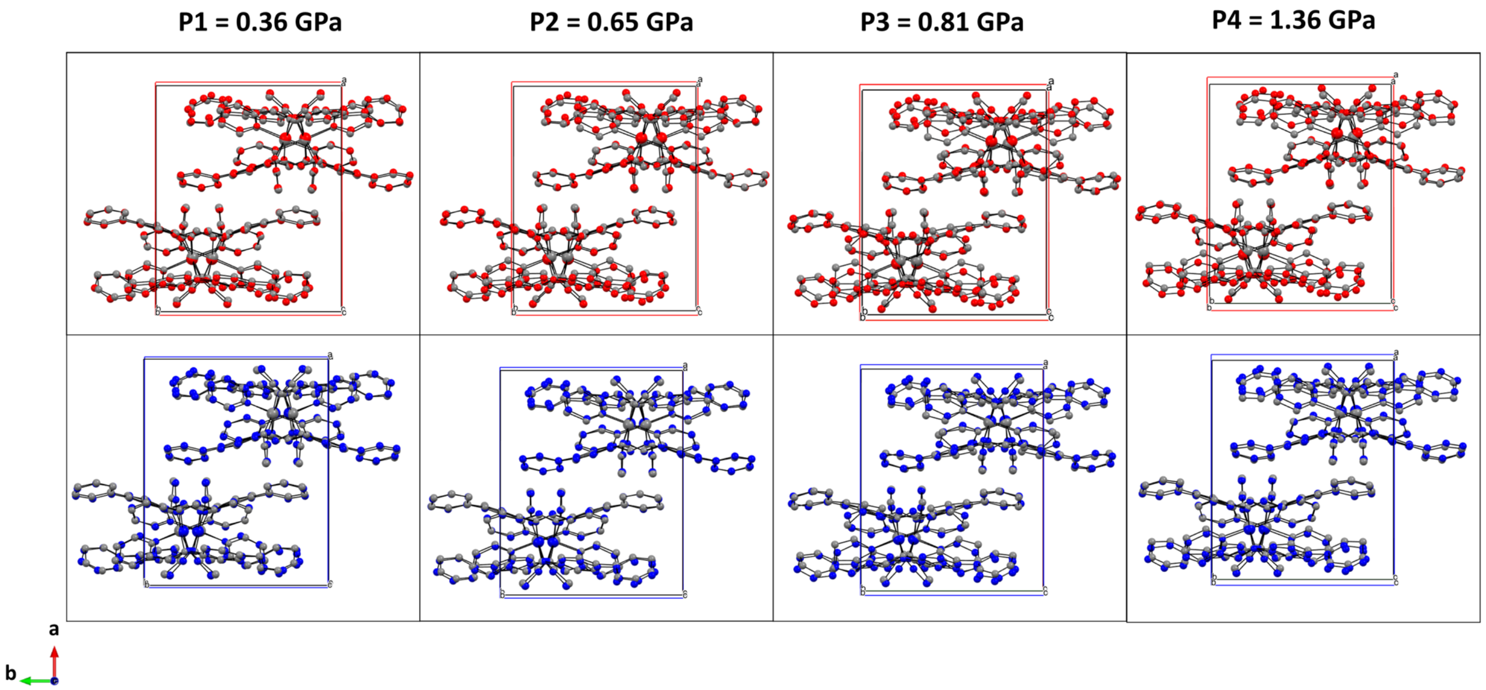

Figure E.17: Overlay of the structure of the HS (red) and LS (blue) states at ambient pressure and the crystal structure with applied pressure (gray) for the monoclinic polymorph projected along the c-direction. Hydrogen atoms are omitted for clarity.

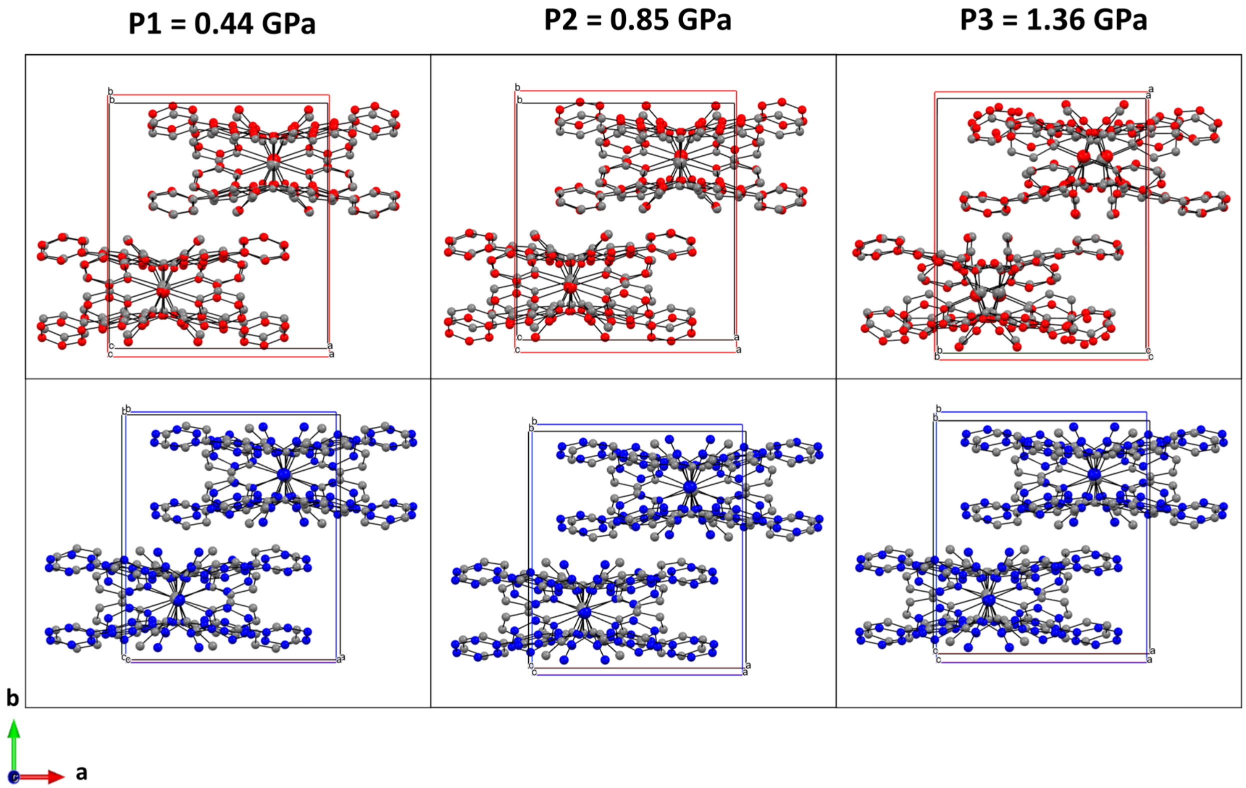

Figure E.18: Overlay of the structure of the HS (red) and LS (blue) states at ambient pressure and the crystal structure with applied pressure (gray) for the orthorhombic polymorph projected along the *c*-direction. Hydrogen atoms are omitted for clarity.

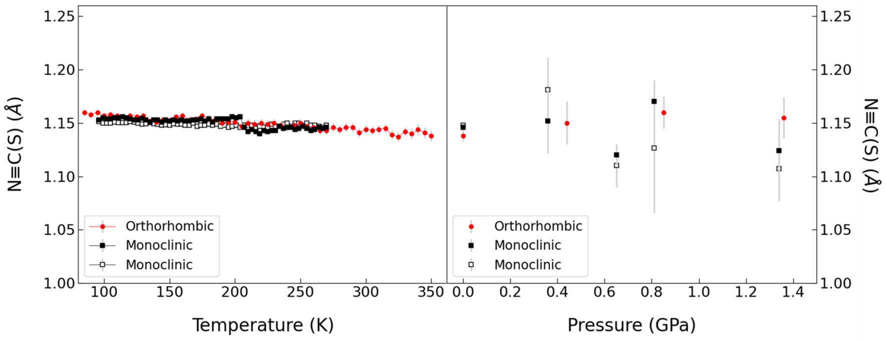

Figure E.19: The $N \equiv C(S)$ bond length as a function of temperature (left) and pressure (right). Red circles correspond to the orthorhombic polymorph, and the full and open black squares correspond to the monoclinic polymorph. Lines are guides to the eyes.

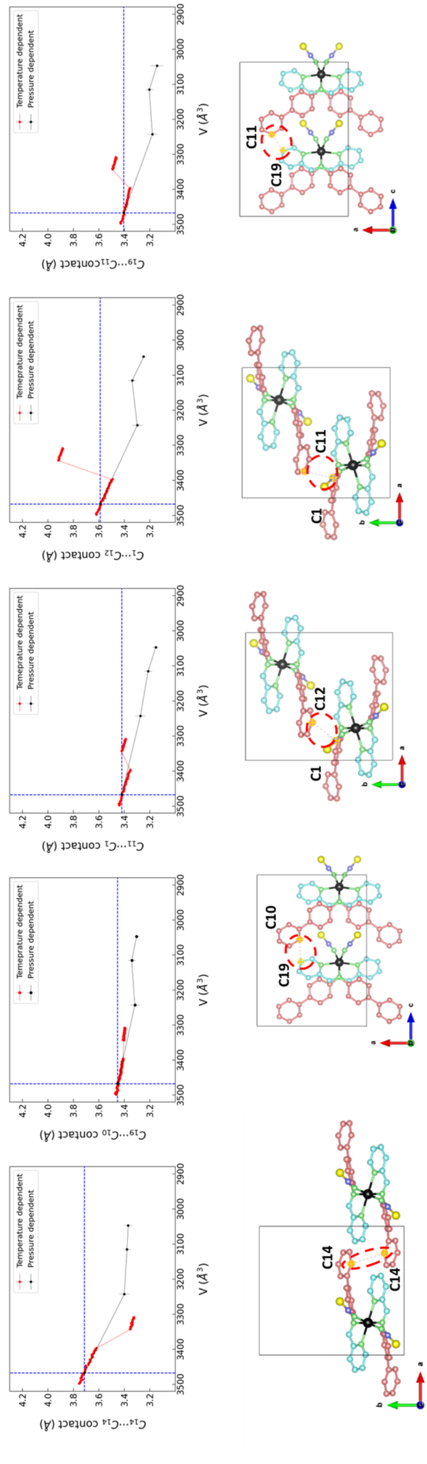

Figure E.20: The shortest intermolecular $C\cdots C$ distance in the orthorhombic polymorph as a function of the unit cell volume. The closed and open symbols are obtained from temperature and pressure studies, respectively.

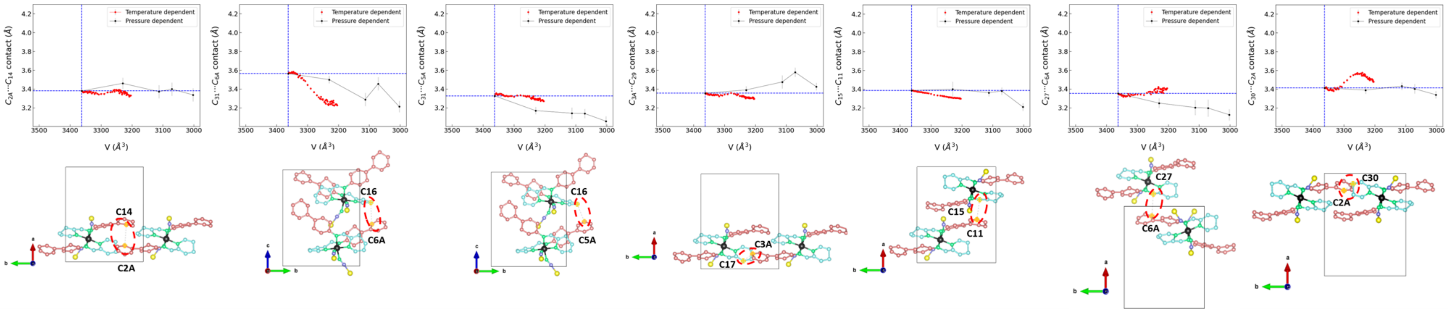

Figure E.21: The shortest intermolecular $C \cdots C$ distance in the monoclinic polymorph as a function of the unit cell volume. The closed and open symbols are obtained from temperature and pressure studies, respectively.

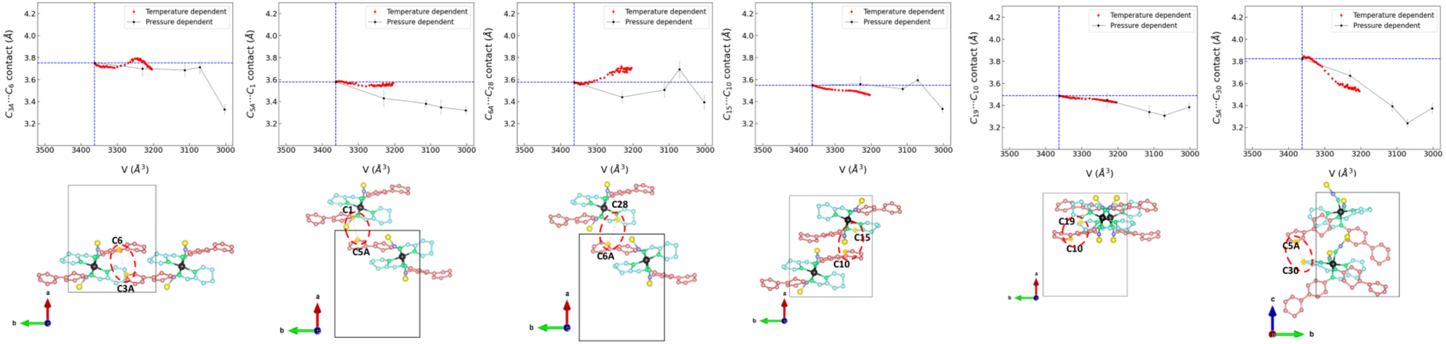

Figure E.22: The shortest intermolecular $C \cdots C$ distance under applied pressure for the monoclinic polymorph as a function of the unit cell volume. The closed and open symbols are obtained from temperature and pressure studies, respectively.

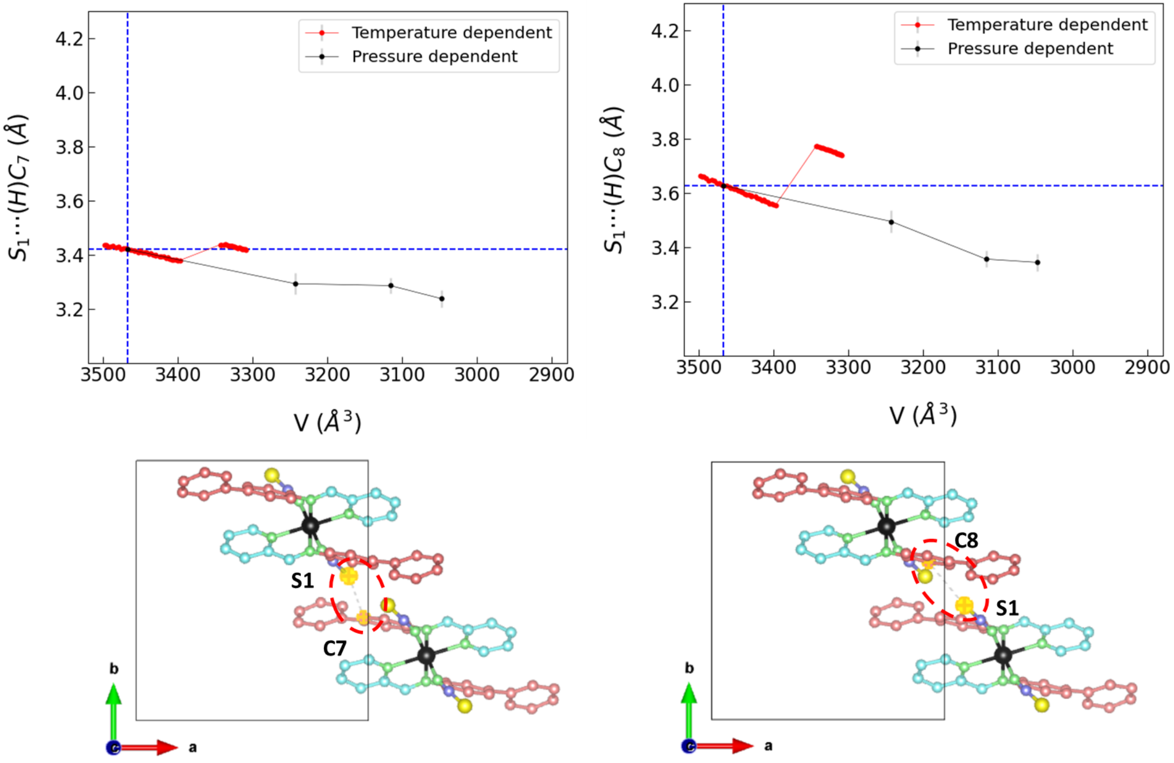

Figure E.23: The shortest intermolecular $S \cdots \cdot (H) - C$ distance for the orthorhombic polymorph as a function of the unit cell volume. The closed and open symbols are obtained from temperature and pressure studies, respectively.

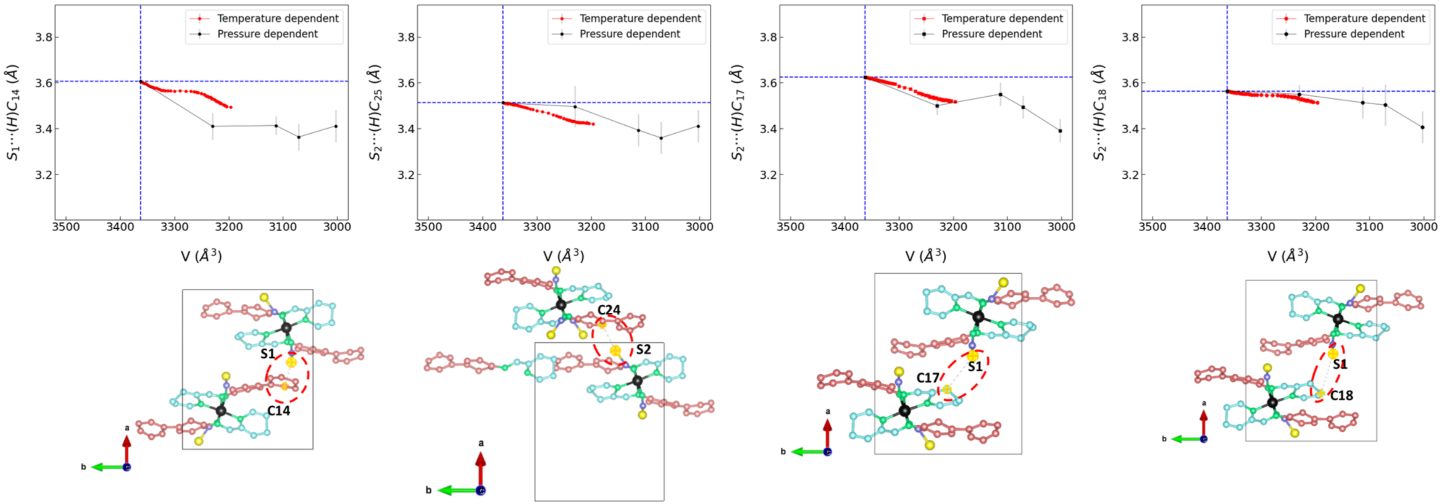

Figure E.24: The shortest intermolecular $S \cdots \cdot (H) - C$ distance for the monoclinic polymorph as a function of the unit cell volume. The closed and open symbols are obtained from temperature and pressure studies, respectively.

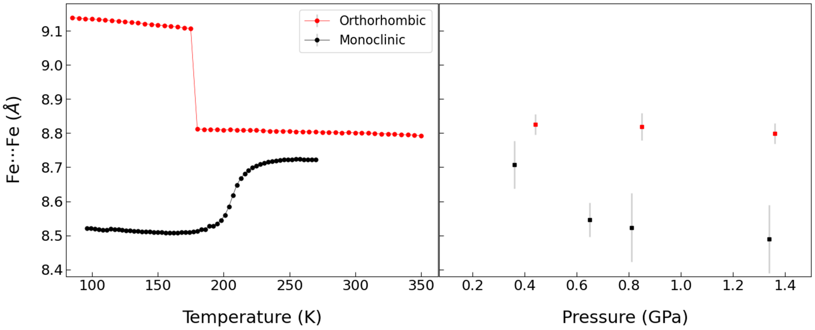

Figure E.25: Evolution of shortest $Fe \cdots Fe$ distance as a function of temperature (left) and pressure (right) for both polymorphs. The red circles and black squares are for orthorhombic and monoclinic polymorphs, respectively. Lines are guides to the eyes.

Table E.1: Experimental data for the orthorhombic polymorph of Fe(PMBia)$_2$(NCS)$_2$ as a function of pressure.

	Orthorhombic		
Chemical Formula	$FeN_6S_2C_{38}H_{28}$		
Pressure (GPa)	0.44	0.85	1.36
a (Å)	12.7982(5)	12.7298(15)	12.6944(5)
b (Å)	14.3600(6)	13.881(6)	13.6380(6)
c (Å)	17.6500(6)	17.6350(18)	17.5970(6)
V (Å^3)	3243.8(2)	3116.1(2)	3046.5(2)
Density (g cm^{-1})	1.4113	1.4691	1.5027
μ (m m^{-1})	0.147	0.154	0.157
Radiation type	Synchrotron		
Wavelength (Å)	0.413(3)		
Diffractometer	κ- diffractometer using a Pilatus 1M CdTe		
No. of measured,	13625	13975	13295
symmetry independent,	1899	1851	1812
and observed [I>2σ(I)] reflections	1034	1123	1050
R$_{int}$	0.1747	0.1443	0.1845
(sinθ/λ)(Å^{-1})	0.67	0.67	0.67
No. of parameters	113	113	95
R[F^2>2σ(F^2)]	0.1583	0.1304	0.1733
wR(F^2)	0.0964	0.0986	0.1425

Table E.2: Experimental data for the monoclinic polymorph of Fe(PM-Bia)$_2$(NCS)$_2$ as a function of pressure.

	Monoclinic			
Chemical Formula	$FeN_6S_2C_{38}H_{28}$			
Pressure (GPa)	0.36	0.65	0.81	1.34
a (Å)	16.8630(2)	16.6940(2)	16.5280(2)	16.3160(2)
b (Å)	12.37500(10)	12.22100(10)	12.18400(10)	12.14190(10)
c (Å)	17.2130(2)	16.9460(2)	16.9020(2)	16.8480(2)
β (°)	116.1200(15)	115.8500(15)	115.8800(15)	115.8600(15)
V (Å^3)	3225.17(7)	3111.34(7)	3062.32(7)	3003.48(7)
Density (g cm^{-1})	1.4183	1.4701	1.4937	1.5229
μ (m m^{-1})	0.147	0.152	0.155	0.158
Radiation type	Synchrotron			
Wavelength (Å)	0.413(3)			
Diffractometer	κ- diffractometer using a Pilatus 1M CdTe			
No. of measured,	13763	13772	12592	13313
symmetry independent	3132	3054	1515	2917
and observed [I>2σ(I)] reflections	1317	1358	859	1376
R$_{int}$	0.227	0.2057	0.306	0.2481
(sinθ/λ)(Å^{-1})	0.55	0.55	0.55	0.55
No. of parameters	153	155	152	155
R[F^2>2σ(F^2)]	0.2145	0.1727	0.2840	0.2078
wR(F^2)	0.1388	0.1275	0.2305	0.1791

Table E.3: π-π interactions of the two polymorphs as identified using the Mercury software [319]. Centroid-to-centroid distances (D) and their relative angle of orientation ($\measuredangle$), are utilized to estimate the strength of the interactions. The term "No." indicates the number of interactions. **"M"** stands for monoclinic polymorph and **"O"** stands for orthorhombic polymorph

	Strong											
	P1$_M$ = 0.36 GPa **P1$_O$ = 0.44 GPa**			**P2$_M$ = 0.65 GPa** **P2$_O$ = 0.85 GPa**			**P3$_M$ = 0.81 GPa** **P3$_O$ = 1.36 GPa**			**P4$_M$ = 1.34 GPa** **P4$_O$ = 2.02 GPa**		
	No.	**D** (Å)	$\measuredangle$ (∘)	**No.**	**D** (Å)	$\measuredangle$ (∘)	**No.**	**D** (Å)	$\measuredangle$ (∘)	**No.**	**D** (Å)	$\measuredangle$ (∘)
Pccn	–	–	–	–	–	–	–	–	–	-	-	-
P2$_1$/c	2	3.97	0	2	4	0	1	3.71	0	2	3.98	0
		4.81	30.8		4.85	31.38					4.8	29.84
	Moderate											
Pccn	3	5.11	33.82	4	5.08	31.95	4	5.06	30	-	-	-
		4.68	53.32		4.5	48.3		4.39	46.42			
		6.63	27.18		6.55	23.36		6.6	23.52			
					6.76	36.08		6.69	34.28			
P2$_1$/c	4	5.55	42.75	5	5.35	41.39	2	5.33	40.66	4	5.12	41.11
		4.95	48.57		4.94	49.65		6.25	18.77		4.84	50.36
		4.68	54.27		6.17	15.21					6.17	13.86
		6.42	13.85		6.73	25.17					6.67	21.93
					4.54	53.38						

E.6 Neutron

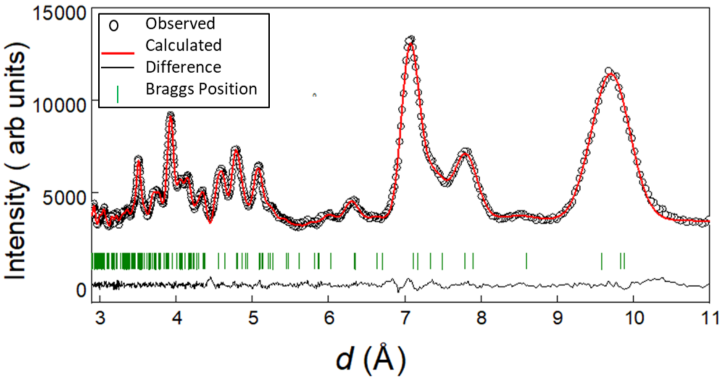

Figure E.26: Room temperature neutron powder diffraction pattern for the monoclinic polymorph (λ =2.45 Å).

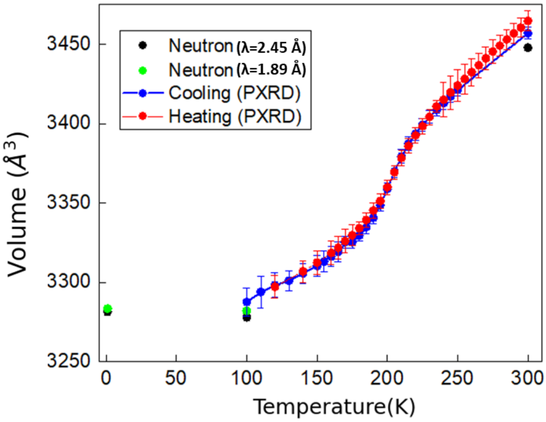

Figure E.27: Temperature dependence of the unit cell volume of the monoclinic polymorph, obtained from neutron powder diffraction data obtained by the Le Bail method by using the program *JANA2006* [288]. The black and green symbols represent the data for λ= 2.45 Å and 1.89 Å, respectively. The red and blue symbols correspond to the data obtained from powder X-ray diffraction during heating and cooling, respectively.

Band / Volume 618
$Na_5YSi_4O_{12}$-type Na^+ superionic conductors for solid-state batteries
A. Yang (2023), X, 150 pp
ISBN: 978-3-95806-731-8

Band / Volume 619
Development of industry-scalable processes for nanocrystalline silicon oxide in silicon heterojunction solar cells
D. Qiu (2023), 202 pp
ISBN: 978-3-95806-734-9

Band / Volume 620
Photonic Sintering of Garnet-Based Solid-State Batteries
W. S. Scheld (2024), XII, 153 pp
ISBN: 978-3-95806-737-0

Band / Volume 621
Ceria-based composites for application in Oxygen transport membranes
L. Fischer (2024), xiii, 216 pp
ISBN: 978-3-95806-739-4

Band / Volume 622
Investigations of Air Quality Aspects with the Urban Climate Model PALM4U
R. Wegener, U. Javed, R. Dubus, and D. Klemp (2024), 93 pp
ISBN: 978-3-95806-741-7

Band / Volume 623
The Chemical Budget of Radicals and Reaction Mechanisms of the Atmospheric Oxidation of Monoterpenes Investigated in the Atmospheric Simulation Chamber SAPHIR
Y. S. Pang (2024), VI, 158 pp
ISBN: 978-3-95806-742-4

Band / Volume 624
Optimizing spectral electrical impedance tomography technology for improved subsurface characterization
H. Wang (2024), xxix, 113 pp
ISBN: 978-3-95806-744-8

Band / Volume 625
On a multi-spectral method for measuring aerosol properties, suitable for operation on iagos passenger aircraft
P. Weber (2024), ca 123 pp
ISBN: 978-3-95806-746-2

Band / Volume 626
Modellierung der flächendifferenzierten Grundwasserneubildung für Schleswig-Holstein
Endbericht
I. McNamara, B. Tetzlaff, T. Wolters, F. Wendland (2024), 96 pp
ISBN: 978-3-95806-748-6

Band / Volume 627
Modeling orographic gravity waves from source to termination to improve parameterization schemes in climate models
S. Rhode (2024), xii, ii, 138 pp
ISBN: 978-3-95806-750-9

Band / Volume 628
Abscheidung kolumnarer Wärmedämmschichten mittels Suspensionsplasmaspritzen (SPS) und Plasma Spray – Physical Vapor Deposition (PS-PVD) Prozess
J. Joeris (2024), vii, 133 pp
ISBN: 978-3-95806-752-3

Band / Volume 629
Structure and properties of electrochemical interfaces from first principles simulations
R. Tesch (2024), xvi, 161 pp
ISBN: 978-3-95806-753-0

Band / Volume 630
Elucidation of Barocaloric Effect in Spin Crossover Compounds
H. Shahed (2024), x, 261 pp
ISBN: 978-3-95806-758-5

Weitere ***Schriften des Verlags im Forschungszentrum Jülich*** unter
http://wwwzb1.fz-juelich.de/verlagextern1/index.asp

Energie & Umwelt / Energy & Environment
Band / Volume 630
ISBN 978-3-95806-758-5

JÜLICH
Forschungszentrum